# Integrating coupled simulation of surface water and groundwater with Artificial Intelligence

Jiangwei Zhang

Submitted in accordance with the requirements for the degree of
Doctor of Philosophy

The University of Leeds
School of Civil Engineering
January 2024

# Declaration

The candidate confirms that the work submitted is his own, except where work which has formed part of jointly authored publications has been included. The contribution of the candidate and the other authors to this work has been explicitly indicated below. The candidate confirms that appropriate credit has been given within the thesis where reference has been made to the work of others.

Publication 1 has been reproduced in some aspects of Chapter 3; Publication 2 has been reproduced in some aspects of Chapter 4; Publication 3 has been reproduced in some aspects of Chapter 5; Publication 4 has been reproduced in some aspects of Chapter 6.

1. **Zhang J,** Chen X, Khan A, Zhang Y-k, Kuang X, Liang X, et al. Daily runoff forecasting by a deep recursive neural network. Journal of Hydrology 2021; 596.

2. **Zhang J**, Liang X, Zhang Y-K, Chen X, Ma E, Schilling K. Groundwater responses to recharge and flood in riparian zones of layered aquifers: An analytical model. Journal of Hydrology 2022; 614.

3. **Zhang J**, Liang X, Zeng L, Chen X, Ma E, Zhou Y, Zhang Y-K. Deep transfer learning for groundwater flow in heterogeneous aquifers using a simple analytical model. Journal of Hydrology, 626: 130293

4. **Zhang J**, Liang X, Chen X, Tian Y, Ma E, Zhou Y, Zhang Y-K. Catchment scale groundwater prediction based on deep transfer learning and a simple analytical model. Journal of Hydrology (to be submitted)

In the first publication, the candidate carried out the data collection, coding, methodology, result analysis and writing the original draft. Dr. Xiaohui Chen provided supervision on conceptualization, theory and writing, Dr. Jonathan Nuttall provided help on review and comment. Prof. You-kuan Zhang, Dr. Xiuyu Liang, Dr. Xingxing Kuang provided assistance with paper revision. And Dr. Amirul Khan, Dr. Maria L. Taccari provided guidance on paper editing.

In the second publication, the candidate carried out the conceptualization, methodology and writing original draft. Dr. Xiuyu Liang provided supervision on conceptualization, theory and writing. Dr. Enze Ma provided help on methodology and software. Prof. You-kuan Zhang, Dr. Xiaohui Chen and Dr. Keith Schilling gave comments on writing.

In the third publication, the candidate carried out the coding, modelling, methodology, result analysis and writing the original draft. Dr. Xiuyu Liang provided supervision on conceptualization, theory and writing. Dr. Enze Ma provided help with methodology and software. Prof. You-kuan Zhang, Dr. Xiaohui Chen and Mr. Yunqiu Zhou gave comments on writing.

In the fourth publication, the candidate carried out the coding, modelling, methodology, result analysis and writing original draft. Dr. Xiuyu Liang and Dr. Xiaohui Chen provided supervision on conceptualization, theory and writing. Prof. You-kuan Zhang, Dr. Enze Ma and Mr. Yunqiu Zhou gave comments on writing.

# Acknowledgement

I am deeply honoured to be a part of the joint project between the University of Leeds and the Southern University of Science and Technology (SUSTech). I would like to express my sincere gratitude to SUSTech for providing the scholarship that has given me the financial support necessary to pursue my studies.

I extend my heartfelt appreciation to my supervisors, Dr. Xiaohui Chen and Dr. Amirul Khan from the University of Leeds, Prof. You-Kuan Zhang and Dr. Xiuyu Liang from SUSTech. Their guidance and advice on the direction of my research were invaluable. During the process of writing my thesis, they patiently provided me with assistance and clarifications whenever I faced challenges or uncertainties. Their valuable feedback and extensive efforts were instrumental in the improvement of my work. I would also like to thank Dr. Xiuyu Liang and Dr. Xiaohui Chen for their recommendations and financial support, which allowed me to participate in academic conferences such as AGU Fall Meeting 2022, The 2022 International Symposium on Resilient and Sustainable Cities, and the 22nd Annual General Meeting of UK-CARE.

I am grateful to the members of the Groundwater Dynamics team at SUSTech, including Dr. Enze Ma, Mrs. Yanli Xiu, Ms. Yanling Tang, Mr. Yunqiu Zhou, and others, for their assistance and support during my time at SUSTech.

Special thanks go to the members of the Geomodelling and AI group at the University of Leeds, including Dr. Yue Ma, Dr. Liyang Xu, Mr. Kai Wang, Mr. Sulaiman Abdullah, Mr. He Yang, Mr. Shangqi Ge, as well as Dr. Jihua Zhai and Miss Yuyan Huang from the School of Civil Engineering. Their support and encouragement during the challenging times of the pandemic were truly uplifting. Moreover, their valuable advice and evaluations greatly contributed to the advancement of my research.

Lastly, I want to express my heartfelt gratitude to my wife, Dr. Qiang Wang, and my parents for their unwavering support throughout this journey.

All these individuals and institutions have played a pivotal role in my academic and personal growth, and I am truly grateful for their contributions to my success.

# Abstract

Surface water and groundwater, integral to the hydrological cycle, engage in complex hydraulic interactions and frequent transformations. Isolating surface water and groundwater systems in individual studies often fails to capture and analyse their interrelationships, limiting the comprehensive understanding of regional water resources. Additionally, conventional physics-based coupled models encounter challenges arising from the complexities and non-linearity of interactions, impeding their accuracy in simulation results.

To address this challenge, this thesis proposes a novel framework that integrates artificial intelligence and physics-based coupled models to simulate variations in surface water and groundwater, establishing a foundation for integrated water resource management. Specifically, the study develops a boundary-coupled framework to model interactions between surface water and groundwater. In this framework, a data-driven deep learning model is employed to simulate surface water flow. Additionally, physics-based analytical models are used to describe groundwater movement in riparian zones, while simplifying river behaviour to a Dirichlet boundary condition to assimilate data from the surface water model. Subsequently, the simulated values from analytical solutions serve as the source data, while groundwater observation data is employed as the target data. A transfer learning model is then be utilized to learn the features of the source data and, in conjunction with the target dataset, facilitate the prediction and regression of groundwater. Finally, the framework is applied at the watershed scale to predict and model catchment-scale surface water flow and groundwater head.

In this framework, the thesis assesses the influence of various input variables on surface water prediction, explores the effect of groundwater layer heterogeneity, and validates the effectiveness of the deep transfer learning approach, particularly in catchment-scale predictions. The main conclusions are as follows:

1. The selection of model inputs greatly influences accuracy. The PCA method effectively enhances the precision of the deep RNN model, especially in scenarios with numerous input variables. It achieves this by distilling essential information, categorizing original data into several comprehensive variables.

2. The two-layer structure significantly influences groundwater flow responses to hydrological events. During recharge events with a less permeable upper layer, lateral discharge to the river is hindered, directing more groundwater downward into the more permeable lower layer. Conversely, when the upper layer is more permeable, greater lateral flow into the river occurs, with less downward flow into the less permeable lower layer. During a flood event with a less permeable upper layer, river water predominantly infiltrates the more permeable lower layer initially, then flows upward into the upper layer, creating a vertical flow. The direction of this flow reverses during the recession period. However, this phenomenon is not evident when the upper layer is more permeable than the lower layer.

3. The transfer learning method can enhance the capacity of analytical solutions for heterogeneous aquifers. By integrating analytical knowledge with the neural network, the analytical solution-transfer learning method significantly improves hydraulic head prediction accuracy. Even for very sparse training data, the analytical solution-transfer learning method still performs more satisfactorily than the traditional deep learning method.

4. The analytical solution-transfer learning method is also effective at the catchment scale. The analytical solution-transfer learning method can obtain more accuracy and robust results than traditional deep learning methods with the same training dataset.

# CONTENT

# LIST OF FIGURES

# LIST OF TABLES

# LIST OF ABBREVIATIONS

| | |
|---|---|
| AI | Artificial Intelligence |
| ANN | Artificial Neural Network |
| BCNN | Bayesian Convolutional Neural Network |
| CATHY | Catchment Hydrology |
| CNN | Convolutional Neural Networks |
| DBPNN | Deep Back Propagation Neural Network |
| DL | Deep Learning |
| DNN | Deep Neural Network |
| GRACE | Gravity Recovery And Climate Experiment |
| GRU | Gated Recurrent Unit |
| GRU-HD | Gru With A 1-D Hydrodynamic Model |
| HBV | Hydrologiska Byråns Vattenbalansavdelning |
| HGS | Hydrogeosphere |
| IQR | Interquartile Range |
| LSTM | Long-Short Term Memory |
| LSTM-ED | Long Short-Term Memory Based Encoder-Decoder |
| MAE | Mean Absolute Error |
| ML | Machine Learning |
| MLP | Multi-Layer Perceptron |
| MSE | Means Square Error |
| NSE | Nash-Sutcliffe Efficiency |
| ODE | Ordinary Differential Equations |
| PCA | Principal Component Analysis |
| PDE | Partial Differential Equations |
| PINN | Physics-Informed Neural Networks |
| R2 | The Coefficient of Determination |
| RCP | Representative Concentration Pathways |
| RCR | Relative Change Rate |
| RMSE | Root Means Square Error |
| RNN | Recurrent Neural Network |
| SVM | Support Vector Machine |
| SWAT | Soil Water Assessment Tool |
| TgCNN | Theory-Guided Convolutional Neural Network |
| TgFCNN | Theory-Guided Fully Convolutional Neural Network |
| TgNN | Theory-Guided Neural Network |
| TL | Transfer Learning |
| VIC | Variable Infiltration Capacity Model |
| WMAPE | Weighted Mean Absolute Percentage Error |

# 462 LIST OF SYMBOLS

| | |
|---|---|
| $b$ | Biase vector in neural network model |
| $B$ | Thickness of aquifer |
| $B_1$ | Thickness of aquifer 1 |
| $B_2$ | Thickness of aquifer 2 |
| $B_D$ | Dimensionless thickness of aquifer |
| $B_s$ | Thickness of saturated zone |
| $B_u$ | Thickness of unsaturated zone |
| $C_0(z)$ | The zero-order approximations of the soil moisture capacity |
| $Ccm$ | Correlation coefficient matrix |
| $Ccr$ | Principal component contribution rate |
| $CCR$ | Cumulative contribution rate |
| $Cs_t$ | Memory cell state in timestep t |
| $D$ | Dataset |
| $\overline{D}$ | Average value of dataset $D$ |
| $D_{max}$ | Maximum values of data $D$ |
| $D_{min}$ | Minimum values of data $D$ |
| $D_N$ | Normalized dataset |
| $D_s$ | Source dataset |
| $D_{sn}$ | Normalized source dataset |
| $D_t$ | Target dataset |
| $Fg_t$ | Forget gate in timestep t |
| $fv$ | Feature values |
| $h$ | Hydraulic head in saturated zone |
| $h_0$ | Initial head |
| $h_1$ | Hydraulic head in aquifer 1 |
| $h_2$ | Hydraulic head in aquifer 2 |
| $h_b(t)$ | Fluctuating river stage |
| $h_D$ | Dimensionless hydraulic head |
| $\tilde{h}$ | Average saturated thickness of aquifer |
| $H_i$ | Output of $i$th hidden layer |
| $Hs_t$ | Hidden state in timestep t |
| $\mathcal{H}e(\cdot)$ | Heaviside function |
| $Ig_t$ | Input gate in timestep t |
| $k_0(z)$ | The zero-order approximations of the relative hydraulic conductivity |
| $K$ | Hydraulic conductivity |
| $K_1$ | Hydraulic conductivity in aquifer 1 |
| $K_{1D}$ | Defined as $K_{1D} = \frac{K_{z1}}{K_{x1}}$ |

| | |
|---|---|
| $K_2$ | Hydraulic conductivity in aquifer 2 |
| $K_{2D}$ | Defined as $K_{2D} = \frac{K_{z2}}{K_{x2}}$ |
| $K_x$ | Hydraulic conductivity in x-direction |
| $K(x,y)$ | Heterogeneous hydraulic conductivity |
| $K_z$ | Hydraulic conductivity in z-direction |
| $l$ | Correlation length |
| $L$ | Distance between of the water divide and the river |
| $M$ | Width of aquifer in the y-direction |
| $n$ | Size of the data |
| $n^*$ | Number of retraining datasets |
| $NN(X,\theta)$ | Result of deep neural network |
| $O$ | The output is a vector $O = NN(X,\theta)$ |
| $q_E(x,t)$ | Darcy's velocity across the interface of the two layers |
| $Q(t)$ | Lateral discharge of groundwater |
| $Q_1(t)$ | Lateral discharge of aquifer 1 |
| $Q_2(t)$ | Lateral discharge of aquifer 2 |
| $Q_D$ | Defined as $Q_D = \frac{Q}{h_0 K_x}$ |
| $Rg_t$ | Reset gate in timestep t |
| $R_K$ | Defined as $R_K = \frac{K_{x2}}{K_{x1}}$ |
| $R_S$ | Defined as $R_S = \sqrt{\frac{S_{s2}}{S_{s1}}}$ |
| $R_v$ | Defined as $R_v = \frac{K_{1D}}{K_{2D} R_K^2}$ |
| $s$ | Groundwater drawdown |
| $S_s$ | Specific storage |
| $S_y$ | Specific yield |
| $S_{yD}$ | Defined as $S_{yD} = \frac{S_y}{S_s L}$ |
| $t_D$ | Dimensionless time |
| $u$ | Hydraulic head in the unsaturated zone |
| $W(t)$ | Recharge rate |
| $W_D$ | Defined as $W_D = \frac{WL}{K_x h_0}$ |
| $W_{diff}$ | Maximum value of $W(t)$ |
| $We$ | Weight matrixes |
| $W^*(t)$ | Recharge rate including the noise |
| $x_D$ | Dimensionless x coordinate |
| $X$ | Input vector |
| $X_s$ | Input vector from a source dataset |

| | |
|---|---|
| $X_t$ | Input vector from a target dataset |
| $Y_s$ | Observation data from a source dataset |
| $Y_t$ | Observation data from a target dataset |
| $z_D$ | Dimensionless z coordinate |
| $Zg_t$ | Update gate in timestep t |
| $\alpha$ | Percentage |
| $\varepsilon$ | Uniform random variable ranging from $-1$ to 1 |
| $\theta_0$ | Parameter of the pre-training model |
| $\theta_N$ | Deep neural network parameter $\theta_N = \{We_i, b_i\}_{i=1}^{m+1}$ |
| $\theta_T$ | Parameters after fine-tuning |
| $\sigma$ | Activation function |
| $\sigma_D$ | Standard deviations of dataset $D$ |
| $\kappa$ | Constitutive exponent |
| $\xi$ | The instantaneous location of the moving water table |
| $\psi(\omega_n, x)$ | Transform kernels |
| $\omega_n$ | Transform eigenvalues |

**Handwritten symbols and double-struck symbols are intermediate variables used for calculation and writing convenience, with no actual significance. Therefore, they are not displayed in this table.*

# LIST OF PUBLICATIONS

**1. Publication list (Papers directly contributing to the thesis):**

The research findings from Chapter 3, focusing on the deep learning model for surface runoff depth have been compiled into Publication 1. The research content from Chapter 4, delving into analytical solutions for layered heterogeneous models in the subsurface flow zone, has been compiled into Publication 2. The research content from Chapter 5, centred on the transfer learning model based on analytical solutions, has been compiled into Publication 3. Publications 1-3 published in the top hydrology journal, the Journal of Hydrology. Part of the research content of Chapter 6 on the watershed-scale groundwater transfer learning model has been compiled into Publication 4 and will be submitted to the Journal of Hydrology. The following are detailed information on the relevant papers:

1. **Zhang J,** Chen X, Khan A, Zhang Y-k, Kuang X, Liang X, et al. Daily runoff forecasting by deep recursive neural network. Journal of Hydrology 2021; 596. (**IF: 6.4, TOP, Citations 62**)
2. **Zhang J**, Liang X, Zhang Y-K, Chen X, Ma E, Schilling K. Groundwater responses to recharge and flood in riparian zones of layered aquifers: An analytical model. Journal of Hydrology 2022; 614. (**IF: 6.4, TOP, Citations 7**)
3. **Zhang J**, Liang X, Zeng L, Chen X, Ma E, Zhou Y, Zhang Y-K. Deep transfer learning for groundwater flow in heterogeneous aquifers using a simple analytical model. Journal of Hydrology, 626: 130293. (**IF: 6.4, TOP**)
4. **Zhang J**, Liang X, Tian Y, Zhang Y-K, Chen X. Catchment scale groundwater prediction based on deep transfer learning and a simple analytical model. Journal of Hydrology (to be submitted). (**IF: 6.4, TOP**)

**2. Other papers indirect contributing to the knowledge of the thesis**

In addition, thanks for my colleagues from the Xiuyu Liang's Research Group at Southern University of Science and Technology and the Xiaohui Chen's Research Group at the University of Leeds for their kind discussions on various academic topics and generously including me as a co-author. The discussions with them have provided me with a lot of inspiration. The following are detailed information of these papers:

(1) Ma E, Liang X, **Zhang J**, Zhang YK. Dynamics in Diffusive Emissions of Dissolved Gases from Groundwater Induced by Fluctuated Ground Surface Temperature. Environ Sci Technol 2022; 56: 2355-2365.

(2) Zhou Y, Liang X, Ma E, Chen K, **Zhang J**, Zhang Y-K. Effect of unsaturated flow on groundwater-river interactions induced by flood event in riparian zone. Journal of Hydrology 2023; 620.

(3) **Zhang J**, Liang X, Wang CY. Capillary Impact on Tidal Response of Groundwater in Unconfined Aquifers With Finite Thickness, Anisotropy and Wellbore Storage—An Analytical Model. Water Resources Research 2023; 59.

(4) Brown. LE, Maavara. T, Chen. X, **Zhang. J**, Klaar. M, Moshe. FO, et al. Integrating sensor data and machine-learning to advance the science and management of river carbon emissions. Nature water (submitted).

# Chapter 1 Introduction

## Hydrological cycle, Surface water and Groundwater

The hydrological cycle, or water cycle (Narasimhan, 2009), describes the continuous circulation of water among Earth's lithosphere, hydrosphere, and atmosphere in various forms. It encompasses processes such as evaporation, precipitation, melting, groundwater flow, and the flow of rivers and lakes (Robinson et al., 2013). The primary driving force behind the water cycle is solar energy. Solar radiation causes surface water to evaporate and form water vapour. The water vapour is then transported to other regions. Upon cooling, the water vapour transforms into precipitation and returns to the Earth's surface. A portion of the precipitation directly flows into rivers, lakes, and oceans, forming surface runoff that ultimately returns to the oceans. Another portion of the precipitation infiltrates into the ground, becoming groundwater. Groundwater can find its way into rivers, lakes, or oceans through springs or subsurface flow. Simultaneously, groundwater can also infiltrate plant root zones through subsurface leakage and be absorbed by vegetation. The water cycle process maintains the distribution and renewal of water resources on Earth, which is crucial for sustaining ecosystem balance, agriculture, and human livelihoods.

In the hydrological cycle, freshwater is primarily stored in glaciers, which are difficult to access, accounting for approximately 69% of the total freshwater volume. Another 30% of freshwater is stored in underground aquifers, and the remaining portion is found in surface water sources. Surface water and groundwater are the primary sources of freshwater for human society's production and daily life. It is evident that surface water and groundwater not only play significant roles in the hydrological cycle but also have vital interactions with human society.

Groundwater can be defined as the water located beneath the Earth's surface (Alley, 2009). The space that stores groundwater is referred to as an aquifer. Based on the characteristics of the groundwater head, it can be categorized into confined aquifer and unconfined aquifer. The widespread occurrence of groundwater underground is the primary reason for its significant use as a water source worldwide. A considerable portion of agricultural production, including most of the world's food supply, relies on groundwater for irrigation. Moreover, groundwater plays a crucial role in sustaining water flow during dry periods, making it vital for the maintenance of numerous lakes and wetlands. Besides its human uses, many plants and aquatic organisms depend on groundwater discharging into streams, lakes, and wetlands.

Surface water refers to any water source that is open to the atmosphere and can potentially flow from the land (Katsanou and Karapanagioti, 2019). It accumulates on the Earth's surface in the form of streams, rivers, lakes, reservoirs, or oceans. The total land area contributing to surface runoff from lakes or rivers is commonly described as the watershed area. The quantity of surface water primarily depends on the amount of rainfall, but it is also influenced by factors like the size of the watershed, land slope, soil type, vegetation, and land use. There are several advantages of using surface water as a source for domestic and industrial water supply. Firstly, surface water is readily accessible and can be easily extracted through direct pumping, and after use, it can be treated and discharged back into rivers. Secondly, rivers and lakes provide a substantial and regular supply of water. As a result, surface water is extensively utilized in large urban water supply systems.

Across diverse landscapes, from small streams and lakes to major river valleys and coastal areas, the interaction between groundwater and surface water is widespread (Winter, 1999). Understanding the interaction between groundwater and surface water is crucial for developing effective water resource management and policies. Managing groundwater and surface water separately often only addresses a partial aspect of the hydrological system, as each component continuously interacts with the others (Winter et al., 1998). Take water supply as an example: excessive groundwater pumping can lead to a reduction in the base flow of rivers, affecting surface water levels.

Simultaneously, declining groundwater levels can affect the compressional structure of aquifers, resulting in land subsidence and altering river courses. These aspects pose significant challenges to water resource management.

Additionally, the movement of water between groundwater and surface water systems leads to amalgamation. A substantial quantity of nutrients or other dissolved chemical substances existing in surface water can be transported into interconnected groundwater systems, and conversely, the reverse is also true. Therefore, it is imperative to comprehensively consider both surface water and groundwater. Fully recognizing the interplay between these two hydrological domains is essential to enhance the efficient utilization and management of water resources.

### Physics-based model and data-based model

A physics-based model serves as a representation that encapsulates the fundamental laws governing the natural world, inherently encompassing the notions of temporal progression, spatial dimensions, causality, and the potential for generalization (Willcox et al., 2021). Within the domain of hydrology, a physics-based model pertains to the formulation of boundary-value problems employing partial difference equations and potential theory (Bittelli et al., 2010; Freeze and Harlan, 1969; Partington et al., 2012). For instance, equations such as the Navier-Stokes equation and the Saint-Venant equation find application in the investigation of surface water phenomena, while the Darcy equation and the Richards equation are employed in the study of groundwater dynamics.

Analytical solutions and numerical solutions are two different approaches for the solution of physics-based model. Analytical models entail relatively lower computational demands and can depict explicit mathematical relationships among variables, rendering them more flexible and convenient. Numerical solutions, on the other hand, are capable of tackling more intricate problems, and they offer a more realistic representation of the complexities found in the real world. Although analytical and numerical solutions have been extensively applied over the past decades for simulating and managing surface water, groundwater and their interaction, achieving precise predictions of surface water flow and groundwater levels through physics-based approaches remains a challenging endeavour. This difficulty arises from the intricate interplay of numerous uncertain, complex, non-stationary, and non-linear factors within the integrated surface water-groundwater system.

Over the last two decades, data-driven approaches have become a viable option for predicting surface water flow and groundwater levels. Fundamentally, data-based methods are statistical approaches that concentrate on the input-output relationship without establishing explicit causality between factors in a specific system (Solomatine and Ostfeld, 2008). Significant attention has been given to methodologies involving Artificial Intelligence (AI), Machine Learning (ML), Artificial neural networks (ANNs) and Deep Learning (DL). AI is characterized by its aim to confer rational thinking or behaviour upon a system (McDermott, 1987; Nilsson, 1998; Poole and Mackworth, 2010). ML, as delineated by Samuel (1959), refers to a discipline enabling computers to learn autonomously without explicit programming. DL, an offshoot of machine learning, encompasses several advanced forms of ANNs (Bishop and Bishop, 2024). A prominent feature of deep networks is the presence of multiple layers in the neural network architecture, which providing a higher capacity for representing complex functions compared to non-deep neural networks (Raghu et al., 2017). The interrelationships among AI, ML, ANNs and DL are depicted in Figure 1.1.

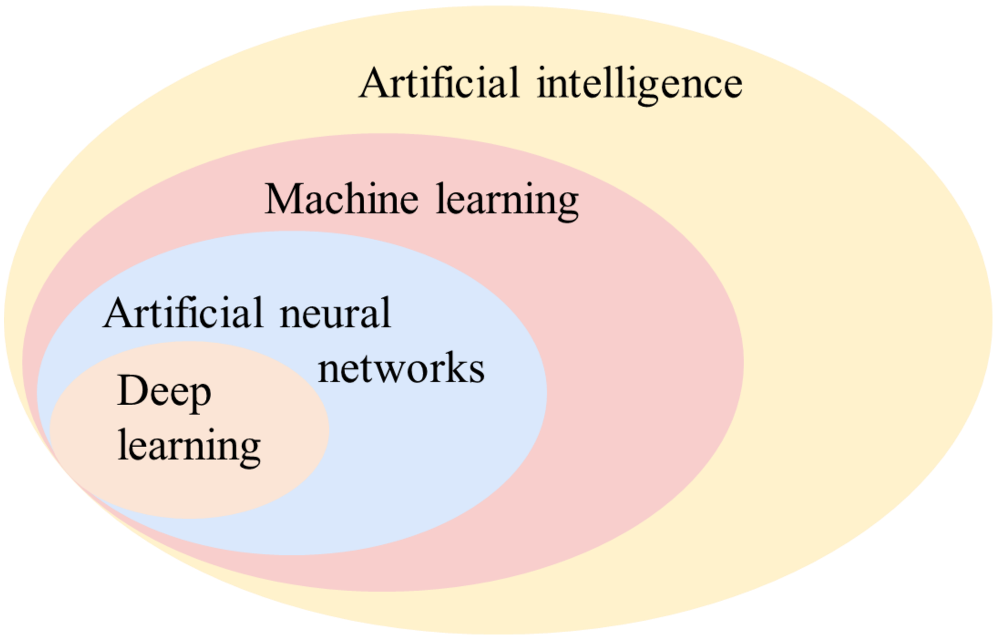


Figure 1.1 The relationship between AI, ML, ANNs and DL

Data-driven models have gained widespread adoption in hydrology research, yet their application in the realm of coupled surface water-groundwater simulation remains relatively limited. Furthermore, inherent limitations within data-driven models continue to constrain their utility and reliability, thus impeding their broader effectiveness in this context. For example, the accuracy of data-based methods depends on the density of observed data but collection of hydrological data like groundwater data is both time-consuming and expensive. Although some researches find that the accuracy of the data-based method would be more satisfactory and credible if the physical information is considered. The related researches are still on very early stage and there remains a pressing need for further research in this direction.

## Objectives and thesis structure

This study aims to propose an innovative integrated model that harmonizes the utilization of both physics-based and data-based methodologies for the simulation of surface water-groundwater interactions, which leverages the strengths of physics-based methods and data-driven approaches in a complementary manner. The overall aim is achieved by a boundary-coupled framework for the surface water groundwater interaction process. In the framework, DL models are applied for the surface water prediction independently. Additionally, within the groundwater model, the Dirichlet boundary condition is employed to describe changes in the river stage and it provides an interface to couple the surface water simulation result with groundwater. Several objectives are established for the scientific inquiries in the framework, including: 1. Presenting a DL model for surface water runoff and a method to improve the performance of DL model by optimize meteorological input variables; 2. Providing a semi-analytical solution for groundwater flow in riparian zone with layered structure; 3. Coupling the physical information from analytical solution and DL by transfer learning method and applying it to fix the heterogeneous problem in riparian zone; 4. Applying the transfer learning model in catchment scale. The relationship of objectives is shown in Figure 1.2.

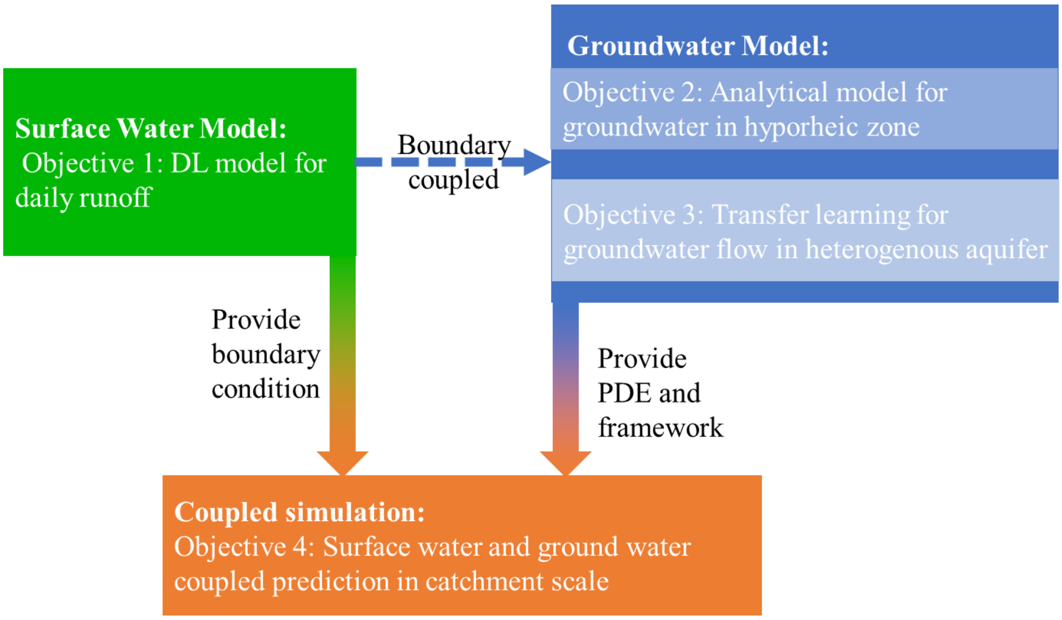


Figure 1.2 Relationship of objectives for integrating coupled simulation of surface water and ground water with Artificial intelligence.

All the objectives are fulfilled, and the aim is achieved. The layout of the thesis is arranged as:

Chapter 2 provides a literature review on the background of this research, including the hydrological cycle, the interaction between groundwater and surface water and the application of deep learning in hydrology research, etc. The key State-of-the-art sketches of techniques for deep learning are introduced to build the foundation for further research work.

Chapter 3 presents a study to evaluate the impact of the selection of multiple input variables on the runoff prediction and provides a method of identifying the best meteorological input variables for a runoff model. Rainfall data and multiple meteorological data have been considered as input to the model in this research. Principal Component Analysis (PCA) has been applied to the data as a contrast, to reduce dimensionality and redundancy within this input data. Two different deep recurrent neural networks (RNN) models, a long-short-term memory (LSTM) model and a gated recurrent unit (GRU) model, were comparatively applied to predict runoff with these inputs. In this study, the Muskegon River and the Pearl River were taken as examples.

Chapter 4 investigates the impacts of layered heterogeneity on water exchange in the riparian zone using a mathematical model for groundwater flow in a two-layer aquifer that is recharged by precipitation and floods. A semi-analytical solution is derived for the hydraulic head, lateral discharge, and fluxes between the layers. The present analytical solution is applied in the riparian zone well of White Clay Creek and provides reasonable estimates of aquifer parameters.

Chapter 5 proposes a novel deep learning model guided by a simple analytical model to predict groundwater flow in heterogeneous aquifers. It differs from previous deep learning research by incorporating the knowledge from a simple analytical model and utilizing transfer learning techniques to further improve the hydraulic head prediction in relatively complicated problems where the analytical model is invalid. The model is tested against the traditional deep learning model Deep Back Propagation Neural Network (DBPNN) in scenarios with unknown homogeneous and heterogeneous hydraulic conductivity fields.

Chapter 6 presents a method to estimate catchment groundwater flow and river stage by analytical model and LSTM model. Then the transfer learning framework was applied in the headwaters of the Miho River catchment with limited observational data availability. A traditional DBPNN without the guidance of analytical model is applied as a baseline model to ensure a reliable conclusion. The computational load and uncertainty caused by locations of observation points are analysed.

Chapter 7 gives the conclusion of the thesis and recommendations for future work.

# Chapter 2 Literature Review for Groundwater and surface water interaction

## Interaction between Groundwater and surface water

In this section, the interaction mechanisms between groundwater and different types of surface water, including rivers, lakes/reservoirs, and oceans is summarized based on the specific characteristics of each surface water type.

### River-groundwater interaction

The interaction between rivers and groundwater can be classified into three relationships: river water recharges groundwater, groundwater recharges river water, and a reciprocal relationship where the groundwater and surface water mutually recharge each other (Winter et al., 1998). Generally, when the groundwater head is higher than the river stage, groundwater replenishes the river through hydraulic gradients. Conversely, when the river stage is higher, surface water flow into the groundwater. However, in local flow systems, the interaction between groundwater and surface water often exhibits complex variations over time and space due to factors such as precipitation, climate, and topography (Winter, 1999).

Hydrologists commonly define the "Riparian zone" as the space influenced by a river's presence (Naiman and Decamps, 1997). Because of its special location, this zone possesses distinctive spatial structure and ecological functions and plays a significant role in maintaining the water balance, the energy balance and water quality(de Mello et al., 2018) (Robert, 1997; Webster et al., 1976). For example, a riparian forest may reduce recharge from precipitation, or agricultural chemicals applied to riparian crops may contaminate groundwater and river water (de Oliveira et al., 2010; Gomez-Velez et al., 2014; Krutz et al., 2005; Ou et al., 2016). The hyporheic zone within the riparian zone is defined by shallow subsurface pathways through river beds and river banks beginning and ending at the river (Boano et al., 2014) and this area is considered a hot spot for hydrologic, geologic, geomorphic, geochemical, and biological processes (Fox et al., 2016).

The groundwater flow in riparian zone (or hyporheic zone) serves as the foundation for other processes. Groundwater flow is the controlling factor for many processes in the riparian and hyporheic zones, and it is greatly influenced by natural events and human activities. Flooding is one of the most important natural events affecting groundwater flow in the riparian and hyporheic zone, as rapid water level fluctuations give rise to lateral propagation of river water into the riparian zone that changes the local flow field (Curry et al., 1994; Liu et al., 2020a). In addition, large-scale human activities like damming can reduce the flood pulse of natural rivers and make the river level fluctuate more intermittently (Arias et al., 2013; Liu et al., 2020a; Nilsson and Berggren, 2000), which may substantially impact hydrologic exchange in the riparian zone (Fritz and Arntzen, 2007) and groundwater flow (Ferencz et al., 2019). Furthermore, due to climate change, the risk of coastal cities being threatened by floods is increasing under current protection standards (Hu et al., 2019; Huang et al., 2020; Xu et al., 2022a). Variable recharge from precipitation further impacts riparian zone hydrology (Schilling et al., 2004), and it should be considered along with flooding to obtain a better understanding of the complex patterns of groundwater flow in the riparian zone.

### Lake/reservoir-groundwater interaction

The interaction patterns between lakes/reservoirs and groundwater are similar to those between rivers and groundwater. They can be categorized into three relationships: groundwater discharging into lakes/reservoirs, lake/reservoir water infiltrating into groundwater, and simultaneous exchange of groundwater discharge and lake/reservoir infiltration. However, unlike river-groundwater interactions, the driving forces for interactions between lakes/reservoirs and groundwater are mainly hydrostatic forces due to the slower flow velocities of surface water in lakes/reservoirs. The relationship between groundwater discharge and lake/reservoir infiltration is often determined by the hydraulic gradient between groundwater and the lake/reservoir. As lakes/reservoirs are usually located at the lowest points of their watersheds, surface runoff and groundwater runoff from the watershed converge into the lakes/reservoirs. Therefore, most lakes/reservoirs receive groundwater discharge, and the mode of groundwater discharging into lakes/reservoirs is the most common.

In some closed-basin lakes without surface runoff inputs, the contribution of groundwater discharge to lake water volume can even exceed 90% (Gurrieri and Furniss, 2004; Stets et al., 2010). For lakes with surface runoff inputs, groundwater can still be a significant source of their water volume. For example, a study on Væng Lake found that the average groundwater discharge intensity was as high as 124.1 mm/d, accounting for 66% of the total inflow to the lake (Kidmose et al., 2013).In plain or wetland areas with varying factors such as rainfall and human activities, groundwater discharge and lake infiltration often fluctuate seasonally between wet and dry periods (Li et al., 2020b). Even in regions with abundant rainfall and surface runoff, the contribution of groundwater to lake water supply should not be overlooked. For instance, in the Poyang Lake and Dongting Lake areas in China, groundwater discharge can still contribute to about 10% of the total inflow to the lakes(Liao et al., 2018; Sun et al., 2021).

In addition to supplying water to lakes, groundwater also carries nutrients that can become a potential source of lake nutrients (Lewandowski et al., 2015; Rosenberry et al., 2015). Nitrogen and phosphorus carried by groundwater entering the lake can exacerbate the lake's nutrient levels, promoting the growth of algae and aquatic microorganisms, severely degrading water quality, and reducing the stability and diversity of aquatic organisms. Numerous studies have shown that groundwater discharge plays an important role in the nutrient balance of lakes(Knights et al., 2017). Even if groundwater discharge has a small contribution to the water balance of lakes, it can still be a significant input of nutrients due to the potentially high nutrient concentration in groundwater (Lewandowski et al., 2015). For instance, in a glacier lake in the Qinghai-Tibet Plateau of China, groundwater discharge at the lake bottom accounts for only 7.0% of the total inflow, but the total nitrogen carried by the groundwater accounts for 42.9% of the total nutrient input (Luo et al., 2018). In the case of Lake Arendsee in Germany, the phosphorus load from groundwater discharge contributes to more than 50% of the total phosphorus load entering the lake (Meinikmann et al., 2015).

**Ocean-groundwater interaction**

In the hydrological cycle, surface water and groundwater eventually return to the ocean. At the regional scale, the interaction pattern between groundwater and the ocean is typically characterized by groundwater discharging to the ocean. However, dynamic changes in the exchange of groundwater and seawater still occur near the intertidal zone due to factors such as ocean tides and coastal groundwater extraction. The main driving forces behind groundwater-ocean interaction can be categorized into land-based factors and ocean-based factors (Li and Wang, 2015; Wilson, 2005). Land-based factors include terrain gradients, density gradients, and thermal gradients, while ocean-based factors involve tides, waves, and climate. Additionally, long-term cyclical changes in sea levels influenced by solar activity are also considered.

From a global perspective, groundwater is not the primary source of replenishment for the ocean, as it accounts for only 0.6% of the total freshwater input into the sea (Luijendijk et al., 2020). However, groundwater plays a crucial role in ensuring water resource security and water environmental protection in coastal areas. Excessive groundwater extraction in coastal regions can lead to a decline in freshwater levels, seawater intrusion, and subsequent ecological issues like soil salinization. Moreover, extraneous substances such as carbon, iron, silicon, and nitrogen present in groundwater can impact coastal ecosystems by affecting nutrient levels and solute concentrations. Groundwater discharges are often concentrated in sensitive coastal ecosystems, such as river mouths, salt marshes, and coral reefs, posing risks of water pollution and eutrophication in these areas.

Currently, research on the interaction between the ocean and groundwater mainly focuses on seawater intrusion, the freshwater-saltwater interface, and submarine groundwater discharge issues. Kaleris and Ziogas (2013) employed numerical models and approximate analytical solutions to investigate the impact of cutoff walls on the progress of submarine groundwater discharge in the presence and absence of groundwater extraction. Muller et al. (2023) combined numerical simulations of radon as a groundwater tracer with advective transport to propose a method for quantifying deep submarine groundwater flow using autonomously measured ocean surface data.

## Physics-based Groundwater-surface water coupled model

### Types of physics-based groundwater-surface water coupled model

In the 1970s, Freeze and Harlan (1969) proposed the concept of coupling surface water and groundwater models. Subsequently, the simulation of coupled surface water-groundwater systems became a hot topic in the field, drawing widespread attention from researchers(Anibas et al., 2011; Dewandel et al., 2006; Freeze, 1972; Govindaraju and Kavvas, 1991; Smith and Woolhise.Da, 1970). Pikul et al. (1974) coupled the one-dimensional Richards equation and the Boussinesq equation to accurately simulate groundwater levels. Govindaraju and Kavvas (1991) developed a one-dimensional coupled model for surface water flow and a three-dimensional model for groundwater flow. Woolhiser et al. (1996) investigated the impact of heterogeneity on groundwater flow by coupling a surface water flow model with the Smith-Parlange infiltration model. With an improved understanding of hydrological mechanisms and advancements in computer technology, various coupling models have been developed and applied(Hassan et al., 2014; Im et al., 2009; Sandu and Virsta, 2015; Sudicky et al., 2008; Zhu et al., 2012). In this thesis, the surface water-groundwater coupling models are categorized into three types: Concept coupled models, Boundary/Sink coupled models, and Fully coupled models.

**1. Concept coupled model**

The Concept coupled model is typically based on the principles of water cycle and water balance for a watershed or study unit. It uses linear equations to calculate the changes in water quantities for different components. In the Concept coupled model, the transformation of water quantities among various hydrological processes is explicit and well-ordered, making it widely applicable for integrated water resource assessment. One of the widely used Concept coupled models is the VIC (Variable Infiltration Capacity model) (Chandel and Ghosh, 2021; Pedretti et al., 2012). The VIC model is a semi-distributed macro-scale hydrological model that simulates macro-scale hydrological processes by computing the water balance equation (Liang et al., 1994; Liang et al., 1996; Liang et al., 1999). For instance, Joseph and Ghosh (2023) developed a new irrigation module for VIC model, and applied to irrigation scenarios in India. Liang et al. (2003) proposed a new parameterization method based on the VIC model to consider the dynamic interactions between surface water and groundwater on soil moisture, evapotranspiration, runoff, and recharge and applied this method to the Tulpehocken Creek and West Conewago Creek watersheds in Pennsylvania. However, these models have significant limitations in their application due to the oversimplified assumptions about the interactions and transformations between surface water and groundwater models.

**2. Boundary/Sink coupled model**

Due to the relative ease of obtaining surface water observation data, the establishment and validation of surface water models are more straightforward. Many researchers use an independent model to calculate surface water process such as runoff and infiltration, which are then used as boundary conditions or source/sink terms for the transient partial differential equations describing the groundwater models in coupled simulations. This type of model is referred to as the Boundary/Sink coupled model in the thesis. The Boundary/Sink coupled model conveniently integrates existing surface water and groundwater models, making the most of hydrological and meteorological data as well as hydrogeological information. One representative example of this model is the combination of the Soil Water Assessment Tool (SWAT) and the MODFLOW groundwater model, known as the SWAT-MODFLOW model. The basic process of connecting SWAT and MODFLOW involves transferring deep percolation calculated by SWAT to supply groundwater flow in MODFLOW's grid cells and exchanging groundwater-surface water interaction fluxes calculated by MODFLOW with SWAT's river network(Bailey et al., 2016; Kim et al., 2008). Since the release of SWATMOD-Prep, a graphical user interface for SWAT-MODFLOW developed by Bailey et al. (2017), SWAT-MODFLOW has been applied in various watersheds in countries such as the United States (Guevara-Ochoa et al., 2020), Iran (Jafari et al., 2021), and Denmark (Liu et al., 2020b).

Spatiotemporal responses to hydrological events with riparian or hyporheic zones and impacts on surface-groundwater exchanges have also been investigated by analytical models in extant literature (Chen and Chen, 2003; Hantush, 2005; McCallum and Shanafield, 2016; Zlotnik and Huang, 1999). Singh (2004) considered stream boundary resistance and presented a 1-D analytical solution for semi-infinite aquifer responses to a sinusoidal river stage fluctuation. Liang et al. (2017c) developed a semi-analytical solution for base flow recession caused by recharge by considering lateral unsaturated discharge. Their results suggest that the unsaturated zone impedes the discharge of saturated flow to the river. These studies, however, only considered groundwater flow in a cross-section of a river-aquifer system. To explore the plane view of the surface-groundwater exchange, Liang et al. (2018a) presented an analytical solution for horizontal 2-D unconfined groundwater flow. The results demonstrated that the proposed 2-D solution performs better than 1-D cross-section solution as the 1-D model overestimates both the hydraulic head near the upstream and underestimates the hydraulic head near the downstream.

## 3. Fully coupled model

The Fully coupled model involves a rigorous description of hydrological processes for surface water and groundwater using transient partial differential equations. This model couples surface water and groundwater by representing their exchange fluxes as source/sink terms and iteratively calculates the movement of both surface water and groundwater within the study area. For instance, the HGS (HydroGeoSphere) model employs the two-dimensional Saint-Venant equation to describe surface water flow and the three-dimensional Richards equation to describe groundwater flow. The exchange fluxes between surface water and groundwater are described using Darcy's law to establish the coupling equations (Brunner and Simmons, 2012; Therrien et al., 2010). This model has been applied to explore changes in surface water-groundwater interactions under climate change conditions (Goderniaux et al., 2009) and during freezing and thawing processes (Lemieux et al., 2008). Other fully coupled models such as CATHY (CATchment Hydrology) (Paniconi and Putti, 1994; Paniconi and Wood, 1993) and ParFlow (Maxwell et al., 2009) have also been widely used for surface water-groundwater coupled simulations (Kollet et al., 2017; Kollet and Maxwell, 2006; Kollet et al., 2010; Maxwell and Condon, 2016; Painter et al., 2016). While the Fully coupled model considers detailed physical processes of the hydrological cycle, its development requires a substantial number of precise parameters and data support. Establishing and calibrating the model can be time-consuming and demands extensive expertise, making it challenging to apply the model on a broader scale.

## Challenge and limitation of physics-based groundwater-surface water coupled model

Although the groundwater-surface water coupled model has impressive development. It is still facing significant fresh and old challenges and limitations now.

1. The impact of human activities on the hydrological cycle poses a significant challenge for groundwater-surface water coupled models. Human activities are highly complex and nonlinear, making it difficult to accurately represent them using partial

differential equations or linear equations. Incorporating human activity into physics-based models based on these equations is a difficult task.

2. Physics-based hydrological models require a thorough understanding of hydrology. Neglecting crucial processes or relationships due to limitations in knowledge may lead to errors in the model. For example, neglecting the vadose zone's role in calculating baseflow recession can affect estimates of aquifer parameters (Liang et al., 2017b).

3. The spatial heterogeneity of groundwater aquifers and surface water underlays at different scales affects the values of hydrological parameters, especially hydrogeological parameters. For instance, the coefficient of dispersion tends to increase with scale, leading to significant differences between field and laboratory measurements(Bear, 2012).

4. Computational cost and efficiency are ongoing challenges. Many hydrological problems, such as flood forecasting, require timely and accurate predictions. However, the complexity of models and the computational limitations of computers make rapid and precise simulations and predictions challenging (Costabile et al., 2017). Parallel computing or simplified models can improve simulation speed. However, parallel computing is costly and challenging, while simplified models may neglect important hydrological processes, compromising result accuracy.

5. The advent of advanced data collection instruments has led to an explosive growth in observational data for both surface water and groundwater. Traditional models based on physical processes necessitate continuous adjustments and validations to effectively leverage new data. However, coping with such vast amounts of data through conventional means is impractical. Addressing and fully harnessing the potential of this abundant data for modelling and prediction requires innovative approaches that surmount the bottlenecks in coupling groundwater and surface water using conventional methods.

## Application of Deep learning in hydrology research

In order to overcome the above shortcomings, data-based methods are used as substitute or supplement to process-based ones in the field of hydrology research. DL has attracted the attention of scholars in various fields, including river hydrology and water quality modelling (Xu and Liang, 2021). The application of Deep Learning in hydrology research can not only works as a stand-alone model in hydrology research but also serves as an auxiliary tool for physics-based method.

### Deep learning as stand-alone model

**1. hydrologic predictions.**

DL has emerged as a potential means to overcome uncertainty and nonlinearity in hydrology sciences(Shen, 2018). Its application in hydrological forecasting is primarily attributed to its capability to handle complex and nonlinear data patterns, utilize extensive data for training, autonomously learn features from data, exhibit robust predictive abilities, and efficiently manage large-scale datasets. These attributes enable DL to capture the intricate nature of hydrological processes and improve the accuracy of hydrological forecasting. Consequently, many scholars have conducted comprehensive reviews of using DL methods in hydrological prediction (Shen, 2018; Xu and Liang, 2021). This section provides a concise overview focusing on groundwater and surface water aspects.

Regarding surface water, Ahmed et al. (2022) introduced an innovative hybrid DL model for forecasting river water levels. This model incorporates Convolutional Neural Networks (CNN), Bidirectional Long Short-Term Memory, and Ant Colony Optimization. To extract essential features from predictive variables, the model employs Complete Ensemble Empirical Mode Decomposition with Adaptive Noise and Variational Mode Decomposition techniques, leading to a significant improvement in the accuracy of river water level prediction. In another study, Xu et al. (2022b) introduced a hybrid DL model that combines CNN with Gated Recurrent Unit (GRU) to predict future average runoff in the Yangtze River. They trained the model using data from six hydrological stations along the Yangtze River's main stem and six tributary stations, with inputs from Global Climate Model forecasts. Furthermore, DL has been applied in optimizing control for hydraulic engineering projects. Xu et al. (2021) proposed a novel DL-based reinforcement learning framework for optimizing hydropower operations. The framework comprises two Artificial Neural Networks (ANNs), one to represent the relationships between states, actions, and rewards, and the other for defining the decision value function used in reward evaluation. Testing on the Hengren hydroelectric system in China demonstrated its superior performance compared to two classical hydropower operation methods - decision trees and random dynamic programming.

For groundwater, Wunsch et al. (2022) applied a 1D-CNN method to build models for 118 observation points in Germany. They then utilized the trained CNN models to predict the future groundwater level response to climate change at selected locations. The climate data used in this research are derived from different Representative Concentration Pathway scenarios. McKenzie et al. (2023) used DL to forecast coastal seawater radon ($^{222}Rn$) content in areas influenced by Submarine Groundwater Discharge. The model provided short-term predictions of radon content, and the fully connected deep neural network achieved accurate predictions using water depth, temperature, salinity, air temperature, and wind speed as input features.

## 2. Data Mining

Deep learning has proven to be an effective approach for uncovering hidden patterns, correlations, and knowledge within big datasets. Consequently, apart from its utilization in forecasting hydrological variables and processes, deep learning has also gained widespread application in the field of hydrological data mining. By delving deeply into hydrological data and analysing concealed patterns, deep learning has been extensively employed for examining relationships among hydrological variables, data reconstruction, and outlier detection.

Understanding the mechanisms of interaction among multiple variables is of paramount importance in the dynamics of water systems. With the continuous increase in the volume of hydrological observational data, the application of deep learning techniques to identify relationships among hydrological variables, independent of reliance on prior physical knowledge, has gradually become feasible. Jing et al. (2023) employed two deep learning models, namely Vanilla-LSTM and encoder-decoder-LSTM, to establish a groundwater model for the North China Plain. They utilized the Gini coefficient and permutation feature importance analysis to determine the contributions of various driving factors in the different models. The results indicated that factors related to human activities exerted a significantly greater influence on groundwater level variations compared to other factors. Li et al. (2023) employed a convolutional recurrent deep learning model to predict the high-resolution spatiotemporal changes in grassland coverage in arid regions. They discovered that ecological flow regulation was the primary driver of grassland greening in the Gobi Desert. Jiang et al. (2022) utilized a Long Short-Term Memory (LSTM) network to establish a flood prediction model for the contiguous United States. Their analysis revealed that 70.7% of the watersheds were primarily dominated by a single flood mechanism.

Time series data is essential for hydrological analysis (Alley and Taylor, 2001). However, due to technical issues such as equipment failures and maintenance, as well as unexpected events like natural disasters, hydrological monitoring often suffers from missing time series data. The application of DL methods for time series data imputation has emerged as one of the most active research areas in the past two decades (Kulanuwat et al., 2021; Yang et al., 2021). For example, the GRACE (the Gravity Recovery and Climate Experiment) Follow-On mission began operating a year after the failure of GRACE. The data gap during this year poses a challenge for quantifying hydrological drought events within that timeframe. Mo et al. (2022) proposed an innovative Bayesian Convolutional Neural Network (BCNN) to reconstruct the missing satellite signals during this interval and tested its performance using previous GRACE data. The test results demonstrated that the proposed BCNN achieved higher R and NSE scores in most regions.

During hydrological monitoring, outliers can occur due to various reasons. These outliers may arise from factors such as equipment failures, which, if directly used, can deteriorate the quality of hydrological system modelling. However, outliers in monitoring data can also represent significant and non-negligible information about abnormal changes in the physical/chemical conditions of the hydrological system. Numerous studies have been conducted to identify outliers using various deep learning techniques(Fang et al., 2020; Hu et al., 2021). For instance, Kim et al. (2022) utilized Long Short-Term Memory (LSTM) as an ensemble regression model. This approach combined statistical features of groundwater data and seasonal variations in precipitation data to estimate the trend and reasonable range of groundwater levels. The study effectively identified outliers in three groundwater monitoring wells located in the southern region of South Korea under seasonal and precipitation pattern backgrounds.

## Deep learning as an auxiliary tool for physics-based method

Deep learning methods can serve as both standalone approaches for hydrological research and as complementary tools to address challenges within process-based modelling. Here, a brief overview of how deep learning has been integrated with process-based modelling to enhance or optimize various components of the latter is provided.

### 1.Parameterization

In most process-based models, the characteristic of media and fluid is described by the specification of parameters. However, the parameters cannot be quantified or measured directly. Moreover, the lots of parameters are affected by the scale required by the model. For example, due to preferential flow, the hydraulic conductivity measured in the laboratory may be several orders of magnitude smaller than that at the watershed scale. Determining appropriate parameter values for hydrological models is a crucial issue in hydrological science. Currently, deep learning is being employed for direct or indirect parameter calibration.

The process of directly calibrating parameters using deep learning is similar to hydrological process prediction. This approach often relies on a large amount of data to establish a model that captures the relationship between factors influencing the target parameter and the target parameter itself. This model is then used to predict the values of the target parameter in a new scenario. For example, Feng et al. (2022) proposed a differentiable parameter learning framework to regionalize the physical parameters for a process-based model, the HBV (Hydrologiska Byråns Vattenbalansavdelning) hydrologic model. In their framework, a deep LSTM neural network is applied to output physical parameters with the inputs of attributes factors like soil, land cover, geology, and forcing factors like precipitation, temperature and evapotranspiration. For the subsurface model, Srisutthiyakorn (2016) demonstrated the feasibility of using CNN to directly predict permeability from rock images. Building upon this work, Wu et al. (2018) extended the application of CNN by incorporating additional information from two parameters, porosity and specific surface area, into the fully connected layers of the network, resulting in the proposed physically informed CNN architecture. The results demonstrated that the physically informed architecture generally exhibited superior predictive performance compared to traditional CNN models in most cases.

The indirect process is solving inverse problems, typically using observed data and a known model. However, solving inverse problems often requires repeatedly running the model, leading to a significant computational burden. Therefore, alternative model approaches are frequently employed. Deep learning methods are also among the commonly used alternative model approaches. The specific details will be discussed in the next section.

## 2.Surrogate model

Physics-based numerical models have long served as the primary quantitative tools in hydrological science. However, these models often incur a high computational burden due to the complex physical processes involved. Consequently, it is challenging to deal with optimizing problems and uncertainty analysis, which require multiple model runs and generate huge computational demands. Surrogate models replicate process-based model outcomes as a function of inputs and/or parameters, offering significantly faster execution. (Razavi et al., 2012). Deep learning techniques excel in representing nonlinear functions, making them well-suited for surrogate modelling.

Generally, the more input or output variables a surrogate model aims to emulate, the larger the training dataset required. When using high-fidelity surrogate models, a substantial amount of data from the original model is needed, which often entails multiple runs and a significant computational burden. Hence, many studies focus on low-fidelity surrogate models that replace only specific features or components of physics-based numerical models. To reduce the number of input variables, sensitivity analysis and other techniques are commonly employed. For example, Wang et al. (2023) conducted a local sensitivity analysis to identify four key parameters that significantly influence pollutant transport. They then generated data specifically for these four parameters and trained a deep belief network-based surrogate model for multiphase flow pollutant source inversion. By focusing on a reduced set of parameters, they greatly alleviated the data generation challenge.

With the advancements in algorithms and computational power, researchers have been exploring alternative approaches to the overall modelling process with high fidelity. For instance, Maxwell et al. (2021) employed six deep learning models with different structures, including 2D CNN, 3D CNN, and U-Net, to construct emulators for the Parflow model. They assessed the emulator's accuracy in simulating surface pressures in The Tilted V Problem. The results indicated that machine learning models can capture general physical behaviours, with deeper networks outperforming models with fewer parameters. Tran et al. (2021) proposed a simulator called ParFlow-ML based on a predictive recurrent neural network. ParFlow-ML takes ParFlow's input as input and predicts ParFlow's output, aiming to provide a comprehensive replacement for the ParFlow model. The results showed a remarkable consistency between the simulator's predictions and ParFlow's simulated results in terms of flow rates, groundwater table depth, and total water storage. Furthermore, the simulator exhibited a speed advantage, performing 42 times faster than ParFlow.

## 3. Uncertainty Analysis and Error Estimation

Errors in hydrological simulations have had significant implications for their applications in flood prediction and water resources management. Accurately characterizing error properties, such as heteroscedasticity and autocorrelation, can enhance hydrological predictions. Solomatine and Shrestha (2009) attempted to employ various machine learning (ML) methods for model uncertainty analysis and utilized the results as correctors for physics-based models. Subsequently, deep learning methods have also been applied to uncertainty analysis and correction of results based on physics-based models.

Sun et al. (2019) apply a CNN to learn the "mismatch" spatiotemporal patterns between the total water storage anomalies observed by GRACE and the simulated data by the NOAH. And then employed the trained CNN to improve the NOAH model performance without requiring GRACE data in the new scenario. Results show that with the assistance from CNN models, the NOAH-simulated result can achieve a 50% improvement in NSE efficiency. Li et al. (2021a) established a MIKE SHE model to simulate the hydrology process in the Yellow River in China from 1992 to 2015. Then they introduced a probabilistic LSTM network to model hydrological residual errors and make probabilistic predictions using the inferred error distribution and optimal predictions. The findings of the study indicate that the suggested approach yields uncertainty intervals that are more than 50% narrower while maintaining the optimal probability coverage. Han and Morrison (2022) employed a LSTM model with sequence-to-sequence structure to estimate errors in hourly streamflow predictions from the National Water Model for the Russian River Basin in California, USA. Utilizing observed precipitation and errors from upstream stage sensors, they developed lead-time hourly streamflow error predictions spanning 1 to 18 hours, improving the predictive performance of the National Water Model. The model demonstrated more satisfactory predictive performance compared to the independent results of the National Water Model.

## 4. Sub model of physics-based model

Physical-based models often utilize partial differential equations (PDE) and ordinary differential equations (ODE) to describe the various processes involved in the hydrological cycle. However, due to the influence of complex nonlinear factors such as heterogeneity, anisotropy, and human activities, accurately describing the interconversion processes of hydrological elements by PDE and ODE becomes challenging. Furthermore, certain hydrological processes are discontinuous, such as the generation of methane bubbles in reservoir sediments and attempting to describe such processes using PDE and ODE would require extensive iterations and may even be infeasible to solve. In recent years, researchers have proposed leveraging the powerful nonlinear mapping and fitting capabilities of deep learning methods to describe processes that are difficult to characterize using PDE and ODE. These methods are then embedded within physical-based models, aiming to enhance the accuracy and computational efficiency of the models.

Bhasme et al. (2022) employed various deep learning methods such as LSTM, B-LSTM and machine learning methods as predictors for forecasting the rainfall-evaporation process and the rainfall-evaporation-surface runoff process. These processes were then integrated into the conceptual hydrological model ABCD (Thomas, 1981) for hydrological prediction. The researchers applied this approach to predict surface runoff in 10 sub-basins in India. The results demonstrate the superior performance of the proposed model in comparison to both the purely conceptual ABCD model and ML algorithms, as the proposed model maintains the physical consistency of water balance. The systematic integration of the conceptual model structure with DL algorithms offers a promising approach to enhance the accuracy of predicting crucial hydrological processes, thereby contributing to improved flood risk assessment.

## Summary

This chapter provides a comprehensive overview of the pertinent literature. Through an analysis of the references, the following conclusions have been drawn:

1. Within the coupled model frameworks mentioned above, the concept of coupling hydrological processes has led to oversimplification, while fully coupled models incur computationally intensive demands. Consequently, this thesis adopts a boundary-coupled framework for investigation.
2. In the cited literature, deep learning methodologies have found extensive use in hydrological prediction. However, limited attention has been given to the impact of different input variables on forecasting. The evaluation of how input variable selection influences model predictions and improves accuracy when multiple input variables are employed constitute unresolved scientific questions.
3. Analytical solutions possess the advantageous traits of flexibility and convenience, rendering them a commonly employed tool for studying interactions between surface water and groundwater in riparian zones. Nevertheless, analytical models considering the layered heterogeneity of aquifers in riparian zones, remain unexplored.
4. Deep learning models exhibit exceptional capacity for nonlinear mapping; however, their black-box nature has been subject to scrutiny. On the other hand, analytical models demand less computational effort and are adept at depicting the fundamental physical principles underlying groundwater flow. Nonetheless, their applicability is confined to specific conditions, such as simple aquifer geometries and homogeneous parameters. Integrating analytical solutions and

deep learning to capitalize on their respective strengths and compensate for their limitations remains an outstanding scientific query.

# Chapter 3 Literature Review for Coupled deep learning and physics-based model

Despite numerous successful DL applications in aquatic sciences, challenges and risks remain in applying these approaches to improve water resources and carbon emission management. The first issue concerns the inadequacy of detection facilities. The accuracy of deep learning methods relies on the quantity of observational data. Without enough observational data, it becomes challenging for deep learning to achieve results of satisfactory precision (Cao et al., 2022; Wang et al., 2020a). However, even in developed countries with well-established infrastructures, the cost of obtaining a substantial volume of high-precision environmental monitoring data still hinders the application of deep learning in the short-term (Reichstein et al., 2019). Secondly, DL methods work well only when the training and test data are drawn from the same data feature space and the same probability distribution (Pan and Yang, 2010). This implies that DL methods must be specifically designed and tailored for specific contexts. Furthermore, due to the influence of factors such as watershed shape and vegetation, the data characteristics of different aquatic systems indicators in various watersheds often differ. Using models from other study areas directly for prediction and decision-made would lead to uncontrollable risks. The black-box nature of DL models is also a contributing factor to the associated risks. The DL model is only trained by the available dataset without considering explicit mechanisms in the training process. Flawed or deliberately crafted hydrological data would result in physically inconsistent or implausible predictions and pose significant risks to water security (Reichstein et al., 2019).

Recently, researchers have investigated methods to enhance the performance of deep learning models and mitigate associated risks (Huang et al., 2022; Reichstein et al., 2019). These research findings have started to find preliminary applications in the field of hydrology. This section provides a brief overview of two latest deep learning techniques, namely Physics-Informed Neural Networks (PINNs) and transfer learning and analyses their applications in the domain of hydrology.

## Physics-Informed Neural Networks (PINN)

Many researchers try to integrate DL and physics-based models and they introduce them as ‘Physics-Informed Neural Networks’ or ‘Physics-Guided Neural Networks’. To provide a clear and concise definition for further discussion in the thesis, the PINN is defined as follows: Physics-Informed Neural Network (PINN) is a framework that tightly integrates the structures of neural networks with mathematical equations, such as PDEs and ODEs, that describe physical laws. This integration allows for a seamless combination of the neural network's architecture and the errors associated with the equations.

Raissi et al. (2019) first proposed a PINN farmwork, in which residual of physics principles (e.g. government equation) is incorporated as a regulation in the loss function to implement physical constraints of the neural network. Since then, they have been applied in various fields such as geometry identification problems in materials (Zhang et al., 2022a), Heat Transfer Problems (Cai et al., 2021), fluid dynamics computations (Cai et al., 2022b; Mao et al., 2020). Chen et al. (2024) makes a review of PINN solver for numerical analysis in geoengineering. The results indicate that, compared to traditional methods, PINNs need more time to train the model and occasionally result in lower accuracy. However, the trained PINN model can be easily applied repeatedly, showcasing its advantages in uncertainty analysis and parameter inversion tasks. Here, a concise review of the application of PINNs in hydrology based on the neural network structures utilized in PINNs is provided

### Multi-Layer Perceptron

One of the neural network structures used in PINNs is the Multi-Layer Perceptron (MLP). Due to its simplicity and effectiveness, the MLP was one of the earliest neural networks applied in the context of PINNs and remains one of the most widely used architectures in PINN research. Due to the potential of PINN to be easily invoked multiple times after training, it is often employed as a surrogate model.

Wang et al. (2020a) proposed the theory guide neural network (TgNN) framework by incorporating physics principles with expert experience into the loss function to simulate groundwater flow. The TgNN was then tested in complicated scenarios like changed boundary conditions, noisy data or outliers. The result showed that Compared with the data-driven DL model, the TgNN achieves far superior results in scenarios such as training from noisy data and predicting with changed boundary conditions. Based on the TgNN framework, (Wang et al., 2021a) then proposed an inverse modelling method for groundwater parameters which incorporate of prior geological statistical information. Test results indicate that, even with sparse spatial measurements or imprecise prior statistics, the TgNN-based inversion method can still effectively perform. Tartakovsky et al. (2020) extended the application of PINN to estimate hydraulic conductivity in unsaturated flow. They demonstrated that incorporating physical constraints improves the accuracy of the DNN approximation for sparse observational functions. Furthermore, they showed that the physics-informed DNN approach outperforms the state-of-the-art maximum a posteriori probability method in terms of accuracy.

Traditional numerical solvers often face computational challenges when dealing with highly nonlinear PDEs in high-dimensional spaces such as the Richardson–Richards equation and Navier-Stokes equations. Although PINN may not achieve the same level of accuracy and efficiency as traditional methods, it still holds the potential to be a competitive numerical solver for such cases. Jin (2021) effectively utilizes PINNs to simulate incompressible laminar and turbulent flows. Developing a Navier-Stokes flow network, the study explores the velocity-pressure formulation and the vorticity-velocity formulation.

The results showcase a remarkable level of accuracy achieved by the PINN methodology. For groundwater, Bandai and Ghezzehei (2022) employed PINN to solve the Richards equation for simulating water flow in unsaturated, homogeneous, and heterogeneous soils. The study discovered that using a suitable activation function could enhance the accuracy of PINN to a comparable level with traditional numerical methods. However, training PINN required longer computational time, and the results also exhibited a strong dependence on the initialization of the neural network. Zhang et al. (2022c) tried to improve the accuracy and efficiency of PINN in solving groundwater equations by considering constraints, sampling strategies, and training schemes. It was found that incorporating a hard-constrained loss function, employing a locally refined sampling strategy (LRS), and adopting a two-stage training strategy using a snowball-like approach was effective in reducing computational load and enhancing model performance.

**Convolutional neural network**

Convolutional Neural Networks (CNNs) serve as another branch of PINN. In comparison to MLP, CNNs offer advantages such as reduced model parameters through local connections and parameter sharing, leading to improved computational efficiency. Additionally, CNNs are commonly used for image processing tasks, extracting pixel-level features through convolutional operations. This characteristic bears similarities to the finite difference method. Therefore, physics-informed CNNs (PICNN) typically transform physics constraints, such as PDEs, into difference forms to accommodate the characteristics of CNNs. This is the primary distinction between PICNN and PIMLP models.

Wang et al. (2021b) developed the Theory-Guided Convolutional Neural Network (TgCNN) aiming at efficiently quantifying uncertainty and assimilating data in reservoir flow with uncertain model parameters. The results indicate that the TgCNN can be constructed with a relatively small amount of training data while achieving satisfactory accuracy and exceptional efficiency. Wang et al. (2022) expanded the Theory-Guided Convolutional Neural Network (TgCNN) framework to address two-phase porous media flow problems. The TgCNN surrogates are also used for permeability field inversion, achieving improved efficiency and satisfactory accuracy. He et al. (2021) proposed a Theory-Guided Fully Convolutional Neural Network (TgFCNN) model to address the inverse problem of subsurface pollutant migration. The TgFCNN model demonstrates strong generalization and extrapolation capabilities, providing satisfactory accuracy in estimating unknown pollutant source parameters and permeability fields.

### Recurrent Neural Network

RNNs serve as the other network structure within the framework of PINNs. RNNs are particularly suitable for handling sequential data and capturing temporal dependencies within the input data. Niu et al. (2019) illustrated the connections between architectural structures in the RNN family and numerical methods. This study offers theoretical support for employing RNNs to tackle problems related to ODEs and system dynamics.

Jiang et al. (2020) incorporated the snowmelt process into streamflow simulation. The authors employed non-analytical solvable ODEs to capture the dynamics of watershed hydrology and integrated these ODEs into an RNN-based model. The research was applied to the continental United States, and the testing results demonstrated the enhanced predictive accuracy, strong transferability, and intelligent inference capabilities of the model. For groundwater, Cai et al. (2022a) proposed a general hybrid model for simulating groundwater levels. This model incorporated a cyclic neural layer based on the water balance equation as a physical constraint into a popular deep learning architecture. The model was applied to simulate groundwater levels in 91 locations across the continental United States. The modelling case demonstrated that the hybrid model outperformed traditional deep learning models in terms of predictive accuracy. Additionally, the hybrid model exhibited greater stability in simulating groundwater levels under different input strategies. The findings highlight the advantages of the hybrid approach in groundwater level simulation, indicating improved performance and reliability compared to solely relying on deep learning models.

## Transfer learning

Transfer learning (TL) is also a trend in applying DL. Transfer learning is effective to recognize the knowledge learned in a previous task to a new task (Pan and Yang, 2010). The previous task is usually an efficient machine learning model which has already been trained on large datasets and the new task is usually a related problem to the previous task but with smaller training datasets. The transfer learning method has been widely used in practical applications (Al-Mubaid and Umair, 2006; Chen et al., 2021; Ding et al., 2020; Fang et al., 2022; Fung et al., 2006; Li et al., 2021c; Raab and Schleif, 2018; Sarinnapakorn and Kubat, 2007; Willard et al., 2021; Zhou, 2020). In this chapter, the applications of transfer learning in geotechnics and hydrology will be discussed.

### Application of transfer learning in geotechnics

In the past five years, transfer learning has gradually been applied in geotechnical engineering. Phoon and Zhang (2023) suggest that the limited amount of information in geotechnical engineering has hindered the application of machine learning methods in geotechnics. Meanwhile, transfer learning is an effective approach to address this issue, although there is currently limited research in this area. This section summarizes the application of transfer learning in three aspects: geological exploration, engineering applications, and prediction and prevention of geological disasters.

In geological exploration and surveying, transfer learning enables the transfer of knowledge from geological exploration or surveying data to new exploration scenarios, thereby enhancing the predictive and interpretive capabilities of geological structures and subsurface geological information. For instance, Zhou et al. (2024) developed a "U-shaped" convolutional neural network (U-Net) to predict the depths of soil stratum boundaries using data from cone penetration testing (CPT), standard penetration testing (SPT), and laboratory index testing. The U-Net model was pretrained on openly accessible data from various sites worldwide and then fine-tuned through transfer learning on a dataset specifically collected for the Suzhou Metro Line 6 project. The soil profiles predicted by the model exhibited considerable consistency with benchmark profiles developed by engineering experts.

In the prediction and prevention of geological disasters, transfer learning facilitates the application of existing geological disaster data and model knowledge to new regions or scenarios for predicting and mitigating geological hazards such as landslides and debris flows, thus reducing disaster losses. Qin et al. (2022) proposed a transfer learning approach based on LSTM deep learning models to evaluate the risk of rock bursts. This method can transfer knowledge learned from complete monitoring data from adjacent sensors to the target sensor with missing monitoring data to enhance prediction. The results demonstrate that transfer learning methods can significantly improve the predictive performance of the target domain and further enhance predictive performance by increasing the size of available training data in the target domain.

In engineering applications, transfer learning allows the application of existing engineering experience to new engineering projects to guide engineering decisions and enhance engineering stability and safety. Zhang et al. (2023) combined principal component analysis (PCA)-based neural networks (NN) with transfer learning (TL) techniques (i.e., PCA-NN-TL) to analyse the stability of slopes with different spatial distributions. They argue that the PCA-NN-TL algorithm also holds great potential for assessing slope stability when training data is limited.

**Application of transfer learning in hydrology**

Since 2020, the transfer learning method has been introduced into the hydrology community (Cao et al., 2022; Li et al., 2021c; Zhao et al., 2021; Zhou, 2020). Most studies have focused on data interpolation and hydrological prediction in areas where observed data is missing or unavailable(Li et al., 2021c; Zhao et al., 2021). For example, Willard et al. (2021) developed a meta-learning model for predicting lake water temperatures in regions lacking monitoring data, drawing knowledge from wellbehaved lake models. They underscored that transfer learning shows promise as an approach suitable for unmonitored systems and environmental variables. Xiong et al. (2022) developed an LSTM model for estimating riverine nitrogen export in China. They further retrained the model for multiple catchments in North America, Europe, and Asia. The retrained model led to a significant improvement in accuracy, nearly doubling the precision of the results obtained by the model without retraining. The other branch of transfer learning in hydrology is to employ it and image-based DL for hydrological automatic observation networks(Eltner et al., 2021; Vandaele et al., 2021). For example, Eltner et al. (2021) derived initial parameters from the widely recognized pre-trained ImageNet segmentation. Subsequently, they trained a CNN to to segment water in images captured by a Raspberry Pi camera, establishing an automatic and reliable water level measurements.

The aforementioned studies primarily focused on gathering knowledge from observed data and then transfering it to study a new area. This approach partially addresses the challenge that the hydrological observation data is difficult to obtain. However, it’s still difficult to find data-rich watersheds. Moreover, transfer learning typically requires a certain level of similarity between the source domain and the target domain. Directly transferring knowledge from other watershed data can lead to uncontrolled transfer learning results. Model data is considered as a form of big data in geosciences. Compared to observed data, model data offers the advantages of being abundant and easily accessible. However, there is limited research regarding the application of transfer learning with numerical models in hydrology. Ma et al. (2022) proposed an LSTM-TL model to transfer the modeled relationship between groundwater table depth and input hydrometeorological forcings to the observation-based estimation in 2569 monitoring wells in European. The LSTM-TL agree with the in-situ data well and shows the advantage of DL and physics-based model by transfer learning.

## PINN and Transfer learning

PINN and transfer learning are two prominent techniques in the field of machine learning, each exhibiting unique advantages and application prospects in solving diverse problems.

Firstly, PINN represents an integration of physics principles and neural networks, aiming to embed known physical laws or constraints directly into neural network models. This approach enhances the model's ability to accurately represent physical phenomena by incorporating the governing equations or constraints as part of the loss function during training. PINN finds extensive applications in solving complex physical problems, such as fluid dynamics, solid mechanics, and heat conduction, primarily dealing with PDEs. By ensuring that the model outputs adhere to physical laws through constraint enforcement during training, PINN achieves precise prediction and solution of physical problems.

In contrast, transfer learning focuses on knowledge transfer and application. Its fundamental concept involves leveraging knowledge or models learned from one domain (source domain) to assist learning tasks in another related but data-scarce domain (target domain). Transfer learning has broad applications across various domains, including natural language processing, computer vision, and medical diagnosis.

Although PINN and transfer learning differ significantly in methodology and application, there exist intersections between them. For example, when we use data generated by PDEs as the source domain data for transfer learning, transfer learning can also be "physics-guided". At the same time, combining transfer learning with the principles of Physics-Informed Neural Networks (PINN) enhances the performance and efficiency of the model (Prantikos et al., 2023).

## Summary

This chapter provides a comprehensive overview of PINN and transfer learning. Through an analysis of the references, the conclusion is: PINN and transfer learning are both hot topics in current machine learning research, with promising prospects in theoretical studies and practical applications in the hydrology domain. Considering the heavy computational burden of PINN training and the abundance of analytical solutions for PDEs in hydrology literature, employing transfer learning for further research appears more suitable.

# Chapter 4 Daily runoff forecasting by deep recursive neural network

Runoff forecasting plays a significant role in water resources planning and management, for example, flood control, dam planning and reservoir operation (Napolitano et al., 2011; Yuan et al., 2018). However, rain-runoff forecasting is a difficult issue in hydrological process simulation, because of the highly non-linear behaviour of the factors governing the hydrology system in the space-time domain (Wang et al., 2009; Zhu et al., 2016). In the past decades, a great deal of effort has been devoted to runoff prediction(Yuan et al., 2018).

Although the physics-based model is widely used in runoff research, the physics-based model is powerless to deal with uncertainties, high complexity, non-stationarity, dynamism and non-linear factors, which affect runoff (Yoon et al., 2011). DL is a new hot topic in mechanical learning. Recently, researchers have paid attention to RNN and its variants (such as LSTMs and GRUs) and have found that deep RNNs have better performance for runoff time-series prediction (Chen et al., 2020; Cheng et al., 2020; Kao et al., 2020; Kratzert et al., 2018; Wang et al., 2020b; Xiang et al., 2020). According to the input variables, the Rainfall-Runoff studies can be divided into 2 categories:(1) Some researchers employ rainfall data as input to predict runoff (Hu et al., 2018; Le et al., 2019); (2) Other researchers prefer to incorporate rainfall data with multiple meteorological as input parameters, enabling various factors related to runoff to be considered within the model (de la Fuente et al., 2019). However, limited research has been focused on the influence of different input variables on rain-runoff forecasting by using deep RNN.

In order to consider the impact of the selection of input variables on the model prediction and find a way to improve accuracy when multiple input variables, this chapter investigates the performance of deep RNN models on runoff forecasting with different input variables and an optimized input is identified based on the PCA method. To make the result more credible, two USGS stations in different climatic zones are chosen as study areas. A general description of different algorithms and data sources are provided in Section 4.1. The predicted results with different inputs are discussed in Section 4.2. A summary is presented in Section 4.3.

The relationship between this chapter and chapter 5-chapter 7 is show in Figure 4.1. The Deep RNN model proposed in this chapter provide a tool for surface water prediction. the predicted surface water will be employed as the boundary conditions for the groundwater prediction model.

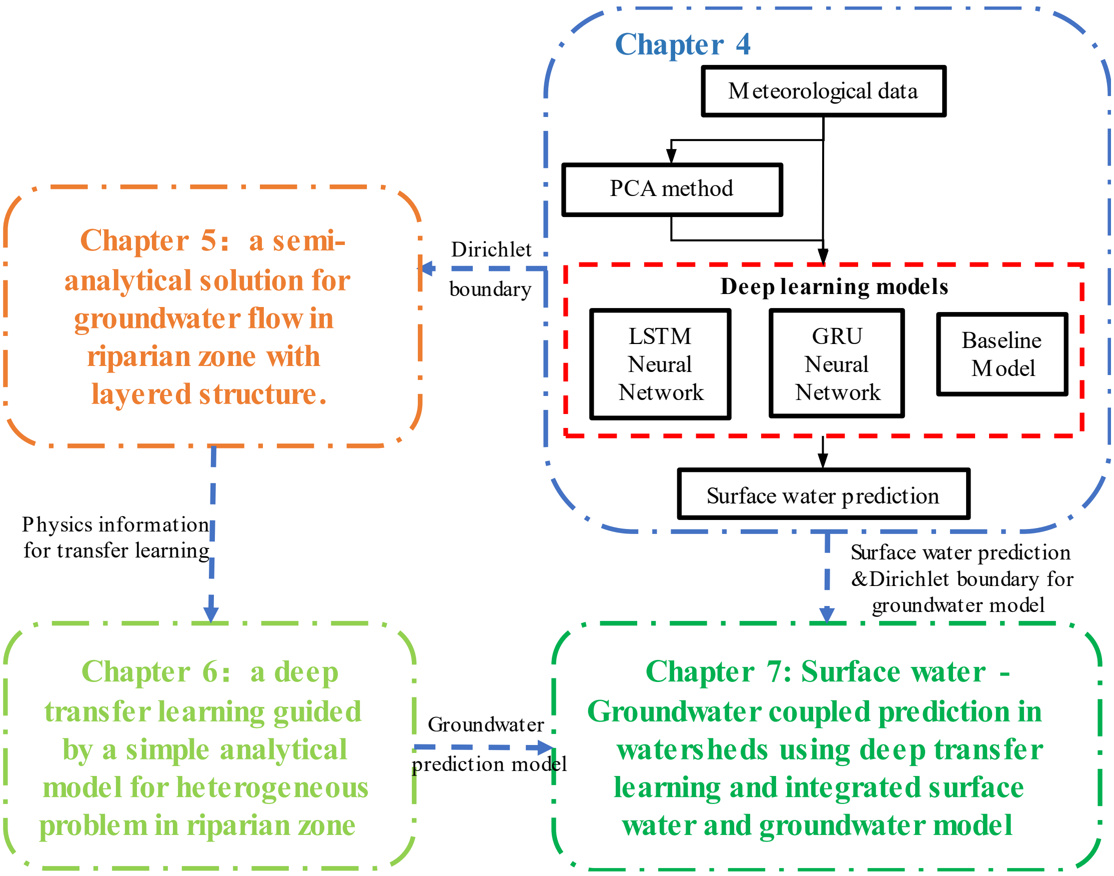


Figure 4.1 Relationship between this chapter and chapter 4, chapter 5 and chapter 6

## Method and data

### Data collection

To cover diverse hydro-climatological regimes, the Muskegon River and the Pearl River were chosen as the study area. As shown in Figure 4.2, The Muskegon River is located at the west of Michigan, U.S. state and it belongs to temperate continental climate. The river comes from Houghton Lake and flows southwest to Muskegon Lake stretching nearly 384km. Muskegon River basin is nearly 6,100 km$^2$ and is composed of 40 sub-watersheds (Ray et al., 2010). Muskegon River plays a crucial role in the social economy and natural ecology of the basin. Rogers Dam, Hardy Dam and Croton Dam on Muskegon River provide nearly 23000 people with a cleaner source of electricity. The runoff of Muskegon River influences the ecosystem and biogeochemistry in Lake Michigan (Johengen et al., 2008).

The Pearl River is in southern Mississippi, U.S. state which belongs to humid subtropical climate. The Pearl River runs from Neshoba County and flows to Lake Borgne with the length of length of 715 km (Taylor and Grace, 1995). The Ross Barnett Reservoir is the most important water facility which provides drinking water for residents in Metropolitan Jackson.

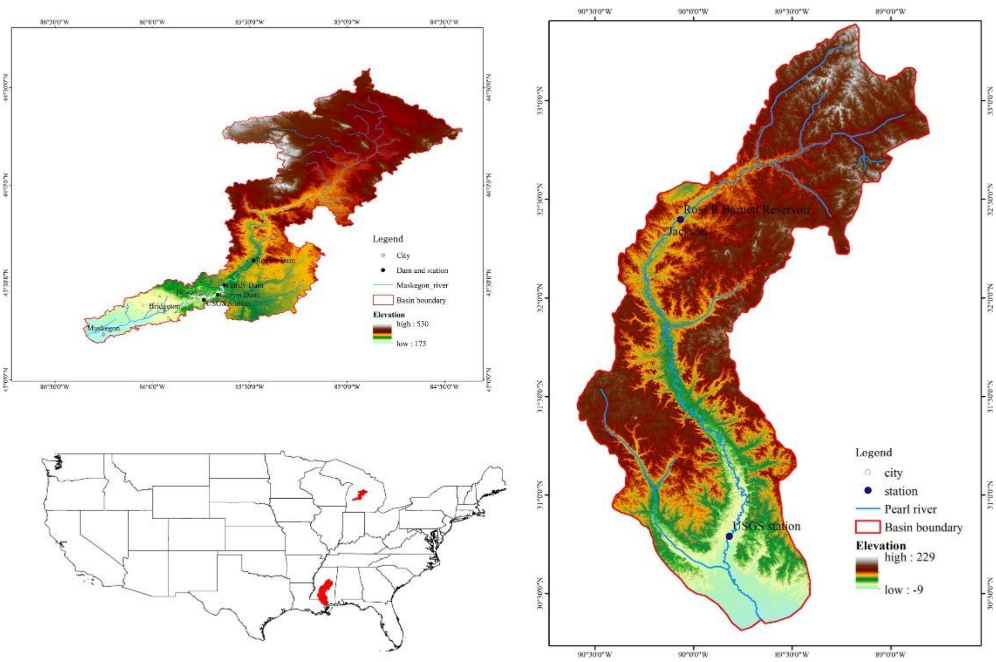


Figure 4.2 Overview of Muskegon river and the pearl river catchment

Daily runoff time series data is gathered from USGS Hydrological station 02489500 and 04121970. Daily meteorological time-series data is collected from

Weather Underground and NOAA. The meteorological data includes the following data (Table 4.1):

**Table 4.1** Details of the meteorological data in the Muskegon River and Pearl River

| | meteorological time series data in the Muskegon River | meteorological time series data in the Pearl River |
|---|---|---|
| Indexes | ● Max-temperature (°C),<br>● Mean-temperature (°C),<br>● Min-temperature (°C),<br>● Max-dew point (°C),<br>● Mean-dew point (°C),<br>● Min-dew point (°C),<br>● Max-humidity (%),<br>● Mean-humidity (%),<br>● Min-humidity (%),<br>● Max-sea level pressure (hPa),<br>● Mean-sea level pressure (hPa),<br>● Min-sea level pressure (hPa),<br>● Max-windspeed (km/h),<br>● Mean-windspeed (km/h),<br>● Min-visibility (km),<br>● Max-visibility (km),<br>● Mean-visibility (km),<br>● Precipitation (mm). | ● Max-temperature (°C),<br>● Mean-temperature (°C),<br>● Min-temperature (°C),<br>● Max-dew point (°C),<br>● Mean-dew point (°C),<br>● Min-dew point (°C),<br>● Max-humidity (%),<br>● Mean-humidity (%),<br>● Min-humidity (%),<br>● Max-sea level pressure (hPa),<br>● Mean-sea level pressure (hPa),<br>● Min-sea level pressure (hPa),<br>● Max-windspeed (km/h),<br>● Mean-windspeed (km/h),<br>● Precipitation (mm). |
| Duration | 01/10/1995-01/01/2020 | 01/01/2000-01/01/2020 |

**Data pre-processing**

Data pre-processing consists of data division and data cleaning. In addition, as 18 indicators of data are collected, PCA is employed to reduce the dimensionality of the input data, to provide an alternate input dataset (See below.)

**Data cleansing:** The missing or outlying points in time series data reduce the accuracy and quality of training and prediction. To discount the influence, the outlying data are identified by the $6\sigma$ rule which assumes data outside the range of $\overline{D} \pm 6\sigma_D$ is outlying data (Jeong et al., 2017), where $\overline{D}$ and $\sigma$ are the average value and the standard deviations of time series data respectively. The outlying points and vacancy are replaced by the average value of the same date in different years.

To avoid the influence of dimension on the training process, data are normalized into a standardized range by the following equation:

$$D_N = \frac{D-\bar{D}}{\sigma_D} \qquad \text{Equation 4.1}$$

**Data division:** To prevent overfitting and test the predictive capabilities of the model, the data is divided into two parts: 80% is used to train the suggested models, and the other 20% is used to test the trained models. In physics-based modelling, the value of past history is tied to the time lag between input and output response, such as the rainfall and the groundwater table response. However, in data-based modelling, the past history is just a hyperparameter which is not directly related to physical behaviour (Jeong and Park, 2019). So, in the training and testing part, the value of history is identified by trial-and-error.

**The PCA method:** The PCA method extracts several principal comprehensive variables from original data by covariance matrix, to persist core information and eliminate noise. PCA has been widely used in the literature and data mining since its introduction by Pearson (1901). The calculation processes of PCA method are as follows (Hotelling, 1933):

1) Processing the normalized data as matrix $D_N$;
2) Calculating the correlation coefficient matrix $Ccm$ based on the matrix $D_N$ as:

$$Ccm_{ij} = Cov(D_{N_i}, D_{N_j}) \qquad \text{Equation 4.2}$$

where $D_{N_i}$ is the indicator vector in matrix $D_N$.

3) Calculating feature values $fv$ and feature vectors of matrix $CCM$ and put feature values in orderas $fv_1 \geq fv_2 \geq \cdots \geq fv_n$.
4) Calculating the principal component contribution rate $Ccr_i$ and the cumulative contribution rate $CCR$:

$$Ccr_i = \frac{\lambda_i}{\sum_{k=1}^{n} \lambda_k} \qquad \text{Equation 4.3}$$

$$CCR = \frac{\sum_{p=1}^{i} \lambda_p}{\sum_{k=1}^{n} \lambda_k} \qquad \text{Equation 4.4}$$

5) When the cumulative contribution rate was greater than 85%, the number of principal components can be determined.

**Baseline model**

In data-based model research, it is recommended to use some simple but effective forecasting method as a baseline model to provide benchmarks (Hyndman and Athanasopoulos, 2018). In this article, ridge regression is employed as the baseline model. Ridge regression (Hoerl, 1959) is an effective method which is widely used in machine learning and hydrology (Chen et al., 2018; Miche et al., 2020). Based on linear regression, an L2 regularization term is applied in the loss function of ridge regression. In this way, ridge regression gains a better ability of generalization. To make the baseline model concise, rainfall data is input as it is the common variable in different inputs considered in this research.

**RNNs**

RNNs consist of the input layer, hidden layer (or hidden layers) and output layer, but different from other ANNs (artificial neural networks), RNNs have fabulous memory ability as these networks introduce state variables to store past information, and then determine the current outputs, together with the current inputs.

The RNNs model can be trained by the BPTT (Back Propagation Through Time) method which calculates not only the gradient of the cost corresponding to the input weights but also the gradient of the cost corresponding to the hidden weights of the previous time steps. However, the error of partial derivative accumulates through time steps in the BPTT method. Meanwhile, when the time step is large, the gradient will either get very small and vanish, or get very large and explode. This problem is commonly known as the vanishing/exploding gradient problem. In recent years, the hidden block in RNNs has been replaced by the LSTM block or GRU block to combat vanishing/exploding grad.

**1. LSTM**

LSTM neural network (Hochreiter and Schmidhuber, 1997) replaces the hidden block in RNNs with three logic gates and a memory cell as shown in Figure 4.3.

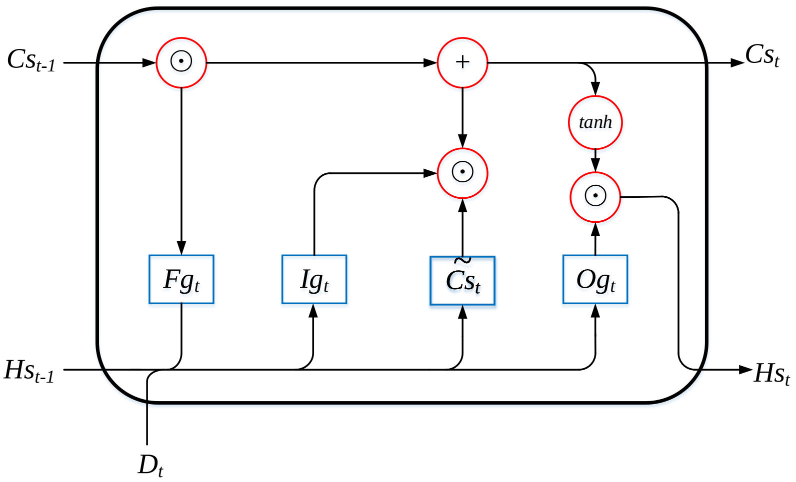


Figure 4.3 Neuron in the hidden layer of LSTM at time step t

In the training process, the memory cell state $Cs_t$ and hidden state $Hs_t$ would be updated selectively based on the input gate $Ig_t$ and output gate $Og_t$. The irrelevant information in long-term memory would be forgotten by the forget gate $Fg_t$. The hidden block of LSTM neural network can be represented as follows (Amiri, 2015):

Input gate:

$$Ig_t = \sigma(D_t We_{xi} + Hs_{t-1} We_{hi} + b_i) \qquad \text{Equation 4.5}$$

Forget gate:

$$Fg_t = \sigma\left(D_t We_{xf} + Hs_{t-1} We_{hf} + b_f\right) \qquad \text{Equation 4.6}$$

Output gate:

$$Og_t = \sigma(D_t We_{xo} + Hs_{t-1} We_{ho} + b_o) \qquad \text{Equation 4.7}$$

Cell state:

$$Cs_t = Fg_t \odot Cs_{t-1} + Ig_t \odot \tilde{Cs}_t \qquad \text{Equation 4.8}$$

$$\tilde{Cs}_t = tanh(D_t We_{xc} + Hs_{t-1} We_{hc} + b_c) \qquad \text{Equation 4.9}$$

Hidden state:

$$Hs_t = Og_t \odot tanh(Cs_t) \qquad \text{Equation 4.10}$$

where $\sigma$ is sigmoid function $\sigma(x) = \frac{1}{1+e^{-x}}$, which can be used as the activation function in this step to transform input to the range of 0-1; $We_{xi}, We_{xf}, We_{xo}, We_{xc} \in R^{d\times h}$, $We_{hi}, We_{hf}, We_{ho}, We_{hc} \in R^{h\times h}$ are weight matrixes;and $b_i, b_f, b_o, b_c \in R^{1\times h}$ are biases. $\odot$ is the Hadamard product of two matrixes. The activation function in this step is $tanh$ which can ensure hidden states range from -1 to1.

**2. GRU**

The GRU (Cho et al., 2014; Chung et al., 2014) neural network is similar to the LSTM neural network. It replaces the hidden block in RNNs with two logic gates and the candidate hidden state $\tilde{Hs}_t$ as it is shown in Figure 4.4.

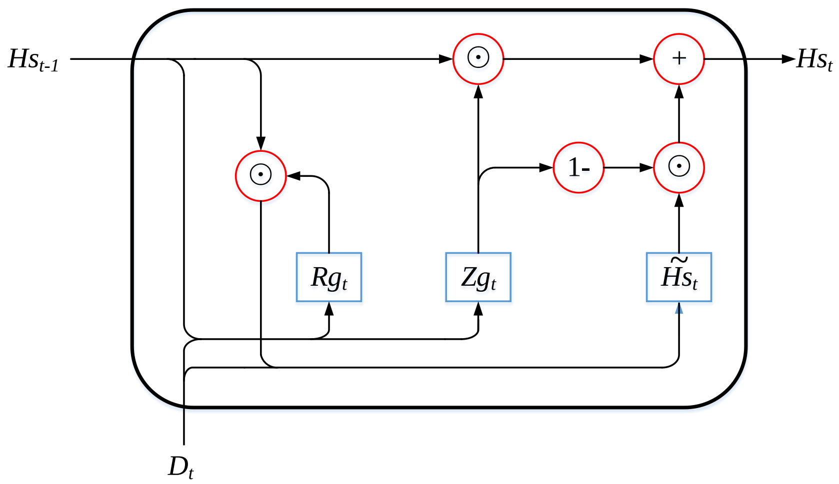


Figure 4.4 Neuron in the hidden layer of GRU at time step t

The hidden block of GRU neural network can be represented as following (Cho et al., 2014; Chung et al., 2014):

Reset gate:

$$Rg_t = \sigma(D_t We_{xr} + Hs_{t-1} We_{hr} + b_r) \qquad \text{Equation 4.11}$$

Update gate:

$$Zg_t = \sigma(D_t We_{xz} + Hs_{t-1} We_{hz} + b_z) \qquad \text{Equation 4.12}$$

Candidate hidden state:

$$\tilde{Hs}_t = tanh(D_t We_{xh} + (Rg_t \odot H_{t-1}) We_{hh} + b_h) \qquad \text{Equation 4.13}$$

Hidden state:

$$Hs_t = Zg_t \odot Hs_{t-1} + (1 - Zg_t) \odot \tilde{Hs}_t \qquad \text{Equation 4.14}$$

where $We_{xr}, We_{xz}, We_{xh} \in R^{d\times h}$ and $We_{hr}, We_{hz}, We_{hh} \in R^{h\times h}$ are weight matrix;$b_r, b_z, b_h \in R^{1\times h}$are biases. The update gate $Zg_t$ is used to capture long-term dependencies in time series. Meanwhile, the reset gate $Rg_t$ and the candidate hidden state are used to learn the short-term dependencies in time series. The candidate hidden state presents the influence of the previous hidden state on present hidden state. If the elements in the reset gate are close to 1, the hidden state of the previous hidden state will be reserved. If the elements in the reset gate are close to 0, the hidden state of the previous hidden state will be forgotten.

**3. Dropout**

Deep RNN is an effective method to deal with big data due to its memory ability. However, it would be overfitting when the input is high-dimensional. Dropout is a regularization method and provides an effective solution for this problem (Srivastava et al., 2014).

The main idea of dropout is that there is a certain probability that every neuron in a certain layer where the dropout method is applied will not be updated during each training iteration. In this way, the output will not be overly dependent on some elements of the hidden layer. However, due to the memory ability of RNNs, the dropout method can only be applied to the no-recurrent connection between layers.

**Model evaluation criteria**

The root means square error (RMSE), Nash-Sutcliffe Efficiency (NSE), the coefficient of determination ($R^2$), the mean absolute error (MAE) and the weighted mean absolute percentage error (WMAPE) are used to evaluate the model performance.

## Results and discussion

### Data pre-processing

Time series datasets are normalized by their mean and standard deviation and the SPSS 21 is used to identify the principal component. The correlation coefficient matrix is shown in Table 4.2 and Table 4.3.

**Table 4.2** The correlation coefficient matrix of data in Muskegon River

| | MAXTEM | MEANTEM | MINTEM | MAXDEW | … | MINSEA | PRE |
|---|---|---|---|---|---|---|---|
| MAXTEM | 1.00 | 0.98 | 0.93 | 0.94 | … | 0.35 | 0.06 |
| MEANTEM | 0.98 | 1.00 | 0.98 | 0.96 | … | 0.32 | 0.09 |
| MINTEM | 0.93 | 0.98 | 1.00 | 0.94 | … | 0.27 | 0.12 |
| MAXDEW | 0.94 | 0.96 | 0.94 | 1.00 | … | 0.18 | 0.18 |
| MEANDEW | 0.93 | 0.96 | 0.96 | 0.99 | … | 0.18 | 0.17 |
| MINDEW | 0.91 | 0.95 | 0.96 | 0.95 | … | 0.19 | 0.14 |
| MAXHUM | 0.16 | 0.16 | 0.17 | 0.35 | … | -0.37 | 0.23 |
| MEANHYM | -0.12 | -0.06 | 0.02 | 0.16 | … | -0.58 | 0.33 |
| MINHUM | -0.30 | -0.21 | -0.10 | -0.02 | … | -0.54 | 0.31 |
| MAXWIND | -0.35 | -0.40 | -0.44 | -0.44 | … | 0.07 | -0.20 |
| MEANWIND | -0.20 | -0.25 | -0.29 | -0.33 | … | 0.19 | -0.27 |
| MAXSEA | -0.07 | -0.11 | -0.15 | -0.21 | … | 0.24 | -0.30 |
| MEANSEA | 0.12 | 0.11 | 0.09 | 0.08 | … | 0.39 | -0.02 |
| MINSEA | 0.35 | 0.32 | 0.27 | 0.18 | … | 1.00 | -0.31 |
| PRE | 0.06 | 0.09 | 0.12 | 0.18 | … | -0.31 | 1.00 |

Table 4.3 The correlation coefficient matrix of data in Pearl River

| | MAXTEM | MEANTEM | MINTEM | MAXDEW | … | MINSEA | PRE |
|---|---|---|---|---|---|---|---|
| MAXTEM | 1.00 | 0.96 | 0.86 | 0.87 | … | -0.38 | -0.10 |
| MEANTEM | 0.96 | 1.00 | 0.94 | 0.93 | … | -0.44 | -0.04 |
| MINTEM | 0.86 | 0.94 | 1.00 | 0.91 | … | -0.43 | 0.02 |
| MAXDEW | 0.87 | 0.93 | 0.91 | 1.00 | … | -0.53 | 0.08 |
| MEANDEW | 0.87 | 0.94 | 0.93 | 0.97 | … | -0.50 | 0.05 |
| MINDEW | 0.80 | 0.87 | 0.91 | 0.87 | … | -0.41 | 0.03 |
| MAXHUM | 0.19 | 0.21 | 0.24 | 0.41 | … | -0.29 | 0.20 |
| MEANHYM | 0.04 | 0.14 | 0.27 | 0.42 | … | -0.33 | 0.30 |
| MINHUM | -0.05 | 0.11 | 0.29 | 0.35 | … | -0.29 | 0.28 |
| MAXWIND | -0.10 | -0.05 | -0.01 | 0.05 | … | -0.27 | 0.16 |
| MEANWIND | -0.27 | -0.18 | -0.12 | -0.08 | … | -0.19 | 0.15 |
| MAXSEA | -0.57 | -0.62 | -0.60 | -0.64 | … | 0.87 | -0.13 |
| MEANSEA | -0.47 | -0.53 | -0.51 | -0.59 | … | 0.93 | -0.19 |
| MINSEA | -0.38 | -0.44 | -0.43 | -0.53 | … | 1.00 | -0.22 |
| PRE | -0.10 | -0.04 | 0.02 | 0.08 | … | -0.22 | 1.00 |

1631

The eigenvalues, variance contribution rates and cumulative variance contribution rates of the correlation coefficient matrix is shown in Table 4.4. 5 components in each study areas are extracted, and the cumulative variance contribution rates are 92.102% and 91.84%.

Table 4.4 The Eigenvalues and variance contribution rates

| Muskegon River | | | | Pearl River | | | |
|---|---|---|---|---|---|---|---|
| Ingredient | Eigenvalues | Variance | Cumulative | Ingredient | Eigenvalues | Variance | Cumulative |
| 1 | 6.41 | 35.63% | 35.63% | 1 | 7.27 | 48.49% | 48.49% |
| 2 | 4.35 | 24.19% | 59.82% | 2 | 2.64 | 17.62% | 66.11% |
| 3 | 2.63 | 14.61% | 74.43% | 3 | 1.82 | 12.11% | 78.23% |
| 4 | 1.16 | 6.42% | 80.84% | 4 | 1.23 | 8.23% | 86.46% |
| 5 | 1.04 | 5.78% | 86.62% | 5 | 0.81 | 5.39% | 91.84% |
| 6 | 0.74 | 4.13% | 90.76% | 6 | 0.54 | 3.58% | 95.42% |
| 7 | 0.61 | 3.39% | 94.14% | 7 | 0.21 | 1.39% | 96.81% |
| 8 | 0.45 | 2.48% | 96.62% | 8 | 0.14 | 0.90% | 97.71% |
| 9 | 0.18 | 1% | 97.62% | 9 | 0.09 | 0.599% | 98.30% |
| 10 | 0.16 | 0.89% | 98.51% | 10 | 0.08 | 0.56% | 98.86% |
| 11 | 0.13 | 0.7% | 99.22% | 11 | 0.06 | 0.41% | 99.26% |
| 12 | 0.05 | 0.26% | 99.48% | 12 | 0.06 | 0.39% | 99.66% |
| 13 | 0.04 | 0.21% | 99.69% | 13 | 0.03 | 0.20% | 99.85% |
| 14 | 0.02 | 0.13% | 99.82% | 14 | 0.02 | 0.12% | 99.97% |
| 15 | 0.01 | 0.08% | 99.9% | 15 | 0.01 | 0.03% | 100.00% |
| 16 | 0.01 | 0.07% | 99.96% | | | | |
| 17 | 0 | 0.03% | 99.99% | | | | |
| 18 | 0 | 0.01% | 100% | | | | |

This section employs the PCA method to reduce the dimensionality of the original data, reducing the 18-dimensional data of the Muskegon River and the 15-dimensional data of the Pearl River to 5 principal components. This dimensionality reduction process does not simply discard some indicators; rather, it identifies the primary directions (principal components) that best represent the data variation. It then projects the original data onto a lower-dimensional space, thereby retaining the main information of the data. In simple terms, each principal component is a combination of the original data. The principal component matrix of time series dataset is shown in Table 4.5.

Table 4.5 The principal component matrix of time series dataset

| Muskegon River | | | | | | Pearl River | | | | | |
|---|---|---|---|---|---|---|---|---|---|---|---|
| Indicator | 1 | 2 | 3 | 4 | 5 | Indicator | 1 | 2 | 3 | 4 | 5 |
| MAXTEMP | 0.92 | 0.33 | -0.01 | 0.10 | -0.03 | MAXTEM | 0.83 | -0.49 | -0.12 | 0.10 | 0.07 |
| MEANTEMP | 0.95 | 0.26 | -0.02 | 0.12 | -0.04 | MEANTEM | 0.90 | -0.37 | -0.10 | 0.16 | 0.08 |
| MAXDEW | 0.97 | 0.06 | 0.06 | 0.13 | 0.01 | MINTEM | 0.90 | -0.24 | -0.02 | 0.23 | 0.08 |
| MINTEMP | 0.95 | 0.18 | -0.01 | 0.13 | -0.04 | MAXDEW | 0.95 | -0.11 | 0.03 | 0.17 | 0.04 |
| MEANDEW | 0.98 | 0.07 | 0.10 | 0.11 | 0.00 | MEANDEW | 0.96 | -0.13 | 0.08 | 0.17 | 0.02 |
| MINDEW | 0.96 | 0.09 | 0.13 | 0.09 | -0.01 | MINDEW | 0.90 | -0.17 | 0.12 | 0.21 | 0.03 |
| MAVHUM | 0.35 | -0.51 | 0.55 | -0.12 | 0.19 | MAXHUM | 0.46 | 0.35 | 0.59 | -0.16 | -0.17 |
| MEANHUM | 0.18 | -0.78 | 0.48 | -0.02 | 0.13 | MEANHYM | 0.48 | 0.62 | 0.57 | 0.05 | -0.13 |
| MINHUM | 0.01 | -0.76 | 0.30 | 0.04 | 0.07 | MINHUM | 0.42 | 0.64 | 0.41 | 0.22 | -0.09 |
| MAXSEA | -0.59 | 0.45 | 0.41 | 0.45 | 0.09 | MAXWIND | 0.06 | 0.61 | -0.53 | 0.42 | -0.06 |
| MEANSEA | -0.46 | 0.61 | 0.51 | 0.38 | 0.05 | MEANWIND | -0.08 | 0.63 | -0.54 | 0.45 | -0.03 |
| MINSEA | -0.32 | 0.66 | 0.55 | 0.30 | 0.03 | MAXSEA | -0.80 | -0.14 | 0.29 | 0.42 | 0.09 |
| MAXWIND | 0.00 | 0.22 | -0.20 | -0.17 | 0.89 | MEANSEA | -0.75 | -0.27 | 0.34 | 0.44 | 0.08 |
| MEANWIND | 0.13 | 0.76 | -0.31 | -0.17 | 0.23 | MINSEA | -0.68 | -0.37 | 0.38 | 0.43 | 0.09 |
| MINVIS | 0.03 | 0.78 | -0.29 | -0.16 | -0.02 | PRE | 0.13 | 0.49 | 0.10 | -0.15 | 0.84 |
| MAXVIS | -0.08 | -0.34 | -0.72 | 0.46 | 0.03 | | | | | | |
| MEANVIS | -0.19 | -0.35 | -0.71 | 0.41 | -0.01 | | | | | | |
| PRECI | 0.18 | -0.46 | -0.05 | 0.41 | 0.35 | | | | | | |

As shown in

This section employs the PCA method to reduce the dimensionality of the original data, reducing the 18-dimensional data of the Muskegon River and the 15-dimensional data of the Pearl River to 5 principal components. This dimensionality reduction process does not simply discard some indicators; rather, it identifies the primary directions (principal components) that best represent the data variation. It then projects the original data onto a lower-dimensional space, thereby retaining the main information of the data. In simple terms, each principal component is a combination of the original data. The principal component matrix of time series dataset is shown in Table 4.5.

Table 4.5, there is a strong positive correlation between the first component and Max-temperature (°C), Mean-temperature (°C), Min-temperature (°C), Max-dew point (°C), Mean-dew point (°C), Min-dew point (°C) in both areas. These indexes reflect the temperature of study areas. However, in Pearl River, there is a negative correlation between the first component and sea level pressure indexes while in Muskegon River it is positive. The second to the fifth component in Muskegon River are the combination of other indexes, while the second to the fifth component in Pearl River are humidity indexes, wind indexes, sea level pressure and precipitation indexes respectively. The similarities and differences between principal components of Muskegon River and Pearl River show that the PCA method can extract climatic characteristics in different areas. The result of the PCA method is shown in Figure 4.5.

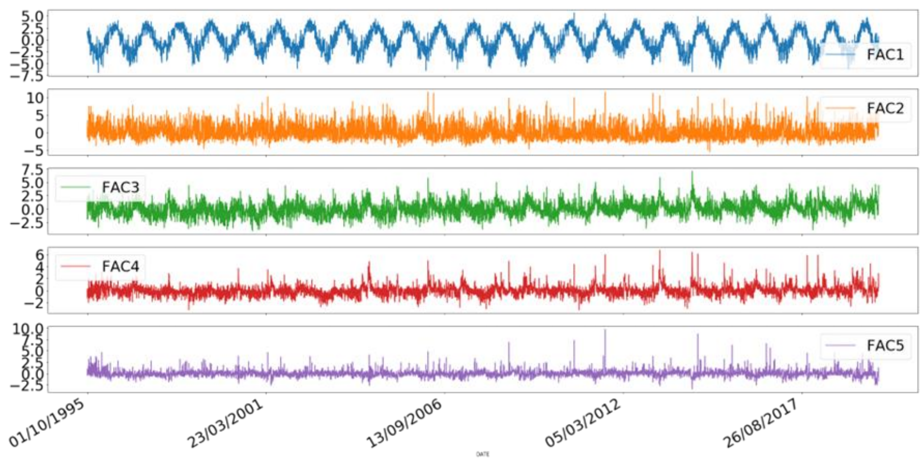


**Figure 3.4 a.** Five Principle components in Muskegon river.

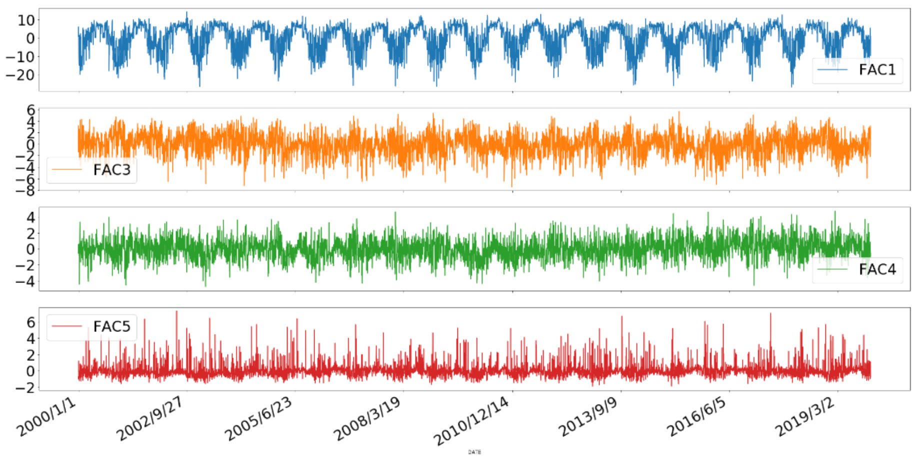


**Figure 3.4 b.** Five Principle components in Pearl river

Figure 4.5 Principle components in Muskegon river and Pearl river

**Training for the ANN**

Different RNN models (LSTM and GRU) are developed to test the influence of different inputs on runoff forecasting. These models are implemented using Python 3.7 and TensorFlow 2.0. The structure includes a input layer, hidden layer 1 with 16 hidden neurons, hidden layer 2 with 8 hidden neurons and a output layer. The dropout method is used between the hidden layers to deal with overfitting. Meanwhile, the RMSprop algorithm is used for training LSTM and GRU in this study. The hyperparameter, past history, is set to 30 days, which means input data of every 30 days is used to predicate runoff of the next day.

**Performance of ANN**

Different hidden blocks and inputs are compared to evaluate their effect on model performance and to identify the best hidden block and input combination. 6 different scenarios are proposed in Table 4.6 to predict the runoff. Ridge regression is used as a baseline model. These models are run on a computer with intel core i7-9750H CPU and 16GB memory.

Table 4.6 Different scenarios of hidden block and input

| | Input | Hidden block kind |
|---|---|---|
| Scenario 1 | Rainfall | LSTM |
| Scenario 2 | Rainfall | GRU |
| Scenario 3 | Multiple meteorological data | LSTM |

| | | |
|---|---|---|
| Scenario 4 | Multiple meteorological data | GRU |
| Scenario 5 | Multiple meteorological data with PCA method | LSTM |
| Scenario 6 | Multiple meteorological data with PCA method | GRU |

Parts of the forecasting results are provided and compared with the baseline model in Figure 4.6. Other results can be found in the support information (Figure S 1-Figure S 14). The model evaluation criteria results are provided in Table 4.7

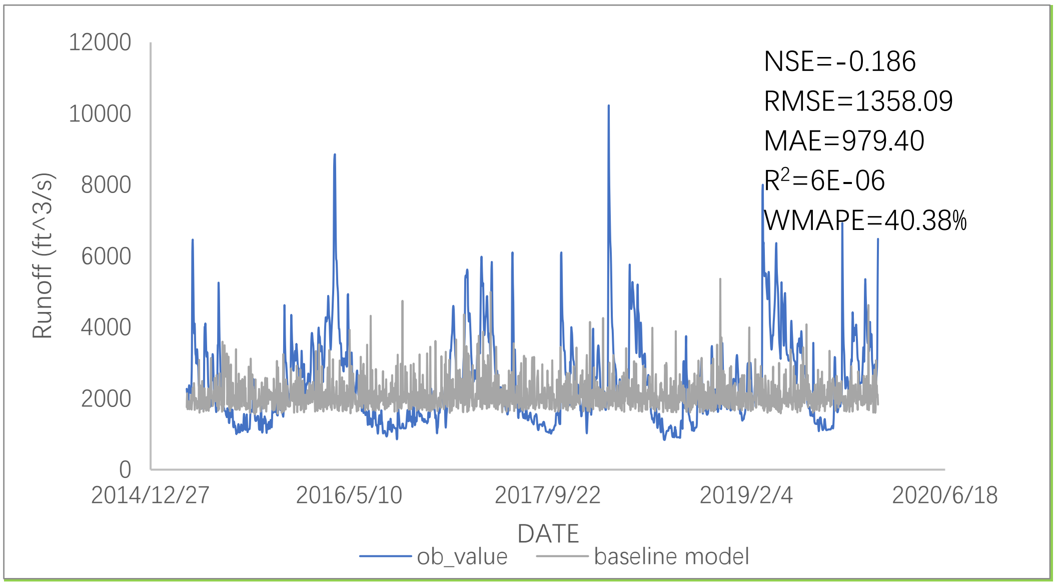


**Figure 3.5a** Baseline model: Ridge regression based on rainfall data in Muskegon river

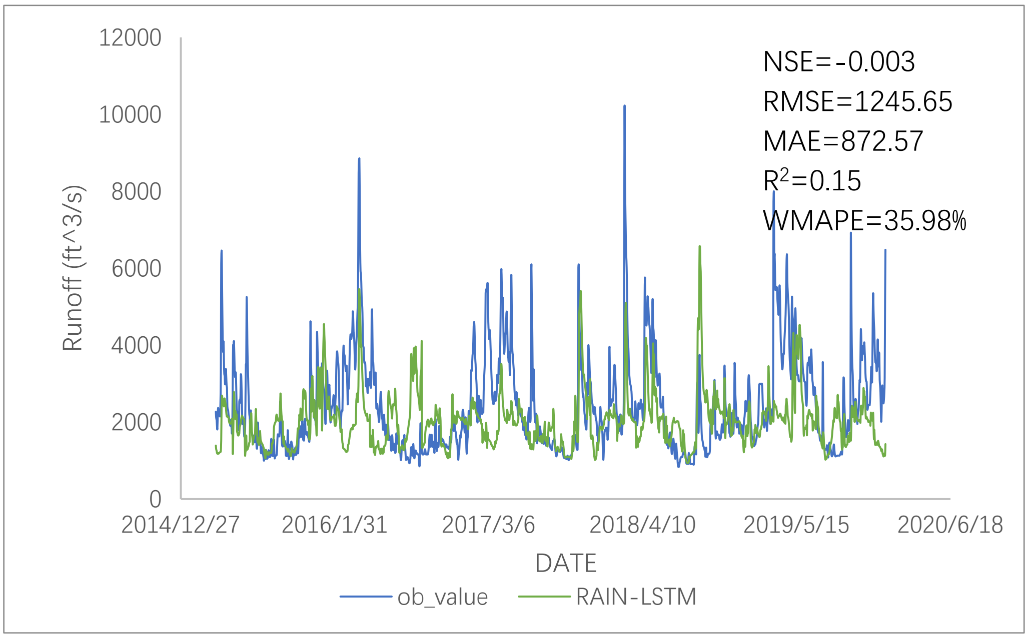


**Figure 3.5b** Scenario 1: LSTM neural network based on rainfall data in Muskegon river

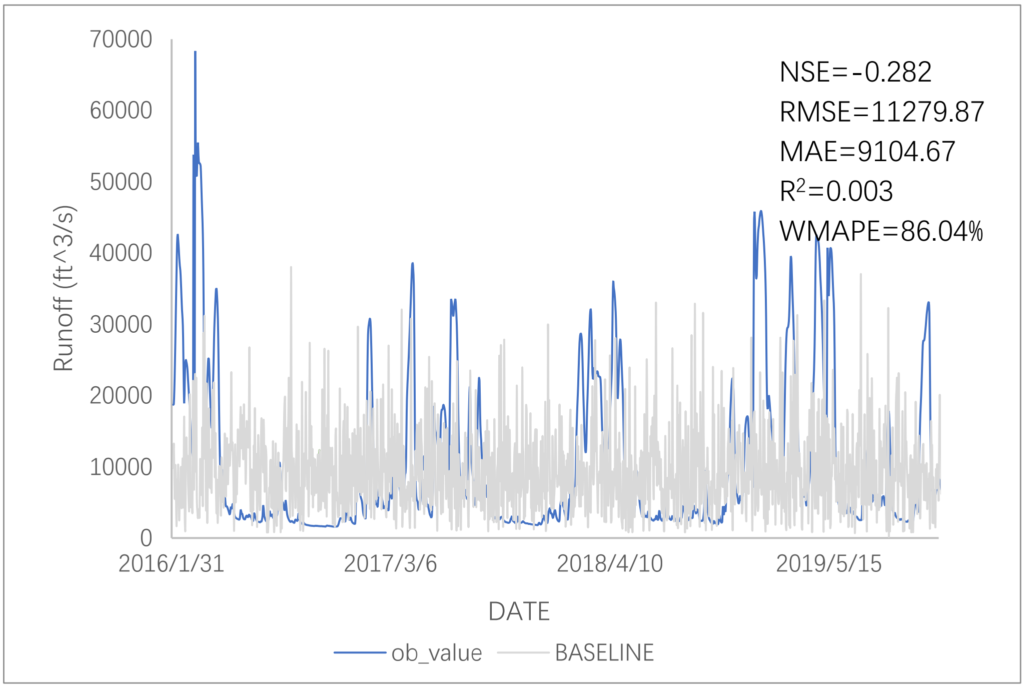


**Figure 3.5c**. Baseline model: Ridge regression based on rainfall data in Pearl river

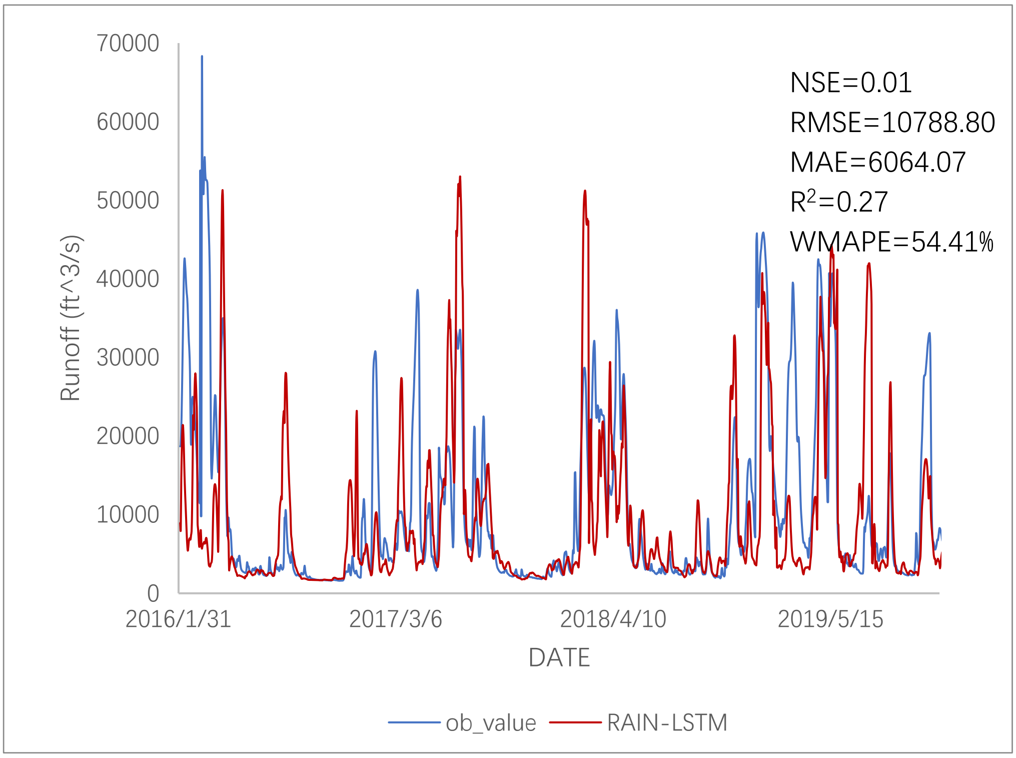


**Figure 3.5d**. Scenario 1: LSTM neural network based on rainfall data in Pearl River

Figure 4.6 Result for all scenarios

Figure 4.6 shows runoff forecasting by different models and inputs. The observation value (blue line) is castrated with different models. (a) Ridge regression based on rainfall data in Muskegon River; (b)LSTM neural network based on rainfall data in Muskegon River; (c) Ridge regression based on rainfall data in Pearl River; (d) LSTM neural network based on rainfall data in Pearl River.

Table 4.7 Model evaluation result

| | | Baseline model | Scenario 1 | Scenario 2 | Scenario 3 | Scenario 4 | Scenario 5 | Scenario 6 |
|---|---|---|---|---|---|---|---|---|
| | Input | Rainfall | Rainfall | Rainfall | multiple meteorological data | multiple meteorological data | multiple meteorological data with PCA method | multiple meteorological data with PCA method |
| Muskegon River | Hidden block kind | - | LSTM | GRU | LSTM | GRU | LSTM | GRU |
| | NSE | -0.186 | 0.003 | -0.012 | 0.343 | 0.372 | 0.844 | 0.842 |
| | RMSE($ft^3/s$) | 1358.09 | 1245.65 | 1254.9 | 1010.72 | 988.31 | 492.23 | 496.54 |
| | MAE($ft^3/s$) | 979.4 | 872.57 | 895.68 | 674.75 | 659.16 | 276.65 | 279.6 |
| | $R^2$ | 6.00E-06 | 0.15 | 0.127 | 0.46 | 0.49 | 0.85 | 0.84 |
| | Time(s) | - | 403 | 403 | 451 | 405 | 436 | 407 |
| Pearl River | NSE | -0.2821 | 0.101 | 0.102 | 0.163 | 0.156 | 0.292 | 0.31 |
| | RMSE($ft^3/s$) | 11279.868 | 10788.8 | 10781.84 | 10410.34 | 10454.19 | 8672.03 | 8549.07 |
| | MAE($ft^3/s$) | 9104.67 | 6064.07 | 6164.57 | 6252.14 | 6341.64 | 5376.65 | 5107.27 |
| | $R^2$ | 0.003198 | 0.27 | 0.25 | 0.37 | 0.31 | 0.38 | 0.41 |
| | Time(s) | - | 410 | 407 | 442 | 409 | 435 | 412 |

As shown in Table 4.7 and Figure 4.6 Result for all s, all deep learning models have better performance than the baseline model with higher NSE and $R^2$ and lower RMSE, MAE and WMAPE, which prove the advantage and effectiveness of the deep learning model.

In Table 4.7, different input has a great influence on model accuracy. Deep RNN models with multiple meteorological data inputs (Scenario 3 and Scenario 4) has a better performance than rainfall data input only (Scenario 1 and Scenario 2). In both areas, the NSEs of Scenario 1 and Scenario 2 are nearly 0, which means the results of deep RNN models with rainfall data input can only reflect the overall trend of runoff. Compared with Scenario 1 and Scenario 2, NSE and $R^2$ in both areas are much higher in Scenario 3 and Scenario 4, meanwhile, RMSE and MAE reduced by nearly 20% in Muskegon River. The improvement of models in Pearl River is relatively small. This may be because multiple meteorological data included not only rainfall data, but also wind speed, temperature and other meteorological indicators that directly or indirectly affect the runoff generation process. This means that meteorological data can provide more effective information to achieve higher accuracy.

With the same hidden block, the accuracy of deep RNN model with PCA input (Scenario 5 and Scenario 6) may outperform the model with normal multiple meteorological data inputs (Scenario 3 and Scenario 4) NSE and $R^2$ of Scenario 5 and Scenario 6 are nearly twice as much as Scenario 3 and Scenario 4 in both areas. Meanwhile, in Muskegon River, RMSE, MAE and WMAPE are nearly 50% less than Scenario 3 and Scenario 4. This means the PCA method can reflect core information by classifying the original data information into several comprehensive variables and prevent the interference of useless information.

With the same input, the deep GRU model can achieve the same accuracy as the deep LSTM model and reduce the computational load. This phenomenon is more obvious when processing high-dimensional input data. When the input data are just rainfall (Scenario 1 and Scenario 2), the calculation time of the deep LSTM model and deep GRU model are the same. With the input data changed to PCA data (Scenario 5 and Scenario 6) and multiple meteorological data (Scenario 3 and Scenario 4), the calculation time of deep LSTM model rises dramatically to 436s and 451s in Muskegon River and 435s and 442s in Pearl River, while the calculation time of deep GRU model ascends slightly to 405s and 407sin Muskegon River and 407s and 412s in Pearl River. This phenomenon could be due to the structure of the hidden block. The number of parameters which need to be identified in each GRU block is 9 (6 weights and 3 biases) while 12 parameters (8 weights and 4 biases) in each LSTM block need to be trained.

With the same optimization method and input data, the fewer the number of identification parameters, the faster to get the optimal solution.

## Summary

In recent years, the deep Recurrent Neural Network (RNN) has been applied to predict daily runoff, as its ability to deal with the high nonlinear interactions among the complex hydrology factors. However, most of the existing studies focus on the model structure and the computational load, without considering the impact of the selection of multiple input variables on the model prediction. This article presents a study to evaluate this influence and provides a method of identifying the best meteorological input variables for a runoff model. Rainfall and multiple meteorological data have been considered as input to the model. Principal Component Analysis (PCA) has been applied to the data as a contrast, to reduce dimensionality and redundancy within this input data. Two different deep RNN models, a long-short-term memory (LSTM) model and a gated recurrent unit (GRU) model, have been comparatively applied to predict runoff with these inputs. In this study, the Muskegon River and the Pearl River were taken as examples. The results demonstrate that the selection of input variables has a significant influence on the predictions made using the RNN while the RNN model with multiple meteorological input data is shown to achieve higher accuracy than rainfall data alone. PCA method can improve the accuracy of the deep RNN model effectively as it can reflect core information by classifying the original data information into several comprehensive variables.

# Chapter 5 Groundwater Responses to Recharge and Flood in Riparian Zones of Layered Aquifers: An Analytical Model

The analytical model has gained widespread adoption in hydrology research, however, one of the limitations in the previous studies is the assumption of the homogeneous condition. In fact, heterogeneity is intrinsic in natural aquifers and has been studied extensively in hydrogeology (Chang and Yeh, 2016; Feng et al., 2020; Hsieh and Yeh, 2014; Li et al., 2020a; Li et al., 2021b; Liang et al., 2019; Sedghi and Zhan, 2021). The riverbank often has a two-layer structure which is composed of non-cohesive and cohesive materials (Thorne and Tovey, 1981). Heterogeneity in riverbank sediments not only controls water exchange by deflecting flow downward into the sediment or upward into the channel (Ward et al., 2011), but it also alters groundwater paths, fluxes, and residence times in the riparian zone (Earon et al., 2020; Gomez-Velez et al., 2014; Pryshlak et al., 2015; Sawyer and Cardenas, 2009). Sawyer and Cardenas (2009) conducted numerical simulations of hyporheic flow and solute transport through immobile bed forms composed of heterogeneous sediments. Their findings showed that the sediment heterogeneity created longer hyporheic mixing paths than the case with homogeneous sediments. Liang and Zhang (2013a) presented an analytical solution for the water table and lateral discharge in a heterogeneous unconfined aquifer with a time-dependent source and fluctuating river stage. The heterogeneity that they considered consists of a number of sections of different hydraulic conductivity values. More recently, Su et al. (2020) evaluated the scale issues inherent in concentration, mixing, heterogeneity, and modelling approaches in hyporheic flow based on a numerical model and Monte Carlo simulations. Their results revealed that flux variance in the streambed is an appropriate metric for assessing the magnitude of hyporheic mixing at all scales.

**Table 5.1** Review of analytical model considering heterogeneity of aquifer.

| | Research | Heterogeneity | Dimension | Type of aquifer | Driver force |
|---|---|---|---|---|---|
| 1 | Monachesi and Guarracino (2011) | linear increase K | 1D | confined | sea |
| 2 | Chuang et al. (2010) | n vertical layers | 1D | confined | sea |
| 3 | Wang et al. (2015) | linear increase K | 2D | confined | sea |
| 4 | Li et al. (2011) | 2 layers | 1D | unconfined | sea |
| 5 | Li and Jiao (2001) | 2 layers | 2D | confined | sea |
| 6 | Jeng et al. (2002) | 2 layers | 2D | unconfined | sea |
| 7 | Rathore et al. (2018) | n layers | 2D | confined | sea |
| 8 | Rathore et al. (2020) | 2D field | 2D | confined | sea |
| 9 | Liang and Zhang (2013a) | n vertical layers | 1D | unconfined | river and recharge |
| 10 | Huang and Yeh (2016) | n vertical layers | 2D | confined | river and well |
| 11 | Rumynin et al. (2019) | exponential decay K | 2D | confined | river and recharge |
| 12 | Butler Jr et al. (2007) | 2 layers | 3D | unconfined | well and river |
| 13 | Samani and Sedghi (2015) | 2 layers | 3D | unconfined | well |
| 14 | Feng et al. (2021a) | 3 layers | 2D | confined | well |
| 15 | Feng et al. (2020) | 3 layers | 2D | confined | well |
| 16 | Feng et al. (2019) | 2 layers | 2D | confined | well |
| 17 | Yeh and Kuo (2010) | 2 layers | 2D | confined | well |
| 18 | Avci and Ufuk Sahin (2014) | n vertical layers | 1D | confined | well |
| 19 | Sedghi and Zhan (2019) | 2 layers | 3D | unconfined | well |
| 20 | Sedghi and Zhan (2021) | 3 vertical layers | 3D | unconfined | well |
| 21 | Chang et al. (2008) | n vertical layers | 1D | unconfined | diriclet boundary and recharge |
| 22 | Saffi (2014) | 2 vertical layers | 1D | confined | leaky |
| 23 | Present solution | 2 layers | 2D | unconfined | river and recharge |

Previous work evaluating the heterogeneity of aquifers in analytical models is summarized in Table 5.1. To the best of our knowledge, a 2-D analytical model describing groundwater flow in the riparian zone (or hyporheic zone) with a two-layer structure has not been reported. Therefore, this study aims to fill this knowledge gap by presenting a semi-analytical solution for this 2-D model. In the semi-analytical model, groundwater flow in the two layers is coupled with the continuity of the hydraulic head and water fluxes across the interface. The proposed semi-analytical model could be used to investigate changes of the hydraulic head and lateral discharge caused by a recharge or flood event in a layered aquifer system. The chapter is organized as follows: the mathematical model and its solution are presented in section 5.1 and section 5.2, respectively. The comparison of the solution with a high-resolution numerical model built with COMSOL is given in section 5.3. The results and discussion are presented in section 5.4 and the application of the solution to field data is described in section 5.5. Section 5.6 presents the summary of this work.

The relationship between this chapter and chapter 3, chapter5 and chapter 6 is show in Figure 4.1. The analytical model presented in this chapter would be used to provide the physics information for chapter 5. Meanwhile, the Dirichlet boundary condition used in the groundwater model provide potential application to couple the surface water simulation result with groundwater. It should be noted that analytical models for unconfined groundwater flow in horizontal section and unsaturated-saturated groundwater flow in vertical section are also presented in the following research.

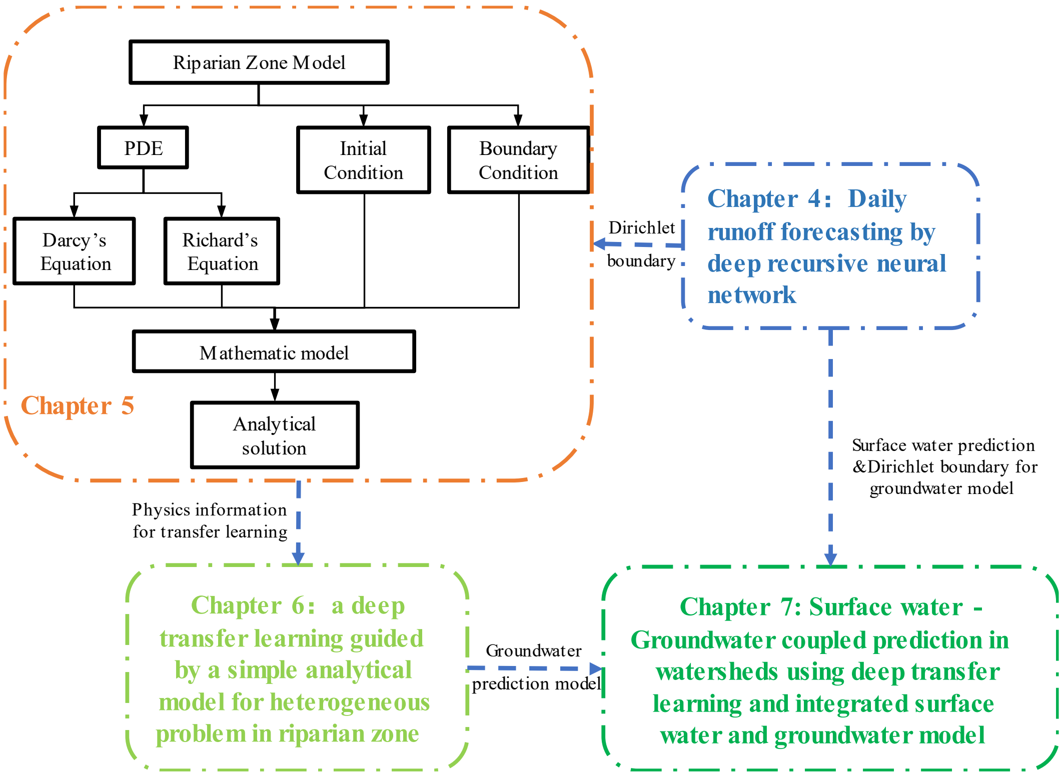


Figure 5.1 Relationship between this chapter and chapter 3, chapter 5 and chapter 6

## Conceptual and Mathematical Models

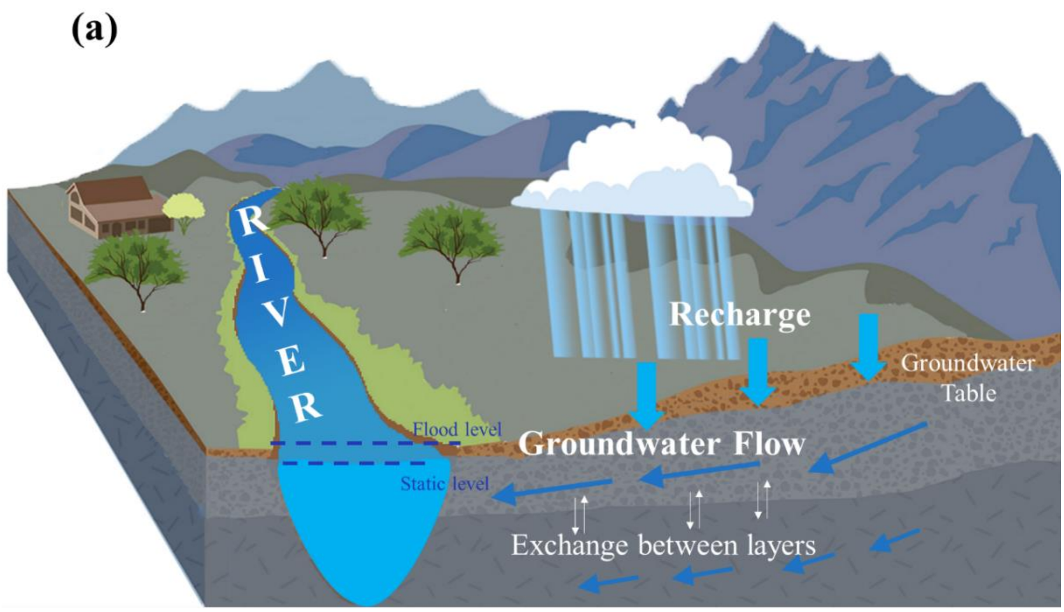

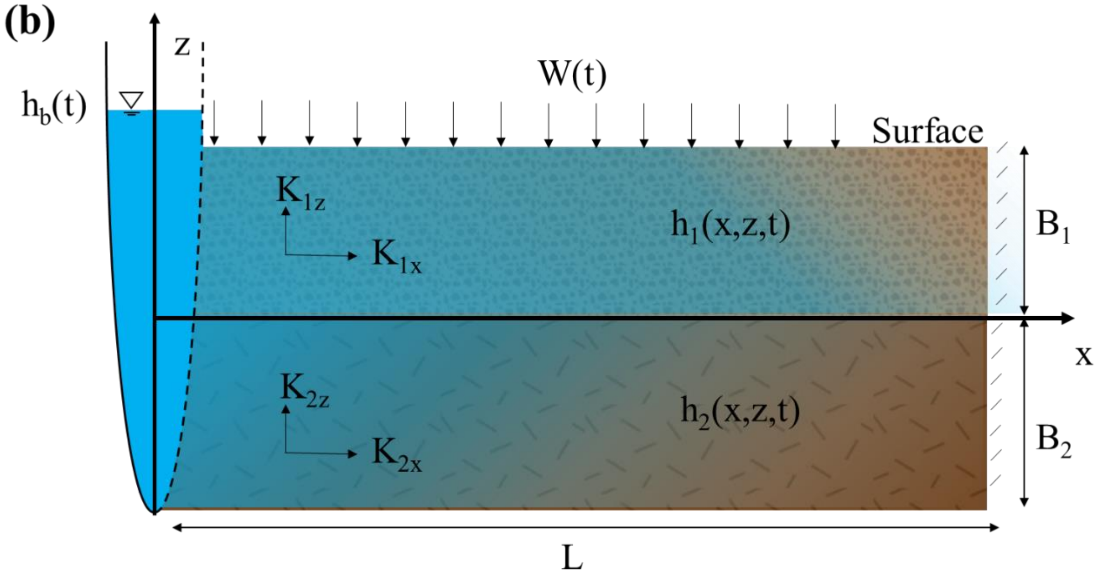


Figure 5.2 (a) Schematic diagram of groundwater flow in a layered aquifer; (b) conceptual model of groundwater flow to a river in an unconfined aquifer with two-layer porous media.

A schematic diagram of groundwater flow along a transect of the riparian zone in a two-layer unconfined aquifer is displayed in Figure 5.2. The layered aquifer is laterally bounded by a watershed divide and a river that fully penetrates the aquifer (Figure 5.2a), which is conceptualized in two dimensions (Figure 5.2b). In Figure. 1b, the x-axis is along the groundwater flow direction toward the divide, and the z-axis is vertically upward. The top of the aquifer is the water table, which receives time-dependent recharge from rainfall events. The bottom of the aquifer is horizontal and impermeable. The upper and lower layers have a uniform initial thickness of $B_1$ [L] and $B_2$ [L], respectively. The upper and lower layers are both homogeneous, but their hydraulic conductivities are different. The governing equation for groundwater flow in the aquifer is given as follows:

$$S_{s1}\frac{\partial h_1}{\partial t} = K_{x1}\frac{\partial^2 h_1}{\partial x^2} + K_{z1}\frac{\partial^2 h_1}{\partial z^2},\ 0 \le z \le \xi,\ 0 \le x \le L \qquad \text{Equation 5.1}$$

$$S_{s2}\frac{\partial h_2}{\partial t} = K_{x2}\frac{\partial^2 h_2}{\partial x^2} + K_{z2}\frac{\partial^2 h_2}{\partial z^2},\ -B_2 \le z \le 0,\ 0 \le x \le L \qquad \text{Equation 5.2}$$

The initial head is defined as a uniform value:

$$h_1(x,z,t) = h_2(x,z,t) = h_0,\ t = 0 \qquad \text{Equation 5.3}$$

and the boundary conditions are defined as:

$$h_1(x,z,t) = h_2(x,z,t) = h_b(t),\ x = 0 \qquad \text{Equation 5.4}$$

$$\frac{\partial h_1}{\partial x}(x,z,t) = \frac{\partial h_2}{\partial x}(x,z,t) = 0,\ x = L \qquad \text{Equation 5.5}$$

$$\frac{\partial h_2}{\partial z}(x,z,t) = 0,\ z = -B_2 \qquad \text{Equation 5.6}$$

where subscripts 1 and 2 represent the upper and lower layer, respectively; $S_s$ is the specific storage [L$^{-1}$]; $h$ is the hydraulic head [L]; $K_x$ and $K_z$ are hydraulic conductivity in x-direction (horizontal) and z-direction (vertical), respectively; $\xi$ is the instantaneous location of the moving water table; $H_0$ is the initial head, which is the same as water table [L]; and $h_b(t)$ is the fluctuating river stage [L].

Equation 5.1 and Equation 5.2 are coupled by the interface conditions representing the continuity of the hydraulic head and vertical fluxes, respectively (Liang et al., 2017a; Liang et al., 2017c):

$$h_1(x,z=0,t) = h_2(x,z=0,t),\ z = 0 \qquad \text{Equation 5.7}$$

$$K_{z1}\frac{\partial h_1}{\partial z}(x,z,t) = K_{z2}\frac{\partial h_2}{\partial z}(x,z,t),\ \ z = 0 \qquad \text{Equation 5.8}$$

The upper boundary ($z = \xi$) of the unconfined aquifer with a recharge term is a free surface (moving water table) that can be described by the following equation (Bear, 2012):

$$[K_{z1} + W(t)]\frac{\partial h_1}{\partial z} = -S_y\frac{\partial h_1}{\partial t} + W(t) + K_{x1}\left(\frac{\partial h_1}{\partial x}\right)^2 + K_{z1}\left(\frac{\partial h_1}{\partial z}\right)^2 \qquad \text{Equation 5.9}$$

where $S_y$ is the specific yield [-]; and $W(t)$ is the time-dependent recharge rate [LT$^{-1}$]. The coupled equations (1)- (3) are difficult to solve analytically because of the nonlinear nature of the upper boundary condition (4a) and the unknown location of the moving water table ξ. To resolve this issue, Equation 5.9 is linearized by using the perturbation technique (Dagan, 1964), which is widely adopted to simulate water flow in unconfined aquifers (Malama et al., 2011; Neuman, 1972a; Zhan and Zlotnik, 2002a). First, the water table is imposed on a fixed position ($z = B_1$) by assuming that the magnitude of water table fluctuation is much less than the aquifer thickness. Second, the two quadratic terms are ignored because they are much smaller than the other terms of Equation 5.9. Finally, the recharge term on the left side of Equation 5.9 is also ignored because the aquifer recharge rate $W$ is usually orders of magnitude smaller than the hydraulic conductivity $K_{z1}$. Based on the above assumptions, the water table boundary can be simplified to the linearized form:

$$K_{z1}\frac{\partial h_1}{\partial z} = -S_y\frac{\partial h_1}{\partial t} + W(t),\ z = B_1 \qquad \text{Equation 5.10}$$

To test the validity of the linearized boundary condition (Equation 5.10), a numerical experiment to compare the nonlinear (Equation 5.9) and linearized boundary conditions (Equation 5.10) is conducted. Specifically, the coupled equations Equation 5.1- Equation 5.8 with the boundary conditions Equation 5.9 and Equation 5.10 are solved numerically, respectively. Then the hydraulic head predicted by the model with the nonlinear boundary (Equation 5.9) is compared to that of the model with the linearized boundary (Equation 5.10). It should be noted that the nonlinear boundary in the numerical model is fixed at $z = B_1$ rather than the moving water table, which requires the magnitude of water table fluctuation to be much less than the aquifer thickness. The details are presented in the supporting information S2.4. The results indicate that the error caused by ignoring the quadratic terms and the recharge term on the left side of Equation 5.9 is very small when the recharge rate is less than one-tenth of the vertical hydraulic conductivity, which is widespread in the real world. It implies that the linearized boundary (Equation 5.10) is an appropriate approximation to the moving water table boundary.

## Solutions

### Solutions for hydraulic head

The governing Equation 5.1 and Equation 5.2 are solved by the Laplace and the Fourier sine transforms, and the details of the derivation are presented in the supporting information S2.1- S2.3. The Laplace domain solutions of Equation 5.1 and Equation 5.2 with the initial condition (Equation 5.3) and boundary conditions Equation 5.4- Equation 5.10 can be respectively written as:

$$\bar{h}_{1D}(x_D, z_D) = \bar{h}_{bD} + \sum_{n=0}^{\infty}[C_{1a}\, exp(-\Omega_{1n} z_D) + C_{1b}\, exp(\Omega_{1n} z_D) - \lambda_1]\sqrt{2}\sin(\omega_n x_D)$$

Equation 5.11

$$\bar{h}_{2D}(x_D, z_D) = \bar{h}_{bD} + \sum_{n=0}^{\infty}[C_{2a}\, exp(-\Omega_{2n} z_D) + C_{2b}\, exp(\Omega_{2n} z_D) - \lambda_2]\sqrt{2}\sin(\omega_n x_D)$$

Equation 5.12

where the subscript 'D' denotes the dimensionless terms hereinafter; the overbar denotes a variable in the Laplace domain; the definition of all dimensionless variables is summarized in Table 5.2 and the supporting information S2.1; and the definitions of variables $C_{1a}, C_{1b}, C_{2a}, C_{2b}, \Omega_{1n}, \Omega_{2n}, \lambda_1, \lambda_2,$ and $\omega_n$ are presented in the supporting information 2.3.

Table 5.2 Definition of dimensionless variables.

| | |
|---|---|
| $h_{1D} = \frac{h_1}{h_0}$ | $h_{2D} = \frac{h_2}{h_0}$ |
| $x_D = \frac{x}{L}$ | $z_D = \frac{z}{L}$ |
| $B_{1D} = \frac{B_1}{L}$ | $B_{2D} = \frac{B_2}{L}$ |
| $K_{xx} = \sqrt{K_{x1}K_{x2}}$ | $S_{ss} = \sqrt{S_{s1}S_{S2}}$ |
| $t_D = \frac{K_x t}{S_s L^2}$ | $R_K = \frac{K_{x2}}{K_{x1}}$ |
| $R_S = \sqrt{\frac{S_{s2}}{S_{s1}}}$ | $K_{1D} = \frac{K_{z1}}{K_{x1}}$ |
| $K_{2D} = \frac{K_{z2}}{K_{x2}}$ | $h_{bD} = \frac{h_b}{h_0}$ |
| $W_D = \frac{WL}{K_x h_0}$ | $S_{yD} = \frac{S_y}{S_s L}$ |
| $R_v = \frac{K_{1D}}{K_{2D}R_K^2}$ | $Q_D = \frac{Q}{h_0 K_x}$ |
| $Q_{1D} = \frac{Q_1}{h_0 K_x}$ | $Q_{2D} = \frac{Q_2}{h_0 K_x}$ |

**Solutions for lateral discharge**

On the basis of Darcy's Law, the lateral discharge of groundwater per unit width along the river channel (at $x = 0$) can be expressed as the sum of lateral discharges for two layers as follows:

$$Q(t) = Q_1(t) + Q_2(t) = -\int_0^{B_1} K_{x1}\frac{\partial h_1}{\partial x}|_{x=0}dz - \int_{-B_2}^{0} K_{x2}\frac{\partial h_2}{\partial x}|_{x=0}dz \quad \text{Equation 5.13}$$

where $Q_1(t)$ and $Q_2(t)$ are the lateral discharge of layer 1 and layer 2, respectively [$L^2 T^{-1}$]. Equation 5.13 can be transformed to its dimensionless form:

$$Q_D(t_D) = Q_{1D}(t_D) + Q_{2D}(t_D) = -\frac{1}{\sqrt{R_K}}\int_0^{B_{1D}}\frac{\partial h_{1D}}{\partial x_D}|_{x_D=0}dz_D - \sqrt{R_K}\int_{-B_{2D}}^{0}\frac{\partial h_{2D}}{\partial x_D}|_{x_D=0}dz_D$$

Equation 5.14

where $R_K = K_{x2}/K_{x1}$; and the other definitions of dimensionless parameters can be found in Table 3.2. Conducting Laplace transform on Equation 5.14 yields the following:

$$\bar{Q}_D = \bar{Q}_{1D} + \bar{Q}_{2D} = -\frac{1}{\sqrt{R_K}}\int_0^{B_{1D}}\frac{\partial \bar{h}_{1D}}{\partial x_D}|_{x_D=0}dz_D - \sqrt{R_K}\int_{-B_{2D}}^{0}\frac{\partial \bar{h}_{2D}}{\partial x_D}|_{x_D=0}dz_D \quad \text{Equation 5.15}$$

Substituting Equation 5.11 and Equation 5.12 into Equation 5.15 leads to:

$$\bar{Q}_{1D} = -\sqrt{\frac{2}{R_K}}\sum_{n=0}^{\infty}\omega_n\left[\frac{C_{1a}(1-\exp(-\Omega_{1n}B_{1D}))+C_{1b}(\exp(\Omega_{1n}B_{1D})-1)}{\Omega_{1n}} - \lambda_1 B_{1D}\right] \quad \text{Equation 5.16}$$

$$\bar{Q}_{2D} = -\sqrt{2R_K}\sum_{n=0}^{\infty}\omega_n\left[\frac{C_{2a}(\exp(\Omega_{2n}B_{2D})-1)+C_{2b}(1-\exp(-B_{2D}\Omega_{2n}))}{\Omega_{2n}} - \lambda_2 B_{2D}\right] \quad \text{Equation 5.17}$$

$$\bar{Q}_D = \bar{Q}_{1D} + \bar{Q}_{2D} = -\sqrt{\frac{2}{R_K}}\sum_{n=0}^{\infty}\omega_n\left[\frac{C_{1a}(1-\exp(-\Omega_{1n}B_{1D}))+C_{1b}(\exp(\Omega_{1n}B_{1D})-1)}{\Omega_{1n}} - \lambda_1 B_{1D}\right] - \sqrt{2R_K}\sum_{n=0}^{\infty}\omega_n\left[\frac{C_{2a}(\exp(\Omega_{2n}B_{2D})-1)+C_{2b}(1-\exp(-B_{2D}\Omega_{2n}))}{\Omega_{2n}} - \lambda_2 B_{2D}\right] \quad \text{Equation 5.18}$$

**Solutions for fluxes between two layers**

Water exchange occurs between the two layers of the aquifer induced by fluctuating river stage and recharge events. Darcy's velocity across the interface of the two layers is:

$$q_E(x,t) = -K_{z1}\frac{\partial h_1}{\partial z}|_{z=0} \qquad \text{Equation 5.19}$$

Based on Equation 5.19, the dimensionless Darcy's velocity across the interface can be written as:

$$\bar{q}_{ED}(x_D) = \sqrt{2}\frac{K_{1D}}{\sqrt{R_K}}\sum_{n=0}^{\infty} \Omega_{1n}(C_{1b} - C_{1a})\sin(\omega_n x_D) \qquad \text{Equation 5.20}$$

Given Equation 5.20, the dimensionless exchange fluxes along the interface of two layers can be obtained by:

$$\bar{Q}_{ED} = \int_0^1 \bar{q}_{ED}(x_D)dx_D = \sqrt{2}\frac{K_{1D}}{\sqrt{R_K}}\sum_{n=0}^{\infty}(C_{1b} - C_{1a})\frac{\Omega_{1n}}{\omega_n} \qquad \text{Equation 5.21}$$

Both solutions of head and discharge presented above involve the time-varying river stage $H_b(t)$ and recharge rate $W(t)$. Both river stage and recharge should be specified if one aims to evaluate the head and discharge. In this study, the river stage is presented by a piecewise-linear function with time, and the recharge rate is presented by a piecewise-constant function with time. Therefore, $h_b(t)$ and $W(t)$ can be written in the following forms:

$$h_b(t) = \frac{h_{bi} - h_{bi-1}}{t_i - t_{i-1}}(t - t_{i-1}) + h_{bi-1}, \quad t_{i-1} \le t < t_i \qquad \text{Equation 5.22}$$

$$W(t) = W_j, \quad t_{i-1} \le t < t_i \qquad \text{Equation 5.23}$$

where $h_{bi}$ is the observed river stage at time $t_i$; and $W_j$ is a constant for the time interval $t_{i-1} \le t < t_i$ with $t_0 = 0$. The piecewise-linear approximation is the most practical approach for treating the actual river stage because it permits approximation of any river hydrograph with desired accuracy if small time increments are used (Liang et al., 2020). Taking dimensionless and Laplace transform on Equation 5.22 and Equation 5.23 yields:

$$\bar{h}_{bD} = \sum_{i=1}^{\infty} e^{-pt_{Di-1}}\frac{\alpha_i + ph_{Di-1}}{p^2} - e^{-pt_{Di}}\left[\frac{\alpha_i(1+pt_{Di})}{p^2} + \frac{(h_{Di-1} - \alpha_i t_{Di-1})}{p}\right] \qquad \text{Equation 5.24}$$

$$\bar{W}_D = \sum_{i=1}^{\infty}\frac{W_{Di}}{p}[\exp(-pt_{Di-1}) - \exp(-pt_{Di})] \qquad \text{Equation 5.25}$$

where $p$ is the Laplace transform parameter; $\alpha_i$ is the variation rate of the hydraulic head during $t_{Di}$ to $t_{Di-1}$; and the definitions of dimensionless variables $h_{bD}$ and $W_D$ are presented in Table 3.2.

Equation 5.11, Equation 5.12, Equation 5.16, Equation 5.17, Equation 5.18, Equation 5.19 and Equation 5.20 are the Laplace domain solutions. Due to the complicated mathematical expressions, it is challenging to obtain closed-form solutions by inverse Laplace transforms analytically. There are, however, several numerical inverse Laplace methods that fix this problem, such as the Zakian method (Zakian, 1969), Fourier series method (Dubner and Abate, 1968), Stehfest method (Stehfest, 1970), Crump technique (Crump, 1976), Talbot algorithm (Talbot, 1979), and de Hoog algorithm (De Hoog et al., 1982). The de Hoog algorithm is used to invert the Laplace solutions into the time domain because a solution involving the piecewise functions Equation 5.25 commonly requires complex versions of the numerical inverse Laplace method (Liang et al., 2017c).

### Comparison with Numerical Solutions

To test the validity of the semi-analytical solutions Equation 5.11, Equation 5.12, Equation 5.16, Equation 5.17 and Equation 5.18, they are compared with the numerical solutions of the dimensionless governing Equation S 1- Equation S 9. The dimensionless parameter values of the model are: $K_{1D} = 1, K_{2D} = 1, R_K = 0.1, B_{1D} = 0.04, B_{2D} = 0.04,$ and $S_{yD} = 0.8$. Synthetic numerical simulations are carried out for two scenarios: (1) groundwater flow induced by two rainfall recharge events which occur at $0.5 \leq t_D < 1.0$ with a constant rate of $W_D = 0.2$, and $3.0 \leq t_D < 3.5$ with a constant rate of $W_D = 0.8$ (Figure 5.3a), and the river stage is constant or $H_{bD} = 1$; and (2) groundwater flow induced by a flood event, in which the dimensionless river hydrograph is described with a diffusive-type flood wave (Figure 5.3b), and no recharge or $W_D = 0$.

The dimensionless governing Equation S 1-Equation S 9 are numerically solved using COMSOL Multiphysics (COMSOL Inc., Burlington, MA, U.S.A.), a Galerkin finite-element software package that includes a partial differential equation (PDE) solver for modelling the type of governing equations of this study. Triangulations are used for the elements of the 2-D cross-section domain. To ensure sufficient accuracy of the simulation, the elements near the water table, the interface between two layers, and the river are refined with the minimum mesh-size of 0.002 and the maximum mesh-size of 0.01, which includes 28860 triangular elements and 14799 nodes. The time step $\Delta t_D$ is 0.0025 for the two scenarios.

Figure 5.3c and Figure 5.3d show the responses of the hydraulic heads in the upper layer and the lower layer to the recharge and flood events, respectively. Figure 5.3e and Figure 5.3f also present the lateral discharge induced by the recharge and the flood events, respectively. These figures indicate that the analytical solutions (solid curves) for both hydraulic head and discharge well agree with those of numerical solutions (circle symbols) over the entire simulation period. Through the above comparison, the analytical solutions of this study appear to be acceptable for predicting the hydraulic heads and the discharges for the model.

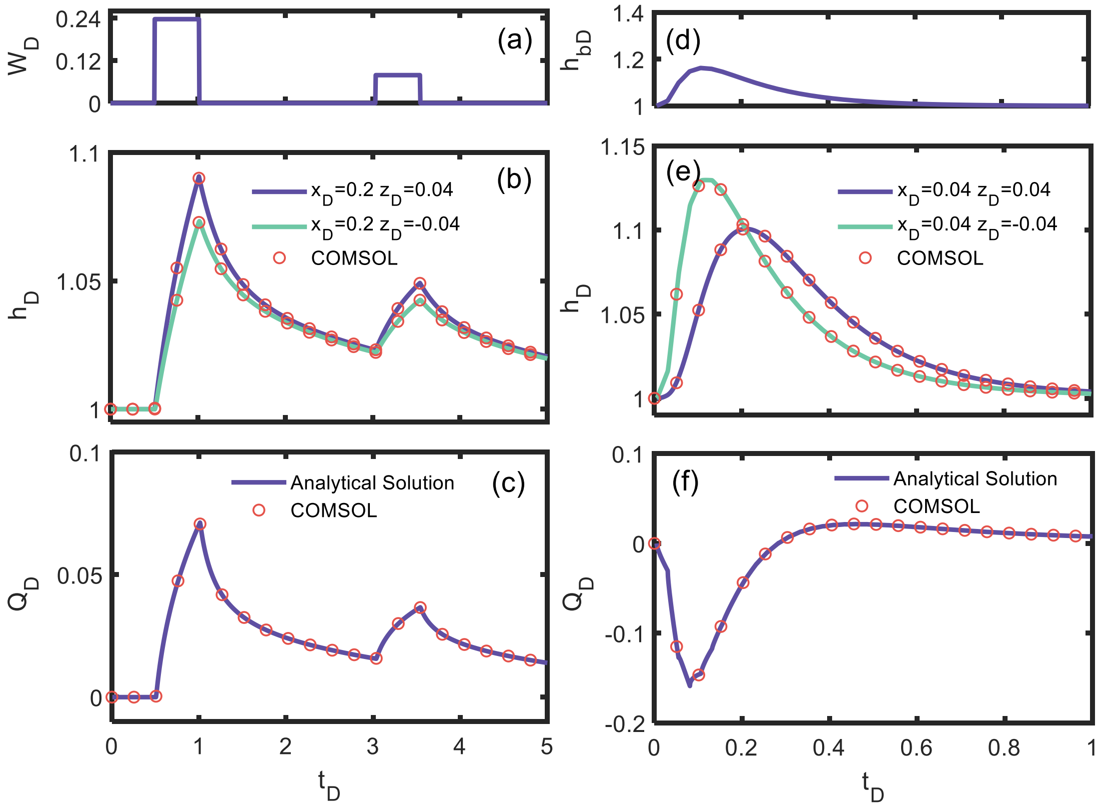


Figure 5.3. Comparison of the analytical solutions (solid curves) and the numerical solutions (open circles) for two recharge events (left column) and a flood event (right column): (a) the dimensionless recharge $W_D$ against dimensionless time $t_D$; (b) the dimensionless hydraulic head $h_D$ against $t_D$ at two locations; (c) the dimensionless discharge $Q_D$ against $t_D$. For the right column: (d) the dimensionless river stage $h_{bD}$ against $t_D$; (e) $h_D$ against $t_D$ at two locations; (f) $Q_D$ against $t_D$.

## Results and Discussion

### Effects of layered heterogeneity on hydraulic heads

In this study, the layered heterogeneity is mainly represented by a dimensionless parameter $R_K = K_{x2}/K_{x1}$ that quantifies the contrast in hydraulic properties of the two layers. This section first investigates how the layered heterogeneity impacts the responses of hydraulic heads to the time-varying recharge and the fluctuating river stage. To clearly demonstrate the impacts of $R_K$, it is assumed that the aquifer is isotropic, and the specific storage of two layers are equal. The other parameters of the aquifer are as follows: $K_{1D} = 1, K_{2D} = 1, R_S = 1, B_{1D} = 0.04, B_{2D} = 0.04,$ and $S_{yD} = 0.8$.

Figure 5.4 displays the responses of the hydraulic heads to a recharge event ($W_D = 0.25$ during $0.5 \leq t_D < 1.0$) and a flood wave for different values of $R_K$ (0.01, 1.0, and 100). Figure. 3b and 3c show that $R_K$ has a significant impact on the responses of hydraulic heads to the recharge event. For the large $R_K$ (=100), the hydraulic head in the upper layer (blue solid curve) is markedly larger than that of the lower layer (blue triangle symbol). For the small $R_K$ (=0.01), the hydraulic head in the upper layer (red solid curve) is close to that of the lower layer (red triangle symbol). Furthermore, for the homogeneous case ($R_K = 1$), the hydraulic head in the upper layer (cyan solid curve) is the same as that of the lower layer (cyan triangle symbol). These observations indicate that the aquifer has a significantly downward hydraulic gradient induced by the recharge when the upper layer has a smaller permeability. In contrast, for the case of the larger permeability in the upper layer, the aquifer has no obvious vertical hydraulic gradient, which is similar to the homogeneous case. These observations imply that the heterogeneous hydraulic conductivity regulates the groundwater flow path. The upper layer with the low permeability hinders groundwater lateral discharging into the river in the upper layer and forces water to flow downward into the highly permeable layer. In contrast, when the upper layer has a high permeability, it provides a fast flow path for the lateral discharge in the upper layer and prevents water from flowing downward into the lower layer.

Figure 5.4e presents the response of the hydraulic heads to the flood event. Similar to the case of the recharge event, there is little difference in hydraulic heads between the upper and lower layers for the homogenous case ($R_K = 1$) and the case in which the upper layer has a higher permeability ($R_K = 0.01$). For the case in which the upper layer has a lower permeability ($R_K = 100$), however, the hydraulic head in the upper layer (blue solid curve) is significantly lower than that of the lower layer (blue triangle symbol) in the early time ($t_D < 0.3$), and the hydraulic head in the upper layer becomes higher in the later time. The hydraulic head profile (Figure 5.4f) further illustrates that for the case of $R_K = 100$ the aquifer has a markedly upward hydraulic gradient at $t_D = 0.1$ (the rise phase of heads), and it has a markedly downward hydraulic gradient at $t_D = 0.4$ (the decline phase of heads). For the cases of $R_K = 0.01$ and 1, the vertical hydraulic gradients are small, which is in accordance with the observations in Figure 5.4d. The diverse hydraulic gradients reflect the impacts of heterogeneity on the water flow path. When the upper layer has a lower permeability, most of the river water initially infiltrates into the lower layer during the flood period and then flows upward into the upper layer. The flow pattern changes in reverse during the recession period. When the upper layer has a higher permeability, the vertical flow in the aquifer is not obvious, which will be further illustrated later.

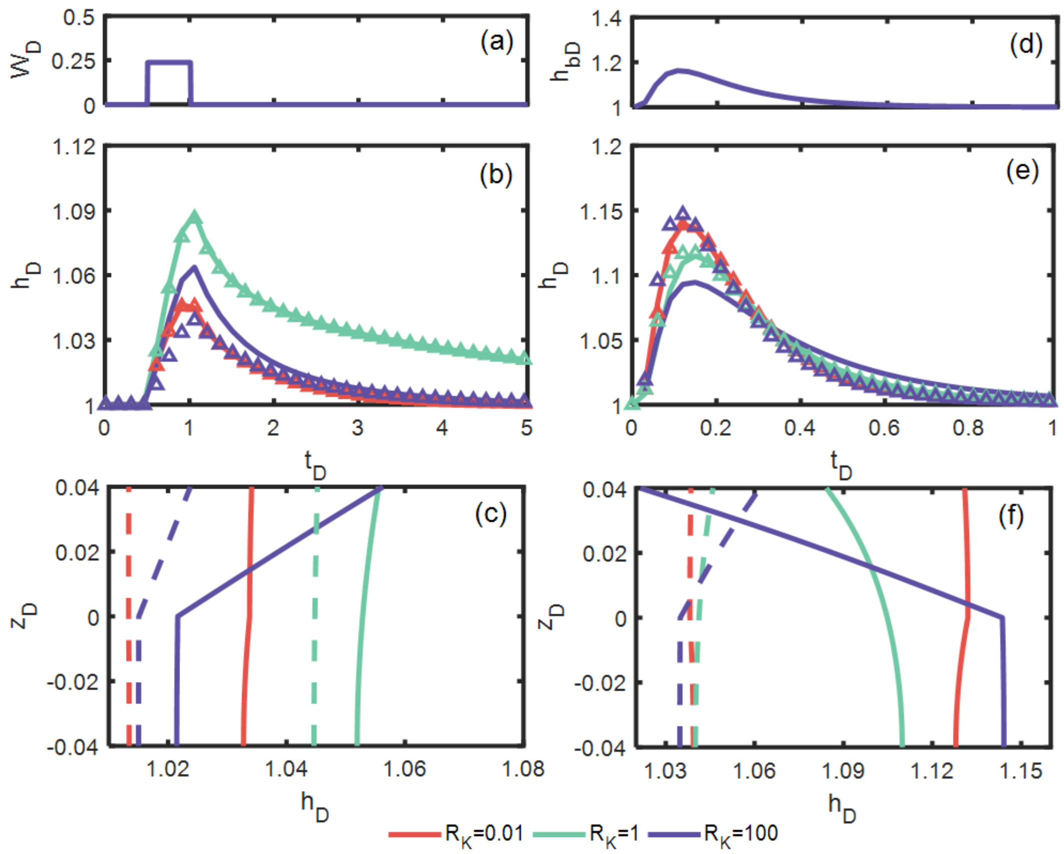


Figure 5.4 Responses of the dimensionless hydraulic heads to the recharge event (left column) and the flood event (right column) for the different $R_K$ (0.01, 1, and 100). For the left column: (a) the dimensionless recharge $W_D$ against time $t_D$ ; (b) the dimensionless hydraulic head $h_D$ against $t_D$ at the upper layer ($x_D$=0.2, $z_D$=0.02, solid curves) and the lower layer ($x_D$=0.2, $z_D$=-0.02, triangle curves); (c) the vertical profiles of $h_D$ for the different times ($t_D$=0.75, solid curves and $t_D$=2, dashed curves). For the right column: (d) the dimensionless river stage $h_{bD}$ against $t_D$; (e) $h_D$ against $t_D$ at the upper layer ($x_D$=0.04, $z_D$=0.02, solid curves) and the lower layer ($x_D$=0.04, $z_D$=-0.02, triangle curves ); (f) the vertical profiles of $h_D$ for the different times ($t_D$=0.1, solid curves and $t_D$=0.4, dashed curves).

To clearly illustrate the effects of the layered heterogeneity, the vertical profiles of the hydraulic heads for the different $R_K$ (0.01, 1, and 100) induced by the recharge event and the flood event based on our semi-analytical solution are presented in Figure 5.5 and Figure 5.6, respectively. The other parameter values are the same as those in Figure 5.4. Figure 5.5 indicates that there is no significant vertical hydraulic gradient when $R_K \leq 1$, while the downward hydraulic gradient is evident when $R_K > 1$. This means that the heterogeneity does not necessarily cause discrepancies in hydraulic heads between the two layers; the differences in hydraulic heads between the two layers only occur when the upper layer is less permeable than the lower layer. In the other case, the difference in hydraulic heads is miniscule. In addition, Figure 5.5 also shows that the hydraulic heads of both cases of $R_K = 0.01$ and $R_K = 100$ are generally larger than that of the case of $R_K = 1$ for different times. This implies that the heterogeneity leads to faster recession processes for the aquifer and results in lower hydraulic heads. For the flood event, the impacts of the heterogeneity are similar to the case of the recharge event. The hydraulic heads between the two layers differ only when the upper layer is less permeable than the lower layer. However, the difference with the case of the recharge event is that the aquifer has an upward hydraulic gradient during the rising phase of the hydraulic heads, and a downward hydraulic gradient during the declining phase. This means that there is a significant water interaction between the two layers induced by the flood event when the hydraulic conductivity of the upper layer is lower than that of the lower layer.

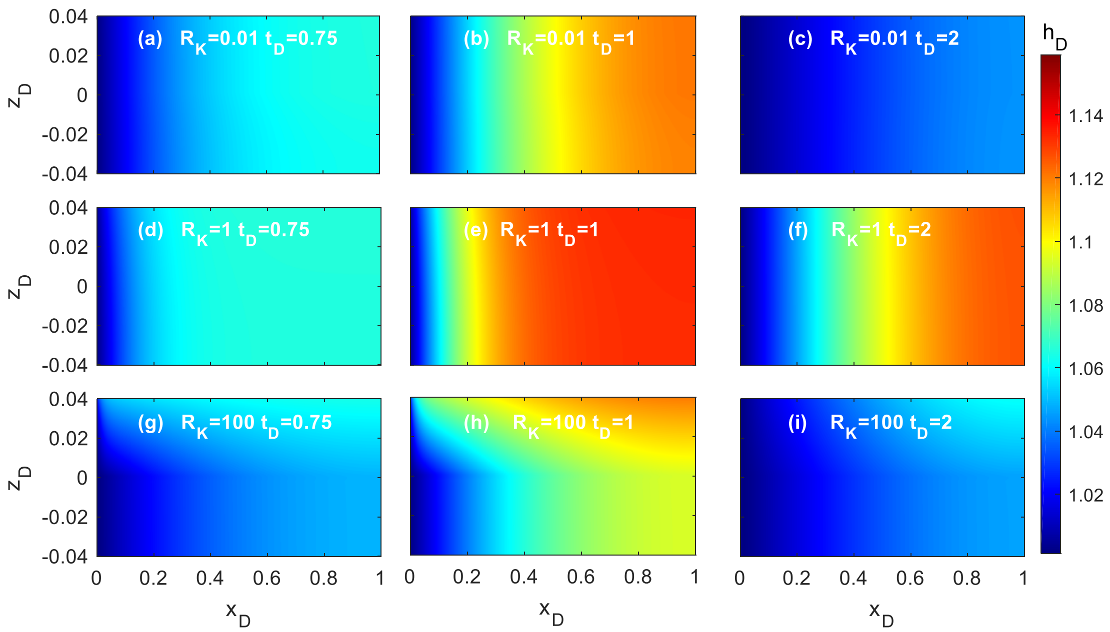


Figure 5.5 Vertical profiles of the dimensionless hydraulic heads induced by the recharge event for the different $R_K$ (0.01, 1, and 100) at different dimensionless times $t_D$ (0.75, 1, and 2).

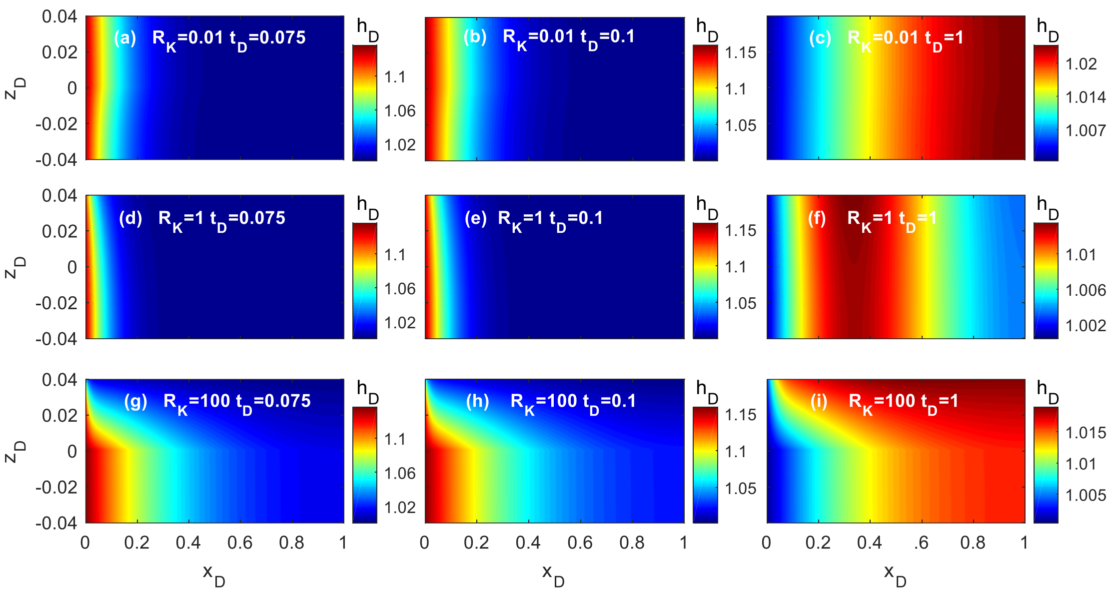


Figure 5.6 Vertical profiles of the dimensionless hydraulic heads induced by the flood event for the different $R_K$ (0.01, 1, and 100) at different dimensionless times $t_D$ (0.075, 0.1, and 1).

**Effects of layered heterogeneity on lateral discharge**

In this section, the effects of layered heterogeneity on the recession processes induced by a recharge event and the river-aquifer exchange induced by a flood event is investigated. Figure 5.7b displays the discharge (baseflow) recession induced by a recharge event (Figure 5.7a) for the different $R_K$ (0.01, 1, and 100). The other parameters are the same as those in Figure 5.4. Figure 5.7b shows that the discharge has a larger peak value and a faster recession process when $R_K$ is small. For the large $R_K$ (=100), the discharge has a smaller peak value and a slower recession process. This means that when the upper layer has a high permeability, water from the recharge event will be quickly discharged into the river. When the upper layer has a low permeability, most of the water from the recharge event will infiltrate into the lower layer. Meanwhile, for the homogeneous case ($R_K = 1$), the discharge has the smallest peak value and the slowest recession process. This is because the geometric mean of the hydraulic conductivity in the heterogeneous case would be controlled by the minimum value.

Figure 5.7d shows the response of river-aquifer exchanges to a flood event (Figure 5.7c) for different $R_K$ (0.01, 1, and 100). The discharge is negative in the early phase and positive in the later phase, which means that the aquifer receives water from the river at the beginning and then releases it to the river. For the small $R_K$ (=0.01), however, the interaction between river and aquifer is much greater and more water migrates into the aquifer and then back into the river. For the large $R_K$ (=100), the interaction is less than that in the small $R_K$ case, and the arrival time of peak inflow and peak discharge lags compared with that in the small $R_K$ case. This indicates that when the upper layer has a high permeability, the exchange between aquifer and river is more rapid. When the lower layer has a high permeability, there is a marked vertical hydraulic gradient (which can be found in Figure 5.6). In the early phase, the vertical hydraulic gradient causes some water in the lower layer to migrate to the upper layer, which reduces peak inflow and delays the arrival time of peak inflow. In the later phase, the hydraulic gradient and exchange flow reverse and water from the upper layer migrates to the lower layer reducing peak discharge and delaying the arrival time of peak discharge. For the homogeneous case ($R_K = 1$), the discharge has the smallest peak inflow and peak discharge. The reason for this is the same as that for the recharge event.

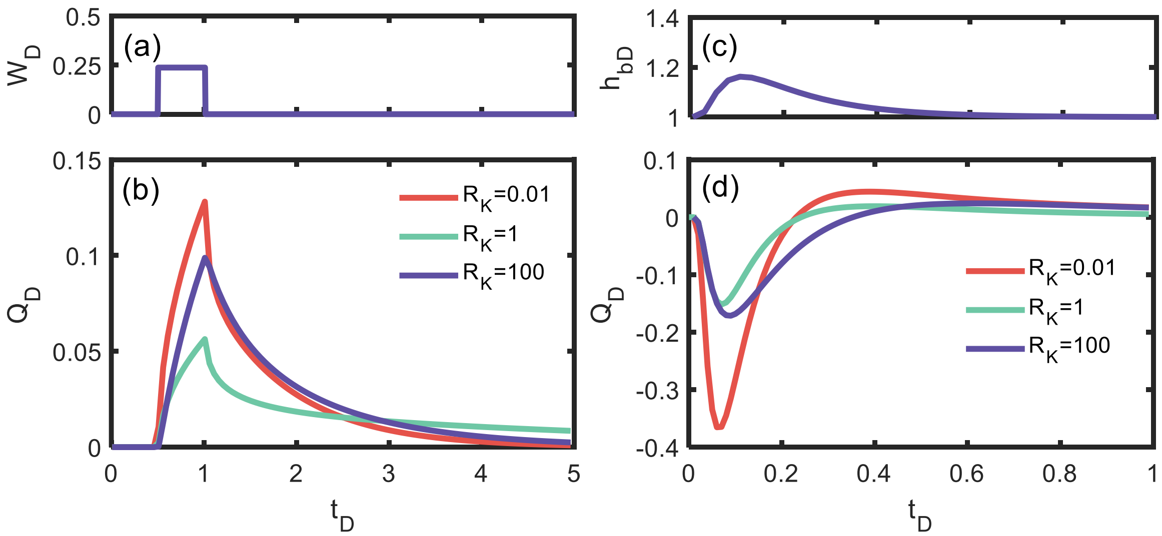


Figure 5.7 Responses of the dimensionless lateral discharge $Q_D$ to the recharge event (left column) and the flood event (right column) for the different $R_K$ (0.01, 1, and 100). For the left column: (a) the recharge $W_D$ against dimensionless time $t_D$; (b) the

dimensionless discharge $Q_D$ against $t_D$. For the right column: (c) the river stage $h_{bD}$ against $t_D$; (d) the dimensionless discharge $Q_D$ against $t_D$.ttt

Equivalent hydraulic conductivity is often employed to simplify heterogeneity. For groundwater flow parallel to aquifer layers, the equivalent hydraulic conductivity is equal to the arithmetic mean of all individual hydraulic conductivities of the layers (Equation 5.26). For groundwater flow perpendicular to aquifer layers, the equivalent hydraulic conductivity is equal to the harmonic mean of all individual hydraulic conductivities of the layers (Equation 5.27).

$$K_p = \frac{\sum_1^n K_i B_i}{\sum_1^n B_i} \quad \text{Equation 5.26}$$

$$K_v = \frac{\sum_1^n B_i}{\sum_1^n \frac{B_i}{K_i}} \quad \text{Equation 5.27}$$

where $K_i$ is the hydraulic conductivity of layer $i$; and $B_i$ is the thickness of layer $i$. However, the equivalent method is derived based on a steady flow. In order to verify the applicability of the equivalent formula in the riparian zone, the equivalent hydraulic conductivity on transient lateral discharge is employed.

It should be noted that the result has to be discussed with dimension, as the hydraulic conductivity influences the dimensionless form of time. In this part, the hydraulic conductivities are $1(m/d)$ and $10(m/d)$ for the upper layer and the lower layer, respectively. Therefore, the arithmetic mean would be $5.5(m/d)$ and the harmonic mean would be $1.8(m/d)$. The other parameters of the aquifer are as follows: $S_{s1} = S_{s2} = 0.001(m^{-1})$, $S_y = 0.2$, $B_1 = B_2 = 10(m)$, $L = 250(m)$. These parameters would be the same as those in Figure 5.3 if they are transformed into dimensionless form.

Figure 5.8a presents the responses of lateral discharge to a recharge event for arithmetic mean, harmonic mean, and the heterogeneous aquifer. When the arithmetic mean (red curve) is employed, the lateral discharge is remarkably smaller than that in the heterogeneous case. Meanwhile, in the recession process, the difference between them decreases. When the harmonic mean (blue curve) is employed, the lateral discharge is similar to that in the heterogenous case at the beginning, but the lateral discharge based on harmonic mean decreases more slowly than that in the heterogenous case after 60 d. Figure 5.8b shows the responses to a flood event. When the arithmetic mean (red curve) is employed, the interaction between river and aquifer is much less, and the arrival time of peak value is earlier than that in heterogeneous case. When the harmonic mean (blue curve) is used, the interaction would be overestimated, and the arrival time of peak value for the harmonic mean is slightly earlier than that in the heterogeneous case. These observations indicate that, for both the recharge event and flood event, the harmonic mean would overestimate the discharge and the arithmetic mean would underestimate it. The reason for this is that the arithmetic mean depends on the large hydraulic conductivity and would overestimate the overall hydraulic conductivity. In comparison, the harmonic mean depends on the small hydraulic conductivity and would underestimate the overall hydraulic conductivity.

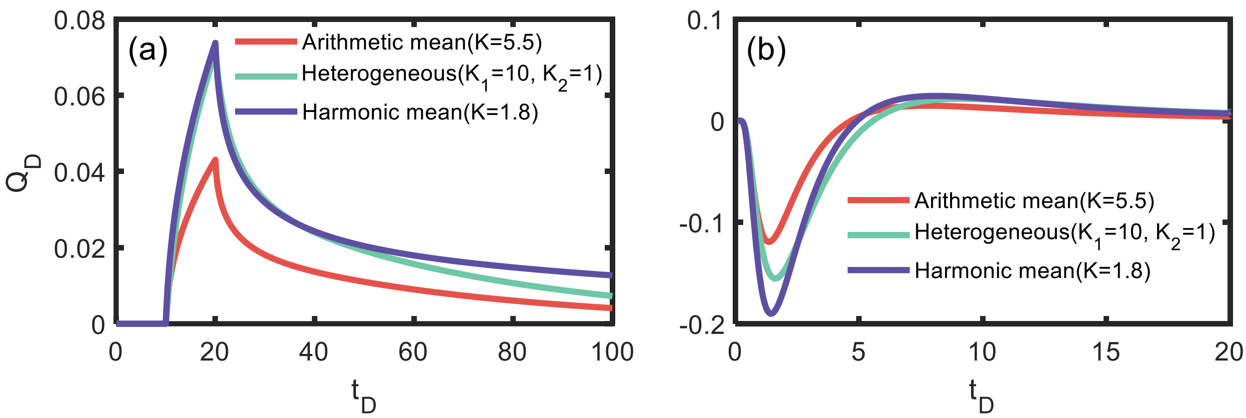


Figure 5.8 Responses of the discharge $Q$ to the recharge event (a) and the flood event (b) for the arithmetic mean, heterogeneous hydraulic conductivity, and harmonic mean. (a) The dimensionless discharge $Q_D$ against dimensionless time $t_D$ in the recharge event; (b) the dimensionless discharge $Q_D$ against $t_D$ in the flood event.

**Exchange fluxes between two layers**

The dimensionless exchange flux across the interface between the two layers $q_D$ is the direct reflection of the impacts of the contrast in properties between the two considered layers on groundwater flow. To gain insight into the pattern of the exchange flux, Figure 5.9 displays the spatial distribution of $q_D$ along the interface at different times for a recharge event (Figure 5.9a) and flood event (Figure 5.9b). The parameters used in Figure 5.9 are the same as those in Figure 5.3. For a recharge event (Figure 5.9a), all $q_D$ values are negative, which means that the groundwater in the upper layer migrates into the lower layer. There is a peak of $q_D$ close to the left boundary in the early phase. This peak value increases over time, and the location of the peak value moves toward the right as time progresses, as well. When the recharge process ends ($t_D = 1$), the flux from the upper layer decreases. However, some groundwater in the upper layer still flows across the interface into the lower layer.

For a flood event (Figure 5.9b), all $q_D$ values are positive in the early phase, which means that water in the lower layer migrates into the upper layer. In addition, $q_D$ varies with $x_D$, and the peak of $q_D$ is close to the left boundary. This peak value increases by $t_D = 0.1$ before decreasing, and the location of the peak value moves toward the right as time progresses. In the flood recession process, the flux at the left region gently becomes negative, which means that the water in the upper zone migrates into the lower layer in this region. However, some water in the lower layer still flows across the interface into the upper layer at the right regions. As time passes, $q_D$ gradually becomes negative at more locations of the interface, which indicates that the water flowing from the upper layer into the lower layer gradually dominates the exchange flux between the two regions.

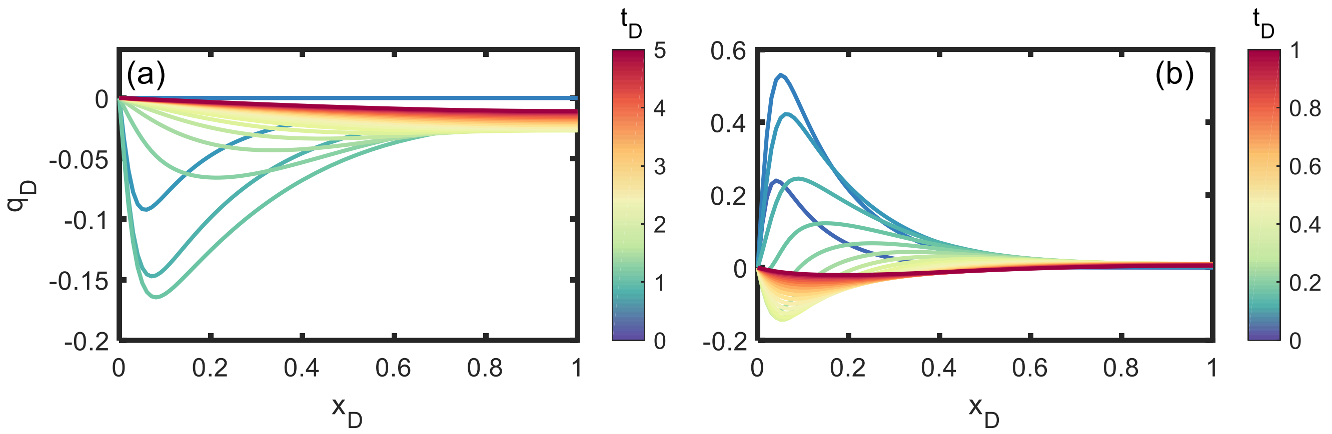


Figure 5.9 Distributions of dimensionless exchange flux across the interface of the two zones along the x-direction at different times in the recharge event (a) and the flood event (b).

To investigate the impacts of the distinction in properties between the two considered layers on the total exchange flux between the two regions, the response of dimensionless total exchange flux over the interface ($Q_{exD}(t_D)$) to a recharge event and a flood event for different $R_K$(0.01, 1, and 100) are presented in Figure 5.10. $Q_{exD}$ is evaluated using the integration of $q_{exD}$ over the interface, i.e., $Q_{exD}(t_D) = \int_0^1 q_{exD} dx_D$. The other parameters used in Figure 5.10 are the same as those in Figure 5.4. For the recharge event (Figure 5.10a), exchange flow from the upper layer to the lower layer increases as the recharge event occurs, and then decreases to zero gradually after the recharge. It can also be noticed that for a larger $R_K$, there is more water migrating into the lower layer. These observations are consistent with the conclusions reached above, namely that an upper layer with the low-permeability forces water to flow downward into the highly permeable layer. When the upper layer has a high permeability, it would provide a fast flow path for the lateral discharge, and the lower layer would function as an aquitard. For the flood event (Figure 5.10b), the total exchange between layers is maximized when $R_K$ increases. For a small $R_K$, the amount of water being exchanged between layers is small. For a large $R_K$, the upper layer releases more water to the lower layer in the early phase. Then the water moves back, and leads to a slight downward vertical exchange. For the homogeneous case, the mechanism of exchange flow is similar to that for a large $R_K$ with a smaller peak and bottom. These findings suggest that when the upper layer has a high permeability, the vertical hydraulic gradient becomes smaller and the upper layer with a low-permeability would result in a larger vertical hydraulic gradient, although the direction is opposite.

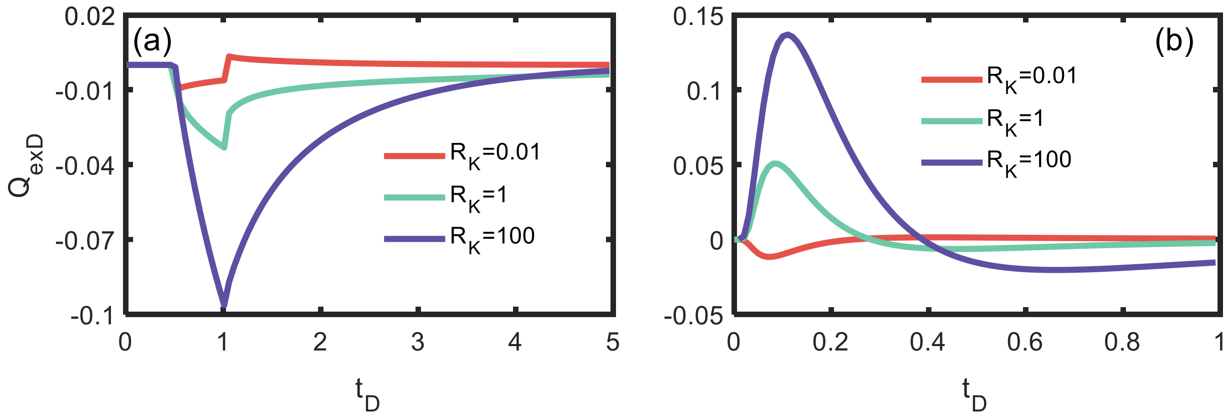


Figure 5.10 Response of dimensionless total exchange flux $Q_{exD}$ to the recharge event (a) and the flood event (b) for different values of $R_x$. (a) The dimensionless total exchange flux $Q_{exD}$ against dimensionless time $t_D$ in the recharge event; (b) the dimensionless total exchange flux $Q_{exD}$ against $t_D$ in the flood event.

## Application to Field Data

The present solution is applied to observed hydraulic heads in a riparian zone on White Clay Creek within the Christina River Basin Critical Zone Observatory in Southeastern Pennsylvania (Sawyer et al., 2014). The riparian zone has a two-layer structure. The upper layer includes organic-rich silt and silty clay, whose hydraulic conductivity ranges from $0.47\times10^{-6}$ m/s to $4.7\times10^{-6}$ m/s. The lower layer is silty gravel, whose hydraulic conductivity ranges from $0.59\times10^{-6}$ m/s to $59\times10^{-6}$ m/s. Five observation wells (referred to as well 110, 119, 120, 121, and 122) are installed on the west bank. The details of the field are provided by Sawyer et al. (2014).

The measured precipitation and river stage are presented in Figure 5.11a. The analytical model is applied to simulate the response of the hydraulic head to the storm. The change of the hydraulic head ($\Delta H$) relative to its initial value is employed to fit the present model. The aquifer recharge is difficult to estimate directly but it is usually proportional to the precipitation, which is helpful in estimating recharge. Here it is assumed that the recharge is proportional linearly to the precipitation with an unknown ratio $R_{pi}$. Thus, the recharge can be obtained by estimating the ratio of the recharge and precipitation $R_{pi}$. The aquifer parameters are estimated by minimizing the sum of the squared differences between simulated and observed heads. The estimated parameters are: $K_1 = 0.1m/d, K_2 = 2m/d, S_y = 0.021, S_{s1} = S_{s2} = 1 \times 10^{-5}\ 1/m, B_1 = 1.0m, B_2 = 6.0m, L = 60m,$ and $R_{pi} = 0.2$. The initial water table is equal to the river stage ($H$=101.4 m), and the interface between the two layers is located at 100.9 m. It should be noted that the thicknesses of the upper and lower layers are presumed by combining the distribution of soils and comparing the analytical solutions with the observation data.

Figure 5.11b-Figure 5.11f shows that the present solution agrees with the observed hydraulic heads of five wells, while it performs poorly for well 122. The reason for this is that the observed values in well 122 might be affected by the unsaturated zone, which is not considered in the present solution. Furthermore, the change of hydraulic head in well 122 is the highest, which implies that the recharge event has a greater impact on the hydraulic head than the flood event. This is because the upper layer with the lower-permeability has a higher hydraulic head in the recharge event and a lower hydraulic head in the flood event, as displayed in Figure 5.5 and Figure 5.6, respectively. Furthermore, a clear tail phenomenon exists in each well and, when the well is further away from the river, this phenomenon is more obvious. This is attributable to the fact that a well that is far from the river needs more time to discharge the water received from precipitation.

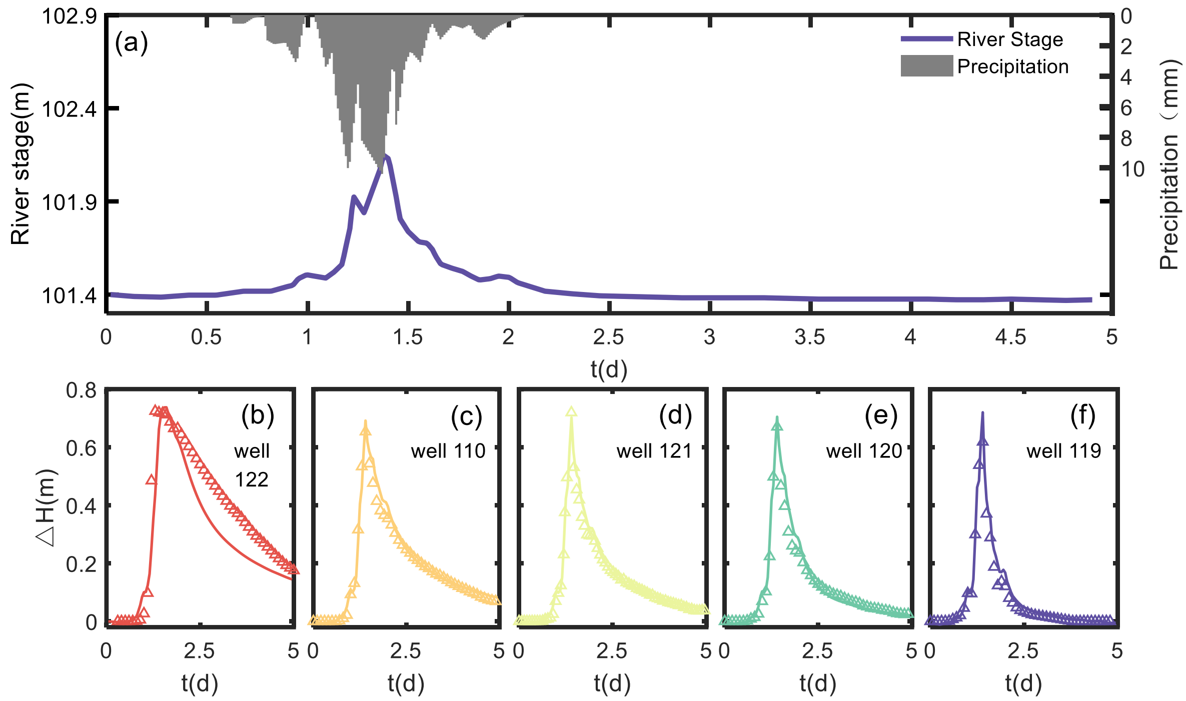


Figure 5.11 Field data observed by Sawyer et al. (2014) and the analytical model solutions. (a) The observed precipitation and river stage against time ($t$); the comparison between the analytical model solutions and the change of observed hydraulic head ($\Delta H$) against time ($t$) for well 122 (b), well 110 (c), well 121 (d), well 120 (e) and well 119 (f). Solid colored lines represent analytical solutions, and colored triangles represent field data

To further investigate the effect of a two-layer structure on this case for the recharge event, precipitation, exchange flux, and discharge are shown in Figure 5.12. Figure 5.12a presents precipitation, total exchange flux between the two layers, and discharge from both layers against time. To make the difference between total exchange flow and discharge clearer, the absolute value of total exchange flow is presented in Figure 5.12a. It can be seen in Figure 5.12a that the peak of precipitation and total exchange flux between the two layers appear in chronological order, and the total exchange flux between the two layers is almost the same as the discharge from the lower layer. The time difference between precipitation and total exchange flux is 0.6 d. The discharge from the upper layer is minimal compared with that from the lower layer. These phenomena reflect the path of groundwater flow in White Clay Creek. With the recharge by precipitation, most of the groundwater would flow into the lower layer and discharge to the river. Four specific times are selected to examine the exchange flux, i.e., before the storm (t = 0.5 d), during the storm (t = 1.22 d), at the peak of total exchange flux (t = 1.75 d) and after the storm (t = 3.75 d), as shown in Figure 5.12b. Before the storm, the exchange flux is almost zero everywhere. During the storm (t = 1.22 d), the location of the peak values of exchange flux is near the left boundary. Moreover, the exchange flux is positive at the left region and negative in the other regions. This means that the water in the lower layer migrates into the upper layer at the left region due to the stage of the rising river; at the other regions, the recharge event and the upper layer with lower-permeability cause a downward vertical exchange flow. When the total exchange flow reaches its maximum (t = 1.75 d), the flux at all regions is negative, and there is a trough near the left boundary. This means that the water in the upper layer migrates into the lower layer, and the decreasing stage of the river would result in a higher exchange flux near the left boundary. After the storm (t = 3.75 d), the flux at all regions is both negative and small. This indicates that the upper layer with the low-permeability exerts a damping effect on downward exchange flow, and the small and longstanding discharge to the lower layer would lead to the tailing phenomenon observed in Figure 5.12a.

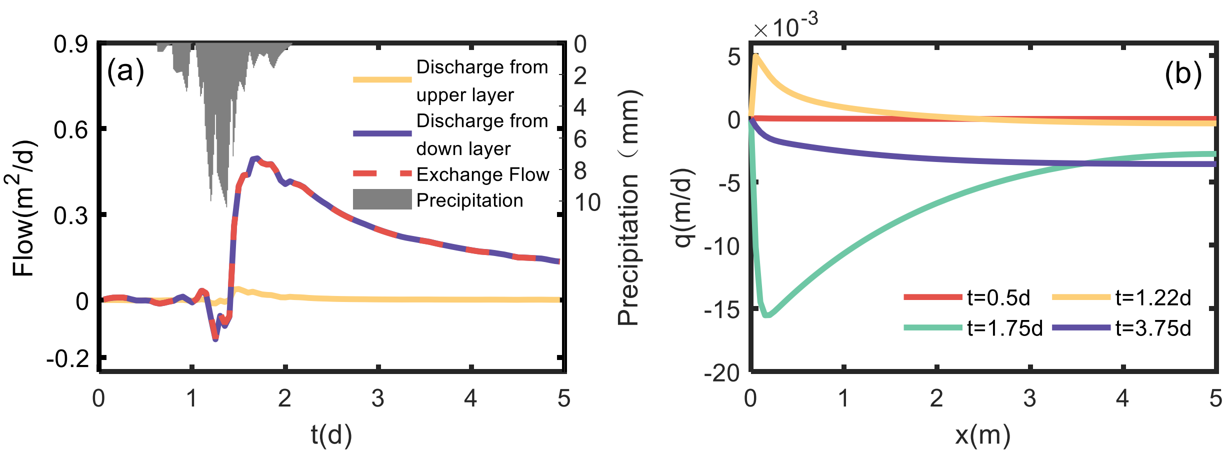


Figure 5.12. The effect of the two-layer structure on the hyporheic flow mechanism. (a) The precipitation, total exchange flow between two layers, discharge from the bottom layer, and discharge from the upper layer; (b) exchange flow between two layers at specific times.

Results from the case study shown above clearly show that the 2-D semi-analytical model is capable of capturing the dynamic interactions of a two-layered aquifer in response to recharge and flooding. Here the utility of the approach more broadly and potential implications is discussed. Two-layered aquifer systems are commonly found in floodplains and riparian zones and in many areas, the upper fine-textured layer is intensely cropped (Devito et al., 2000; Kalkhoff et al., 1992; Wang and Squillace, 1994). Applications of nitrogen fertilizer (Kalkhoff et al., 1992) and herbicides (Wang and Squillace, 1994) applied to the upper layer are potentially mobilized to the more permeable lower layer during recharge and flood events. Similarly, two-layered systems occurring in riparian zones will have implications for implementing conservation practices designed to remediate subsurface contamination such as riparian buffers (Mayer et al., 2007) and saturated buffers (Jaynes and Isenhart, 2014). These riparian buffer practices are most effective when groundwater flow high in nitrogen interacts with the organic-rich sediments. Hence, two-layered alluvial aquifers and riparian zones found along many rivers and streams may be severely compromised by variable hydraulic gradients imposed from periodic recharge and flood events and more work is needed to apply the 2-D semi-analytical model to these conditions.

Finally, there are a number of limitations that should be addressed for better application of the semi-analytical solution of this study. First, the present solution does not consider the impacts of the semipervious riverbed. The hydraulic conductivity of the riverbed is usually lower than that of the aquifer and it will dampen surface-groundwater exchanges, depending on the riverbed hydraulic conductance (Huang et al., 2014; Sun and Zhan, 2007). The impacts of the semipervious riverbed can be considered by replacing the Dirichlet boundary condition on the river with a Robin (or third-type) boundary condition. Second, the heterogeneous aquifer considered in the research is caused by the layered structure of the riparian zone. The heterogeneity of the realistic riparian zone, however, is more complicated. For example, the macropores will provide preferential vertical flow paths. The lens and plant roots in the riparian zone will obstruct groundwater flow. These all enhance the heterogeneity of the aquifer and limit the application of the present solution. Third, the linearized water table boundary (4b) requires that the magnitude of water table fluctuation is much less than the aquifer thickness. However, it is difficult to address exactly how small is “much less”. This question may be addressed by comparing the present model with a numerical model that considers a free moving water table. However, such a model will involve complicated moving-mesh treating and iterative solving on an unknown water table, which could be future work.

## Summary

A riparian zone is an important element in a river-aquifer system, controlling water exchange and other chemical and biological processes between a river and an aquifer. Complex groundwater flow patterns may occur due to aquifer heterogeneity within a riparian zone. The purpose of this study is to investigate the impacts of layered heterogeneity on water exchange in the riparian zone using a mathematical model for groundwater flow in a two-layer aquifer that is recharged by precipitation and floods. A semi-analytical solution is derived for the hydraulic head, lateral discharge, and fluxes between the layers. Results demonstrate that the hydraulic conductivity difference between the two layers enhances lateral flow in the higher permeable layer and, more importantly, generates vertical flow between the two layers. The vertical flow induced by the recharge event is downward while it could be upward or downward induced by the flood event, which is determined by the contrast in permeabilities of the two layers. Using an equivalent hydraulic conductivity approach underestimates the discharge of the two-layer aquifer due to recharge or flood. The analytical solution closely matched the observed hydraulic heads in the riparian zone well of White Clay Creek and provided reasonable estimates of aquifer parameters. The present solution provides a valuable basis for further study of chemical and biological processes in the riparian zone.

# Chapter 6 Deep transfer learning for groundwater flow in heterogeneous aquifers using a simple analytical model

Aquifer heterogeneity is one of the key factors to model groundwater flow properly (Li et al., 2019) as it is the main source of uncertainty in groundwater modelling (Refsgaard et al., 2012). Unfortunately, it is unrealistic to fully characterize the aquifer heterogeneity using traditional parameter estimation methods, such as pumping tests, due to technical and financial limitations (Binley et al., 2015; Yeh and Liu, 2000). Therefore, the accurate predictions of water flow and contaminant transport in heterogeneous aquifers is always a challenge.

Analytical models commonly provide simple and convenient tools in groundwater flow modelling, e.g., they are commonly applied to the parameter estimation of aquifer tests (Chang and Yeh, 2013; Liang et al., 2018b; Neuman, 1972b; Wen et al., 2013; Zhan and Zlotnik, 2002b), the quantification of simple aquifer systems (Liang et al., 2017d; Liang and Zhang, 2012), and the verification of numerical models (Walton, 1979). However, they are valid only under very specific conditions, such as simple aquifer geometry and homogeneous parameters. Although several studies have developed the analytical models that account for the layered heterogeneities (Feng et al., 2021b; Liang and Zhang, 2013b; Zhang et al., 2022b), the more complicated heterogeneous field is still out of the capacity of analytical models. Despite all this, the analytical model requires less computational effort and has the ability to present the first-order physical principle of groundwater flow. This characteristic would provide important information for the data-based machine learning model.

To the best of the authors' knowledge, the model that integrates the analytical solution and the DL model by transfer learning method has not been reported before. Therefore, this study aims to fill this knowledge gap by incorporating the knowledge of a simple analytical model into a deep neural network by transfer learning technique. The proposed transfer learning model could significantly improve the prediction of groundwater flow in a heterogeneous aquifer by incorporating the knowledge of the analytical solution of a homogeneous aquifer. The section is organized as follows: Section 5.1 presents the problem and the method. Section 5.2 presents the results of the experiments performed with the method. Finally, Section 5.3 provides a summary.

The relationship between this chapter and chapter 3, chapter 4, chapter 6 is show in Figure 6.1. A deep transfer learning model guided by a simple analytical model to predict groundwater flow in heterogeneous aquifers. Transfer learning is used to improve the hydraulic head prediction in relatively complicated problems where the analytical model is invalid. The result of this chapter provide a basement for the catchment groundwater prediction in the chapter 6.

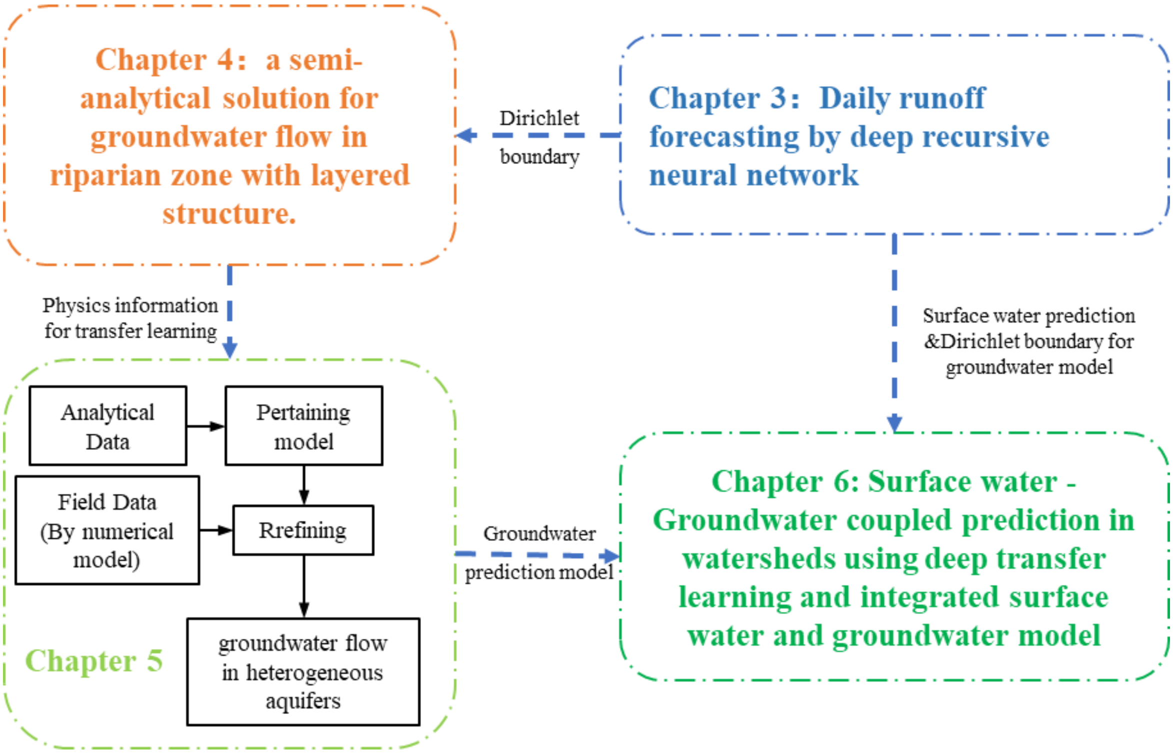


Figure 6.1 Relationship between this chapter and chapter 3, chapter 4 and chapter 6

## Methodology

### Mathematical models and solution

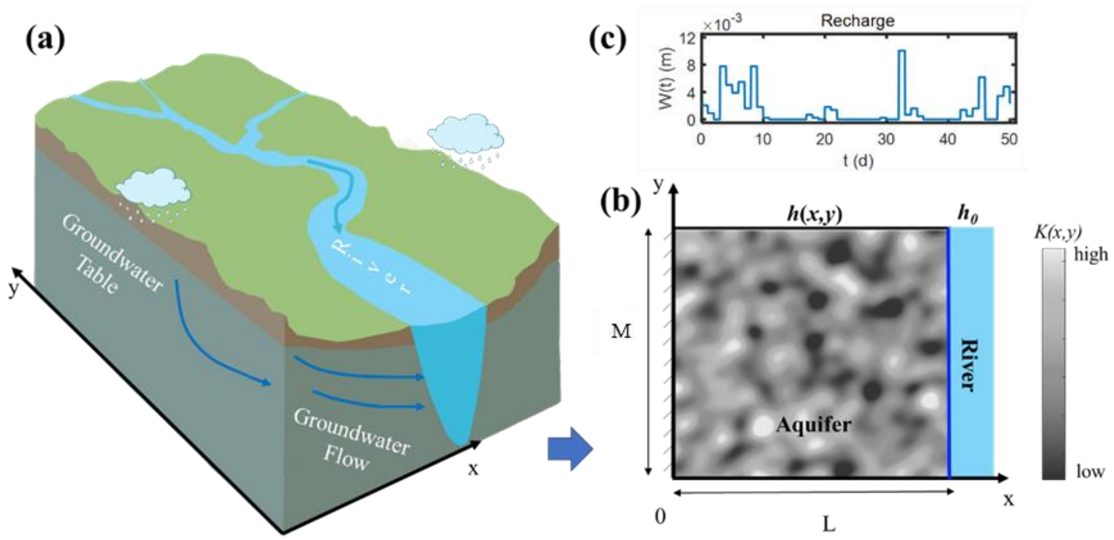


Figure 6.2 (a) Schematic diagram of groundwater flow in an unconfined aquifer; (b) The recharge $W$ for unconfined aquifer against time $t$; (c) conceptual model of groundwater flow to a river in a heterogeneous unconfined aquifer.

A schematic diagram of horizontally two-dimensional (2-D) groundwater flow in an unconfined aquifer is displayed in Figure 6.2. The aquifer is laterally bounded by a watershed divide and a river that fully penetrates the aquifer (Figure 6.2a). The x-axis is along the groundwater flow direction toward the divide, and the y-axis is parallel to the river channel. The top of the aquifer is the water table, which receives time-varying recharges from precipitation. The bottom of the aquifer is horizontal and impermeable. The aquifer is heterogeneous and anisotropic. Given the Dupuit assumption, groundwater flow can be described by the following 2-D Boussinesq equation:

$$\frac{\partial}{\partial x}\left(K(x,y)h\frac{\partial h}{\partial x}\right)+\frac{\partial}{\partial y}\left(K(x,y)h\frac{\partial h}{\partial y}\right)+W(t)=S_y\frac{\partial h}{\partial t} \qquad \text{Equation 6.1}$$

$$h(x,t)=h_0,\ \ t=0 \qquad \text{Equation 6.2}$$

$$h(x,t)=h_b,\ \ x=L \qquad \text{Equation 6.3}$$

$$\frac{\partial h}{\partial x}=0,\ \ x=0 \qquad \text{Equation 6.4}$$

$$\frac{\partial h}{\partial y}=0,\ \ y=0 \text{ and } y=M \qquad \text{Equation 6.5}$$

where $h$ is the hydraulic head [L]; $K(x,y)$ is the heterogeneous hydraulic conductivity [$LT^{-1}$]; $W(t)$ is the time-varying recharge rate [$LT^{-1}$]; $S_y$ is the specific yield [-]; $h_0$ is the initial hydraulic head [L]; $h_b$ is the river stage [L]. L is the distance between of the water divide and the river [L]; *M* is the width of aquifer in the y-direction [L]. The time-varying recharge rate $W(t)$ could be any function form. In this study a pricewise function with time is used to represent the recharge rate

$$W(t)=W_i,\quad t_{i-1}\le t<t_i,\ \ i=1,2,3\ldots \qquad \text{Equation 6.6}$$

where $W_i$ is constant for a giving time interval $t_{i-1}\le t<t_i$. It should be noted that Equation 6.6 is more flexible to describe the any time-varying recharge rate when the time interval is small sufficiently.

In this study, the log hydraulic conductivity field is assumed to be Gaussian and stationary, with isotropic exponential correlation. The heterogeneous hydraulic conductivity field is generated by the sequential Gaussian simulation of the *GStools* which is a toolbox for geostatistical modelling in Python (Muller et al., 2022). The governing equation (1a) with its initial and boundary conditions is numerically solved using COMSOL Multiphysics (COMSOL Inc., Burlington, MA, U.S.A.), a Galerkin finite-element software package that includes a partial differential equation (PDE) solver for modelling the type of governing Equation 6.1. The numerical model is mainly used to generate training and testing data and to be a benchmark to validate the DL model.

For a homogeneous and isotropic aquifer, the governing Equation 6.1-Equation 6.4 reduce to a one-dimensional (1-D) Boussinesq equation as follows

$$K\frac{\partial}{\partial x}\left(h\frac{\partial h}{\partial x}\right)+W(t)=S_y\frac{\partial h}{\partial t} \qquad \text{Equation 6.7}$$

$$h(x,t)=h_0,\ \ t=0 \qquad \text{Equation 6.8}$$

$$h(x,t)=h_b,\ \ x=L \qquad \text{Equation 6.9}$$

$$\frac{\partial h}{\partial x}=0,\ \ x=0 \qquad \text{Equation 6.10}$$

Equation 6.7 with its initial and boundary conditions and the time-varying recharge rate (Equation 6.6) can be analytically solved using the integral transform method. The solution of the hydraulic head of Equation 6.7-Equation 6.10 can be written as (Liang and Zhang, 2012)

$$h^2(x,t)=h_0^2+\frac{4}{LK}\sum_{n=0}^{\infty}\cos(\omega_n x)\frac{(-1)^n}{\omega_n^3}\left[W_i-W_1e^{-\omega_n^2\beta t}+\mathcal{H}e(i-1)\sum_{j=1}^{i-1}\left(W_j-W_{j+1}\right)W_1e^{\omega_n^2\beta(t_j-t)}\right],\quad t_{i-1}\le t<t_i,\ i=1,2,3\ldots \qquad \text{Equation 6.11}$$

Where:

$$\omega_n = \frac{(2n+1)\pi}{2L},\ \beta = \frac{K\bar{h}}{S_y} \qquad \text{Equation 6.12}$$

$\bar{h}$ is the average saturated thickness of aquifer [L]; and $\mathcal{H}e(\cdot)$ is Heaviside function. In the solution (Equation 6.11), the static river stage $h_b$ is assumed to be equal to the initial head $h_0$. The analytical solution will provide the prior physics knowledge for the DL model.

**Deep Neural Network**

The Deep Neural Network (DNN) is a powerful machine learning method, which has a higher ability to represent complex systems than traditional neural networks (Raghu et al., 2017) due to multiple neuron layers in neural network architectures. Besides the hidden layers, there is an input layer and an output layer in the neural network architecture, each of which consists of several neurons. It is assumed that there are $m$ hidden layers, the input is a vector $X$, and the output is a vector $O$. The forward formulation of the DNN can be written as:

$$H_1 = \sigma(We_1 X + b_1) \qquad \text{Equation 6.13}$$
$$H_2 = \sigma(We_2 H_1 + b_2) \qquad \text{Equation 6.14}$$
$$\vdots$$
$$H_m = \sigma(We_m H_{m-1} + b_m) \qquad \text{Equation 6.15}$$
$$O = \sigma(We_{m+1} H_m + b_{m+1}) \qquad \text{Equation 6.16}$$

where $H_i$ is the output of $i$th hidden layer; $We$ and $b$ are matrix of weight and vector of bias, respectively; $We$ and $b$ is usually combined as a DNN parameter $\theta_N = \{We_i, b_i\}_{i=1}^{m+1}$; $\sigma$ is the activation function. Hyperbolic tangent (Tanh) and sigmoid are widely adopted as activation functions of the DNN for a regression problem. In this study, the Tanh function $\sigma(x) = \frac{2}{(1-e^{-2x})-1}$ is adopted to avoid the zigzag problem. The result of DNN can be expressed as $O = NN(X,\theta)$, and the loss function can be defined as the mean square error between the DNN result $NN(X,\theta)$ and the observed data $Y$, which can be written as:

$$L(\theta) = \frac{1}{n}\sum_{i=1}^{n}|NN(x_i,\theta) - y_i|^2 \qquad \text{Equation 6.17}$$

where $n$ is the total number of training data. The DNN parameters $\theta$ can be estimated by minimizing the loss function:

$$\theta = \arg\min_{\theta^*}\frac{1}{n}\sum_{i=1}^{n}|NN(x_i,\theta^*) - y_i|^2 \qquad \text{Equation 6.18}$$

It should be noted that in order to avoid the influence of dimension on the training process, training and testing data are normalized as follows in pre-processing.

$$D_{ni} = 2\frac{D_i - D_{min}}{D_{max} - D_{min}} - 1 \qquad \text{Equation 6.19}$$

where $D$ represents data used in the model, $D_{max}$and $D_{min}$ are the maximum and minimum values of data $D$.

**Transfer Learning**

Transfer learning (TL) addresses problems with smaller training datasets, by repurposing efficient machine learning models, already trained on related large datasets of well-known problems (Vandaele et al., 2021). The traditional deep learning model is aimed to find a function $NN$ to link the input vector $X$ and the observe data $Y$ from the dataset $D = \{(x_i, y_i)_{i=1}^{n}, : x_i \in X, y_i \in Y\}$, where $n$ is the number of input or observed data. The function $NN$ should be able to accurately reproduce the output of the model with a given input. For the TL model, the aim is also to train a function to link the input vector $X_t$ and the observe data $Y_t$ from a target dataset $D_t = \{(x_{ti}, y_{ti})_{i=1}^{n}, : x_{ti} \in X_t, y_{ti} \in Y_t\}$ that could be a relatively sparse dataset. The TL model transfers the knowledge from a source task $s$ with the input vector $X_s$, the observed data $Y_s$, and the dataset $D_s$ to the target dataset. In this study, the target dataset is the hydraulic head of the heterogeneous aquifer calculated by the numerical model and the source dataset is the hydraulic head of the homogeneous aquifer calculated by the analytical model.

The pre-training and fine-tuning is a very popular TL method, which is also known as the parameter-transfer approach. In this method, it is assumed that the source tasks and the target tasks share the same parameters or prior distributions of the hyperparameters of models. Firstly, the pre-training model will be identified using the source tasks database $D_s$ that is generated by the analytical solution. Then, several layers of the pre-training model would be frozen. The parameters of the remaining layers $\theta_T$ will be fine-tuned by the target tasks dataset that is generated by the numerical model. These parameters will be finally estimated by minimizing the loss function:

$$\theta_T = \arg\min_{\theta^*} \sum_{i=1}^{n^*} \frac{1}{n^*} |NN(\theta^*|\theta_0, x_{ti}) - y_{ti}|^2 \qquad \text{Equation 6.20}$$

where $n^*$ is the number of target training datasets used to fine-tune the pretraining model. $\theta_0$ is the parameter of the pre-training model. The flowchart of the pre-training with fine-tuning method is illustrated in Figure 6.3.

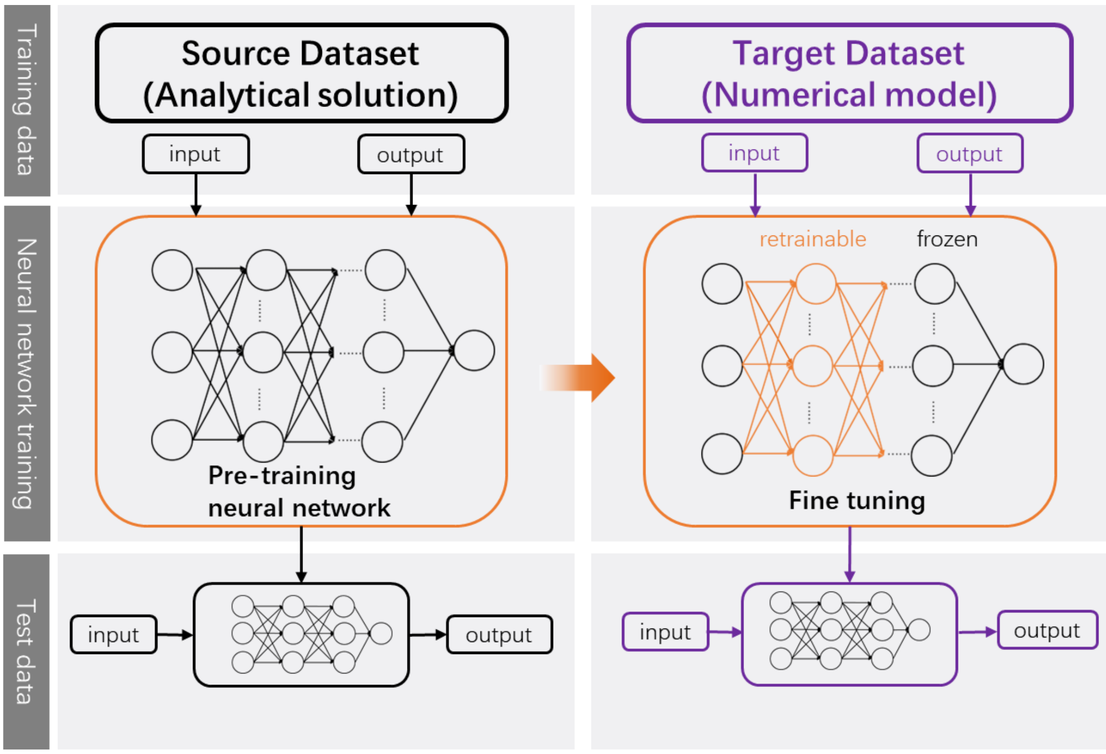

Figure 6.3 Workflow of the pre-training and fine-tuning methods in the transfer learning model.

## Overview of framework

The purpose of this study is to propose a transfer learning framework to predict hydraulic heads of heterogeneous aquifers. The analytical solution of a homogeneous aquifer provides the source dataset and prior physics knowledge, and the numerical model of a heterogeneous aquifer is employed as a proxy to generate the target dataset and test the capacity of TL model. The TL model is implemented in the following steps.

Firstly, the analytical model is employed to generate the source dataset $D_1$ with a specific hydraulic conductivity $K_1$. Then, the source dataset is normalized by the maximum and minimum values of dataset $D_1$ as Equation 6.19. A DNN model is trained by the normalized source dataset $D_{n1}$ and serves as a pre-training model, where the output data are the normalized hydraulic heads and the input data are the locations of the observed points, the observed times, and the recharge rates.

The difference between the source dataset and the target dataset is they are generated by different hydraulic conductivity. If layers of the pre-training model which are more sensitive to hydraulic conductivity are identified and then set retrainable, the TL model will be more effective. To analyse the impact of hydraulic conductivity on layers of the pre-training model, a new DNN model is established to provide a comparison. The new DNN model has the same structure as the pre-training model, but it is trained by a new dataset $D_2$ which is generated by the analytical model with hydraulic conductivities $K_2$. The effects of the hydraulic conductivity on layers of the pre-training model are identified by comparing the two models. After that, the layers in pre-training model, which are insensitive to the hydraulic conductivity, will be frozen and the remaining layers will be set to retrainable.

Several scenarios are designed to test the TL model. A homogeneous scenario is implemented first. In the homogeneous scenario, the target dataset is generated with $K_3$. For heterogeneous scenarios, the spatial and temporal performance of the TL model, the effect of heterogeneity and recharge uncertainty on the TL model result are discussed respectively. In these scenarios, target datasets are generated with hydraulic conductivity fields.

For each scenario above, the target dataset is divided into training data and testing data. The observation points are randomly selected and the daily hydraulic head in each point is set to the training data. Retrainable parameters in the pre-training model would be fine-tuned by these training data. The groundwater field at a specific time or temporal hydraulic head at a specific point is applied as a reference to evaluate the performance of the TL model. To make the result more reliable, the Deep Back Propagation Neural Network (DBPNN) is used as a baseline model. The benchmark model is trained solely on observed data generated by the numerical model. On the other hand, the proposed model is trained using observed data and analytical knowledge based on the transfer learning method. Both the proposed model and the benchmark model have the same structure, including the number of layers and neurons, and are trained using the same optimization methods. By comparing the proposed model and the benchmark model, it would be easy to determine if incorporating analytical knowledge can effectively improve the accuracy of groundwater prediction. It should be noted that hydraulic conductivity is used only in mathematical models to generate data. Moreover, the source dataset and target dataset are both normalized by the maximum and minimum values of dataset $D_1$ to make the prediction comparable.

## Result and Discussion

This section first investigates the effect of hydraulic conductivity on the pre-training model, then test the performance of the TL model for the predication of hydraulic heads in a homogeneous aquifer (homogeneous scenario) and the predication of hydraulic heads in a heterogeneous aquifer (heterogeneous scenarios), respectively. For the heterogeneous scenario, the section further investigates the impacts of heterogeneity of the conductivity and recharge uncertainty on the performance of the TL model.

### Pre-training

A fully connected neural network with 6 hidden layers and 15 neurons in each hidden layer is used as the pre-training neural network. The dataset $D_1$ is generated by the 1D analytical solution with 34 grid blocks and 50-time steps, where $K = 3m/d$, $S_y = 0.1, L = 100m$, and $h_0 = 20m$. The recharge rate is presented in Figure 1b. The pre-training model is validated by the normalized dataset $D_{n1}$ using the 80/20 rules which means 80% of the data will be used to train the suggested models, and the remaining 20% will be used to test the models. With the same input of testing data, the normalized hydraulic head forecasting by the pre-training neural network is very close to the analytical solution with the mean square error (MSE) of 1.6E-08, indicating that the pre-training neural network has been well trained and could be used to surrogate the analytical solution. The well-trained neural network can provide an important foundation for follow-up transfer learning.

To identify the influence of hydraulic conductivity on weight and bias, a new DNN model is established. The new DNN model has the same structure as the pre-training model, but it is trained by a dataset $D_2$ generated with $K = 5m/d$ using the 80/20 rules. The difference between the new DNN model and the pre-training model is evaluated by relative change rate (RCR). The RCR is defined as:

$$RCR = \frac{1}{I}\sum_{i}^{I}\frac{|\theta_{pre}i - \theta_{DNN}i|}{\theta_{pre}i} \qquad \text{Equation 6.21}$$

where $\theta_{pre}$ and $\theta_{DNN}$ are parameter matrix in the pre-training model and the new model respectively, $I$ is the number of elements in the parameter matrix. To make trials more comparable and convincing, the new DNN model is trained for 15 times with the randomly selected training data from the dataset $D_2$. Figure 6.4 displays the average relative change rate of each layer in the new neural network and the pre-training neural network of 15 times comparison. The result shows that the relative change rate of bias is relatively stable, except for bias in layer 4. Compared with bias, the change of weights is more pronounced, especially in layers 2, 3 and 4. The relative change rate of weights in layer 3 is at least 6 times more than that of the bias. It suggests that the parameters in layers 2, 3 and 4 of the pre-training models are much more sensitive to the hydraulic conductivity. Therefore, layers 2, 3 and 4 of the pre-training model will be set as retrainable and other layers will be frozen.

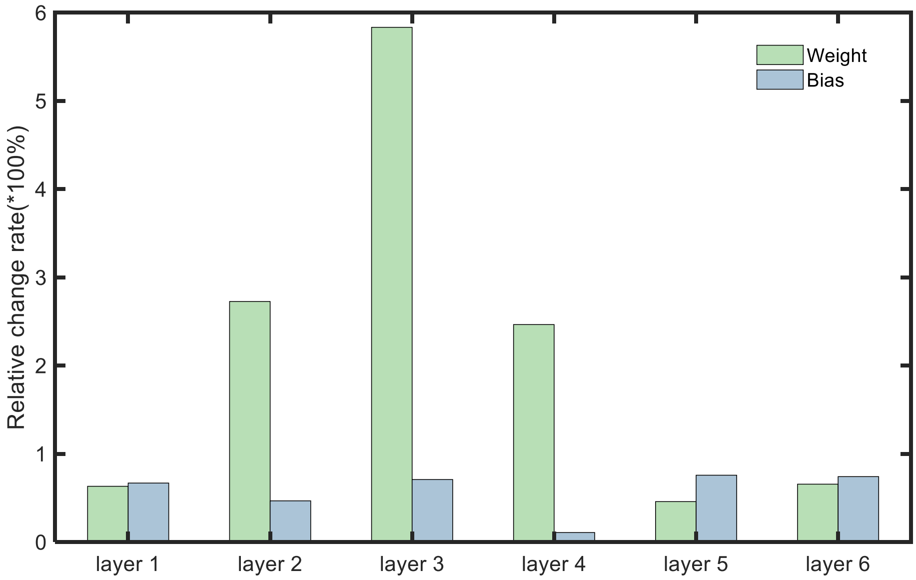

Figure 6.4 The average relative change rate of weight and bias in the neural network for 15 times comparison between pre-training neural network and a new neural network. The pre-training neural network is trained and tested by data $D_{n1}$ generated by the analytical model with $K_1 = 3m/d$ . The new neural network has the same structured as the pre-training neural network but is trained for 15 times with the randomly selected training data from the dataset $D_{n2}$.

**Homogeneous scenario**

For the homogeneous scenario, the time series (50 days) of hydraulic heads are respectively generated at 2, 5, 10, 15, and 20 observe points with 50-time steps, where $K = 7\ m/d$ and the other parameters are the same as that in Figure 6.5. These observation points are randomly selected and the locations of them are summarized in Table 6.1.

**Table 6.1** The positions of the observe points for the homogeneous scenario

| Number of observe points | location (in x-direction, m) | | | | |
|---|---|---|---|---|---|
| 2 observe points | 51.5 | 35.5 | | | |
| 5 observe points | 43.5 | 11.5 | 36.5 | 19.5 | 14.5 |
| 10 observe points | 66.5 | 44.5 | 52.5 | 36.5 | 17.5 |
| | 1.5 | 93.5 | 78.5 | 11.5 | 39.5 |
| 15 observe points | 86.5 | 60.5 | 94.5 | 27.5 | 92.5 |
| | 81.5 | 32.5 | 0.5 | 78.5 | 21.5 |
| | 40.5 | 87.5 | 34.5 | 71.5 | 62.5 |
| 20 observe points | 57.5 | 4.5 | 67.5 | 34.5 | 83.5 |
| | 52.5 | 6.5 | 59.5 | 8.5 | 90.5 |
| | 44.5 | 20.5 | 47.5 | 65.5 | 13.5 |

| | | | | | |
|---|---|---|---|---|---|
| | 21.5 | 12.5 | 97.5 | 75.5 | 74.5 |

The groundwater field on the 33rd day is employed as testing data, which is discretized to 34 grids. Figure 6.5 displays the testing result of the TL model, the TL model (all retrainable), and the DBPNN model for the homogeneous scenario, where the red curves are the reference head and the blue curves are the predicted heads of the neural networks. It indicates that for a given training data, both the TL and TL (all retrainable) models well agree with the reference heads while the DBPNN model generally fails to fit the reference heads even though its trained data includes the 20 observation points. It implies that the prior knowledge of the analytical solution in the pre-training model significantly improves the performance of neural networks. The pre-training model that implants the physic knowledge provides a better initial neural network parameter, which in turn reduces the search range in the fine-tuning process. While the DBPNN model initializes the parameters randomly and requires more training data to explore the whole parameter space. It may be encouraging to point out that even in the case of sparse data, the results of the TL and TL (all retrainable) models are satisfactory as well (Figure 6.5).

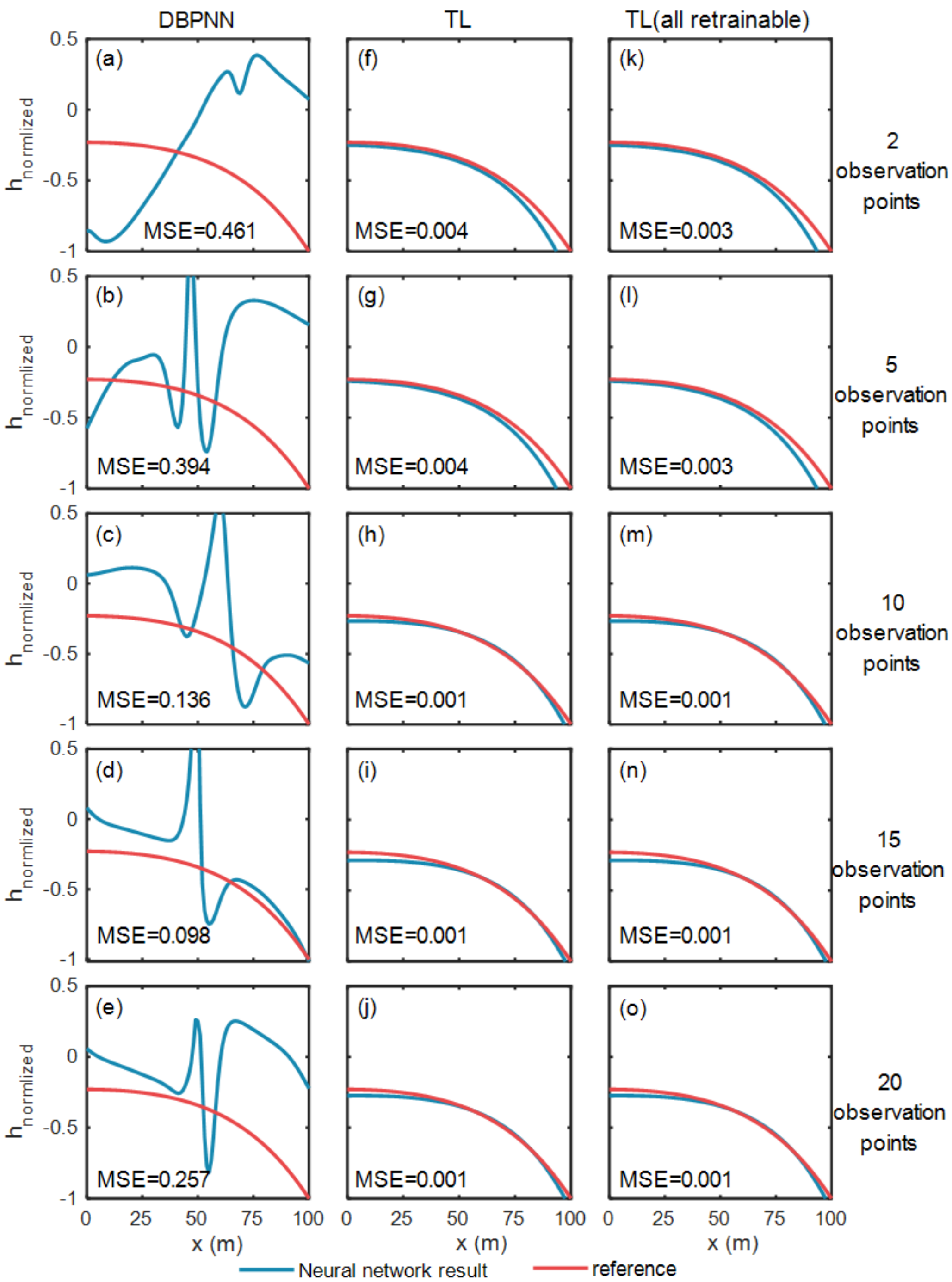


Figure 6.5 Comparisons of the predicted hydraulic head (blue curve) using the TL, TL (all retrainable) and DBPNN models with the reference head (red curve) for the different cases which have the different number of observe points. The pretraining phase of both TL and TL (all retrainable) models are trained by $D_{sn}$ which is generated by the analytical model with $K = 3m/d$. The reference head is the normalized groundwater head on 33rd day, which is generated by the analytical model with $K = 7\ m/d$.

Why the DBPNN poorly performs even with the large amounts of training data is explained as follows. These three models share the same convergence criteria in fine-tuning process. The epoch is limited to ensure all of these neural networks are comparable and would not overfit in the sparse data. With the limited epoch, the DBPNN model may be not fully trained for the dense training data. The performances of TL and TL (all retrainable) models appear similar. It further confirms the conclusion above that the layers 2, 3 and 4 of the pre-training model are much more sensitive to the hydraulic conductivity.

It should be noted that the location of the observation point for training data may affect the results of three models. To investigate this impact and to further demonstrate the capacity of the TL model, the location of each observation point is generated randomly 50 times. The MSE of the three models training by each realization are evaluated by comparing them to the true values. The distributions of MSE for three models at different numbers of observation points are displayed in Figure 6.6, where the model parameters are the same as those in Figure 6.5. It shows that with the same number of observation points, both the interquartile range (IQR) and mean of MSE of TL and TL (all retrainable) models are much smaller than that of the DBPNN model. For example, for the 2 observation points the mean of MSE for the DBPNN model is about 1.5 while that for the TL and TL (all retrainable) models are 0.004 and 0.003, respectively. Moreover, the IQR and mean of MSE drop remarkably with the observation points increasing until the number of observation points reaches to 10. When the number of observation points is more than 10, the MSE almost remains a constant value with the number of observation points increasing. It is consistent with the observations in Figure 6.5, which further proves the advantages of the TL model.

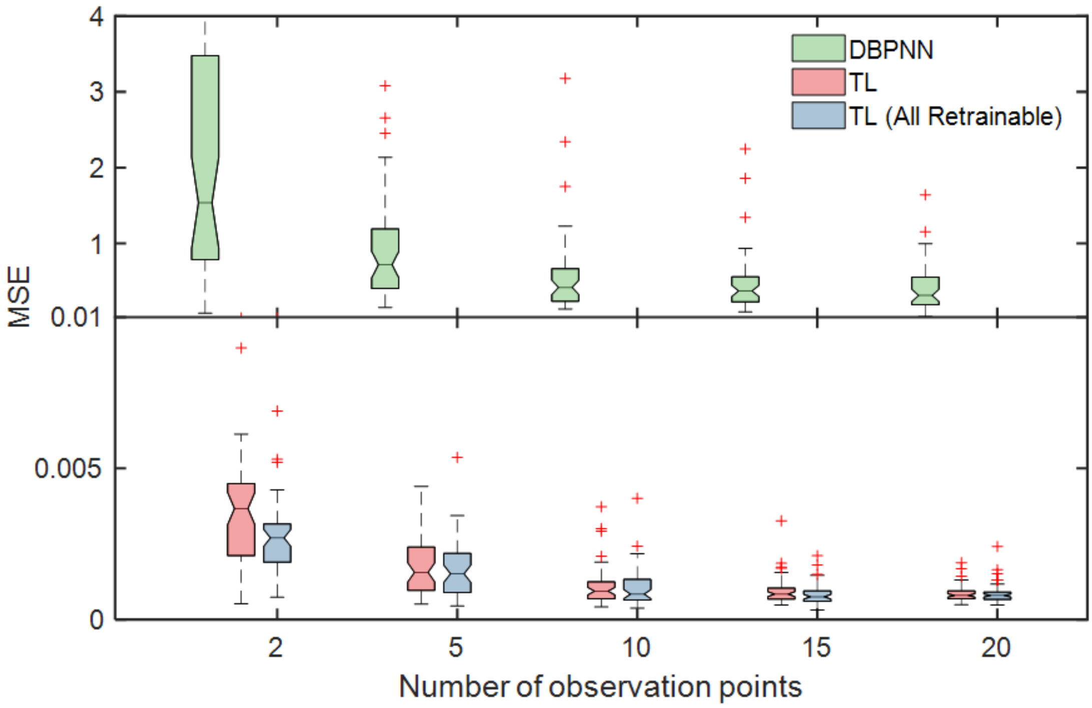


Figure 6.6 The MSE distribution of the TL, TL (all retrainable) and DBPNN models plotted against number of observe points, where the observe points are randomly realized for 50 times and the reference head is generated by the analytical model with K=7 m/d.

**Heterogenous scenario**

In this scenario, the performance of the TL model on the prediction of hydraulic head in heterogeneous aquifers is investigated. The heterogeneous $\ln K$ field is described by the exponential covariance function with mean $\mu = 0$, variance $\sigma^2 = 2$ and correlation length $l = 20m$, which is generated using the *GStools* (Figure 6.7a). The recharge rate and other parameters are the same as that of the homogeneous scenario. The hydraulic heads of the heterogeneous aquifer are obtained by the numerical solution. The time series of numerical hydraulic heads from 10, 20, 50, 100 and 200 observation points are extracted as the five training datasets for the TL, TL (all retrainable), and DBPNN models. The hydraulic heads on the 33rd day are employed as the testing data (Figure 6.7b, reference heads), where the groundwater flow field is discretized to 100*100 grids.

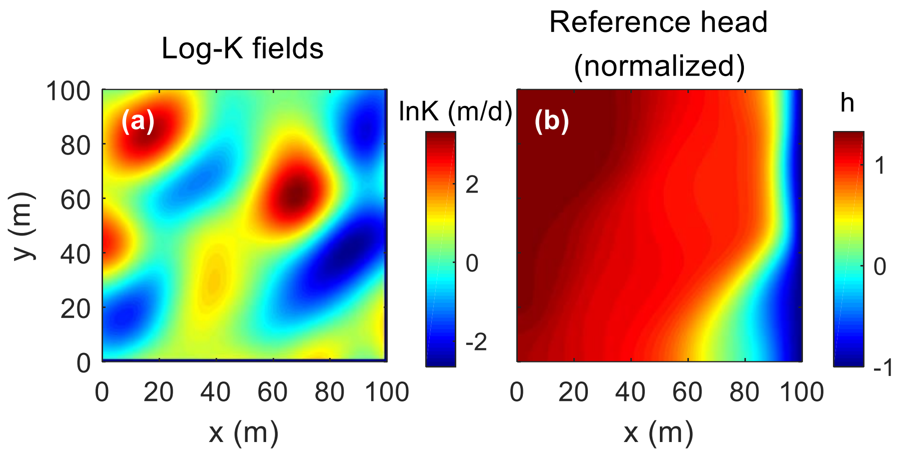


Figure 6.7 (a) The heterogeneously hydraulic conductivity field, and (b) the reference hydraulic head on 33rd day predicted by the numerical model using the conductivity field (a).

**1) the spatial performance**

The absolute difference between the reference heads and the predicted heads by TL, TL (all retrainable), and DBPNN models using the five training datasets are presented in Figure 6.8, where the left column is the randomly selected observation points corresponding to the different training datasets. Figure 6.8 shows that the errors of TL and TL (all retrainable) models are very close, and both are significantly lower than the errors of the DBPNN model. It is interpreted that such improvement of the TL model is majorly benefit from a better initial parameter in the fine-tuning process due to the physic knowledge from the analytical solution. It may also be interesting to note that the DBPNN model performs better for more training data but the performances of both TL and TL (all retrainable) models do not improve substantially as the amount of training data increases. This implies that, based on the knowledge provided by the analytic solution, the transfer learning model can reproduce the hydraulic heads of the heterogeneous aquifer more accurately, even for very sparse training data (e.g., hydraulic heads from 10 observation points). However, the performance of the DBPNN model mainly depends on the amount of training data, which performs poorly for a small amount of data.

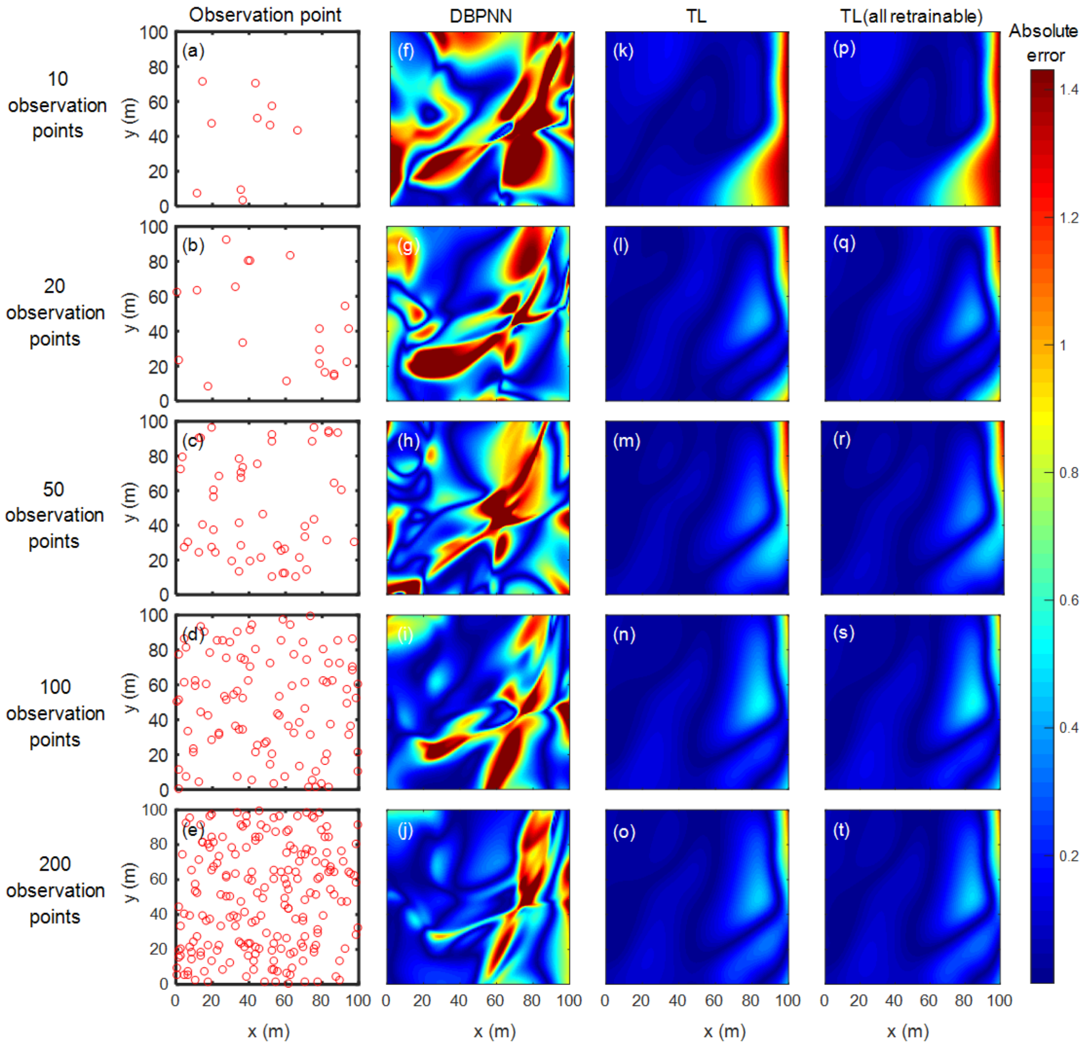


Figure 6.8 Absolute errors between the predicted hydraulic heads using the TL, TL (all retrainable) and DBPNN models and the reference head for the different cases. The pretraining phase of both TL and TL (all retrainable) model are trained by $D_{n1}$ which is generated by the analytical model with $K = 3m/d$. The reference head is the normalized groundwater head on 33rd day, which is generated by the numerical model with the heterogeneously hydraulic conductivity field.

To reduce the impacts of the sampling campaign of observation points for each training dataset, each sampling campaign is randomly implemented 200 realizations. For each realization, the TL, TL (all retrainable) and DBPNN models are trained and tested, respectively. The distributions of MSE for three models are displayed in Figure 6.9. With the observation points increasing until the number of observation points reaching 20, the IQR and mean MSE of TL, TL (all retrainable) and DBPNN all drop greatly. When number of observation points is more than 20, the IQR and mean of

MSE changed slightly. This is in agreement with Figure 6.8. With the same number of observation points, the mean MSE of TL and TL (all retrainable) is about 20 times smaller than that of DBPNN. It proves that the transfer learning method has the capacity of transferring homogeneous knowledge to heterogeneous problem and improve the accuracy of hydraulic head prediction.

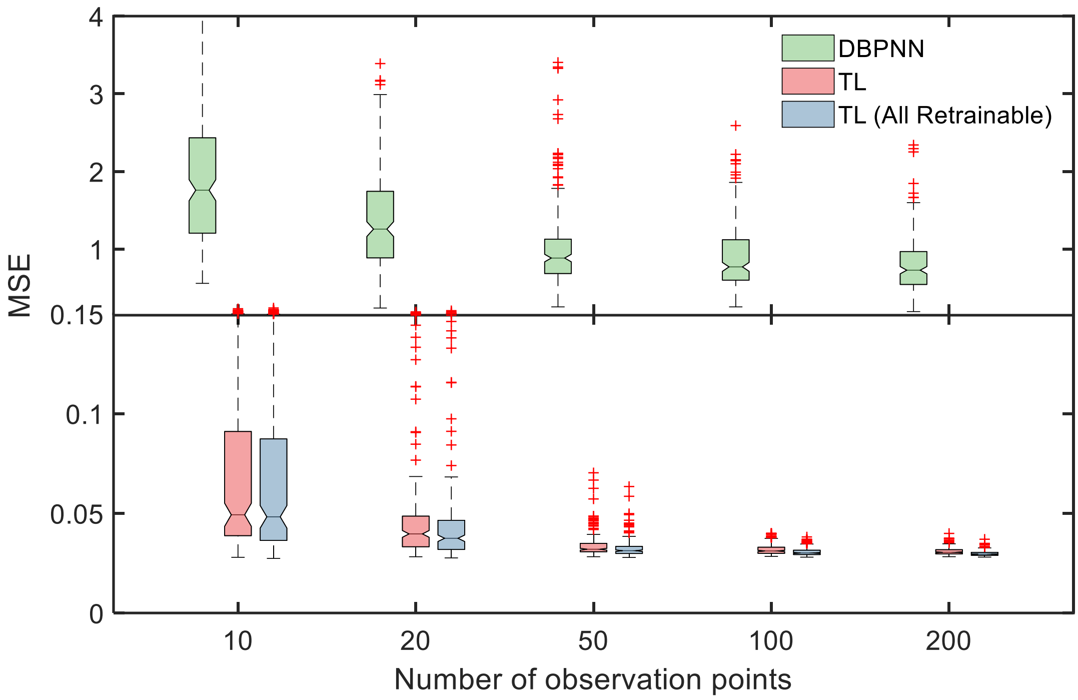


Figure 6.9 MSE distribution of the TL, TL (all retrainable) and DBPNN model plotted against number of observe points, where the observe points are randomly realized for 200 times and the reference head is generated using the numerical model with the heterogeneously hydraulic conductivity field.

It should also be noted that if the analytical model is directly used to predict the hydraulic head of the heterogenous aquifer directly, the MSE is 1.38. Compared with Figure 6.9, the result is close to the mean MSE of the DBPNN model with 20 observation points but falls behind that for both TL and TL (all retrainable) models. It implies that the transfer learning method combines the physical knowledge from the analytical model and has a higher prediction ability than both of analytical model and the classic DL model.

A statistics analysis of a minimum number of iterations required for convergence in the 200 times training processes mentioned earlier is also carried on to discuss the computational efficiency of the proposed method in comparison to the baseline models. All these models were implemented in Python 3.8 using the TensorFlow 2.3 framework. The experiments were conducted on a workstation equipped with an Intel Xeon W2255 CPU and 128 GB of memory. It should be noted that the convergence criteria are set to a maximum of 3000 iterations and a minimum gradient change of 5E-6 during the training process. The iteration counts are summarized in Table 6.2 below:

**Table 6.2** Number of iterations in the training process of proposed method and baseline model

| Number of observation points | Training iterations | | |
|---|---|---|---|
| | pre-training | transfer learning | baseline model |
| 10 | | 1530 | 3000 |
| 20 | | 1645 | 3000 |
| 50 | 1305 | 2048 | 3000 |
| 100 | | 2256 | 3000 |
| 200 | | 2328 | 3000 |

Table 6.2 indicates that the pre-training process of the proposed method requires approximately 1300 iterations. During the transfer learning process of the proposed model, as the number of observation points increases, the number of training

iterations also increases, rising from 1500 to 2300 iterations. In contrast, the baseline model consistently required 3000 training iterations, as constrained by the maximum iteration setting. This implies that the baseline model exhibited lower training efficiency, and it may need significantly more than 3000 training iterations to achieve training performance comparable to that of the proposed model.

**2) the temporal performance**

To illustrate the performance of the TL model on time series, the TL model is employed to predict the temporal hydraulic heads. Figure 6.10 displays the time series of hydraulic heads predicted by the three models at a giving point ($x = 27m, y = 30m$), where the model parameters are the same as those in Figure 4. It shows that the TL model reproduces the time fluctuation of hydraulic heads better than the DBPNN model.

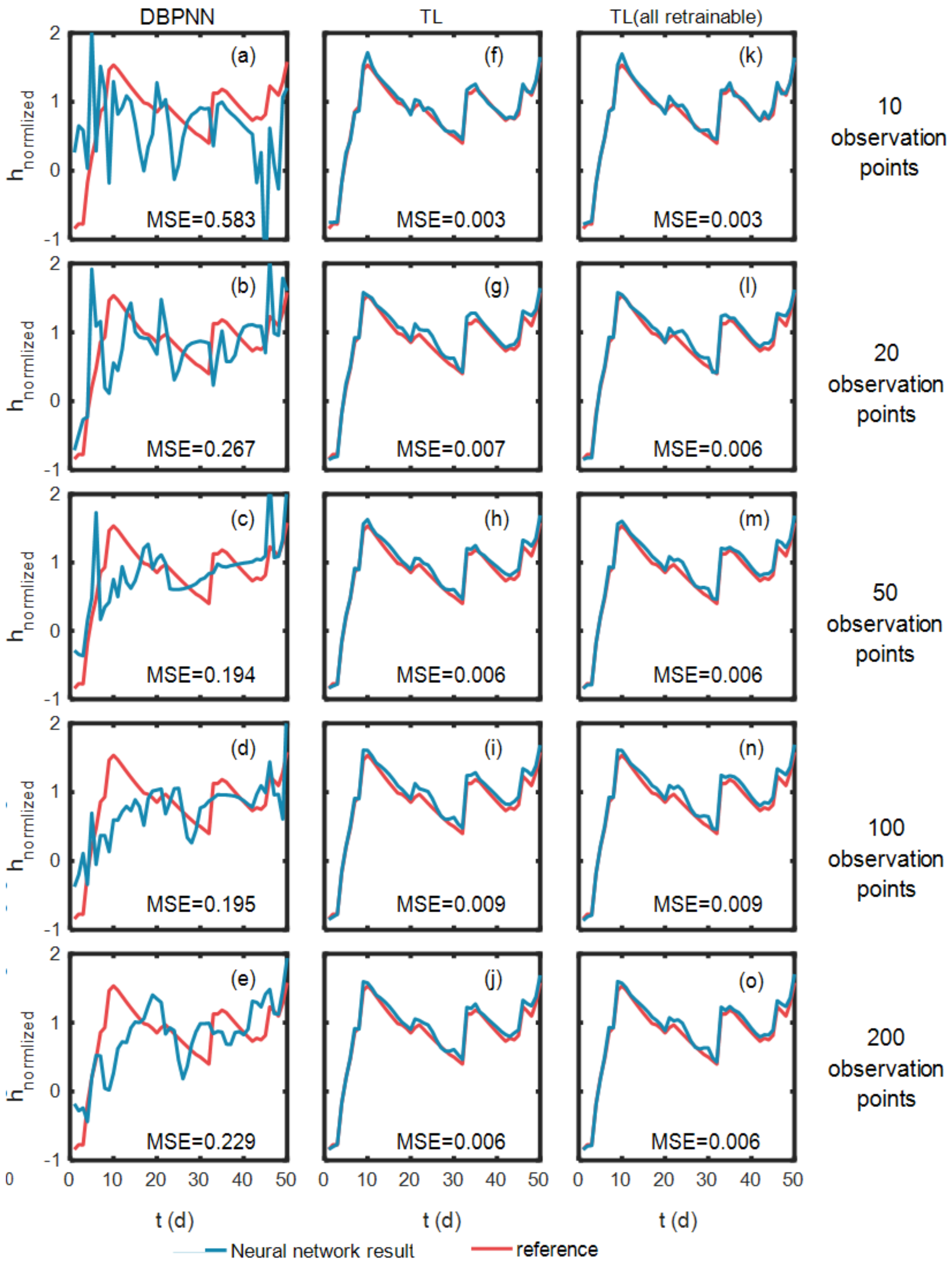


Figure 6.10 Comparisons of the predicted hydraulic head (blue curve) using the TL, TL (all retrainable) and DBPNN models to the reference head (red curve) for the different cases. The pretraining model of TL and TL (all retrainable) is trained by $D_{n1}$ which is generated by the analytical model with $K = 3m/d$. The reference head is the daily normalized groundwater head in point ($x = 27m, y = 30m$ ), which is generated by the numerical model with the heterogeneously hydraulic conductivity field.

For the spare training dataset (10 observation points), the MSE of the TL model is about 150 times less than that of the DBPNN model. The results of TL and TL (all retrainable) models are similar for each case. These phenomena are consistent with the observations in Figure 6.9. It is interpreted these results to imply taking time and recharge as an input variable of the neural network may not be enough to provide sufficient temporal information for the neural network, as the recharge is considered as input variable in all these models. Meanwhile, it implies that the pre-training model trained by the adequate hydraulic head time series from the analytical model would contain some effective temporal information and in turn improve hydraulic head time series prediction.

It may be interesting to note that the performances of TL and TL (all retrainable) models seem independent on the number of observation points (training data). The reasons are as follows. First, the location of observation points is randomly selected. When there is an observation point near the testing point, all networks work well. The opposite is true. Second, the TL model learns enough temporal information from the analytical solution so there may be no urgent requirement for the amount of observation points. The performances of TL and TL (all retrainable) models in the whole domain is showed to prove our hypothesis.

Figure 6.11 shows the performance of TL and TL (all retrainable) models in the whole domain on the $10^{th}$ and $20^{th}$ day with different numbers of observation points, where the training data is the same as that in Figure 6.9. The results in Figure 6.11 are consistent with those in Figure 6.9. These results all show that, at different times, the increase of observation points only improves the prediction on hydraulic heads near the right boundary. For using more observation points (training data), the improvement of the TL model is unremarkable on the $10^{th}$, $20^{th}$ and $33^{rd}$ days. This also implies that the temporal information from the analytical solution constrains and guides the neural network.

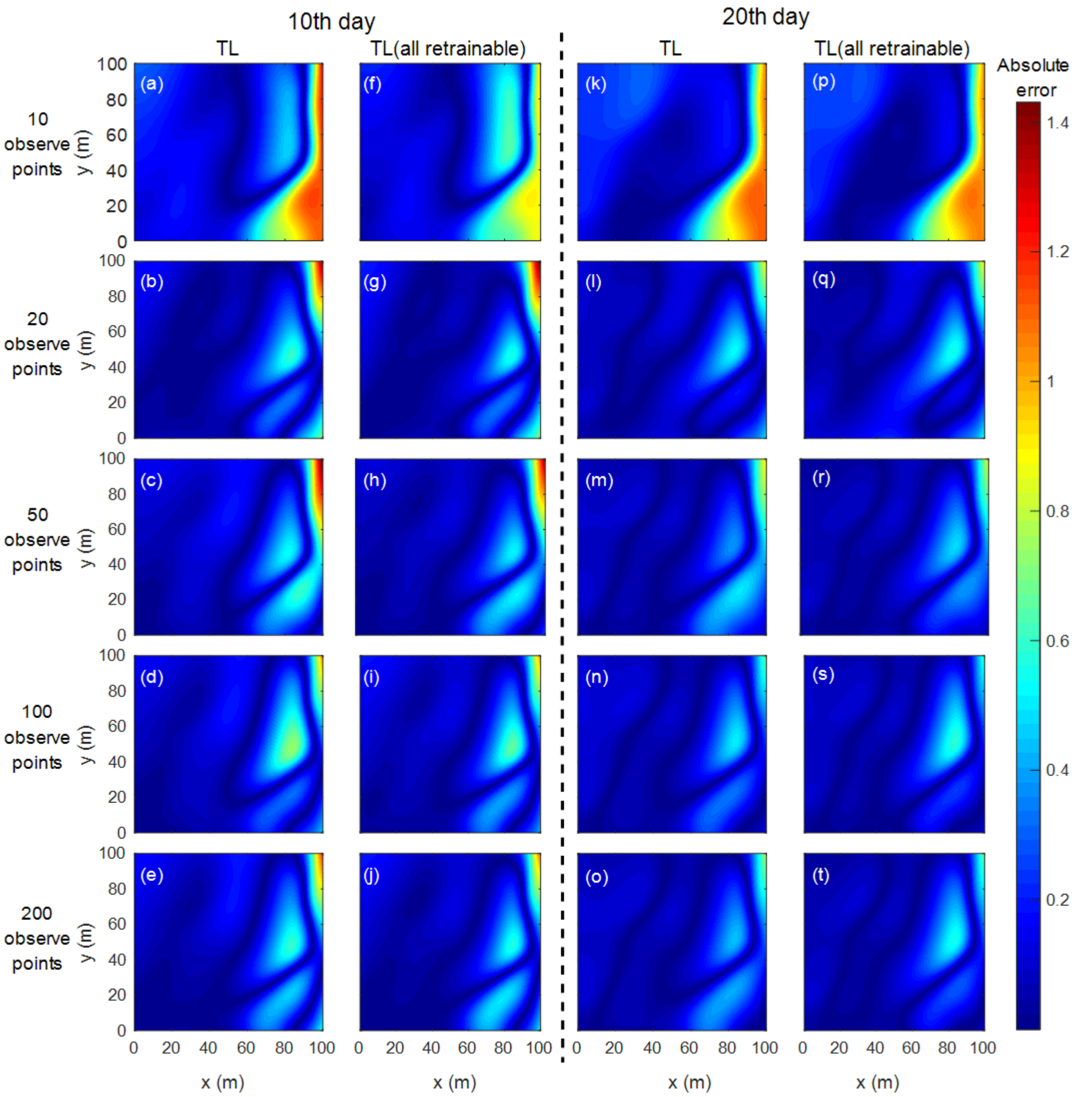


Figure 6.11 Absolute error between predicted hydraulic head using the TL and TL (all retrainable) models. The pretraining model of TL and TL (all retrainable) is trained by $D_{n1}$ which is generated by the analytical model with $K = 3m/d$. (a)-(j) the reference head is the normalized groundwater head on 10th day, which is generated by the numerical model with the heterogeneously hydraulic conductivity field. (k)-(t) the reference head is the normalized groundwater head on 20th day, which is generated by numerical model with the heterogeneously hydraulic conductivity field.

**3) Effect of heterogeneity**

The heterogeneity of the hydraulic conductivity field is described by its variance and correlation length. To investigate the effect of heterogeneity on the performance of the TL model, three realizations of random field with different correlation length L are employed in this section. Figure 6.12 shows the random $\ln K$ fields for three correlation length $l$ (20, 10, and 5 m) and the reference hydraulic head on the 33rd day for each $\ln K$ field, where the mean and variance are the same as those in Figure 6.7. Training datasets are obtained from 10, 20, 50, 100 and 200 observation points and the observation points are randomly selected for 200 times. For each realization, the TL, TL (all retrainable) and DBPNN models are trained and tested, respectively.

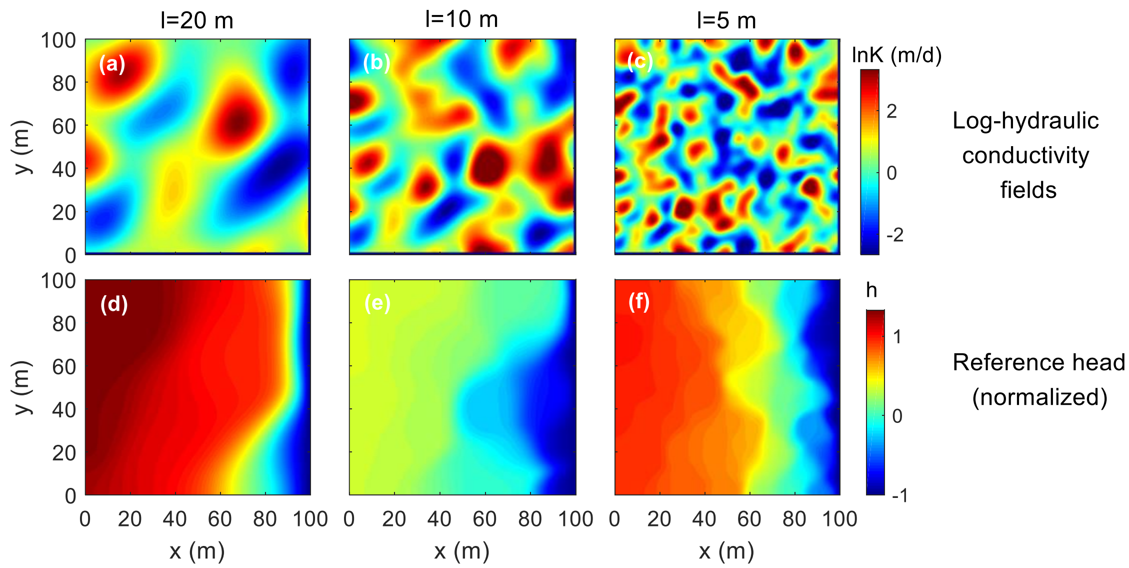


Figure 6.12 The heterogeneously hydraulic conductivity field with the different correlation length (*l*=5, 10, and 20m) (a, b and c), which are respectively used to generate the reference hydraulic heads (d, e, and f).

Figure 6.13 shows distributions of MSE for TL models at hydraulic conductivity fields with different correlation length. With the observation points increasing until the number of observation points reaching 20, the IQR and mean of MSE drop greatly. When the number of observation points is over 20, the IQR and mean of MSE improve slightly and when there are more than 50 observation points, the mean of MSE remains static where the mean of MSE for $l = 20\ m$ is about 0.03, the mean of MSE for $l = 10\ m$ is about 0.02 and the mean of MSE for $l = 5\ m$ is about 0.01. This observation is consistent with that of Figure 6.10.

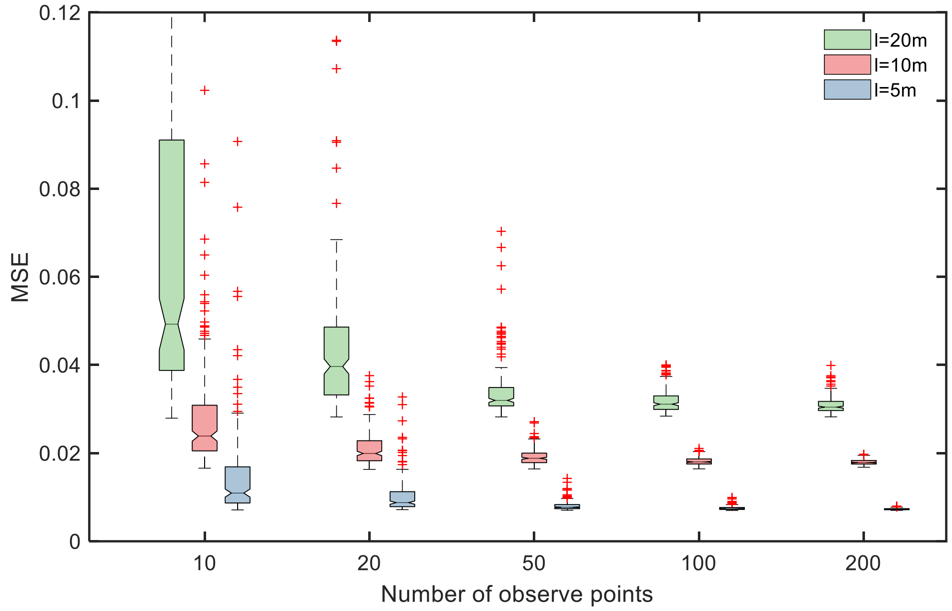


Figure 6.13 MSE distribution of transfer learning plotted against number of observe points for hydraulic conductivity fields with the different correlation length (*l*=5, 10, and 20m ) in the case that the observe points are randomly realized for 200 times.

It is also interesting to note that, with the same observation points, a better result can be obtained with a smaller IQR and lower mean of MSE for the case with a smaller correlation length $l$. This result can be explained that the presented transfer learning model would be more effective to transfer knowledge between two datasets with similar structure or characteristics. When the correlation length is smaller, the hydraulic conductivity field is more stochastic to be considered as a stationary field and the hydraulic head data generated from it would have a more similar structure or characteristic to data generated from the analytical solution. It can also be proved in Figure 6.13 MSE distribution of transfer learning plotted against number of observe points for hydraulic conductivity fields with the different correlation length (*l*=5, 10, and 20m ) in the case that the observe points are randomly realized for 200 times. that with a smaller correlation length $l$, groundwater flow in the x-direction is more dominant, which means it is more analogous to the 1-D analytical solution proving the physics knowledge for the pre-training model.

**4) Effects of recharge uncertainty**

To assess the impact of different values of hydraulic conductivity K in the analytical solution, the analytical model with three distinct K values (0.3 m/d, 3 m/d, and 30 m/d) is employed as pre-training models. The reference head, consistent with Figure 6.12 The heterogeneously hydraulic conductivity field with the different correlation length (*l*=5, 10, and 20m) (a, b and c), which are respectively used to generate the reference hydraulic heads (d, e, and f)., was generated using the numerical model, assuming a heterogeneous conductivity field with an average value of 3 m/d. To minimize the impact of the observation point sampling campaign, 200 random realizations for each sampling campaign are conducted. In each of these realizations, the transfer learning model was trained and tested, and the corresponding results are depicted in Figure 6.14.

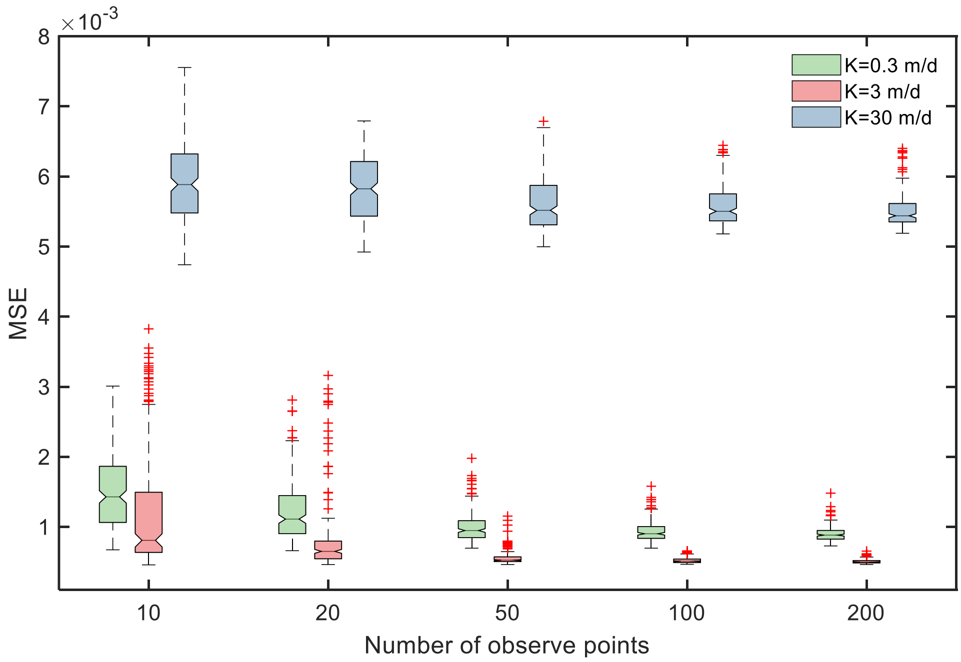

Figure 6.14 MSE distribution of reverse normalization result from the TL models plotted against number of observe points for the analytical solution with K=0.3m/d. 3m/d and 30 m/d.

Figure 6.14 displays the distributions of MSE for the TL models. It is worth noting that the normalization process relies on the maximum and minimum values of the groundwater head derived from the analytical solution. Given the different K values in the analytical model, comparing results in normalized form could be challenging. Therefore, the comparisons is based on the reverse normalization results. The vertical axis in Figure 6.14 represents the distribution of reverse normalization results from the TL models. It is evident that when the number of observation points is the same, the mean of the MSE is minimized at K = 3 m/d. This suggests that when the K value in the analytical solution aligns with the mean of the hydraulic conductivity field, the source dataset becomes more similar to the target dataset, resulting in a more effective transfer.

Furthermore, when K is set to 30 m/d in the analytical solution, the mean of MSE is larger compared to that of K = 0.3 m/d. This is due to the fact that when K is larger, the water table obtained from the analytical solution becomes closer to a straight line, indicating fewer inherent data features. Therefore, when using the proposed method in sites with unknown hydraulic conductivity, assigning a smaller value to K in the analytical solution can yield better results.

**5) Effects of recharge uncertainty**

In the previous cases, the recharge is the known input variable. However, recharge cannot be determined accurately in the fieldwork. Therefore, in this subsection, the performance of the TL model by considering the effects of recharge uncertainty will be tested. Noise is added into the recharge data in the following manner:

$$W^*(t) = W(t) + W_{diff} \times \alpha\% \times \varepsilon \tag{9}$$

where $W^*(t)$ is recharge rate including the noise; $W(t)$ is recharge rate estimated by expert experience or field testes; $W_{diff}$ is the maximum value of $W(t)$; $\alpha$ is a percentage; $\varepsilon$ is the uniform random variable ranging from $-1$ to 1. In this case, 5%, 10% and 15% noise are added to the estimated recharge $W(t)$ to present the uncertainty of recharge rate. The respective $W^*(t)$ is employed to generate the hydraulic head by the numerical solution, where the other model parameters are same as that in Figure 6.10. The hydraulic heads on 33$^{rd}$ day are employed as the testing data. The time series of numerical hydraulic heads from 10, 20, 50, 100 and 200 observation points are extracted as the five training datasets for TL and BPNN. To reduce the impacts of the sampling campaign of observation points for each training datasets, each sampling campaign are randomly implemented 200 realizations.

Figure 6.15 shows the distributions of MSE for the TL and DBPNN models trained by data generated with different noise. It is found that with the same observation points, the mean MSE of the TL model is obviously lower than that of the DBPNN model, which is consist with the observations in Figure 6.9. The performances of the TL and DBPNN models are both affected by the noise, i.e., the TL and DBPNN models produces worse predictions for the case with higher noise. However, the TL model is much less affected by the recharge uncertainty relative to the DBPNN model. For example, for the 10 observation points, the mean MSE of the DBPNN model ranges from 2.2 to 1.7, with the noise decreasing from 15% to 5%. However, the mean MSE of the TL model only range from 0.067 to 0.042. This indicates that the TL model possesses superior robustness to the DBPNN model.

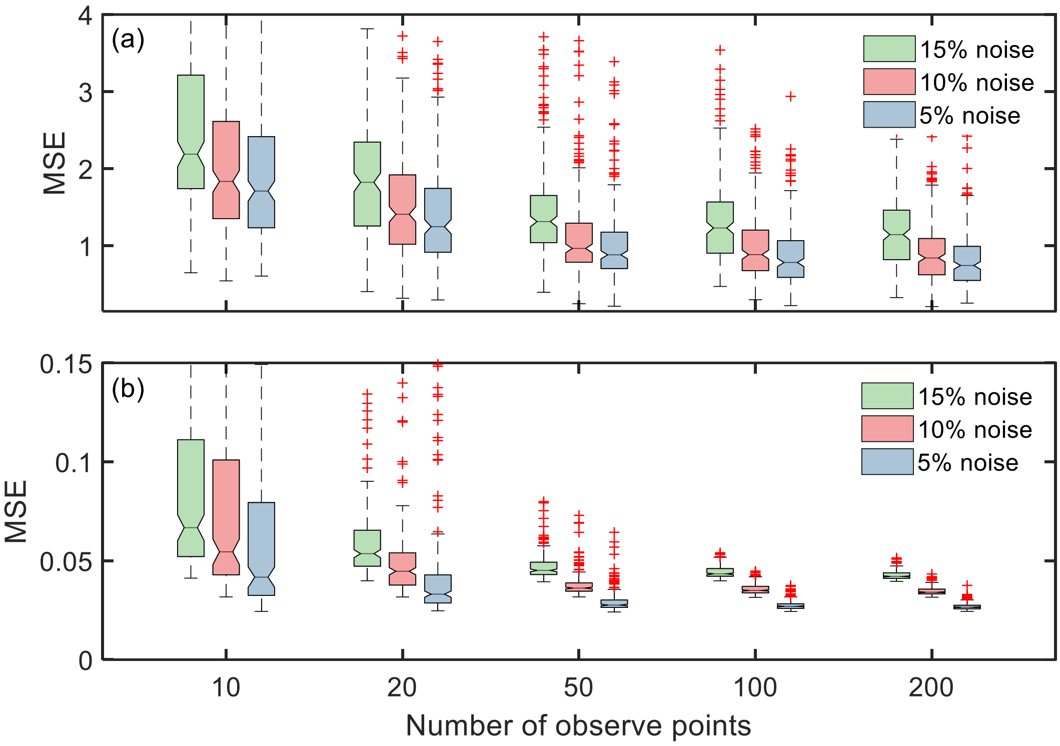


Figure 6.15 MSE distribution of the DBPNN (a) and TL (b) models plotted against number of observe points for the recharge rate with the different noise in the case that the observe points are randomly realized for 200 times, where 5%, 10%, and 15% noise are respectively employed.

## Summary

Deep learning models have a good interpolating ability, while their performance is limited by data scarcity in groundwater problems. Analytical models present the first-order physical principle of groundwater flow, but they are only valid under very specific conditions, such as aquifers are homogeneous. This study proposes a novel transfer learning framework to integrate the advantages of these two methods. A deep learning model guided by a simple analytical model to predict groundwater flow in heterogeneous aquifers is presented in this research. It differs from previous deep learning research by incorporating the knowledge from a simple analytical model and utilizing transfer learning technique to further improve the hydraulic head prediction in relatively complicated problems where the analytical model is invalid. The model is tested against the traditional deep learning model Deep Back Propagation Neural

Network (DBPNN) in scenarios with unknown homogeneous and heterogeneous hydraulic conductivity fields. The results show that the proposed model can improve the accuracy of the hydraulic head predictions by fusing the analytical knowledge with the neural network. The hydraulic conductivity mainly affects the parameters of the shallow layers in the neural network, making it possible to employ transfer learning in more complicated problems. For all test scenarios, the prediction errors of the proposed model are much smaller than that of the DBPNN. The proposed model performs satisfactorily even with sparse training data.

Nevertheless, it is essential to acknowledge several limitations associated with the proposed method in this study.

Firstly, the applicability of the proposed method is constrained by its lack of extrapolation capability. The proposed method relies on transfer learning techniques to harmonize analytical solutions with observational data. During the transfer learning process, the observational data serves as the target dataset, which is a fundamental component of transfer learning. Therefore, the method faces limitations when it comes to extrapolation due to the absence of observational data beyond the training domain.

Secondly, the performance of the proposed method can be sensitive to the choice of hydraulic conductivity (K) value in the analytical solution. If the estimated value of K exhibits a significant bias, it may compromise the accuracy of the proposed method. This sensitivity becomes more pronounced when K is either overestimated or underestimated.

Finally, the transfer learning framework outlined in this study primarily focuses on heterogeneous aquifers. It is worth noting that in the transfer learning model, greater dissimilarity between the source domain and the target dataset can result in poorer transfer performance. Specifically, the application of analytical solutions requires that the spatial domain of the model is regular. However, in reality, the spatial domain of the study area (such as watersheds) is irregular. It introduces the disparities between the groundwater flow field in the study area and the analytical solution, potentially affecting the performance of the transfer learning model.

# Chapter 7 Surface water - Groundwater coupled prediction in watersheds using deep transfer learning and integrated surface water and groundwater model

In the preceding chapter, the transfer learning method for groundwater flow prediction is discussed in a numerical experiment conducted using a simplified two-dimensional Darcy model as an example. However, the actual field conditions are far more complex than the case presented earlier due to the complex shape of the study area, heterogeneity, and the influence of the unsaturated zone. The applicability of the proposed groundwater transfer learning method at the watershed scale remains to be explored. Furthermore, the method relies on known surface water levels and other hydrological variables, making it unable to independently predict future changes in groundwater levels.

To address these issues, this chapter focuses on a real-world study area to validate the applicability of the proposed groundwater transfer learning method at the watershed scale. Meanwhile, the LSTM neural network introduced in Chapter 4 will be utilized to forecast future surface water levels and other hydrological variables. Building upon this, the transfer learning method will be employed for coupled catchment-scale prediction of surface water and groundwater.

The workflow diagram is depicted in Figure 7.1. A two-dimensional profile groundwater model considering the influence of hydrological variables like surface water and rainfall recharge is established, and its analytical solution is derived and validated. Next, the analytical solution is applied to the watershed to obtain the source domain dataset. The pre-training model is then trained based on the source domain data. Subsequently, the transfer learning method is used based on source domain data and observation data from the study area to regress the watershed scale groundwater head.

When the framework for catchment-scale groundwater and surface water prediction is employed, the hydrological variables and groundwater observation data will be predicted by a Deep LSTM neural network first and then the analytical model and transfer learning method will be applied in the same way as regression. A Deep Back-Propagation Neural Network (DBPNN) is employed as the baseline model to provide a benchmark. The baseline model is trained solely based on the observed data generated from the numerical model. It is important to note that both the source domain and target domain data undergo standardization prior to their utilization.

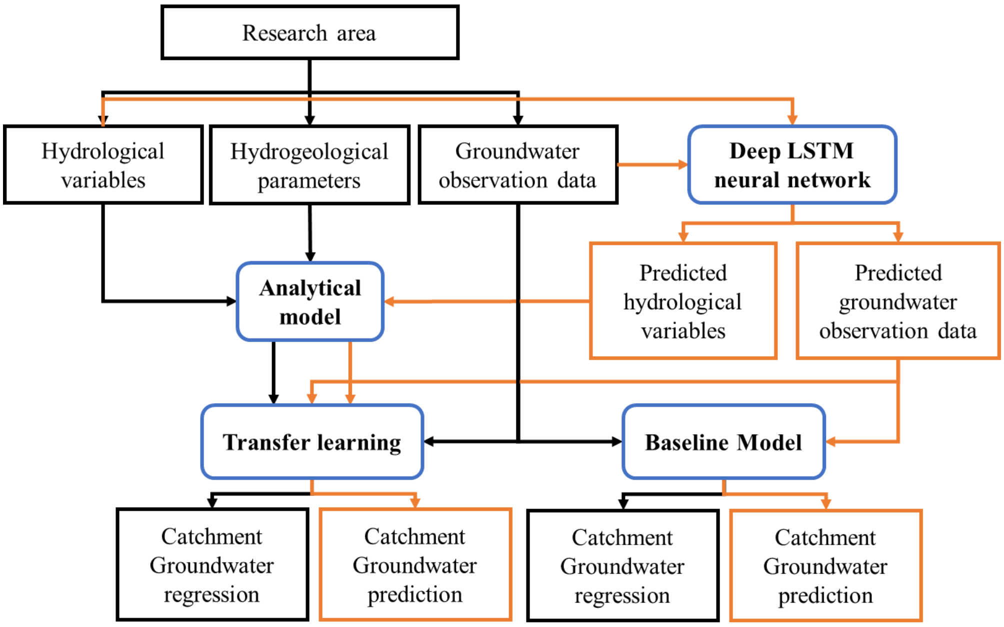


Figure 7.1 The workflow diagram of this research

This section is organized as follows: Section 6.1 presents the research area and data collection. Section 6.2 presents the methodology. The results of the experiments performed with the method are shown in Section 6.3. Finally, Section 6.4 provides a summary.

## Research Area and Data Collection

### Research Area

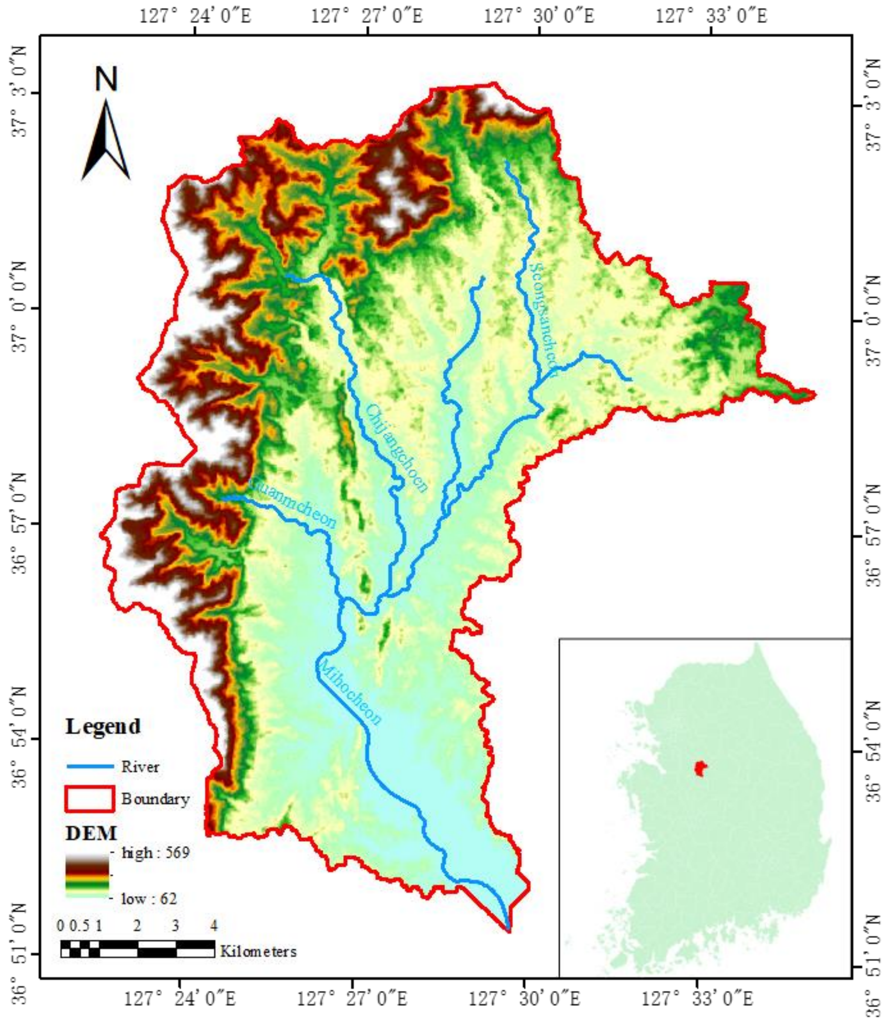


Figure 7.2 Topography and river distribution map of the study area

Our study area is situated in the central-western region of South Korea and serves as one of the headwaters of the Miho River (Figure 7.2). The study area covers an approximate area of 194 square kilometres and encompasses the cities of Anseong and Icheon in Gyeonggi Province, as well as the counties of Eumseong and Jincheon in Chungcheongbuk Province. The elevation ranges from 62 meters to 569 meters, showcasing a significant variation in height. The topography within the study area exhibits a northwest-to-southeast gradient, with the western region predominantly characterized by mountainous and hilly terrain, while the eastern region is primarily composed of expansive plains.

The annual average flow in this watershed is around 600 millimetres. The region displays marked characteristics of a dry season (October to May) and a rainy season (June to September). Approximately 70% of the annual precipitation occurs during the rainy season. Temperature in the region correlates with precipitation. Average temperature during the dry season is 6.9 degrees Celsius and that during rainy season is 23.6 degrees Celsius. In the study area, the focal river is Insan-ri, situated in the upstream Mihocheon watershed, with a length of approximately 25 kilometres. | Improved clarity and conciseness. The tributaries in the basin include Seongsancheon, Chijangcheon and Guamcheon, which converge into the Mihocheon near Sandang-ri.

The watershed area has relatively smaller urban and forested areas, with the urban areas being dispersed throughout the region. Forested areas are primarily concentrated in the western mountainous region. The dominant land use types within the watershed are paddy fields, with agricultural land playing a supplementary role. The aquifer system within the watershed is primarily composed of unconsolidated sediments, while the western mountainous region consists of aquifers formed by Cretaceous volcanic rocks, Cretaceous sedimentary rocks, and paragneiss. Groundwater extraction is primarily utilized for agricultural irrigation and domestic purposes.

**Data collection**

Due to the limited number of groundwater level monitoring points and surface water flow and depth observation points in the actual field, it is challenging to validate the effectiveness of the proposed method globally by available observation data. Therefore, in this study, a surface water-groundwater coupled model for the Miho catchment (Joo et al., 2018) is applied to generate enough amount of surface water and groundwater data within the watershed to validate the proposed method.

Joo et al. (2018) established the surface water-groundwater coupled model of Miho catchment by Visual HEIFLOW. In the model, both surface and subsurface components utilize a unified grid, where the Miho watershed is divided into 2141 grid cells with a cell size of 1×1 km. Our research area is a part of the Miho catchment and occupies about 200 grid cells. It is important to note that the daily surface water and groundwater observation data from 2004 to 2014 were used to calibrate and validate the Miho GSFLOW model, which yielded satisfactory results during the calibration and validation periods. This indicates that the Miho GSFLOW model is capable of reflecting the surface water and groundwater conditions for generating data in this study.

Additionally, for computational efficiency, it is worth noting that only the data from every 5 days between 2004 and 2007 were utilized to verify the proposed method in this study. The location of the observation point, time and recharge at the respective time are considered as input variables and the groundwater head is considered as the output for the proposed method.

## Methodology

### Analytical Model and Solution

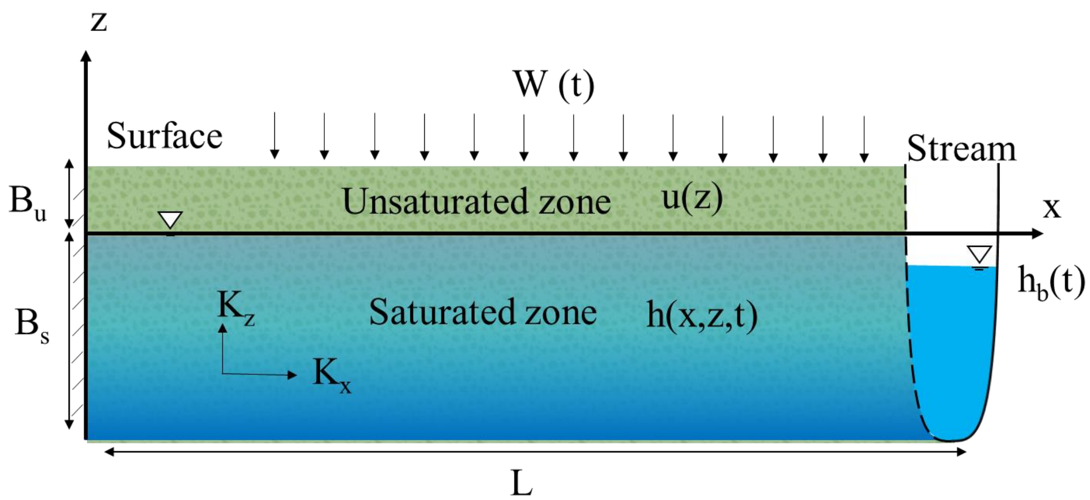


Figure 7.3 Conceptual model of unsaturated-saturated groundwater flow interaction with river

The schematic diagram in Figure 7.3 illustrates the interaction between groundwater and a river within an unsaturated-saturated porous medium. The lateral boundaries of the aquifer consist of a watershed and a river that completely traverses the aquifer. The groundwater receives time-varying recharge from precipitation trough upper boundary. The aquifer's bottom is both horizontal and impermeable. The saturated and unsaturated zones, characterized by uniformity, vertical anisotropy, and lateral extent, meet at the interface corresponding to the free groundwater table.

The government equation of groundwater flow in saturated zone can be given by:

$$K_x \frac{\partial^2 h}{\partial x^2} + K_z \frac{\partial^2 h}{\partial z^2} = S_s \frac{\partial h}{\partial t}, \qquad -B_s < z \leq 0 \qquad \text{Equation 7.1}$$

$$\frac{\partial h}{\partial z} = 0, \qquad z = -B_s \qquad \text{Equation 7.2}$$

$$h(x, z, t) = H(t), \qquad x = L \qquad \text{Equation 7.3}$$

$$\frac{\partial h}{\partial x} = 0, \qquad x = 0 \qquad \text{Equation 7.4}$$

$$h(x, z, t) = 0, \qquad t = 0 \qquad \text{Equation 7.5}$$

where $K_x$ and $K_z$ are the horizontal and vertical hydraulic conductivity respectively [$LT^{-1}$]; $h$ is the hydraulic head [L]; $S_s$ is the specific storage [$L^{-1}$]; $B_s$ is the thickness of saturated zone [L]; $H(t)$ is an interpolation function to describe river stage [L]; L is the length of the concept model [L].

Owing to the low conductivity in the unsaturated zone, the angle between the flow lines in this layer and the water table is nearly zero. This makes it reasonable to assume that groundwater flow in unsaturated zone is vertically one-dimensional and Richard's equation is applied to govern the flow of groundwater in the unsaturated zone. In order to facilitate obtaining analytical solutions, this study employs the linearized form of Richard's equation (Kroszynski and Dagan, 1975) as follows:

$$K_z \frac{\partial}{\partial z}\left(k_0(z) \frac{\partial u}{\partial z}\right) = C_0(z) \frac{\partial u}{\partial t}, \qquad 0 \leq z \leq B_u \qquad \text{Equation 7.6}$$

$$K_z k_0(z) \frac{\partial u}{\partial z} = I(t), \qquad z = B_u \qquad \text{Equation 7.7}$$

$$u(x, z, t) = 0, \qquad t = 0 \qquad \text{Equation 7.8}$$

Where, Moreover, where $u$ is the hydraulic head in the unsaturated zone [L]; $k_0(z)$ and $C_0(z)$ are the relative hydraulic conductivity and the soil moisture capacity [$L^{-1}$] at the initial water content respectively; $B_u$ is the thickness of saturated zone in the z-direction [L]; $I(t)$ is the infiltration rate [$LT^{-1}$], which is described by piecewise functions.

The (Gardner, 1958) exponential constitutive model is adopted for unsaturated flow:

$$k_0(z) = e^{-\kappa z} \qquad \text{Equation 7.9}$$

$$C_0(z) = S_y \kappa e^{-\kappa z} \qquad \text{Equation 7.10}$$

Where $\kappa$ is the constitutive exponent[$L^{-1}$] and $S_y$ is the specific yield. Interface conditions are used to couple the flow, which are same as Equation 5.7 and Equation 5.8:

$$h - u = 0, \qquad z = 0 \qquad \text{Equation 7.11}$$

$$\frac{\partial h}{\partial z} - \frac{\partial u}{\partial z} = 0, \qquad z = 0 \qquad \text{Equation 7.12}$$

The coupled equation Equation 7.1-Equation 7.12 can be solved by the Laplace and the Fourier sine transforms. S3.1-S3.3 in the supporting information present the details of the derivation. The Laplace domain solutions of unsaturated and saturated zone flow can be respectively written as:

$$\bar{h}(x,z,p) = \sum_{n=0}^{\infty}(\mathbb{C}_2\, exp(-\Phi_n z) + \mathbb{C}_3\, exp(\Phi_n z) - \zeta)\psi(\omega_n, x) + \overline{h_b}(p) \qquad \text{Equation 7.13}$$

$$\bar{u}(z,p) = \sum_{n=0}^{\infty}(\mathbb{C}_1' e^{\mathbb{M}z} + \mathbb{C}_2' e^{\mathbb{N}z})\psi(\omega_n, x) \qquad \text{Equation 7.14}$$

where the definitions of variables $\mathbb{C}_1', \mathbb{C}_2', \mathbb{C}_2, \mathbb{C}_3, \Phi_n, \zeta, \mathbb{M}, \mathbb{N}$ and $\omega_n$ can be found in S3.1-S3.3.

### The application method of analytical solutions at the watershed scale

The previous section introduced an analytical solution model for vertical profiles. However, due to the curvature of rivers and the irregular shape of watershed boundaries, direct application of this analytical solution at the watershed scale is challenging. To address this issue, this section proposes a method for estimating groundwater dropdown in a watershed by vertical profile analytical model based on the concept of weighted averages. The specific method is described as follows:

1. Hydrological analysis is conducted based on the elevation of the watershed. The watershed is divided into several sub-watersheds according to the watershed boundaries, and the main rivers within each sub-watershed are identified.
2. When the sub-watershed is small enough, the river in respective sub-watershed can be assumed as a polyline. The river polyline is segmented into several river segments by breaking at the inflexion points.

3. Buffer zones are created for each river segment. Then the buffer zones are extended to the boundaries of the sub-watersheds, as shown in Figure 7.4a. At this stage, the sub-watersheds can be classified into the following three categories: Zone 1. Buffer areas influenced by only one river segment; Zone 2. Buffer areas influenced by multiple river segments; Zone 3. Areas other than Zone 1 and 2.
4. Vertical lines are drawn perpendicular to the river segments on the plane. The profiles are generated along the z-direction. These profiles are approximately consistent with the assumed analytical solution. As shown in Figure 7.4b, the discrete data points of the profile are obtained, and the analytical solution (Equation 13) is applied to calculate the average drawdown corresponding to the groundwater table in the saturated zone. During the calculation process, the parameters such as K are estimated as the averages along the profile.
5. If a data point falls within the spatial range of Zone 1, the drawdown of groundwater level at that point is considered as the calculated value.
6. If a data point falls within the spatial range of Zone 2, it is influenced by multiple river segments. In this case, drawdown of the groundwater level at that point needs to be calculated separately for each river segment. It is assumed that $s_i$ represents the drawdown caused by the i-th river segment and $x_i$ represents the distance from the point to the i-th river segment. The drawdown at the point can be expressed as $s = \sum_i^N \frac{1/x_i}{\sum_i^N \frac{1}{x_i}} s_i$, where $N$ represents the total number of river segments influencing the point.
7. There should be no data point within the spatial range of Zone 3. The drawdown of groundwater in Zone 3 can be obtained through interpolation using the data from Areas 1 and 2.

It should be noted that this method is not an accurate approach for estimating the drawdown of groundwater in a watershed using analytical solutions. This method only provides a rough indication of the groundwater flow trends within the watershed. However, this information can serve as prior knowledge and by leveraging the prior knowledge obtained through this method, transfer learning techniques can be applied to improve the precision of groundwater forecasting.

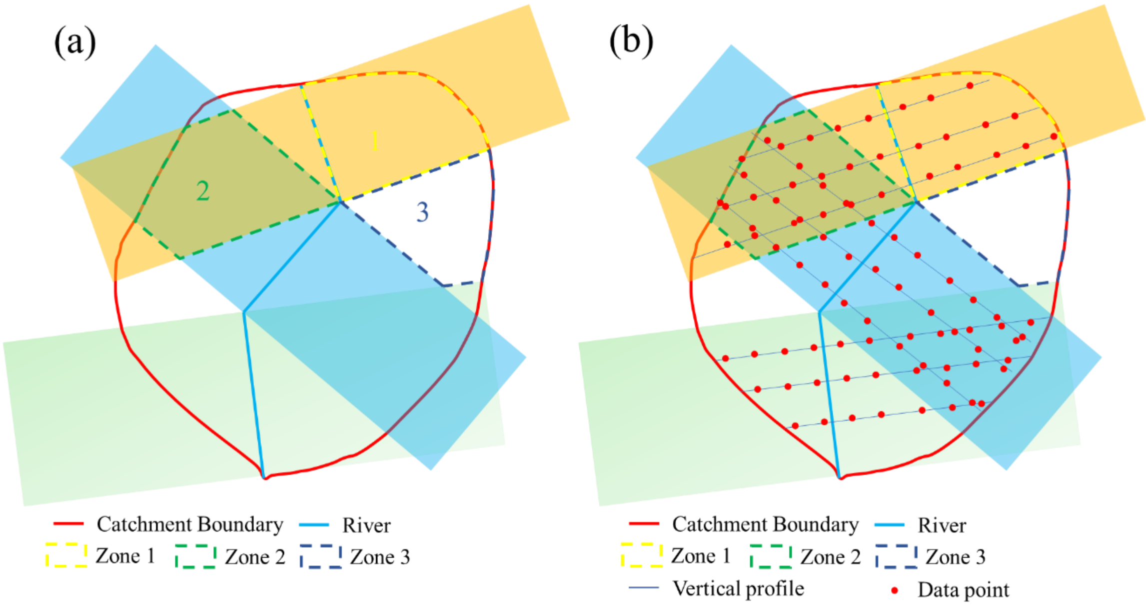


Figure 7.4 Diagram of buffer zone generation (a) and data point placement (b) in the application of analytical solutions at the watershed scale.

## Deep LSTM neural network and Deep Transfer Learning

The Deep LSTM neural network is a branch of deep RNN neural network. It is widely used in hydrological variables prediction for its excellent temporal data processing ability. The details of the deep LSTM neural network can be found in Section 0 Due to the lack of meteorological data, this chapter only uses past river water level data and groundwater level data (from 2004 to 2007) to predict river water level and groundwater level data in next 2 month. The hyperparameter, past history, was set to 7 days. The structure and other parameters of deep LSTM neural network employed here are same as Chapter 3.

Deep transfer learning is an emerging technique in the realm of deep learning, which applies transfer learning methods within a deep learning framework. It leverages the knowledge and representations learned from one task or domain to enhance the performance of another task or domain. By utilizing the learned representations from pre-trained models, deep transfer learning enables the target task to benefit from the source task's knowledge and feature extraction capabilities, even when labelled data is limited. It helps overcome the need for large-scale labelled data and can result in performance improvements, faster convergence rates, and reduced training time. The details of deep transfer learning can be found in Section 0 and 0.

## Result and Discussion

This section first validates the semi-analytical solutions by comparing it with numerical model. Then the semi-analytical solutions are applied to generate source data, and the transfer learning technique is employed to predicate groundwater drawdown in the research area. Finally, the uncertainty caused by sampling campaign of observation points is investigated.

### Validation of analytical solutions

To validate semi-analytical solutions Equation 7.13 and Equation 7.14, numerical solutions obtained from Equation 7.1-Equation 7.8 are employed to compare with the semi-analytical solutions. The model parameters used in the study are as follows: $H_u = 2m$, $H_s = 10m$, $L = 80m$, $\kappa = 1.48\ 1/m$ $K_x = K_z = 10^{-5}m/s$, $S_y = 0.18$ and $S_s = 10^{-6}$. For the synthetic numerical simulations, two scenarios are considered: (1) groundwater flow induced by two rainfall infiltration events which occur at $2\ day \leq t < 3\ day$ with a constant rate of $I = 1.04 \times 10^{-7}\ m/s$, and $7\ day \leq t_D < 8\ day$ with a constant rate of $I = 5.18 \times 10^{-7}\ m/s$, and the river stage is constant or $H = 0\ m$; and (2) groundwater flow induced by a flood event with no infiltration.

COMSOL Multiphysics is employed to numerically solve the governing equations, Equation 7.1-Equation 7.8. The mesh is refined at the interface between two layers and the river in COMSOL, with a minimum mesh size of 0.001m and a maximum mesh size of 0.1m. This results in a total of 61,694 triangular elements and 31,419 nodes. In both scenarios, a time step of $\Delta t = 0.1\ day$ is used for the simulations.

Figure 7.5c and Figure 7.5d illustrate the groundwater head comparison result in the recharge and flood events, respectively. Meanwhile, Figure 7.5e and Figure 7.5f depict the average groundwater head. These figures demonstrate a close agreement between the analytical solutions (solid curves) and the numerical solutions (circle symbols). Through comparison, the analytical solution proposed in this study is considered accurate and reliable.

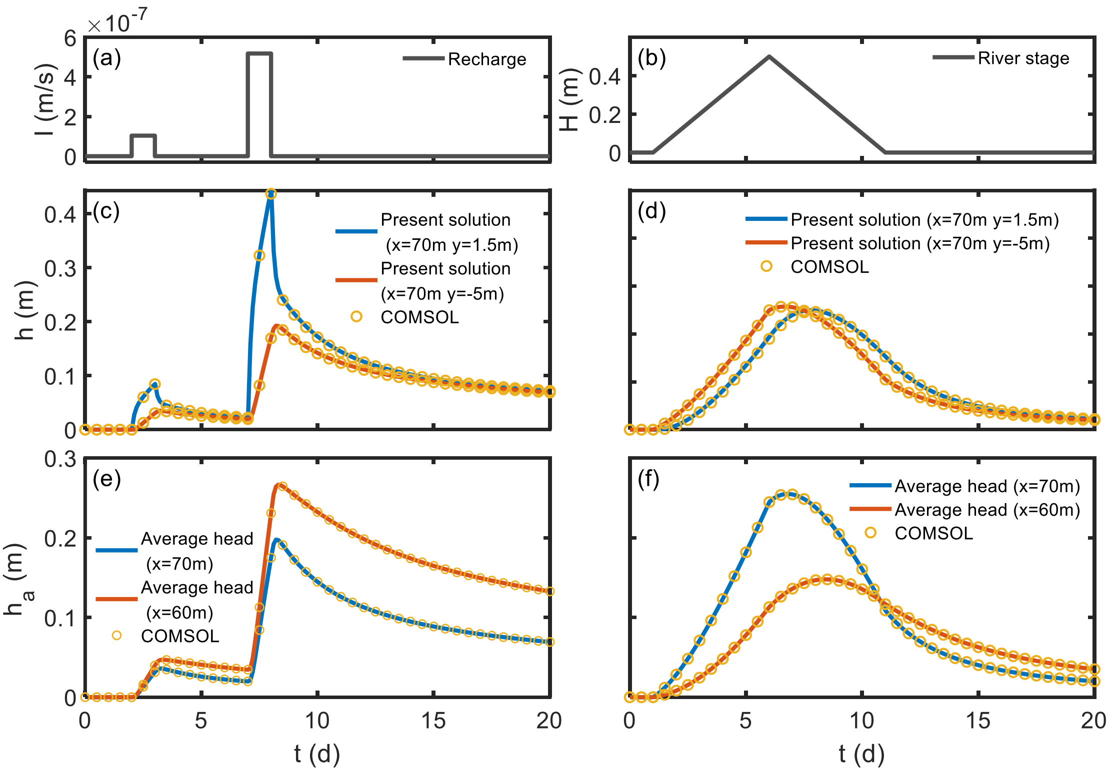


Figure 7.5 Comparison of the analytical solutions (solid curves) and the numerical solutions (open circles) for two infiltration events (left column) and a flood event (right column): (a) the rainfall infiltration $I(t)$ against time $t$; (b) the river stage $H(t)$ against time $t$; (c) the response of hydraulic head $h$ (or $u$) to recharge events against time $t$ at two locations; (d) the response of hydraulic head $h$ (or $u$) to flood event against time $t$ at two locations; (e) the response of average hydraulic head $h_a$ to recharge events against time $t$ at two locations; (f) the response of average hydraulic head $h_a$ to flood event against time $t$ at two locations;

## Deep Transfer learning

A fully connected neural network with 6 hidden layers and 50 neurons in each hidden layer is used as the pre-trained neural network. The source domain data is generated using the analytical solution. A total of 193 spatial points and 220 time steps (2004 to 2007, with a 5-day interval) are generated. The source domain data is normalized before being used to train the neural network. The input variables for the pre-training model are coordinates (x,y), time(t), and corresponding recharge rates(I(t)), while the output is groundwater drawdown. The Adam optimizer is employed in the pretraining process and the learning rate is set as 1%.

Ten, twenty, and fifty observation points are randomly generated, and the time series of groundwater drawdown at these observation points for the period from 2004 to 2007, with a 5-day interval, are generated as target domain data. The pre-trained model is then fine-tuned. During the fine-tuning process, the Adam optimizer is also employed and the learning rate is set as 0.5%. The convergence criteria are set as the maximum training iterations of 3000 or a change in the loss function less than 1e-5. In order to ensure the reliability of the results, a Deep Back-Propagation Neural Network (DBPNN) is used as the baseline model to provide a benchmark. It is important to point out that the baseline model is trained only using the observation data generated from the numerical model. Apart from that, the network structure and optimization methods of both the baseline model are the same as the deep transfer learning model.

Figure 7.6 shows the test results of the deep transfer learning model and the DBPNN model under the same scenario. The accuracy of the time series for each point is described using RMSE, where the blue colour represents lower RMSE. The figure indicates that the deep transfer learning model aligns well with the observed data given the training data, while the DBPNN model often fails to fit the reference heads. This suggests that the prior knowledge from the analytical solution embedded in the pre-trained model significantly enhances the performance of the neural network. The pre-trained model with the incorporation of physical knowledge provides better initial parameters for the neural network, which in turn reduces the search space during fine-tuning. On the other hand, the DBPNN model with randomly initialized parameters requires more training data to explore the entire parameter space. It is encouraging that the deep transfer learning model yields satisfactory results even in the case of sparse data.

The subpar performance of the DBPNN model, even with a large amount of training data, can be elucidated as follows. Under the same convergence criteria, both models underwent a finite number of training iterations, with a maximum of 3000 iterations or a change in the loss function below 1e-5. With limited training iterations, the DBPNN model may have been insufficiently trained to adapt to the dense training data. In contrast, the deep transfer learning model required only a small amount of training, specifically fine-tuning the parameters of the pre-trained model, to achieve more accurate results. Due to the pre-trained model's exposure to prior knowledge provided by the analytical solution, it possesses superior parameter configurations from the initial state, enabling it to adapt to the target task more swiftly. Consequently, even with a finite number of training iterations, the deep transfer learning model attains commendable results, while the DBPNN model necessitates a greater volume of training data to explore the entirety of the parameter space more effectively.

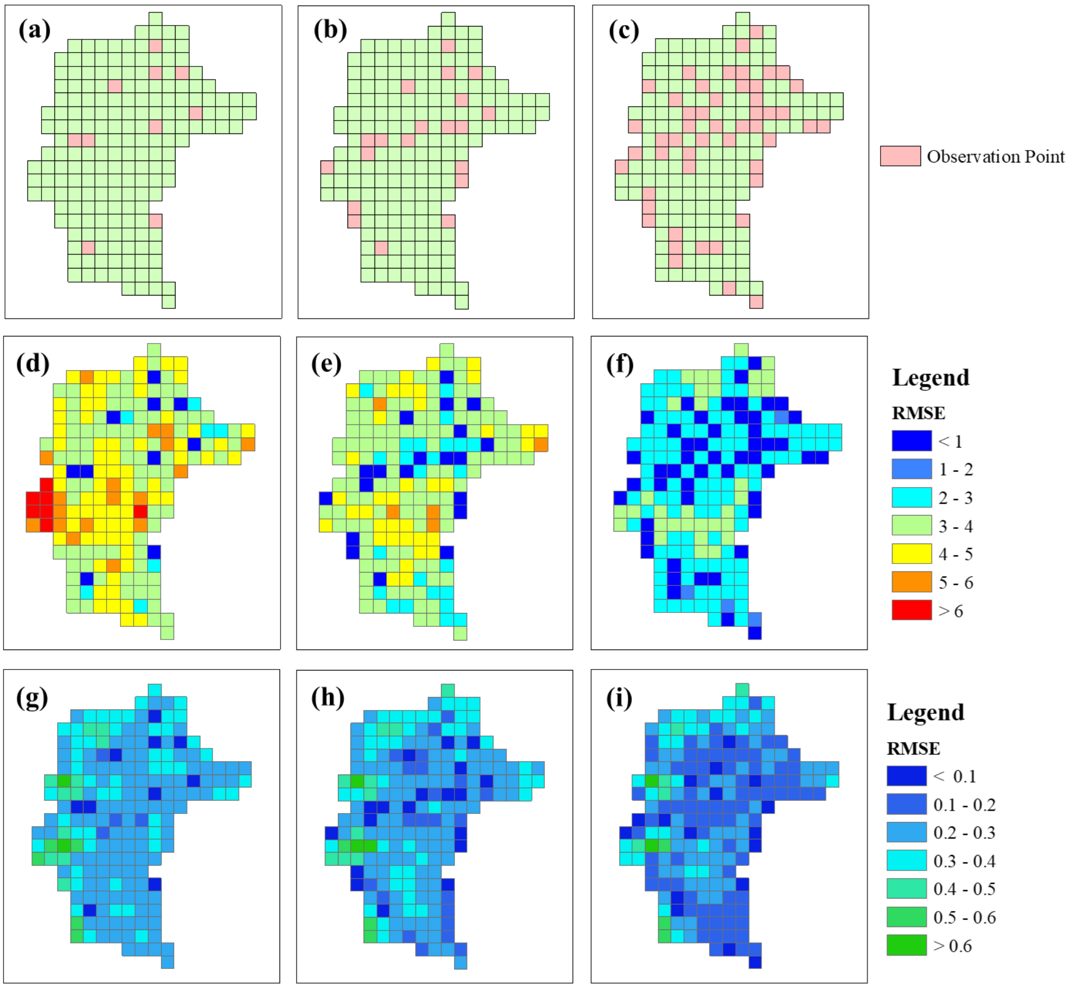


Figure 7.6 Comparison of accuracy between the proposed method and DBPNN for 10, 20 and 50 observation points. (a), (b) and (c) the positions of 10, 20 and 50 observation points. (d), (e) and (f) RMSE errors between the regressed hydraulic heads using DBPNN model for 10, 20 and 50 observation points. (g), (h) and (i) RMSE errors between the regressed hydraulic heads using the proposed method for 10, 20 and 50 observation points.

**Computational load analysis**

To further compare the computational efficiency of the proposed method with the baseline models, this section conducts a comparative analysis of the loss function variations during the training process for different scenarios. It is important to note that these models were implemented in Python 3.8 using TensorFlow 2.3 framework. The experiments were conducted on a workstation equipped with an Intel Xeon W2255 CPU and 128 GB of memory.

Figure 7.7 shows the normalized loss of the deep transfer learning model and the DBPNN model in training iterations under the Ten, twenty, and fifty observation points. As mentioned above, the MSE is employed as the loss function. The convergence criteria are set as the maximum training iterations of 3000 or a change in the loss function less than 1e-5. The location of observation points and other parameters are the same as in Figure 7.6.

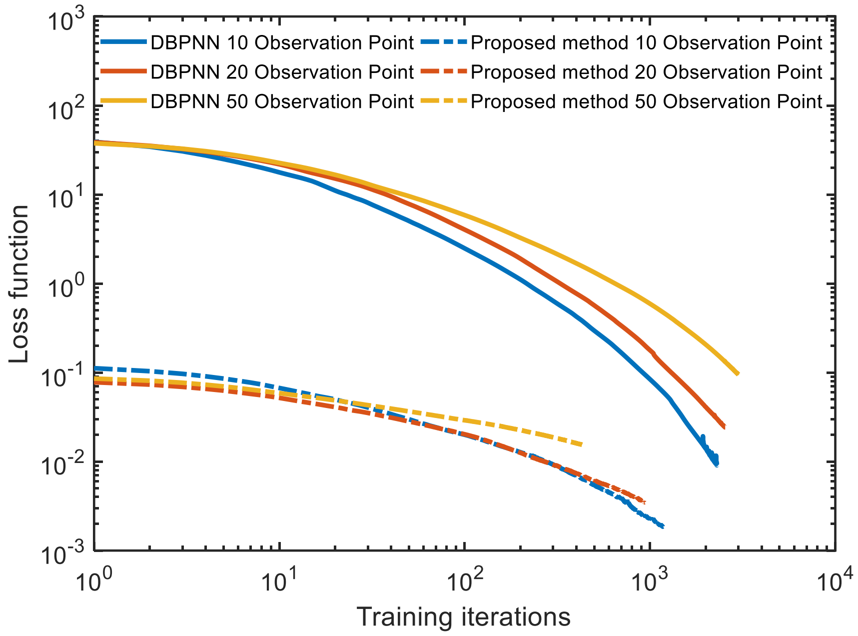


Figure 7.7 Loss function of proposed method (dashed curves) and DBPNN (solid curves) against the training iterations in the training process for 10, 20 and 50 observation points.

It can be observed from Figure 7.7 that at the beginning of the training process, the proposed model's loss function is significantly lower than that of the baseline model. Throughout the training process, although the loss function of the baseline model decreases rapidly, the proposed model consistently maintains a lower loss function. Additionally, the proposed model achieves convergence, with the minimum gradient descent threshold of 1e-5, within only 400-1000 iterations, while the baseline models require approximately 2000 iterations. This indicates that the prior knowledge provided by the analytical solution endows the neural network with more reasonable initial parameter values and constrains the search space during training. As a result, the proposed method requires fewer iterations to train a more accurate model.

**Uncertainty caused by sampling campaign of observation points**

It is important to note that the locations of observation points in the training data can impact the model's outcomes, leading to model uncertainty. To investigate this uncertainty and further demonstrate the capabilities of the deep transfer learning model, the positions of each observation point were randomly generated 50 times. Similar to the previous discussion, 10, 20, and 50 observation points were randomly generated, and the resulting time series of groundwater depth measurements every 5 days from 2004 to 2007 were used as the target domain data for retraining the pre-trained model. The root mean square error (RMSE) was employed to quantify the discrepancy between the model regressions and the observed values in each realization. The distributions of RMSE for the deep transfer learning model and the DBPNN model across different numbers of observation points in the 50 realizations are depicted in Figure 7.8.

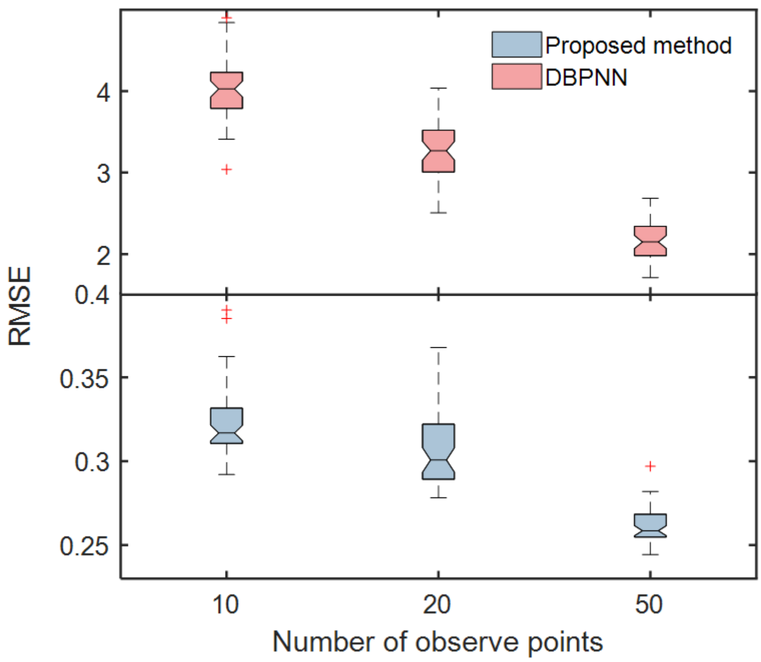


Figure 7.8 RMSE distribution of proposed method and DBPNN plotted against number of observe points, where the observe points are randomly realized for 50 times.

The results reveal that, for the same number of observation points, the deep transfer learning model consistently exhibits significantly lower mean RMSE values compared to the DBPNN model. For instance, with 10 observation points, the average RMSE of the DBPNN model is approximately 4, while the corresponding average

RMSE of the deep transfer learning model is 0.032. Furthermore, as the number of observation points increases, the average RMSE values exhibit a pronounced decrease.

Moreover, the interquartile range (IQR) of the RMSE for the deep transfer learning model is considerably smaller than that of the DBPNN model, indicating that the proposed transfer learning model outperforms the traditional DBPNN model in situations where the data is extremely sparse. This indicates that the proposed model effectively handles model uncertainty by integrating analytical knowledge.

### Watershed groundwater and surface water prediction

This section employs a Deep LSTM neural network to forecast hydrological variables (river stage, recharge), and groundwater observation data for the next two months based on data from the years 2004 to 2007. The locations of groundwater observation points are depicted in Figure 7.6. The forecasting results of the Deep LSTM neural network for hydrological variables and groundwater observation data are illustrated in Figure 7.9. It should be noted that this chapter discusses scenarios involving 10, 20, and 50 groundwater observation points. For clarity, Figure 7.9d provides a comparison between predicted and target values for all 50 groundwater observation points.

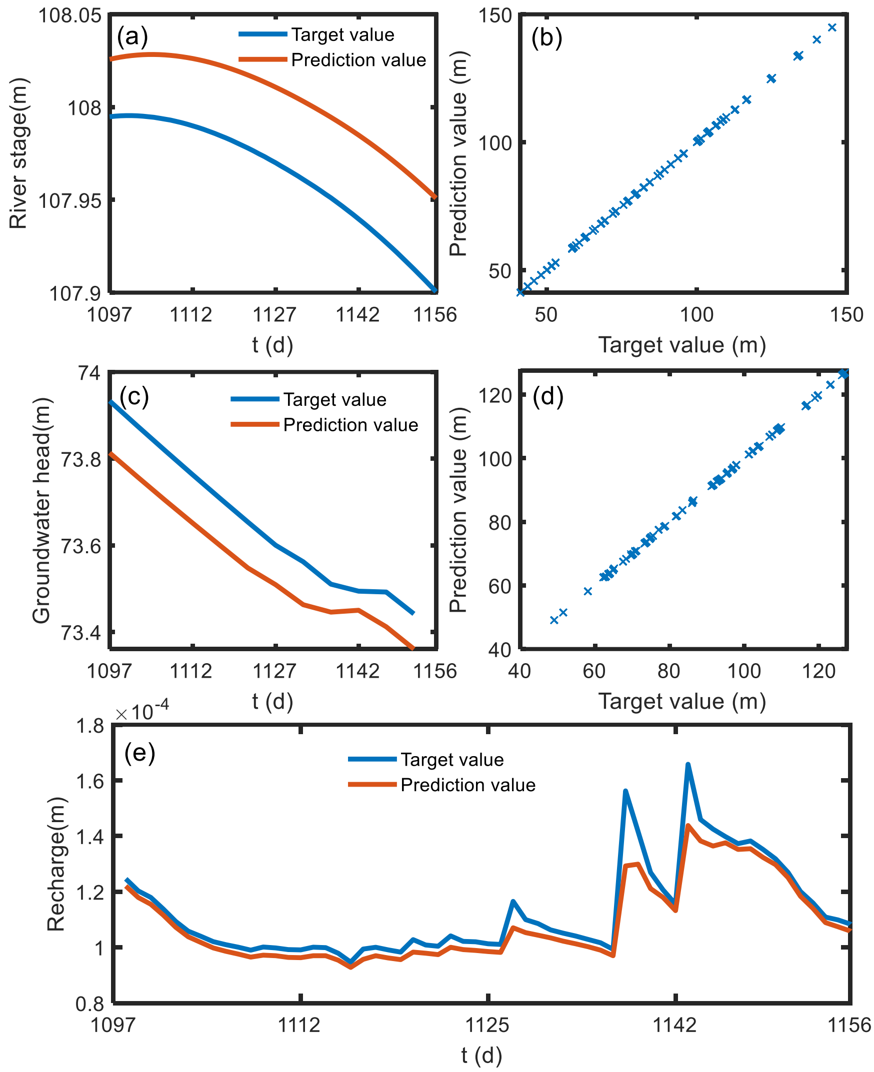


Figure 7.9 Deep LSTM neural network prediction result of river stage, recharge and observation groundwater head and the comparison between it and target value from 109th day to 1156th day. (a) comparison between predicted river stage and target value in grid HURID 26. (b) comparison between predicted all river stage and target value. (c) comparison between predicted observation groundwater head and target value in grid in HRUID 351. (d) comparison between all predicted observation groundwater head and target value. (e) comparison between predicted recharge and target value.

Figure 7.9a and 6.9c indicate that the Deep LSTM neural network exhibits certain errors in forecasting river stage and groundwater observation data. The forecast for river stage exceeds the actual value by 0.05m, while the forecast for groundwater observation data is lower by 0.09m. However, Figure 7.9b and d demonstrate that the Deep LSTM neural network can capture the overall trend of hydrological variables (river stage, recharge) and groundwater observation data for the next two months. Prediction errors are almost negligible under the influence of the position head. Figure 7.9e suggests that despite suboptimal forecasting results for the peak value of recharge, the predictions reflect the overall trend of recharge for the next two months. Statistical analysis yields a Nash-Sutcliffe Efficiency (NSE) of 0.86, indicating reasonably accurate forecasting results that can be applied to groundwater research in the watershed.

Figure 7.10 shows the prediction results of the deep transfer learning model and the DBPNN model under the same scenario. RMSE is applied to describe the accuracy of the time series for each point, which is the same as in Figure 7.6. In alignment with Figure 7.6, Figure 7.10 reveals that as the number of groundwater observation points increases, both the DBPNN and the deep transfer learning model exhibit improved prediction accuracy. Furthermore, under equivalent conditions of groundwater observation point numbers, the RMSE of the deep transfer learning model is significantly lower than that of DBPNN, indicating a markedly higher prediction accuracy. This reaffirms the conclusion drawn in the preceding section, highlighting that in the context of transfer learning models, the analytical solution provides additional physical information for the pre-trained model and effectively enhances the precision of groundwater prediction and regression compared to traditional deep learning methods. It is noteworthy that, in Figure 7.10, the prediction accuracy of both DBPNN and the deep transfer learning model is worse than the regression accuracy presented in Figure 7.6. This may be attributed to the cumulative errors in LSTM forecasting of hydrological variables and groundwater observation data.

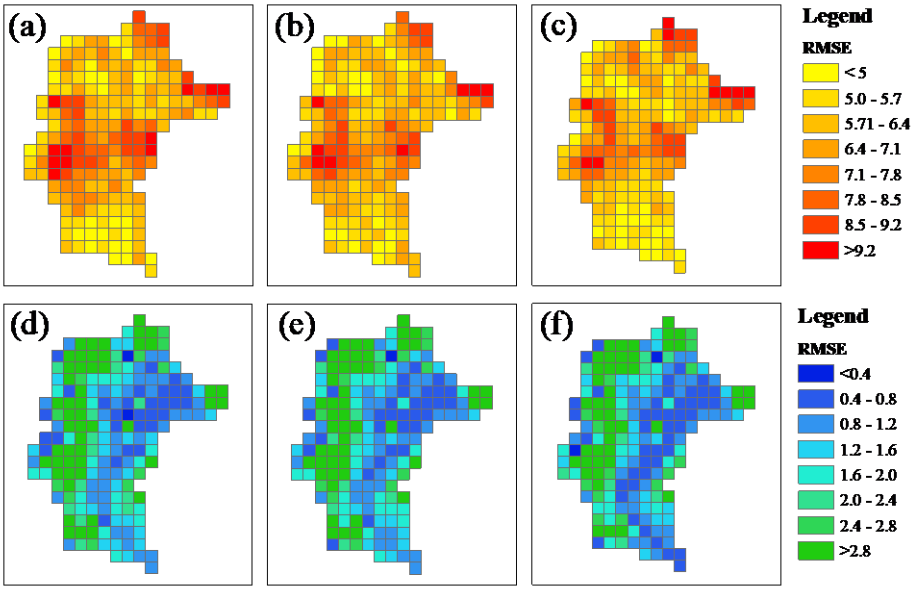


Figure 7.10 Comparison of watershed hydraulic head prediction accuracy between the proposed method and DBPNN for 10, 20 and 50 observation points. (a), (b) RMSE errors between the predicted hydraulic heads using DBPNN model for 10, 20 and 50 observation points. (d), (e) and (f) RMSE errors between the predicted hydraulic heads using the proposed method for 10, 20 and 50 observation points.

## Summary

This chapter validates an AI-based methodology that combines analytical solutions with transfer learning, aiming to generate reliable groundwater flow estimates at the watershed scale, particularly under conditions of sparse groundwater flow observational data. The fundamental concept of this approach involves employing a pretraining model to capture the essential spatial and temporal distribution of groundwater within the watershed based on analytical solutions. Subsequently, this acquired physical knowledge is transferred through the application of transfer learning, facilitating accurate groundwater predictions in real-world scenarios characterized by limited data availability. A deep LSTM neural network is utilized to forecast hydrological variables such as groundwater observation levels and surface water levels. The predictions generated by the deep LSTM neural network serve as the input required for the transfer learning process, endowing the proposed transfer learning method with predictive capabilities.

A traditional DBPNN without the guidance of analytical model is applied as a baseline model to ensure a reliable conclusion. The results demonstrate the proposed method significantly improves the accuracy of the groundwater flow predictions by fusing the analytical knowledge with the neural network. For all test scenarios, the errors of the proposed method are much smaller than those of the DBPNN. Even for very sparse training data, the transfer learning model still performs satisfactorily. The computational load of the proposed method is much smaller than DBPNN. Prior knowledge provided by the analytical solution endows the neural network with more reasonable initial parameter values and constrains the search space during training. The performance of the proposed method and DBPNN model are all affected by the locations of observation points. However, with the same amount of observation points, the proposed method is more robust than the DBPNN model.

Transfer learning often benefits from similarities between source and target domain data, resulting in better transfer learning outcomes. Therefore, theoretically speaking, if the hydrological and hydrogeological characteristics of a new site closely resemble those of the original site, it is possible to fine-tune the pre-trained model of a specific site using the groundwater observation data from the new site. However, considering the rarity of watersheds with identical similar sizes, meteorological conditions, and hydrogeological conditions, It’s not recommended to use directly the transfer learning method proposed for predictions of other sites using the pre-trained model of a specific site. At the same time, it is worth emphasizing that using the transfer learning method for predictions of other sites using the pre-trained model of a specific site is not impossible. If suitable mathematical expressions can be found to describe the differences in hydrological and hydrogeological characteristics between the new site and the original site and incorporated into the loss function of transfer learning, this issue should be addressable. Some existing literature has attempted transfer learning for different-shaped study areas, but such research is still in its infancy and requires further exploration.

# Chapter 8 Conclusion and recommendations

## Conclusion

This thesis proposes a new framework that combines artificial intelligence and physics-based coupled models for simulating variations in surface water and groundwater and details the impact of multiple input variables on surface runoff prediction, heterogeneity of groundwater layers, and the utilization of deep learning methods to enhance the applicability of the proposed framework.

Chapter 4 presents a DL model for surface water runoff and shows that the selection of model inputs has a great influence on model accuracy. A deep RNN model with multiple meteorological data inputs achieves higher accuracy than rainfall data input for runoff forecasting. PCA method can be applied to improve the accuracy of the deep RNN model effectively as it can reflect core information by classifying the original data information into several comprehensive variables. The accuracy of the deep LSTMs model and the deep GRUs model is much the same, but the computational load of the deep GRUs model is lower, especially with high-dimension input.

Chapter 5 provides a semi-analytical solution for groundwater flow in riparian zone with layered structure and shows that the two-layer structure has a significant effect on the responses of groundwater flow to hydrological events. For recharge events when the upper layer is less permeable, lateral discharge to the river in this layer is impeded and more groundwater flows downward into the more permeable lower layer. In contrast, when the upper layer is more permeable, more groundwater flows laterally into the river and less downward into the less permeable lower layer. For a flood event when the upper layer is less permeable, river water infiltrates mostly into the more permeable lower layer during the initial time of the flood period and then flows upward into the upper layer, creating a vertical flow from the more permeable lower layer to the less permeable upper layer. The direction of the vertical flow is reversed during the recession period. However, this phenomenon is not evident when the upper layer is more permeable than the lower layer. The comparison of discharge for the equivalent hydraulic conductivity and heterogeneous hydraulic conductivity shows that the equivalent hydraulic conductivity method can lead to large errors in discharge. For the recharge event, the peak discharge simulated with the harmonic mean of hydraulic conductivities is reasonable, but the discharge is overestimated during the recession process. The peak discharge simulated with the arithmetic mean of hydraulic conductivities would underestimate the peak discharge. For the flood event, the discharge simulated with the equivalent hydraulic conductivity method peaks earlier than it should be. Moreover, the interaction between river and aquifer simulated with the harmonic mean of hydraulic conductivities is overestimated, and that with the arithmetic mean of hydraulic conductivities is underestimated. The present solution is applied to model the observed hydraulic head and discharge in White Clay Creek within the Christina River Basin Critical Zone Observatory in Southeastern Pennsylvania, and the estimated values of the aquifer parameters are reasonable. Riparian flow controls the active chemical and biological processes in riparian zone, the present solution is a convenient calculation method for riparian flow in two-layer aquifer and will provide a valuable and solid foundation to clarify chemical and biological reactions in riparian zones and alluvial aquifers.

Chapter 6 shows that the transfer learning method significantly improves the accuracy of the hydraulic head predictions by fusing the analytical knowledge with the neural network. An analytical solution for unconfined groundwater flow in horizonal section is provided for test. For all test scenarios, the errors of the transfer learning model are much smaller than those of the BPNN. Even for very sparse training data, the transfer learning model still performs satisfactorily. The hydraulic conductivity mainly affects the parameters of the shallow layers in the neural network, making it possible to employ the transfer learning model to predict groundwater flow in an aquifer with a more complicated heterogeneous field. The accuracy of the transfer learning model depends on the correlation length of the heterogeneously hydraulic conductivity field. The transfer learning model performs better for a small correlation length. The performance of the transfer learning model is affected by the recharge uncertainty. With the same recharge uncertainty, the transfer learning model is more robust than the DBPNN model. Moreover, under heterogeneous conditions, the proposed transfer learning method achieves higher accuracy compared to directly using analytical solutions, even with only 10 observation points, MSE of the transfer learning method is an order of magnitude smaller than that of the analytical solution.

Chapter 7 provides an analytical solution for unsaturated-saturated groundwater flow in vertical section and applies the transfer learning model in catchment scale. It is proved that the deep transfer learning method proposed in Chapter 6 is still working on the watershed scale. The deep transfer learning method can significantly improve the accuracy of the hydraulic head predictions, even for very sparse training data. Moreover, the computational load of the proposed method is much smaller than the baseline model. It also should be noted that the three different analytical solutions provided in Chapters 5, 6, and 7, as well as the analytical solutions provided by previous studies, can all be utilized to generate source domain data and applied to the proposed transfer learning framework. Given the similarity between the source domain and target domain data in transfer learning, the better the transfer learning results. Analytical solutions can be selected based on site characteristics and research focus. For example, if considering unsaturated flow, the analytical solution provided in Chapter 7 of this thesis can be adopted.

## Flowchart of surface water and groundwater coupled simulation by the proposed method

The Flowchart for coupled surface water-groundwater simulation using the methods provided in this thesis is shown in Figure 8.1. Similar to traditional methods, it begins with site investigation for collecting hydrological data, and hydrogeological information. Hydrological data mainly include rainfall recharge data and river water level fluctuation data for groundwater. Hydrogeological information comprises groundwater observation data, lithological data, and hydrogeological parameters estimated based on lithological data.

If only regression of groundwater flow during the observation period is required, the process shown by the black line should be followed. Analytical solution models are established using hydrological data and estimated hydrogeological parameters to provide source domain data for subsequent transfer learning. It should be noted that the analytical solutions provided in this thesis or other analytical solutions can be selected based on site characteristics and research focus. Finally, groundwater observation data are used as target domain data for transfer learning to interpolate the groundwater flow field in the watershed.

If prediction of both surface water and groundwater in the watershed is required, the process shown by the orange line should be followed. A deep RNN model is used to predict hydrological data and groundwater head from observation data. Subsequently, analytical solution models are established using the predicted hydrological data and estimated hydrogeological parameters to generate source domain data. Finally, predicted groundwater observation data are used as target domain data for transfer learning to predict the future groundwater flow field in the watershed.

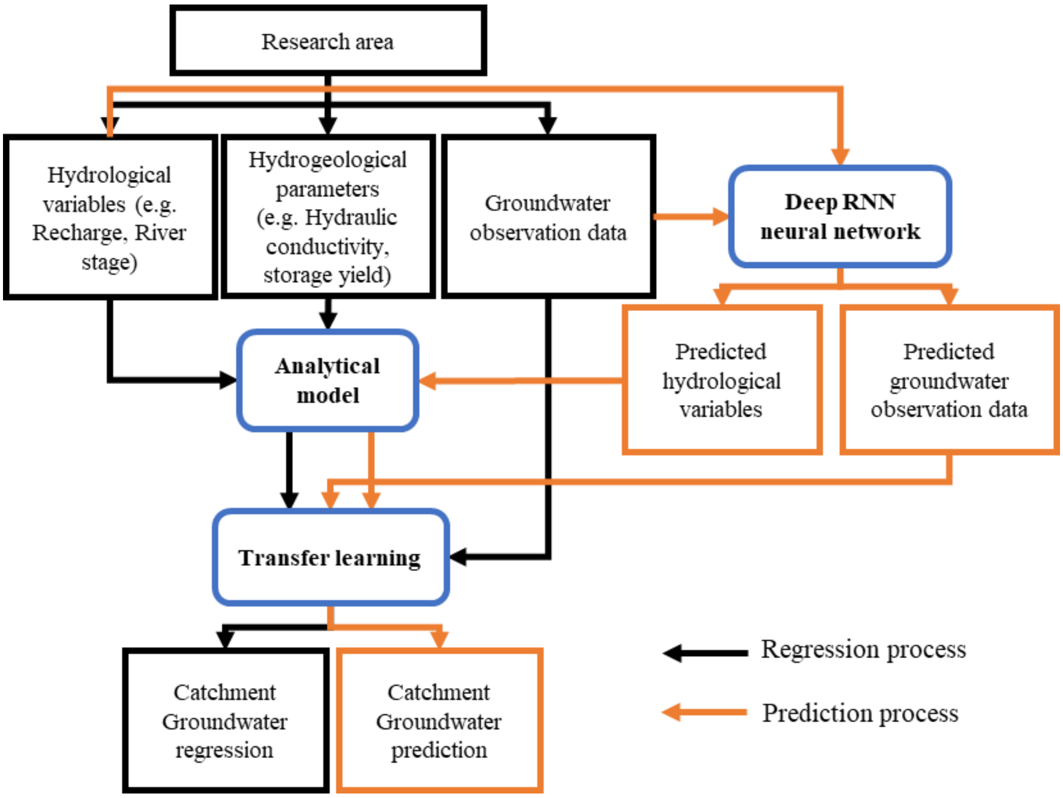


Figure 8.1 Flowchart of surface water and groundwater coupled simulation by the proposed method

## Recommendation for future work

The thesis proposes a new framework that combines artificial intelligence and physics-based coupled models for simulating variations in surface water and groundwater, providing a foundation for integrated water resource management. More work could be done in the future:

1. Deep neural networks are employed to predict surface water flow variations, but the uncertainty problems are not considered. Training data inevitably includes uncertainty (data uncertainty) due to observation errors, and the deep neural network model itself also contains uncertainty due to the incomplete understanding of the network and the use of random initializations during its establishment. To overcome these limitations, providing uncertainty estimates is crucial to either disregard uncertain predictions or convey them to human experts. The provision of uncertainty estimates is particularly important in high-risk domains, such as safety decision-making.
2. Analytical solutions are used to describe groundwater movement, which involved significant simplifications in the representation of aquifers and groundwater flow processes. For instance, in Chapter 5, the upper boundary condition is linearized, and in Chapter 7, the unsaturated flow is linearized. While these assumptions facilitated the derivation of analytical solutions, they led to inaccuracies in predicting results under heavy rainfall conditions. Future work may involve considering more realistic assumptions and derivations for boundary conditions to improve the accuracy of analytical solutions.
3. In the proposed framework of coupling surface water and groundwater, the boundary coupling method is employed by considering river water levels as groundwater boundary conditions. However, due to the significant flow velocity in surface water and the complex shapes of riverbeds, the interaction interface between surface water and groundwater is intricate. A reasonable consideration of

the interface interaction between surface water and groundwater remains a feasible avenue for future research.

4. This study introduces, for the first time, the utilization of analytical solutions as the source dataset for predicting and regressing groundwater heads through transfer learning methods. In Chapters 6 and 7, to simplify the validation process, a known quantity for recharge is assumed. In practical research, determining the exact amount of recharge is challenging, and the quantification of uncertainty stemming from unknown recharge remains a critical area requiring further investigation. In Chapters 6 and 7, proposed deep transfer learning framework involved fine-tuning the model solely using observational data, without considering specific characteristics of the actual study area, such as its shape and topography. Previous studies have shown that transfer learning with deep operator networks can transfer knowledge from simple-shaped source domains to complex-shaped target domain data. However, such research has yet to be applied in the hydrological field.
5. In Chapter 7, the use of transfer learning to incorporate prior physical information with observational data to predict groundwater heads in the study area is demonstrated. This approach can also be extended to address water environment problems, such as the migration of compounds, especially organic compounds, in surface water or groundwater, which are influenced by processes such as adsorption and dissolution, making their quantification challenging. Utilizing convection-dispersion equations as prior physical knowledge and combining them with observational data can significantly simplify this problem.
6. In recent years, Physics-Informed Neural Networks (PINN) have shown better predictability, reliability, and generalizability. However, the extensive time required to train PINNs has often been criticized. In Chapter 7, it is demonstrated that deep transfer learning can effectively reduce the computational burden. Combining transfer learning with PINNs may promote their application. Initially, it is necessary to gather existing deep-learning models to build a basic database.

Subsequently, using methods like Generative Adversarial Networks (GANs), models that are more closely related to the target problem can be selected from the basic database. Lastly, transfer learning methods can be employed to retrain the selected models to address the target problem.

# Support Information

## S1 Support Information for chapter4

### S1.1. Prediction results for Muskegon River and Pearl River

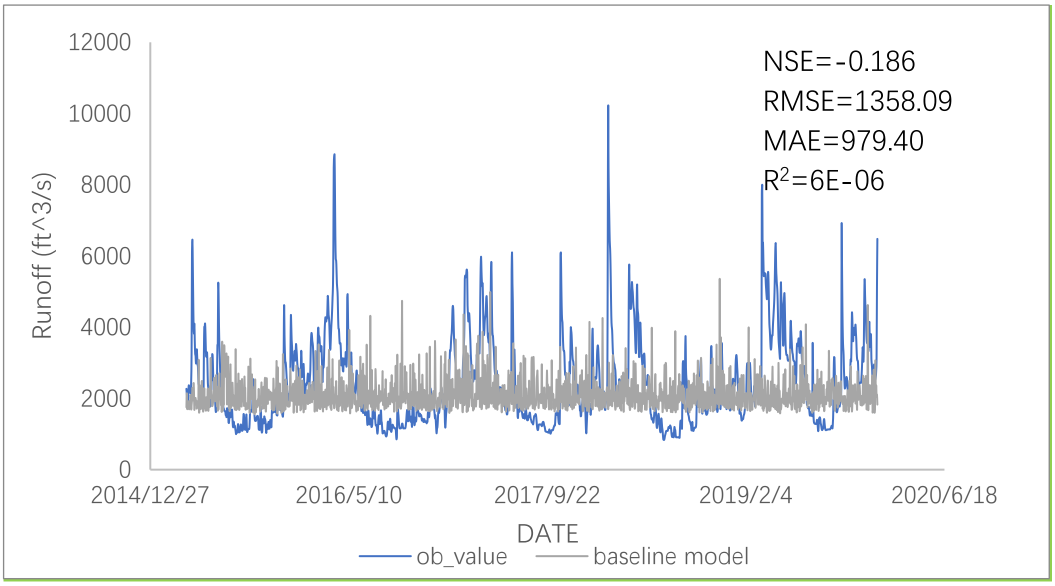


**Figure S 1** Baseline model: Ridge regression based on rainfall data in Muskegon

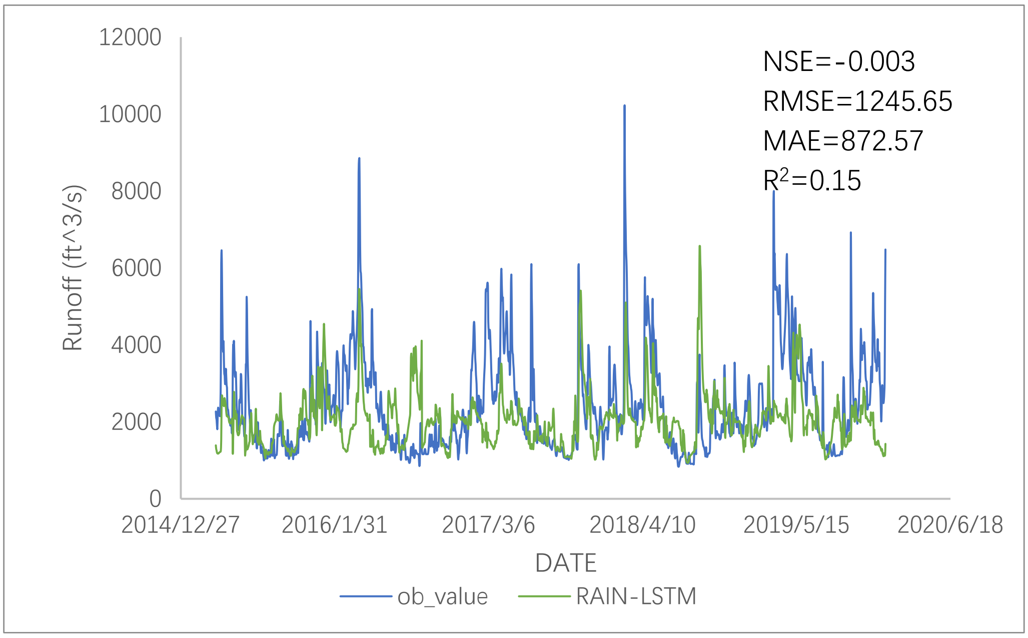

**Figure S 2** Scenario 1: LSTM neural network based on rainfall data in Muskegon river

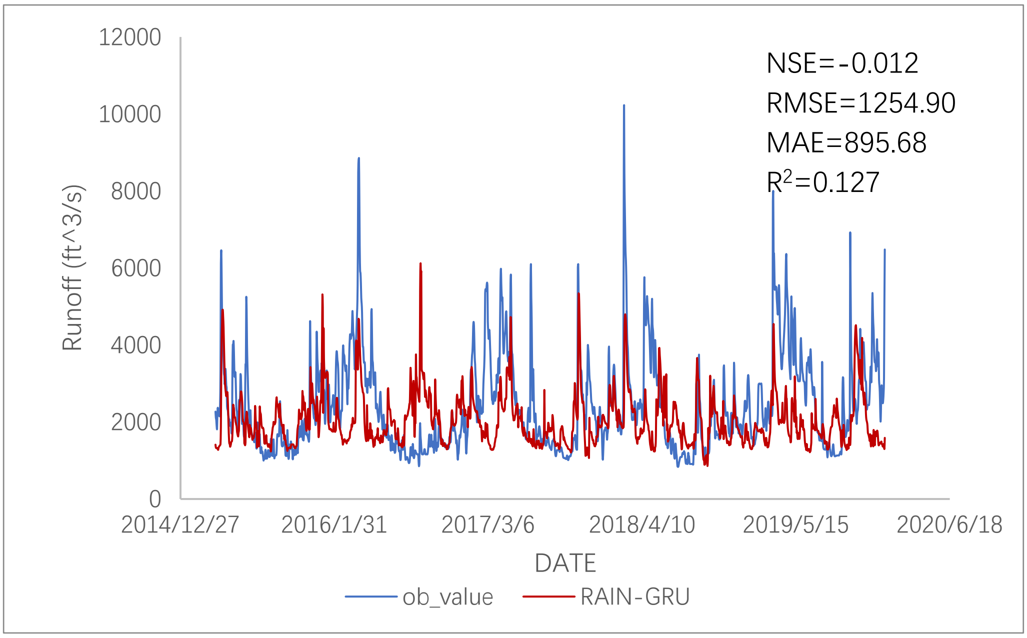


**Figure S 3** Scenario 2: GRU neural network based on rainfall data in Muskegon river

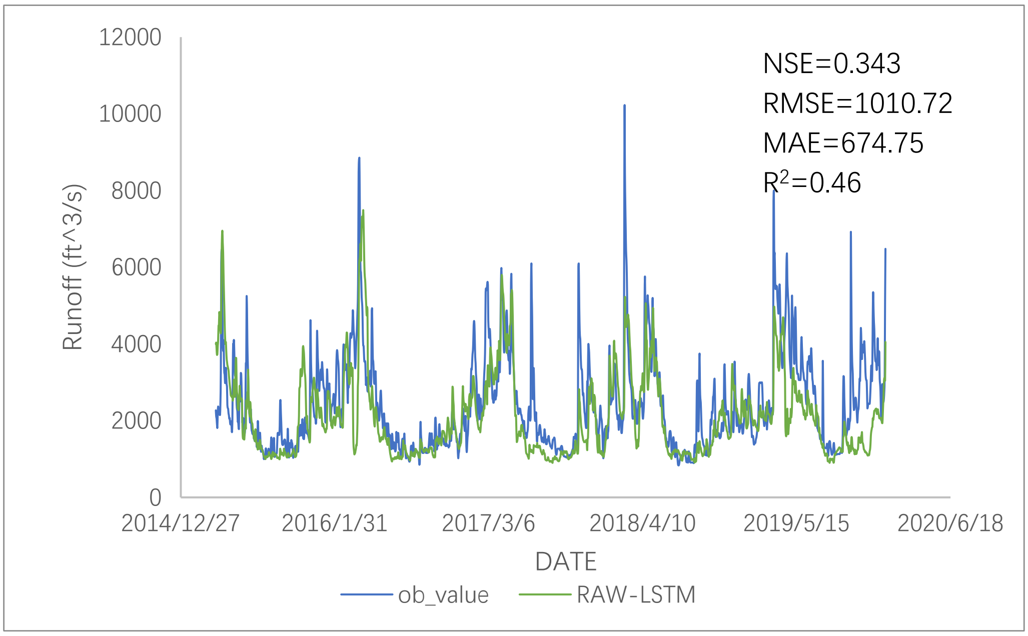


**Figure S 4** Scenario 3: LSTM neural network based on multiple meteorological data in Muskegon river

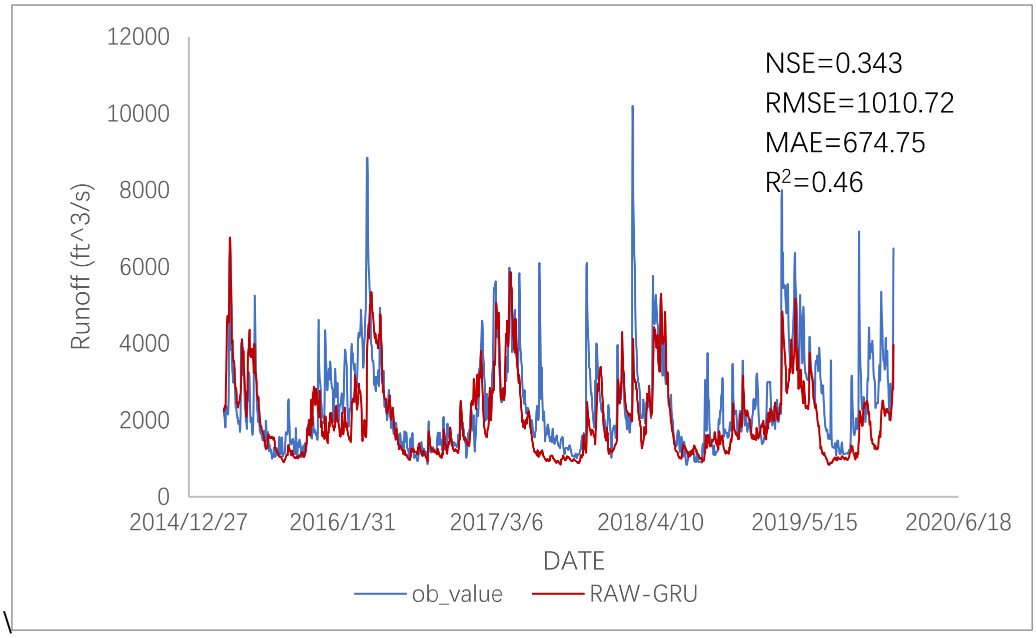


**Figure S 5** Scenario 4: GRU neural network based on multiple meteorological data in Muskegon river

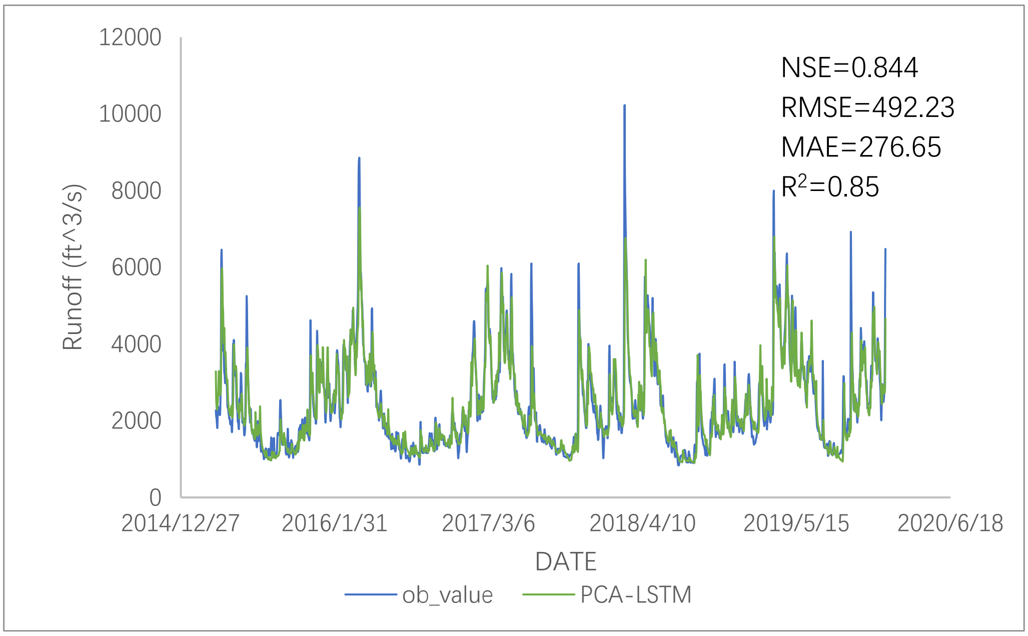


**Figure S 6** Scenario 5: LSTM neural network based on multiple meteorological data with PCA method in Muskegon river

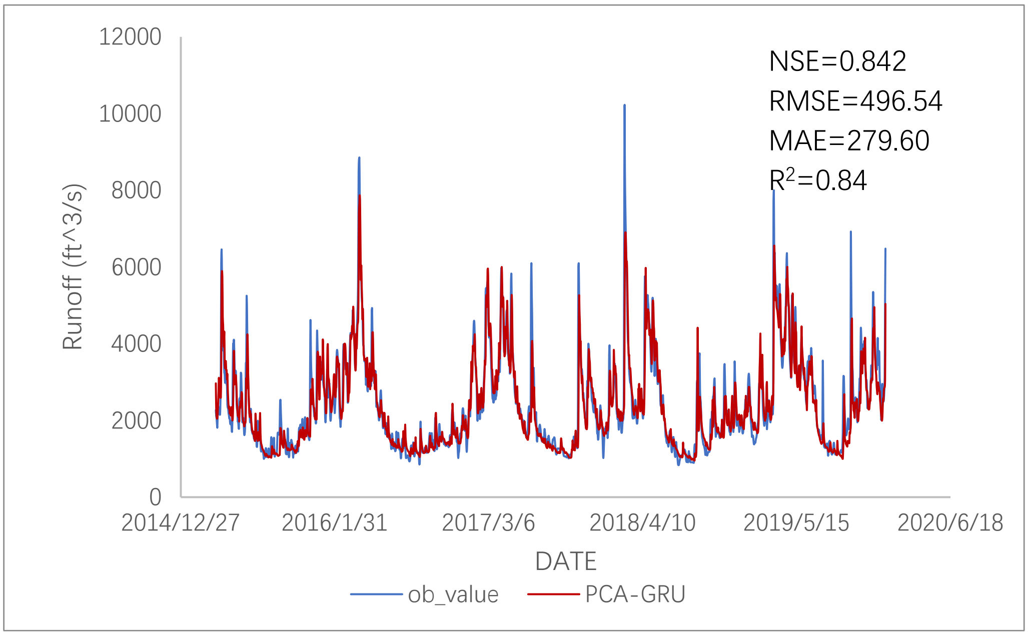


**Figure S 7** Scenario 6: GRU neural network based on multiple meteorological data with PCA method in Muskegon river

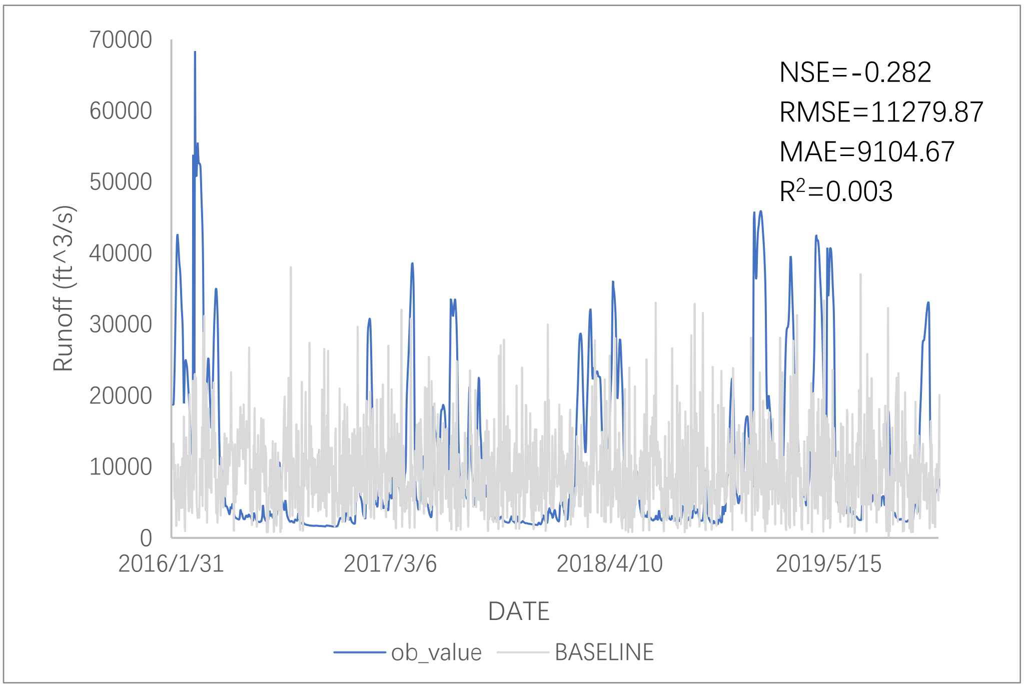


**Figure S 8** Baseline model: Ridge regression based on rainfall data in Pearl river

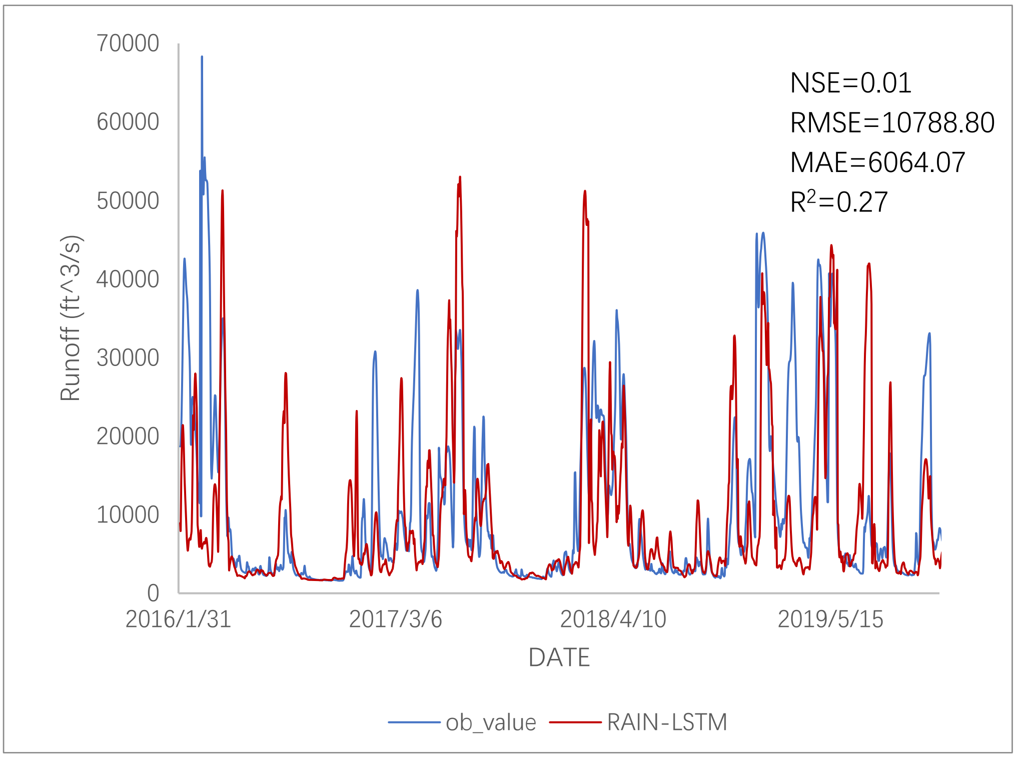


**Figure S 9** Scenario 1: LSTM neural network based on rainfall data in Pearl river

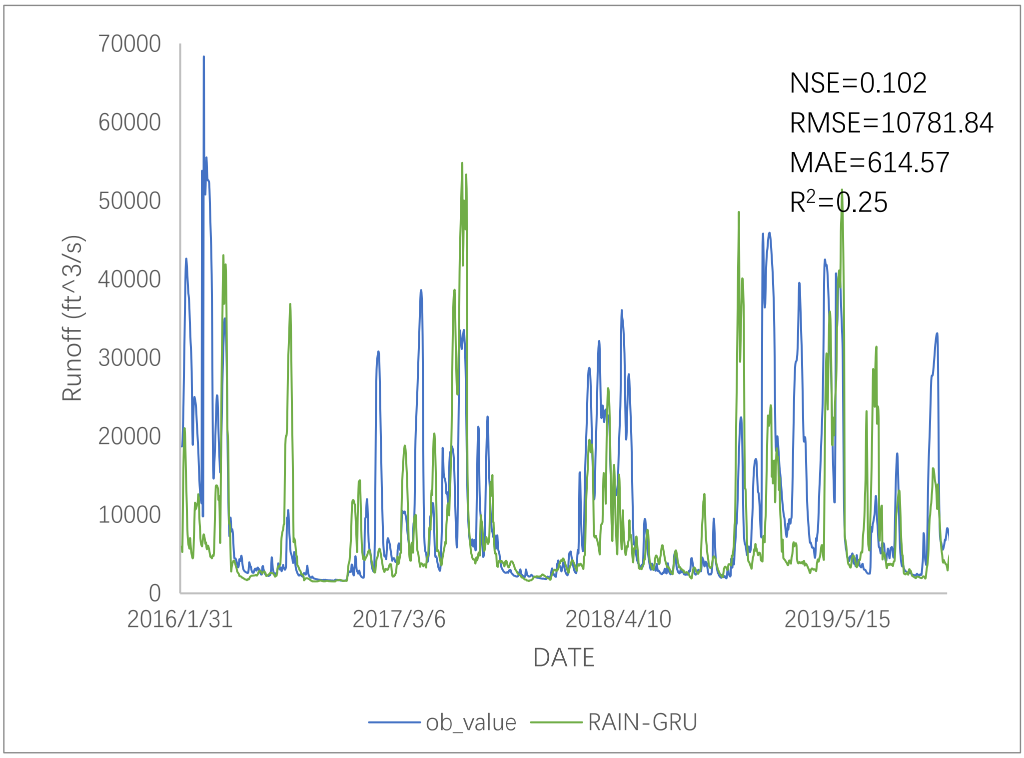


**Figure S 10** Scenario 2: GRU neural network based on rainfall data in Pearl river

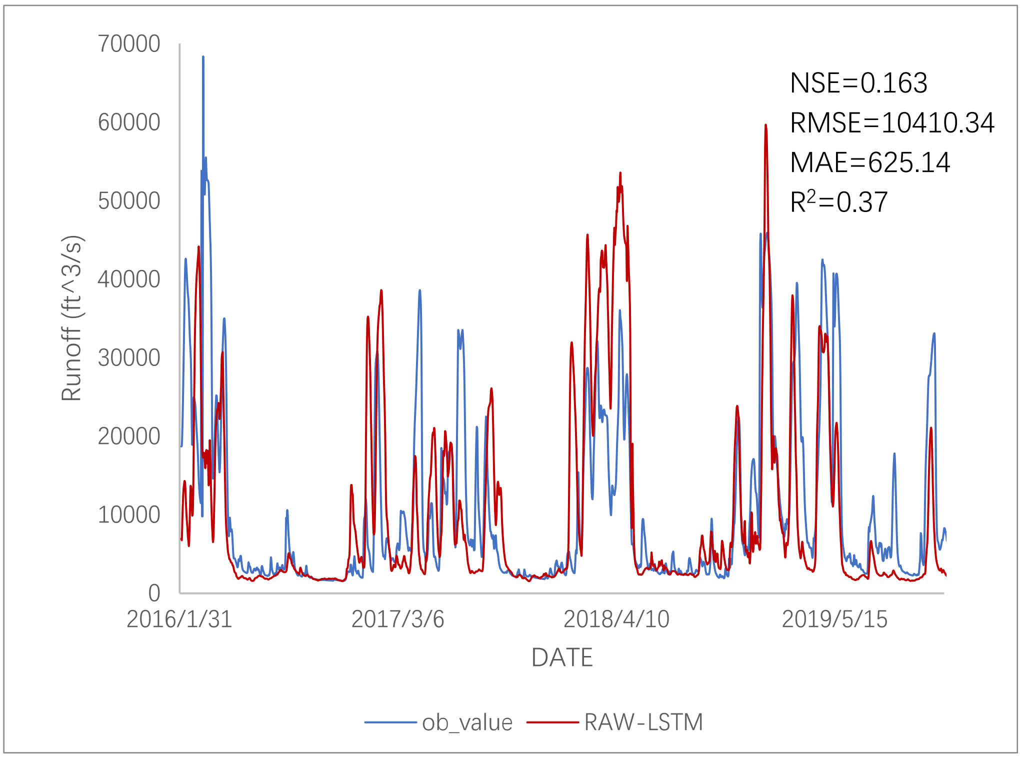


3587 **Figure S 11** Scenario 3: LSTM neural network based on multiple meteorological data in Pearl river

3588

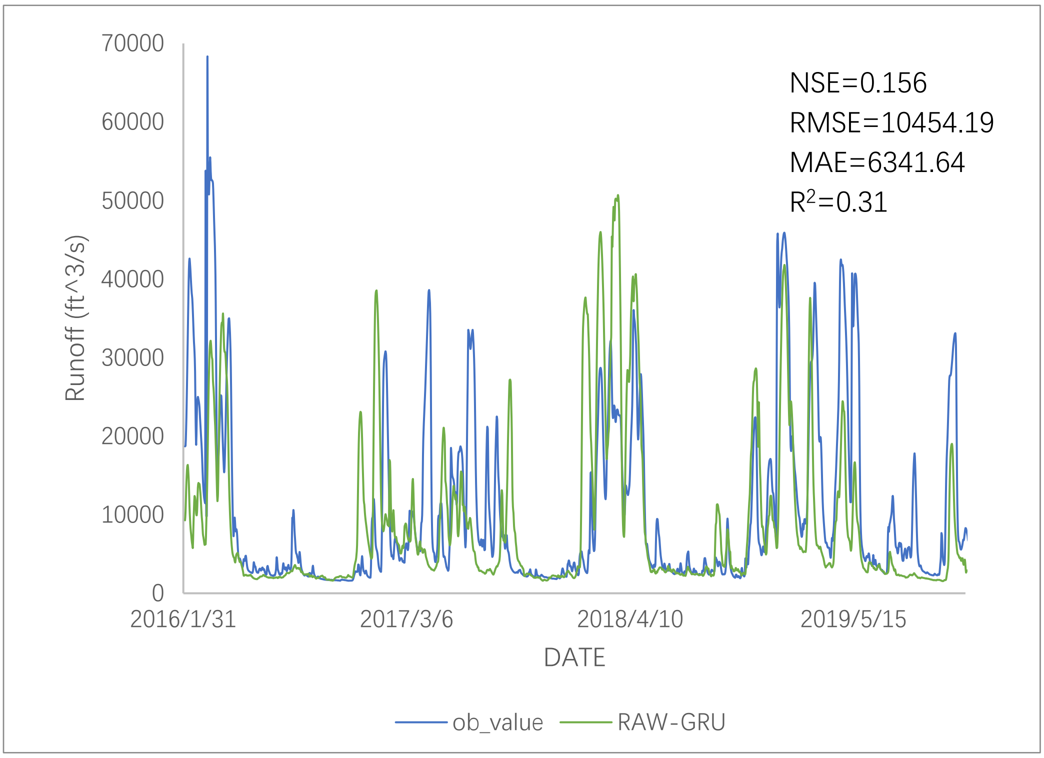


**Figure S 12** Scenario 4: GRU neural network based on multiple meteorological data in Pearl river

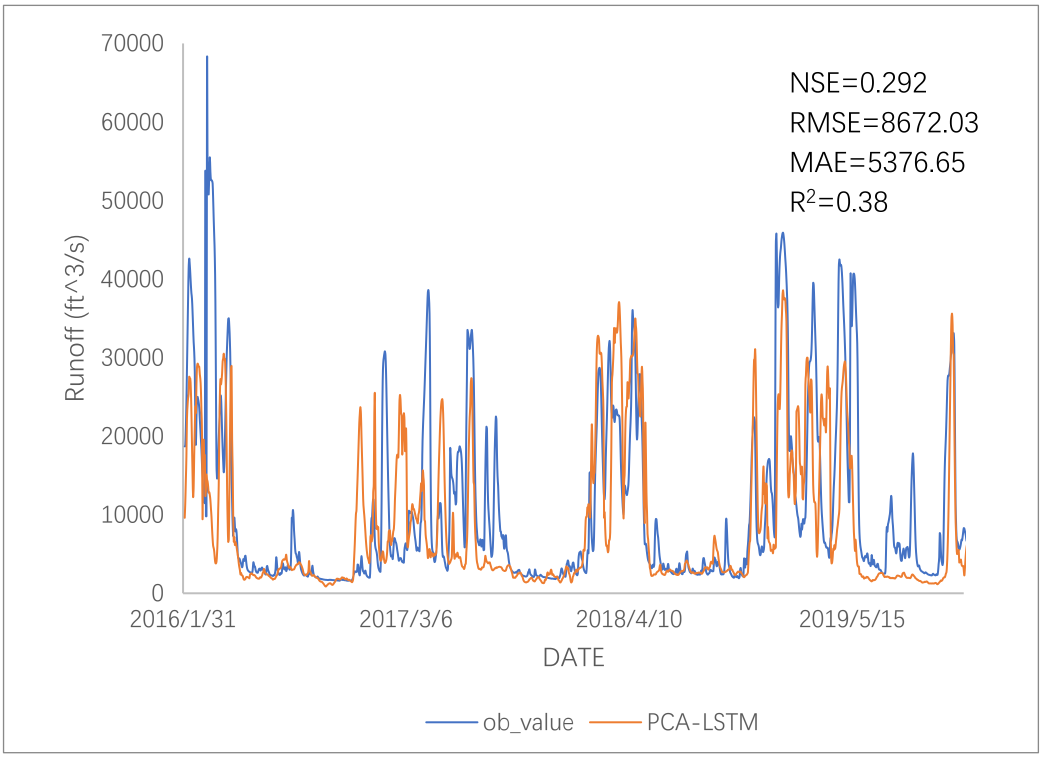


**Figure S 13** Scenario 5: LSTM neural network based on multiple meteorological data with PCA method in Pearl river

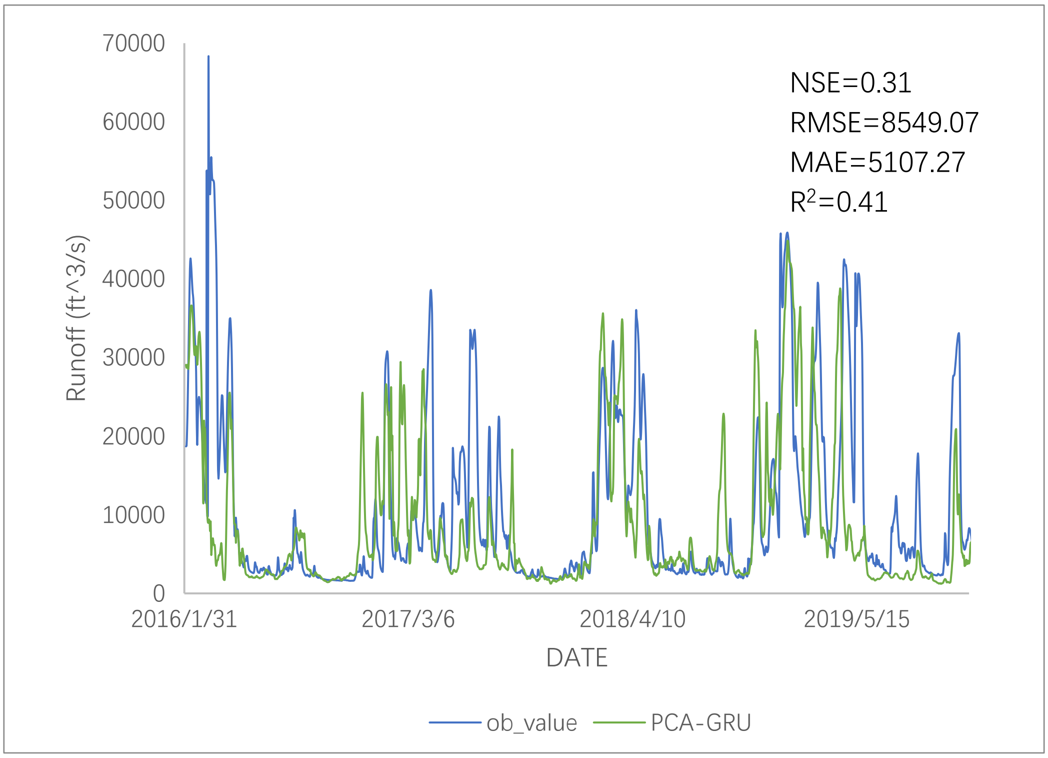


**Figure S 14** Scenario 6: GRU neural network based on multiple meteorological data with PCA method in Pearl river

**S1.2. Discussion on data cleanse and outlier value**

Outliers are data objects that significantly differ from other data. In hydrological data, outliers can occur due to extreme events, human intervention, and equipment malfunction, among other reasons. Due to the complex nature of outlier occurrence, outliers are typically removed during the machine learning process to ensure result accuracy. According to Chebyshev's inequality, the $u \pm 6\sigma$ range contains 97% of the data for any distribution shape. Therefore, this study uses a $6\sigma$ range to process the data. Equation 4.1 is used for data standardization, and the statistical results are shown in the table below. If the absolute values of the maximum and minimum values of each indicator exceed 6, they are considered outliers. It is observed that indicators such as MAXWIND and PRE have extreme values considered as outliers. Statistical analysis of outliers reveals that only about 1% of the total number of outliers are found in the MAXWIND indicator for the Muskegon River, while outliers in other indicators account for less than 0.5% of the total. Therefore, the $6\sigma$ range is considered reasonable.

It should be noted that due to the presence of hydraulic facilities such as dams in both study areas, it is difficult to determine whether outliers in the data are caused by extreme events. Furthermore, in this study, outliers in runoff data account for 0.12% and 0.03% of the total, and since the number of outlier samples is small, their impact on results is likely minimal even if not removed.

Under climate change conditions, extreme hydrological events occur frequently, making predictions of extreme hydrological events crucial. There is still significant potential in using machine learning for extreme hydrological event forecasting. Frame et al. (2022) found that data-driven models outperformed baseline models in predicting peak flow under almost all conditions. Building upon this study, predicting extreme hydrological events can involve extracting information on extreme events using indicators such as return periods of peak annual flows. Compared to this study, predicting extreme hydrological events would first require using indicators such as return periods of peak annual flows to extract information on extreme events and then training the models used in this study. However, due to the scarcity of data on extreme events, related research still faces significant challenges.

Table S 1 statistical results of outlier values in Muskegon River and Pearl River

| Muskegon River | | | | Pearl River | | | |
|---|---|---|---|---|---|---|---|
| | max | min | The proportion of outlier values to the total number | | max | min | The proportion of outlier values to the total number |
| MAXTEM | 3.56 | -2.89 | 0.00% | MAXTEM | 1.97 | -3.39 | 0.00% |
| MEANTEM | 2.16 | -3.02 | 0.00% | MEANTEM | 1.72 | -3.25 | 0.00% |
| MINTEM | 2.22 | -3.46 | 0.00% | MINTEM | 2.03 | -3.47 | 0.00% |
| MAXDEW | 2.09 | -3.05 | 0.00% | MAXDEW | 1.49 | -3.61 | 0.00% |
| MEANDEW | 1.94 | -3.12 | 0.00% | MEANDEW | 1.42 | -3.24 | 0.00% |
| MINDEW | 2.20 | -3.21 | 0.00% | MINDEW | 1.32 | -2.27 | 0.00% |
| MAXHUM | 1.17 | -9.45 | 0.02% | MAXHUM | 1.07 | -8.58 | 0.07% |
| MEANHUM | 2.49 | -6.46 | 0.02% | MEANHYM | 2.32 | -4.26 | 0.00% |
| MINHUM | 3.19 | -3.73 | 0.00% | MINHUM | 3.12 | -2.92 | 0.00% |
| MAXSEA | 6.40 | -5.49 | 0.01% | MAXWIND | 9.31 | -2.69 | 0.01% |
| MEANSEA | 3.76 | -5.52 | 0.00% | MEANWIND | 5.00 | -1.91 | 0.00% |
| MINSEA | 3.47 | -5.74 | 0.00% | MAXSEA | 4.41 | -3.74 | 0.00% |
| MAXWIND | 7.45 | -14.63 | 1.04% | MEANSEA | 3.78 | -34.67 | 0.08% |
| MEANWIND | 3.08 | -3.54 | 0.00% | MINSEA | 0.60 | -25.52 | 0.15% |
| MINVIS | 2.51 | -1.37 | 0.00% | PRE | 15.08 | -0.29 | 0.50% |
| MAXVIS | 5.05 | -2.06 | 0.00% | RUNOFF | 10.13 | -0.73 | 0.03% |
| MEANVIS | 6.07 | -2.01 | 0.01% | | | | |
| PRE | 16.38 | -0.38 | 0.36% | | | | |
| RUNOFF | 11.37 | -1.19 | 0.12% | | | | |

### S1.3. Discussion on hyperparameters in neural network

This section discusses the determination methods and existing issues of two hyperparameters, the number of hidden layers and Past-history, in RNNs models.

Determining the number of hidden layers in neural networks is an important yet sometimes challenging task due to the black-box nature of neural networks, which makes the interpretation of hyperparameters difficult. It is generally believed that for simple problems, fewer hidden layers may be sufficient, while for complex problems, multiple hidden layers may be needed. Experimental observations have also revealed the problem of degradation in neural networks as the network depth increases. Due to the difficulty in obtaining hydrological data at the watershed scale, RNN models applied in hydrology often have a limited number of hidden layers. For example, Jeong and Park (2019) utilized data from 10 years of groundwater levels at the Pohang Gibuk monitoring well to establish LSTM and GRU neural networks with two hidden layers. Hao et al. (2024) employed a LSTM neural network with three hidden layers to describe the glacio-hydrological process in the Urumqi Glacier. The study most closely related to this is that of Frame et al. (2022), who developed rainfall-runoff models for 241 watersheds using LSTM, which included two LSTM hidden layers. Following this paper, our study also sets the number of hidden layers in the neural network to two. It is worth noting that, since our study was conducted earlier, it did not incorporate emerging technologies. For instance, the advent of residual neural networks (He et al., 2016) allows related research to use as many hidden layers as possible without worrying about the degradation problem in neural networks.

In the context of RNNs, "Past-history" refers to the input sequence preceding the current time step. In the early studies applying RNNs in hydrology, Past-history was considered as a hyperparameter (Jeong and Park, 2019). In recent years, some scholars have regarded this parameter as reflecting the travel time from rainfall to the observation point of runoff (Hao et al., 2024). In this study, it is treated as a hyperparameter and calibrated using a trial-and-error method, setting it to 30. Taking multiple meteorological data in the Pearl River as an example, Figure S 15 demonstrates the prediction accuracy of the model using different Past-history values (measured by $R^2$). It can be observed that when Past-history is less than 20, the prediction accuracy of the model significantly increases with an increase in Past-history. When Past-history ranges from 20 to 40, the prediction accuracy of the model stabilizes, with some fluctuations. The appropriate Past-history for this study is considered to be between 20 and 40, with the average value of 30 being chosen as the model parameter. The parameters for the Muskegon River are also determined using this method. It is important to note that the focus of this study is to investigate the impact of different inputs on runoff prediction. From a controlled variables perspective, the comparison of results corresponding to different inputs is made under the same model parameters. Although the aforementioned parameter calibration method is relatively crude, it does not affect the main conclusions of this study.

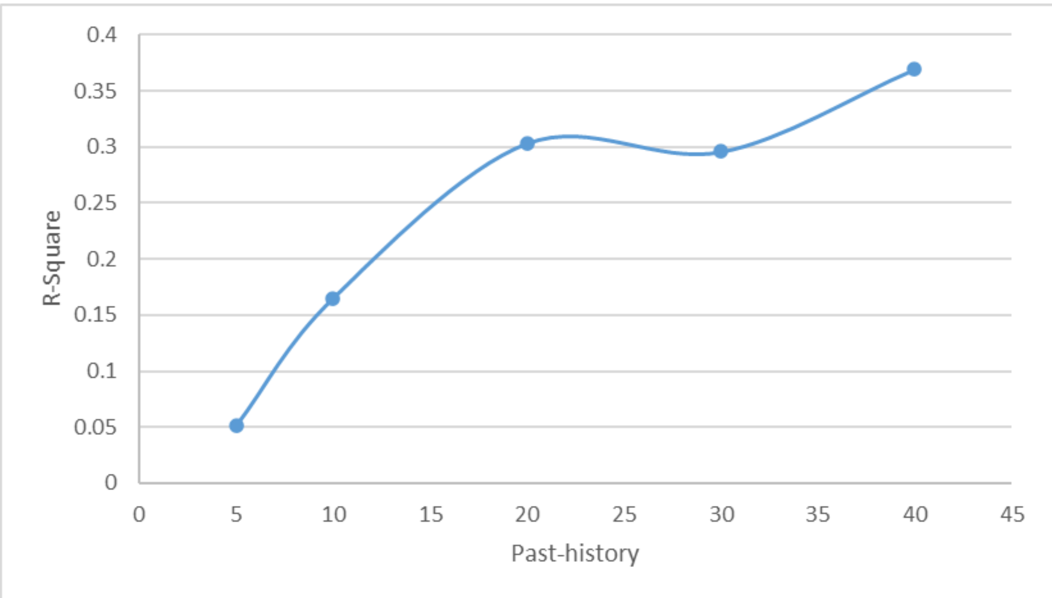


Figure S 15 Relationship between Past-history and prediction accuracy

## S2 Support Information for chapter 5

### S2.1. Dimensionless transform

For the purpose of mathematical convenience, the following dimensionless variables are defined:

$$h_{1D}=\frac{h_1}{h_0},\ h_{2D}=\frac{h_2}{h_0},\ x_D=\frac{x}{L},\ z_D=\frac{z}{L},\ t_D=\frac{K_x t}{S_S L^2},\ R_K=\frac{K_{x2}}{K_{x1}},\ R_S=\sqrt{\frac{S_{s2}}{S_{s1}}},\ K_x=\sqrt{K_{x1}K_{x2}},\ S_S=\sqrt{S_{s1}S_{S2}},\ K_{1D}=\frac{K_{z1}}{K_{x1}},\ K_{2D}=\frac{K_{z2}}{K_{x2}},\ h_{bD}=\frac{h_b}{h_0},\ W_D=\frac{WL}{K_x H_0},\ S_{yD}=\frac{S_y}{S_S L},\ R_v=\frac{K_{1D}}{K_{2D}R_K}$$

where the subscript *D* denotes the dimensionless terms hereinafter. Substituting the above dimensionless variables into Equation S 1-Equation S 9, one obtains the following dimensionless forms of the governing equations for the hyporheic zone:

$$\frac{\sqrt{R_K}}{R_S}\frac{\partial h_{1D}}{\partial t_D}=K_{1D}\frac{\partial^2 h_{1D}}{\partial z_D^2}+\frac{\partial^2 h_{1D}}{\partial x_D^2},\ 0\le z_D\le B_{1D},\ 0\le x_D\le 1 \qquad \text{Equation S 1}$$

$$\frac{R_S}{\sqrt{R_K}}\frac{\partial h_{2D}}{\partial t_D}=K_{2D}\frac{\partial^2 h_{2D}}{\partial z_D^2}+\frac{\partial^2 h_{2D}}{\partial x_D^2},\ -B_{2D}\le z_D\le 0,\ 0\le x_D\le 1 \qquad \text{Equation S 2}$$

Initial and boundary condition:

$$h_{1\mathrm{D}}(x_D,z_D,t_D)=h_{2\mathrm{D}}(x_D,z_D,t_D)=1,\ t_D=0 \qquad \text{Equation S 3}$$

$$h_{1\mathrm{D}}(x_D,z_D,t_D)=h_{2\mathrm{D}}(x_D,z_D,t_D)=h_{bD}(t_D),x_D=0 \qquad \text{Equation S 4}$$

$$\frac{\partial h_{1\mathrm{D}}}{\partial x_D}(x_D,z_D,t_D)=\frac{\partial h_{1\mathrm{D}}}{\partial x_D}(x_D,z_D,t_D)=0,x_D=1 \qquad \text{Equation S 5}$$

$$\frac{K_{1D}}{\sqrt{R_K}}\frac{\partial h_{1D}}{\partial z_D}=-S_{yD}\frac{\partial h_{1D}}{\partial t_D}+W_D(t_D),z_D=B_{1D} \qquad \text{Equation S 6}$$

$$\frac{\partial h_{2\mathrm{D}}}{\partial z_D}(x_D,z_D,t_D)=0,z_D=-B_{2D} \qquad \text{Equation S 7}$$

and at the interface:

$$h_{1\mathrm{D}}(x_D,z_D,t_D)=h_{2\mathrm{D}}(x_D,z_D,t_D),z_D=0 \qquad \text{Equation S 8}$$

$$R_v\frac{\partial h_{1D}}{\partial z_D}(x_D,z_D,t_D)=\frac{\partial h_{2D}}{\partial z_D}(x_D,z_D,t_D),z_D=0 \qquad \text{Equation S 9}$$

### S2.2 Homogenization

For the purpose of homogenization of initial conditions, it is assumed that $s_{1D} = h_{1D} - 1$, $s_{2D} = h_{2D} - 1$ and $s_{bD}(t_D) = h_{bD}(t_D) - 1$. One can obtain the following governing equations:

$$\frac{\sqrt{R_K}}{R_S}\frac{\partial s_{1D}}{\partial t_D} = K_{1D}\frac{\partial^2 s_{1D}}{\partial z_D^2} + \frac{\partial^2 s_{1D}}{\partial x_D^2},\ 0 \le z_D \le B_{1D},\ 0 \le x_D \le 1 \qquad \text{Equation S 10}$$

$$\frac{R_S}{\sqrt{R_K}}\frac{\partial s_{2D}}{\partial t_D} = K_{2D}\frac{\partial^2 s_{2D}}{\partial z_D^2} + \frac{\partial^2 s_{2D}}{\partial x_D^2},\ -B_{2D} \le z_D \le 0,\ 0 \le x_D \le 1 \qquad \text{Equation S 11}$$

Initial and boundary condition:

$$s_{1D}(x_D, z_D, t_D) = s_{2D}(x_D, z_D, t_D) = 0,\ t_D = 0, \qquad \text{Equation S 12}$$

$$s_{1D}(x_D, z_D, t_D) = s_{2D}(x_D, z_D, t_D) = s_{bD}(t_D), x_D = 0 \qquad \text{Equation S 13}$$

$$\frac{\partial s_{1D}}{\partial x_D}(x_D, z_D, t_D) = \frac{\partial s_{1D}}{\partial x_D}(x_D, z_D, t_D) = 0,\ x_D = 1 \qquad \text{Equation S 14}$$

$$\frac{K_{1D}}{\sqrt{R_K}}\frac{\partial s_{1D}}{\partial z_D}(x_D, z_D, t_D) = -S_{yD}\frac{\partial s_{1D}}{\partial t_D} + W_D(t_D),\ z_D = B_{1D} \qquad \text{Equation S 15}$$

$$\frac{\partial s_{2D}}{\partial z_D}(x_D, z_D, t_D) = 0, z_D = -B_{2D} \qquad \text{Equation S 16}$$

and the interface condition:

$$s_{1\mathrm{D}}(x_D, z_D, t_D) = s_{2\mathrm{D}}(x_D, z_D, t_D), z_D = 0 \qquad \text{Equation S 17}$$

$$R_v\frac{\partial s_{1D}}{\partial z_D}(x_D, z_D, t_D) = \frac{\partial s_{2D}}{\partial z_D}(x_D, z_D, t_D),\ z_D = 0 \qquad \text{Equation S 18}$$

### S2.3. Laplace domain solution of the saturated zone

The Laplace transformation of Equation S 10 and Equation S 11 are written as:

$$\frac{\sqrt{R_K}}{R_S} p\bar{s}_{1D} = K_{1D}\frac{\partial^2 \bar{s}_{1D}}{\partial z_D^2} + \frac{\partial^2 \bar{s}_{1D}}{\partial x_D^2}, 0 \le z_D \le B_{1D},\ 0 \le x_D \le 1 \qquad \text{Equation S 19}$$

$$\frac{R_S}{\sqrt{R_K}} p\bar{s}_{2D} = K_{2D}\frac{\partial^2 \bar{s}_{2D}}{\partial z_D^2} + \frac{\partial^2 \bar{s}_{2D}}{\partial x_D^2}, -B_{2D} \le z_D \le 0,\ 0 \le x_D \le 1 \qquad \text{Equation S 20}$$

with boundary conditions:

$$\bar{s}_{1D}(x_D, z_D, p) = \bar{s}_{2D}(x_D, z_D, p) = \bar{s}_{bD}(p), x_D = 0 \qquad \text{Equation S 21}$$

$$\frac{\partial \bar{s}_{1D}}{\partial x_D}(x_D, z_D, p) = \frac{\partial \bar{s}_{2D}}{\partial x_D}(x_D, z_D, p) = 0, x_D = 1 \qquad \text{Equation S 22}$$

$$\frac{K_{1D}}{\sqrt{R_K}}\frac{\partial \bar{s}_{1D}}{\partial z_D}(x_D, z_D, p) = -S_{yD}p\bar{s}_{1D} + \bar{W}_D(p), z_D = B_{1D} \qquad \text{Equation S 23}$$

$$\frac{\partial \bar{s}_{2D}}{\partial z_D}(x_D, z_D, p) = 0, z_D = -B_{2D} \qquad \text{Equation S 24}$$

Interface:

$$\bar{s}_{1D}(x_D, z_D, p) = \bar{s}_{2D}(x_D, z_D, p), z_D = 0 \qquad \text{Equation S 25}$$

$$R_v\frac{\partial \bar{s}_{1D}}{\partial z_D}(x_D, z_D, p) = \frac{\partial \bar{s}_{2D}}{\partial z_D}(x_D, z_D, p), z_D = 0 \qquad \text{Equation S 26}$$

where $p$ is the Laplace transform parameter; and the overbar indicates a variable in the Laplace domain hereinafter. In order to solve Equation S 19 and Equation S 20 using the integral transform method, the boundary condition Equation S 21 is homogenized by adopting the following variable substitution:

$$\bar{s}_{1D}(x_D, z_D, p) = \mathcal{H}_1(x_D, z_D, p) + \bar{s}_{bD}(p) \qquad \text{Equation S 27}$$

$$\bar{s}_{2D}(x_D, z_D, p) = \mathcal{H}_2(x_D, z_D, p) + \bar{s}_{bD}(p) \qquad \text{Equation S 28}$$

Then, Equation S 19-Equation S 26 can be transformed as:

$$K_{1D}\frac{\partial^2 \mathcal{H}_1}{\partial z_D^2} + \frac{\partial^2 \mathcal{H}_1}{\partial x_D^2} - \frac{\sqrt{R_K}}{R_S}p(\mathcal{H}_1 + \bar{s}_{bD}) = 0,\ 0 \le z_D \le B_{1D}, \qquad \text{Equation S 29}$$

$$K_{2D}\frac{\partial^2 \mathcal{H}_2}{\partial z_D^2} + \frac{\partial^2 \mathcal{H}_2}{\partial x_D^2} - \frac{R_S p(\mathcal{H}_2 + \bar{s}_{bD}(p))}{\sqrt{R_K}} = 0,\ -B_{2D} \le z_D \le 0, \qquad \text{Equation S 30}$$

With boundary conditions:

$$\mathcal{H}_1(x_D, z_D, p) = \mathcal{H}_2(x_D, z_D, p) = 0,\ x_D = 0 \qquad \text{Equation S 31}$$

$$\frac{\partial \mathcal{H}_1}{\partial x_D}(x_D, z_D, p) = \frac{\partial \mathcal{H}_2}{\partial x_D}(x_D, z_D, p) = 0, x_D = 1 \qquad \text{Equation S 32}$$

$$\frac{K_{1D}}{\sqrt{R_K}}\frac{\partial \mathcal{H}_1}{\partial z_D}(x_D, z_D, p) = -S_{yD}p(\mathcal{H}_1 + \bar{s}_{bD}) + W_D(p), z_D = B_{1D} \qquad \text{Equation S 33}$$

$$\frac{\partial \mathcal{H}_2}{\partial z_D}(x_D, z_D, p) = 0, z_D = -B_{2D} \qquad \text{Equation S 34}$$

Interface boundaries:

$$\mathcal{H}_1(x_D, z_D, p) = \mathcal{H}_2(x_D, z_D, p), z_D = 0 \qquad \text{Equation S 35}$$

$$R_v \frac{\partial \mathcal{H}_1}{\partial z_D}(x_D, z_D, p) = \frac{\partial \mathcal{H}_2}{\partial z_D}(x_D, z_D, p), z_D = 0 \qquad \text{Equation S 36}$$

The partial different Equation S 29 and Equation S 30 can be transformed into the order ordinary differential equation by eliminating the $x_D$ terms using the integral transform method (Özisik, 1968). The integral transform of $\mathcal{H}(x_D, z_D, p)$ is defined as:

$$\widetilde{\mathcal{H}_1}(z_D, p) = \int_0^1 \mathcal{H}_1(x_D, z_D, p)\, \psi(\omega_n, x_D) dx_D \qquad \text{Equation S 37}$$

$$\widetilde{\mathcal{H}}_2(z_D, p) = \int_0^1 \mathcal{H}_2(x_D, z_D, p)\, \psi(\omega_n, x_D) dx_D \qquad \text{Equation S 38}$$

The corresponding inversion formula is defined as:

$$\mathcal{H}_1(x_D, z_D, p) = \sum_{n=0}^{\infty} \widetilde{\mathcal{H}}_1(z_D, p)\psi(\omega_n, x_D) \qquad \text{Equation S 39}$$

$$\mathcal{H}_2(x_D, z_D, p) = \sum_{n=0}^{\infty} \widetilde{\mathcal{H}}_2(z_D, p)\psi(\omega_n, x_D) \qquad \text{Equation S 40}$$

where $\psi(\omega_n, x_D)$ and $\omega_n$ are transform kernel and eigenvalue, respectively. On the basis of the boundary conditions Equation S 31 and Equation S 32, the kernel and eigenvalue are given as (Özisik, 1968):

$$\psi(\omega_n, x_D) = \sqrt{2}\sin(\omega_n x_D) \qquad \text{Equation S 41}$$

and:

$$\omega_n = \frac{(2n+1)\pi}{2} \qquad \text{Equation S 42}$$

respectively. Taking the integral transform Equation S 37 and Equation S 38 for Equation S 29 and Equation S 30 subject to boundary conditions Equation S 31 and Equation S 32 leads to:

$$K_{1D} \frac{\partial^2 \widetilde{\mathcal{H}}_1}{\partial z_D^2} - \left(\omega_n^2 + \frac{\sqrt{R_K}}{R_S} p\right) \widetilde{\mathcal{H}}_1 - \frac{\sqrt{2}\frac{\sqrt{R_K}}{R_S} p \bar{s}_{bD}}{\omega_n} = 0, \quad 0 \le z_D \le B_{1D}, \qquad \text{Equation S 43}$$

$$K_{2D} \frac{\partial^2 \widetilde{\mathcal{H}}_2}{\partial z_D^2} - \left(\omega_n^2 + \frac{R_S p}{\sqrt{R_K}}\right) \widetilde{\mathcal{H}}_2 - \frac{\sqrt{2} p \bar{s}_{bD}}{\omega_n \frac{\sqrt{R_K}}{R_S}} = 0, \quad -B_{2D} \le z_D \le 0, \qquad \text{Equation S 44}$$

with:

$$\frac{K_{1D}}{R_K}\frac{\partial \widetilde{\mathcal{H}}_1}{\partial z_D}(z_D,p) = -S_{yD}p\widetilde{\mathcal{H}}_1 - \frac{\sqrt{2}S_{yD}p\bar{s}_{bD}}{\omega_n} + \frac{\sqrt{2}W_D(p)}{\omega_n}, z_D = B_{1D} \qquad \text{Equation S 45}$$

$$\frac{\partial \widetilde{\mathcal{H}}_2}{\partial z_D}(z_D,p) = 0, z_D = -B_{2D} \qquad \text{Equation S 46}$$

$$\widetilde{\mathcal{H}}_1(z_D,p) = \widetilde{\mathcal{H}}_2(z_D,p), z_D = 0 \qquad \text{Equation S 47}$$

$$R_v\frac{\partial \widetilde{\mathcal{H}}_1}{\partial z_D}(z_D,p) = \frac{\partial \widetilde{\mathcal{H}}_2}{\partial z_D}(z_D,p), z_D = 0 \qquad \text{Equation S 48}$$

The ordinary differential Equation S 43 and Equation S 44 can be solved straightforwardly. The general solution of Equation S 43 and Equation S 44 can be written as:

$$\widetilde{\mathcal{H}}_1 = C_{1a}\,exp(-\Omega_{1n}z_D) + C_{1b}\,exp(\Omega_{1n}z_D) - \lambda_1,\ 0 \le z_D \le B_{1D}, \qquad \text{Equation S 49}$$

$$\widetilde{\mathcal{H}}_2 = C_{2a}\,exp(-\Omega_{2n}z_D) + C_{2b}\,exp(\Omega_{2n}z_D) - \lambda_2,\ -B_{2D} \le z_D \le 0, \qquad \text{Equation S 50}$$

where

$$\Omega_{1n} = \sqrt{\frac{\omega_n^2 + \frac{\sqrt{R_K}}{R_S}p}{K_{1D}}},\ \Omega_{2n} = \sqrt{\frac{\omega_n^2 + \frac{R_S}{\sqrt{R_K}}p}{K_{2D}}},\ \lambda_1 = \frac{\sqrt{2}\sqrt{R_K}p\bar{s}_{bD}}{K_{1D}\Omega_{1n}^2\omega_n R_S}, \lambda_2 = \frac{\sqrt{2}p\bar{s}_{bD}R_S}{K_{2D}\Omega_{2n}^2\omega_n\sqrt{R_K}} \qquad \text{Equation S 51}$$

and $C_{1a}$, $C_{1b}$, $C_{2a}$, and $C_{2b}$ are z-independent parameters. Substituting Equation S 49 and Equation S 50 into Equation S 45-Equation S 48, yields,

$$C_{1a} = \frac{(\lambda_1-\lambda_2)\mathcal{D}(\mathcal{B}-\mathcal{A})-2\mathcal{E}\mathcal{A}}{2\mathcal{A}\mathcal{C}+2\mathcal{B}\mathcal{D}} \qquad \text{Equation S 52}$$

$$C_{1b} = \frac{(\lambda_1-\lambda_2)\mathcal{C}(\mathcal{A}-\mathcal{B})-2\mathcal{E}\mathcal{B}}{2\mathcal{A}\mathcal{C}+2\mathcal{B}\mathcal{D}} \qquad \text{Equation S 53}$$

$$C_{2a} = -\frac{(\lambda_1-\lambda_2)(\mathcal{D}+\mathcal{C})+2\mathcal{E}}{2\mathcal{A}\mathcal{C}+2\mathcal{B}\mathcal{D}}\exp(-2B_{2D}\Omega_{2n}) \qquad \text{Equation S 54}$$

$$C_{2b} = -\frac{(\lambda_1-\lambda_2)(\mathcal{D}+\mathcal{C})+2\mathcal{E}}{2\mathcal{A}\mathcal{C}+2\mathcal{B}\mathcal{D}} \qquad \text{Equation S 55}$$

where

$$\mathcal{A} = \frac{(R_v\Omega_{1n}+\Omega_{2n})\exp(-2B_{2D}\Omega_{2n})+R_v\Omega_{1n}-\Omega_{2n}}{2R_v\Omega_{1n}} \qquad \text{Equation S 56}$$

$$\mathcal{B} = \frac{(R_v\Omega_{1n}-\Omega_{2n})\exp(-2B_{2D}\Omega_{2n})+R_v\Omega_{1n}+\Omega_{2n}}{2R_v\Omega_{1n}} \qquad \text{Equation S 57}$$

$$\mathcal{C} = S_{yD}p - \frac{K_{1D}}{R_K}\Omega_{1n} \qquad \text{Equation S 58}$$

$$\mathcal{D} = \exp(2\Omega_{1n}B_{1D})\left(\frac{K_{1D}}{R_K}\Omega_{1n} + S_{yD}p\right) \qquad \text{Equation S 59}$$

$$\mathcal{E} = \sqrt{2}\exp(\Omega_{1n}B_{1D})\left[\frac{S_{yD}p\bar{s}_{bD}}{\omega_n} - \frac{W_D}{\omega_n} - \frac{\sqrt{R_K}\bar{s}_{bD}S_{yD}p^2}{(R_S\omega_n^2+\sqrt{R_K}p)\omega_n}\right] \qquad \text{Equation S 60}$$

Taking inverse integral transform for Equation S 49 and Equation S 50 and combing Equation S 27 and Equation S 28, yields:

$\bar{s}_{1D}(x_D, z_D, p) = \sum_{n=0}^{\infty}[C_{1a}e^{-\Omega_{1n}z_D} + C_{1b}e^{\Omega_{1n}z_D} - \lambda_1]\sqrt{2}\sin(\omega_n x_D) + \bar{s}_{bD}$ Equation S 61

$\bar{s}_{2D}(x_D, z_D, p) = \sum_{n=0}^{\infty}[C_{2a}e^{-\Omega_{2n}z_D} + C_{2b}e^{\Omega_{2n}z_D} - \lambda_2]\sqrt{2}\sin(\omega_n x_D) + \bar{s}_{bD}$ Equation S 62

And the solution for hydraulic head can be written as:

$\bar{h}_{1D}(x_D, z_D, p) = \sum_{n=0}^{\infty}[C_{1a}e^{-\Omega_{1n}z_D} + C_{1b}e^{\Omega_{1n}z_D} - \lambda_1]\sqrt{2}\sin(\omega_n x_D) + \bar{h}_{bD}$ Equation S 63

$\bar{h}_{2D}(x_D, z_D, p) = \sum_{n=0}^{\infty}[C_{2a}e^{-\Omega_{2n}z_D} + C_{2b}e^{\Omega_{2n}z_D} - \lambda_2]\sqrt{2}\sin(\omega_n x_D) + \bar{h}_{bD}$ Equation S 64

### S2.4. Testing on validity of linearized boundary condition (Equation 5.10)

To test the validity of the linearized boundary condition (Equation 5.10), the coupled Equation 5.1- Equation 5.8 with the boundary conditions (Equation 5.9) and (Equation 5.10) are numerically solved using COMSOL Multiphysics (COMSOL Inc., Burlington, MA, U.S.A.), a Galerkin finite-element software package. Figure S 1 presents the hydraulic heads predicted by the model with the nonlinear boundary (Equation 5.9) (solid curves) and that of the model with the linearized boundary (Equation 5.10) (circle symbols) at two observation points for the different ratio of $W(t)$ and $K_{z1}$. It shows that when the ratio of $W(t)$ and $K_{z1}$ is smaller than 0.1, the hydraulic heads for the linearized boundary agree that for the nonlinear boundary very well during the entire modelling period. It implies that the linearized boundary (Equation 5.10) is an appropriate approximation to the moving water table boundary when the recharge rate is less than one tenth of the vertically hydraulic conductivity.

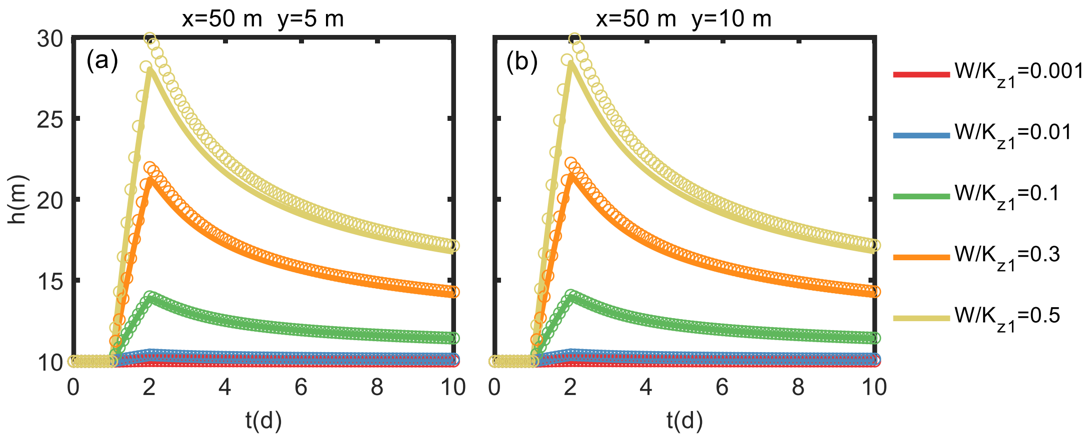


Figure S 16 Changes of hydraulic head in observation point (x=50m, y=5m) (a) and (x=50m, y=10m) (b) with different ratio of $W(t)$ and $K_{z1}$ plotted against t. The solid curves represent the solution with the nonlinear water table boundary (Equation 5.9) and the circle symbols represent the solution with the linearized water table boundary (Equation 5.10). Parameters fixed in the calculation are $K_{z1} = K_{x1} = K_{z2} = K_{x2} = 10 m/d$, $S_{s1} = S_{s2} = 0.001\ 1/m$, $S_y = 0.2$, $L = 250\ m$ and $B_1 = B_2 = 10\ m$.

**S2.5. Discussion of analytical solutions and numerical result**

In this chapter, Equations S 1 to Equation S 9 are directly solved using COMSOL, and analytical solutions are obtained from the same set of equations. Thus, the consistency between the analytical and numerical solutions confirms the accuracy of the analytical solutions. Such comparisons are common in the groundwater field (see references). Due to the convenience of analytical solutions, verified analytical solutions can rapidly process site data, which is much more cost-effective and convenient when dealing with large volumes of site data compared to numerical solutions.

Additionally, although the analytical and numerical solutions are not entirely identical, there are still some discrepancies when magnified. We believe this is due to inherent errors in numerical solutions, such as grid partitioning. This, in turn, indirectly demonstrates the efficiency of analytical solutions

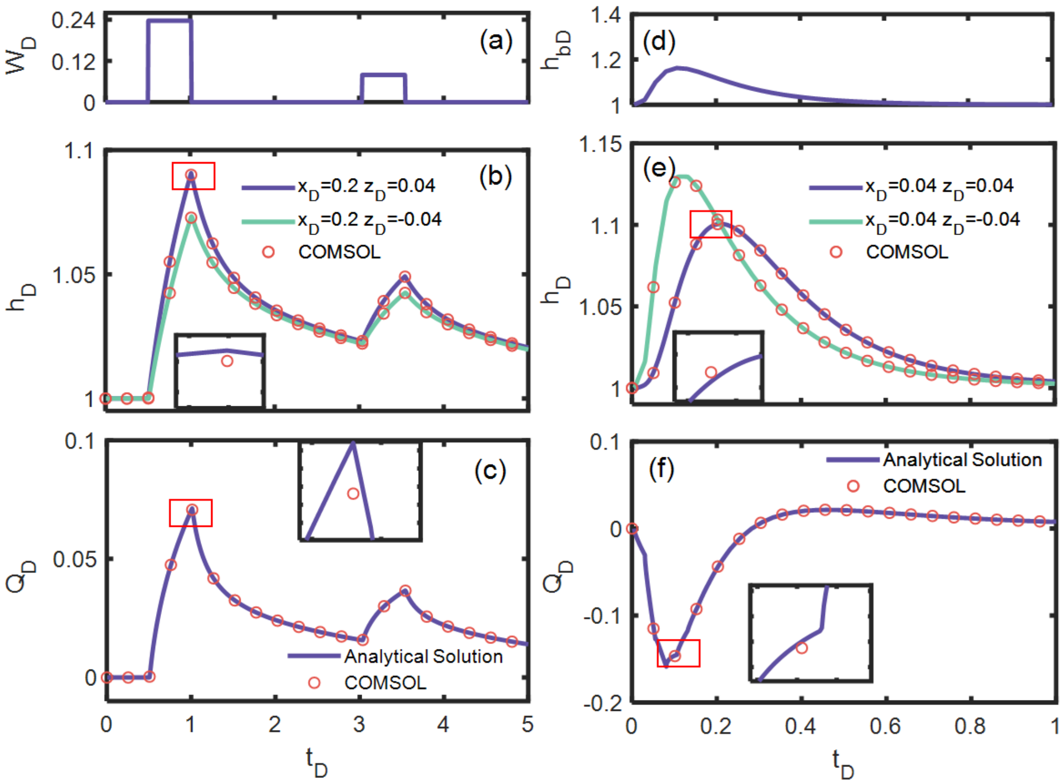


Figure S 17 analytical solutions and numerical result

**S2.6. Mesh used in COMSOL**

In Section 5.3, it is mentioned, '...they are compared with the numerical solutions of the dimensionless governing Equation S 1- Equation S 9.' In the process of defining dimensionless parameters, the dimensionless lengths in the x and z directions are defined as $x_D = \frac{x}{L}$, $z_D = \frac{z}{L}$, respectively. Similarly, the mesh size can be regarded as the ratio of the actual grid size to the length L, thus having no units. The mesh generated in Comsol is shown in the figure. The advantage of this approach is its convenience in calculation and application. If we determine the actual size of the study site, it can be easily converted into dimensional form. For example, in the research case $B_{1D} = B_{2D} = 0.04$, assuming the thickness $B_1 = B_2 = 10m$, then $L = 250m$, and the mesh size ranges from 0.4m to 2m.

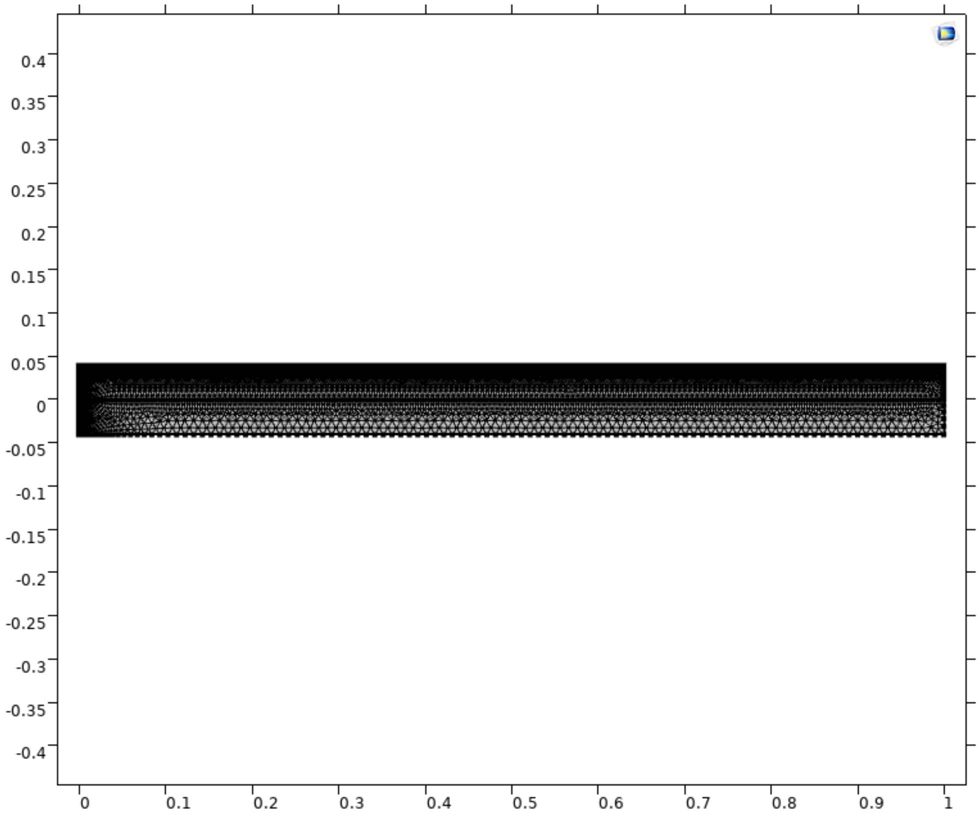


Figure S 18 Mesh used in COMSOL

### S2.7. Effects of thickness of layer on hydraulic heads

The dimensionless thickness of layer also affects the responses of the hydraulic heads in the two layers structure on the infiltration event and flood event. Effect of different values of $B_{2D}$ (0.02, 0.04, 0.06 and 0.08) on hydraulic heads is shown in Figure S 19, where $R_x$ is 0.1 and other parameters are same as parameters used in Figure 5.4. For the infiltration event, the hydraulic heads of both upper layer and down layer and the influence of $B_{2D}$ decrease as $B_{2D}$ increasing. When the thickness of down layer gets larger, the flow section becomes bigger which would accelerate the discharge process and reduce hydraulic head. At the same time, the recharge from the upper layer is constant. Consequently, the influence of $B_{2D}$ decrease as $B_{2D}$ increasing. For the flood event, the hydraulic heads of both upper layer and down layer are positively correlated to $B_{2D}$ while the influence of $B_{2D}$ is negatively. The upper layer has damping effect on the bottom layer and when the bottom layer is thicker, the damping effect becomes weaker in the lower part of the bottom layer, leading to higher hydraulic head in it and hydraulic head in the upper layer would rise too because of the vertical flow.

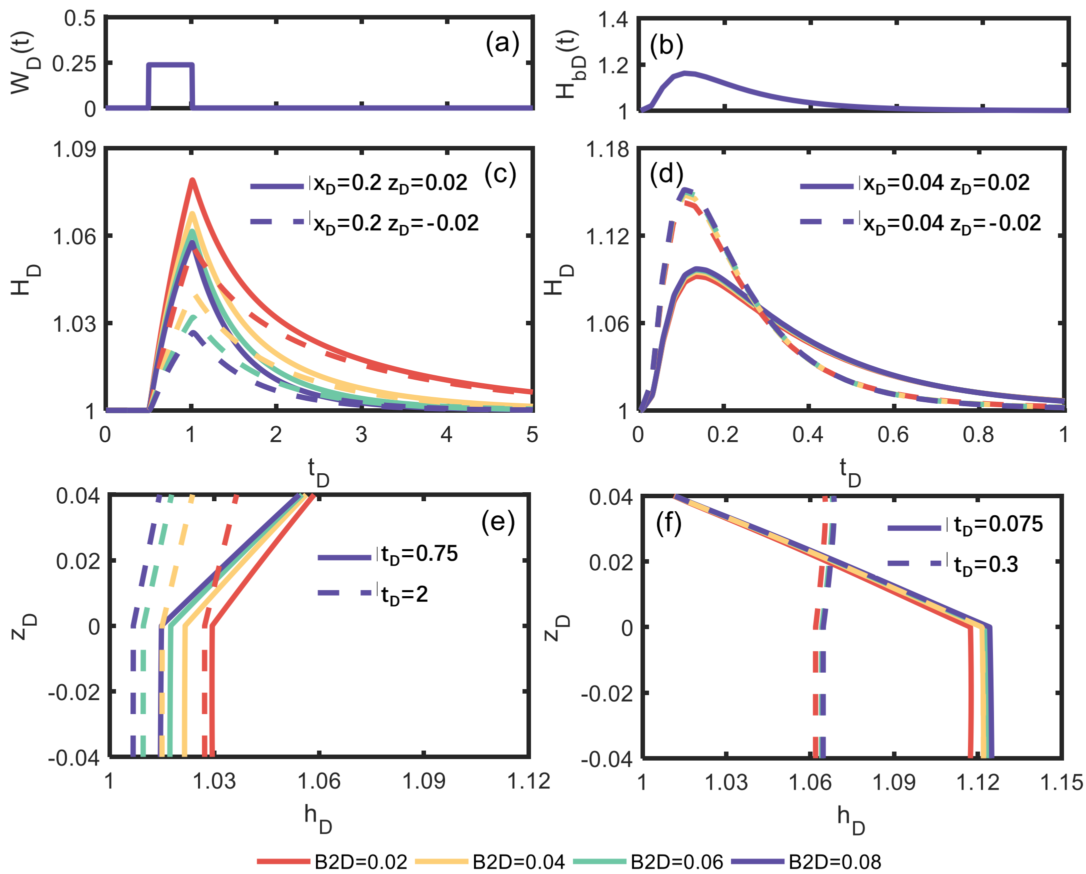

Figure S 19 Response of hydraulic heads on the scenarios of infiltration events (left column figures) and flood events (right column figures) for different values of the dimensionless thickness of the bottom $B_{2D}$.(a) Response of hydraulic heads ($H_D$) on a infiltration events in a certain position in upper layer ($x_D$=0.04, $z_D$=0.02); (b) Response of hydraulic heads ($H_D$) on a flood events in a certain position in upper layer ($x_D$=0.04, $z_D$=0.028); (c) Response of hydraulic heads ($H_D$) on a infiltration events in a certain position bottom layer ($x_D$=0.04, $z_D$=-0.02); (d) Response of hydraulic heads ($H_D$) on a flood events in a certain position bottom layer ($x_D$=0.04, $z_D$=-0.02);

**S2.8 Tailing phenomenon observed in Figure 5.12a.**

In hydrology, the tailing phenomenon of base flow refers to the continuous increase of base flow in a river for a period of time after rainfall stops. Typically, surface runoff decreases rapidly after rainfall ceases, while base flow may continue to increase. This is because the groundwater supplied by rainfall needs time to be absorbed and released into the river by the groundwater system.

The occurrence of the tailing phenomenon depends on various factors, including the hydrogeological characteristics of the groundwater system, groundwater flow rate, soil type, and river topography. In this study, the tailing phenomenon observed in Figure 4.11a is attributed to the presence of low-permeability aquifers, which slows down groundwater flow rates and consequently delays the process of groundwater recharge into the river, resulting in tailing

## S3 Support Information for chapter 6

### S3.1. Laplace domain solution of unsaturated zone

The governing equations for the unsaturated zone (Equation 7.6-Equation 7.8) in Laplace domain is written as:

$$K_z \frac{\partial}{\partial z}\left(e^{-\kappa z}\frac{\partial \bar{u}}{\partial z}\right) = S_y \kappa e^{-\kappa z} p \bar{u}, \qquad 0 \le z \le B_u \qquad \text{Equation S 65}$$

$$K_z e^{-\kappa z}\frac{\partial \bar{u}}{\partial z} = \bar{I}(p), \qquad z = B_u \qquad \text{Equation S 66}$$

The general solution of Equation S 65 can be written as

$$\bar{u} = \mathbb{C}_1 e^{\mathbb{M}z} + \mathbb{C}_2 e^{\mathbb{N}z} \qquad \text{Equation S 67}$$

Where $\mathbb{M} = \frac{\kappa + \sqrt{\kappa^2 + 4\frac{S_y \kappa p}{K_z}}}{2}$, $\mathbb{N} = \frac{\kappa - \sqrt{\kappa^2 + 4\frac{S_y \kappa p}{K_z}}}{2}$

### S3.2. Laplace domain solution of the saturated zone

The governing equations for the saturated zone (Equation 7.1-Equation 7.5) in Laplace domain:

$$K_x \frac{\partial^2 \bar{h}}{\partial x^2} + K_z \frac{\partial^2 \bar{h}}{\partial z^2} = S_s p \bar{h}, \qquad -B_s < z \le 0 \qquad \text{Equation S 68}$$

$$\frac{\partial \bar{h}}{\partial z} = 0, \qquad z = -B_s \qquad \text{Equation S 69}$$

$$\bar{h}(x, z, t) = \bar{H}(p), \qquad x = L \qquad \text{Equation S 70}$$

$$\frac{\partial \bar{h}}{\partial x} = 0, \qquad x = 0 \qquad \text{Equation S 71}$$

The governing equations (Equation 7.11 and Equation 7.12) for interface in Laplace domain:

$$\bar{h} - \bar{u} = 0, \qquad z = 0 \qquad \text{Equation S 72}$$

$$\frac{\partial \bar{h}}{\partial z} - \frac{\partial \bar{u}}{\partial z} = 0, \qquad z = 0 \qquad \text{Equation S 73}$$

For the purpose of homogenization of the boundary condition, Equation S 70 is homogenized by adopting the following variable substitution:

$$\bar{h}(x, z, p) = \mathcal{H}(x, z, p) + \bar{H}(p), \qquad \text{Equation S 74}$$

Then the governing equations for the saturated zone in Laplace domain are:

$$K_x \frac{\partial^2 \mathcal{H}}{\partial x^2} + K_z \frac{\partial^2 \mathcal{H}}{\partial z^2} = S_s p(\mathcal{H} + \bar{H}(p)), \qquad -B_s < z \le 0 \qquad \text{Equation S 75}$$

$$\frac{\partial \mathcal{H}}{\partial z} = 0, \qquad z = -B_s \qquad \text{Equation S 76}$$

$$\mathcal{H}(x, z, p) = 0, \qquad x = L \qquad \text{Equation S 77}$$

$$\frac{\partial \mathcal{H}}{\partial x} = 0, \qquad x = 0 \qquad \text{Equation S 78}$$

The governing equations for interface in Laplace domain:

$$\mathcal{H} + \overline{h_b}(p) = \bar{u}, \qquad z = 0 \qquad \text{Equation S 79}$$

$$\frac{\partial \mathcal{H}}{\partial z} = \frac{\partial \bar{u}}{\partial z}, \qquad z = 0 \qquad \text{Equation S 80}$$

The solution satisfying boundary conditions (Equation S 77 and Equation S 78) can be written Fourier series forms as follow [Dougherty and Babu, 1984; Zhan and Zlotnik, 2002]

$$\mathcal{H}(x,z,p) = \sum_{n=0}^{\infty} \widetilde{\mathcal{H}}(z)\psi(\omega_n, x) \qquad \text{Equation S 81}$$

$$\widetilde{\mathcal{H}}(z,p) = \int_0^L \mathcal{H}(x,z,p)\psi(\omega_n, x)dx \qquad \text{Equation S 82}$$

where $\psi(\omega_n, x)$ and $\omega_n$ are transform kernels and eigenvalues. On the basis of the boundary conditions Equation S 76 and Equation S 77, the kernels and eigenvalues are given as

$$\psi(\omega_n, x) = \sqrt{\frac{2}{\mathrm{L}}}\cos(\omega_n x) \qquad \text{Equation S 83}$$

and

$$\omega_n = \frac{(2n+1)\pi}{2\mathrm{L}}, \qquad \text{Equation S 84}$$

Taking the Cosine transform on Equation S 75-Equation S 80 using the formula Equation S 82 leads to

$$\frac{\partial^2 \widetilde{\mathcal{H}}}{\partial z^2} - \frac{[\omega_n^2 K_x + S_s p]}{K_z}\widetilde{\mathcal{H}} = \frac{S_s p \widetilde{H}(p)}{K_z}, \qquad -B_s < z \leq 0 \qquad \text{Equation S 85}$$

$$\frac{\partial \widetilde{\mathcal{H}}}{\partial z} = 0, \qquad z = -B_s \qquad \text{Equation S 86}$$

Where

$$\widetilde{H}(p) = \sqrt{\frac{2}{\mathrm{L}}}\frac{\sin(\omega_n L)}{\omega_n}\overline{H}(p) \qquad \text{Equation S 87}$$

The general solution of Equation S 85 can be written as

$$\widetilde{\mathcal{H}} = \mathbb{C}_3\, exp(-\Omega_n z) + \mathbb{C}_4\, exp(\Omega_n z) - \zeta, \;\; -B_s < z \leq 0 \qquad \text{Equation S 88}$$

where

$$\Phi_n = \sqrt{\frac{\omega_n^2 K_x + S_s p}{K_z}}, \; \zeta = \frac{S_s p \widehat{H}(p)}{K_z \Phi_n^2} \qquad \text{Equation S 89}$$

The governing equations for interface in Laplace domain:

$$\widetilde{\mathcal{H}} + \widetilde{H}(p) = \tilde{u}, \qquad z = 0 \qquad \text{Equation S 90}$$

$$\frac{\partial \widetilde{\mathcal{H}}}{\partial z} = \frac{\partial \tilde{u}}{\partial z}, \qquad z = 0 \qquad \text{Equation S 91}$$

$$\tilde{u}(p) = \int_0^L (\mathbb{C}_1 e^{Mz} + \mathbb{C}_2 e^{Nz})\psi(\omega_n, x)dx \qquad \text{Equation S 92}$$

The model couples a 1D unsaturated zone with 2D saturated zone, so $\mathbb{C}_1$ and $\mathbb{C}_2$ may be dependent on x. It can be assumed that $\mathbb{C}_1'$ and $\mathbb{C}_2'$ are Cosine transformation of $\mathbb{C}_1$ and $\mathbb{C}_2$

$$\tilde{u}(p) = \mathbb{C}_1' e^{\mathbb{M}z} + \mathbb{C}_2' e^{\mathbb{M}z} \qquad \text{Equation S 93}$$

Taking the Cosine transform on Equation S 75-Equation S 80 using the formula Equation S 66 leads to

$$K_z e^{-\kappa z}\frac{\partial \tilde{u}}{\partial z} = \tilde{I}(p), \qquad z = B_u \qquad \text{Equation S 94}$$

Where

$$\tilde{I}(p) = \sqrt{\frac{2}{\mathrm{L}}}\frac{\sin(\omega_n L)}{\omega_n}\bar{I}(p) \qquad \text{Equation S 95}$$

Substituting the boundary conditions (Equation S 66 and Equation S 86), and the interface conditions Equation S 90 and Equation S 91 into Equation S 88 and Equation S 93, respectively, leads to

$$\mathbb{C}_1' = \frac{\mathbb{AM}(\mathbb{BN}-\mathbb{B}'\Phi_n)+\mathbb{B}'\Phi_n\mathbb{B}e^{B_u(\mathbb{N}-\mathbb{M})}(\widetilde{H}(p)-\zeta)}{(\mathbb{D}'\mathbb{B}-\mathbb{DB}'\Phi_n)\mathbb{M}} \qquad \text{Equation S 96}$$

$$\mathbb{C}_2' = \frac{\mathbb{B}'\Phi_n(\mathbb{A}+\zeta-\widetilde{H}(p))-\mathbb{AMB}}{\mathbb{D}'\mathbb{B}-\mathbb{DB}'\Phi_n} \qquad \text{Equation S 97}$$

$$\mathbb{C}_3 = \frac{C'(\mathbb{A}+\zeta-\widetilde{H}(p))-\mathbb{AMD}}{\mathbb{D}'\mathbb{B}-\mathbb{DB}'\Phi_n} \qquad \text{Equation S 98}$$

$$\mathbb{C}_4 = \frac{\mathbb{D}'(\mathbb{A}+\zeta-\widetilde{H}(p))-\mathbb{AMD}}{\mathbb{D}'\mathbb{B}-\mathbb{DB}'\Phi_n}exp(2\Phi_n H_s) \qquad \text{Equation S 99}$$

Where $\mathbb{A} = \frac{\tilde{I}(p)}{\mathbb{M}K_z e^{\mathbb{M}B_u-\kappa B_u}}$, $\mathbb{B} = 1 + exp(2\Phi_n B_s)$, $\mathbb{B}' = exp(2\Phi_n B_s) - 1$, $\mathbb{D} = \left(1 - \frac{N}{M}e^{B_u(\mathbb{N}-\mathbb{M})}\right)$, $\mathbb{D}' = \left(\mathbb{N} - \mathbb{N}e^{B_u(\mathbb{N}-\mathbb{M})}\right)$.

Taking inverse Cosine transforms for Equation S 88 and Equation S 93, then substituting them into Equation S 74, respectively, yields the Laplace domain solution for the saturated zone

$$\bar{h}(x,z,p) = \sum_{n=0}^{\infty}(\mathbb{C}_2\, exp(-\Phi_n z) + \mathbb{C}_3\, exp(\Phi_n z) - \lambda)\psi(\omega_n, x) + \bar{H}(p), \qquad \text{Equation S 100}$$

$$\bar{u}(z,p) = \sum_{n=0}^{\infty}(\mathbb{C}_1' e^{\mathbb{M}z} + \mathbb{C}_2' e^{\mathbb{N}z})\psi(\omega_n, x) \qquad \text{Equation S 101}$$

**S3.3 Laplace domain solution of the average head in the saturated zone**

The average water head $h_a$ in saturated zone can be defined as follows:

$$h_a = \frac{1}{B_s}\int_{-B_s}^{0} h\,dz \qquad \text{Equation S 102}$$

In Laplace domain, Equation S 102 can be written as follows:

$$\overline{h_a} = \frac{1}{B_s}\int_{-B_s}^{0} \bar{h}\,dz \qquad \text{Equation S 103}$$

Substituting Equation S 100 into Equation S 103 yields the Laplace domain solution for average water head in saturated zone:

$$\overline{h_a} = \sum_{n=0}^{\infty}\left[\frac{\mathbb{C}_4(1-exp(-B_s\Phi_n))+\mathbb{C}_3(exp(B_s\Phi_n)-1)}{\Omega_n B_s} - \lambda\right]\psi(\omega_n,x) + \overline{H}(p) \qquad \text{Equation S 104}$$

### S3.4 Selection of random field

In groundwater risk analysis and other types of probability assessment problems, spatial variability of hydraulic conductivity is often described using probability distributions.(Benson and Daniel, 1994; Bogardi et al., 1990) The stationary lognormal distribution is simple to use and it can effectively fit hydraulic conductivity data and is therefore widely applied (Freeze, 1975; Kohlbecker et al., 2006; Zhai and Benson, 2006).

Hydraulic conductivity random fields are typically characterized and generated using a covariance model to construct the semi-variogram. Covariance models such as the exponential, Gaussian, and cubic covariance models can all be used to generate random fields. However, the exponential covariance model can better fit observed hydraulic conductivity data and is thus widely employed in generating hydraulic conductivity random fields(Bailey and Baù, 2010; El Idrysy and De Smedt, 2007; Gómez-Hernández and Gorelick, 1989).

## S3.5 Discussion for sensitive layers in neural network

Data with different hydraulic conductivity values is generated through analytical solutions, used this data to train neural networks, and compared the changes in neural network parameters to confirm that differences in hydraulic conductivity lead to significant changes in the shallow layers (layers 2, 3, and 4) of the neural network. Therefore, we designated the shallow layers as retrainable for transfer learning. Subsequent numerical experiments revealed that the results of transfer learning with only retraining the shallow layers were essentially the same as those of transfer learning with retraining all neural network parameters, which indirectly confirms this conclusion.

However, it must be acknowledged that neural networks are black-box models, making it difficult to seek their physical explanations, and transfer learning exhibits similar characteristics. It is generally experimental to determine which layers should be frozen during the transfer learning process, and there are no general conclusions (Jang et al., 2019; Rozantsev et al., 2018; Yosinski et al., 2014). I speculate that the shallow layers of the neural network in this chapter are more sensitive to hydraulic conductivity because hydraulic conductivity is a significant factor influencing groundwater flow fields, and heterogeneous hydraulic conductivity greatly affects the fundamental data characteristics of groundwater heads in the study area. Additionally, since recharge is considered known, the short-term fluctuation characteristics of groundwater levels should be consistent. If we consider the neural network as a feature extractor, the shallow layers of the neural network should be responsible for extracting basic features, while the deep layers are responsible for extracting specific features. Therefore, the deep layers (layers 5 and 6) in this chapter are less sensitive.

# Reference

Ahmed AAM, Deo RC, Ghahramani A, Feng Q, Raj N, Yin ZL, et al. New double decomposition deep learning methods for river water level forecasting. Science of the Total Environment 2022; 831: 21.

Al-Mubaid H, Umair SA. A new text categorization technique using distributional clustering and learning logic. Ieee Transactions on Knowledge and Data Engineering 2006; 18: 1156-1165.

Alley WM. Ground Water. In: Likens GE, editor. Encyclopedia of Inland Waters. Academic Press, Oxford, 2009, pp. 684-690.

Alley WM, Taylor CJ. The value of long-term ground water level monitoring. Ground Water 2001; 39: 801-802.

Amiri E. Forecasting daily river flows using nonlinear time series models. Journal of Hydrology 2015; 527: 1054-1072.

Anibas C, Buis K, Verhoeven R, Meire P, Batelaan O. A simple thermal mapping method for seasonal spatial patterns of groundwater-surface water interaction. Journal of Hydrology 2011; 397: 93-104.

Arias ME, Cochrane TA, Norton D, Killeen TJ, Khon P. The flood pulse as the underlying driver of vegetation in the largest wetland and fishery of the Mekong Basin. Ambio 2013; 42: 864-876.

Avci CB, Ufuk Sahin A. Assessing radial transmissivity variation in heterogeneous aquifers using analytical techniques. Hydrological Processes 2014; 28: 5739-5754.

Bailey R, Baù D. Ensemble smoother assimilation of hydraulic head and return flow data to estimate hydraulic conductivity distribution. Water Resources Research 2010; 46.

Bailey R, Rathjens H, Bieger K, Chaubey I, Arnold J. SWATMOD-Prep: Graphical user interface for preparing coupled SWAT-MODFLOW simulations. JAWRA Journal of the American Water Resources Association 2017; 53: 400-410.

Bailey RT, Wible TC, Arabi M, Records RM, Ditty J. Assessing regional-scale spatio-temporal patterns of groundwater-surface water interactions using a coupled SWAT-MODFLOW model. Hydrological Processes 2016.

Bandai T, Ghezzehei TA. Forward and inverse modeling of water flow in unsaturated soils with discontinuous hydraulic conductivities using physics-informed neural networks with domain decomposition. Hydrology and Earth System Sciences 2022; 26: 4469-4495.

Bear J. Hydraulics of groundwater: Courier Corporation, 2012.

Benson CH, Daniel DE. Minimum thickness of compacted soil liners: I. Stochastic models. Journal of Geotechnical Engineering 1994; 120: 129-152.

Bhasme P, Vagadiya J, Bhatia U. Enhancing predictive skills in physically-consistent way: Physics Informed Machine Learning for hydrological processes. Journal of Hydrology 2022; 615.

Binley A, Hubbard SS, Huisman JA, Revil A, Robinson DA, Singha K, et al. The emergence of hydrogeophysics for improved understanding of subsurface processes over multiple scales. Water Resour Res 2015; 51: 3837-3866.

Bishop CM, Bishop H. The Deep Learning Revolution. In: Bishop CM, Bishop H, editors. Deep Learning: Foundations and Concepts. Springer International Publishing, Cham, 2024, pp. 1-22.

Bittelli M, Tomei F, Pistocchi A, Flury M, Boll J, Brooks ES, et al. Development and testing of a physically based, three-dimensional model of surface and subsurface hydrology. Advances in Water Resources 2010; 33: 106-122.

Boano F, Harvey JW, Marion A, Packman AI, Revelli R, Ridolfi L, et al. Hyporheic flow and transport processes: Mechanisms, models, and biogeochemical implications. Reviews of geophysics 2014; 52: 603-679.

Bogardi I, Kelly W, Bardossy A. Reliability model for soil liner: Post construction. Journal of geotechnical engineering 1990; 116: 1502-1520.

Brunner P, Simmons CT. HydroGeoSphere: A Fully Integrated, Physically Based Hydrological Model. Ground Water 2012; 50: 170-176.

Butler Jr JJ, Zhan X, Zlotnik VA. Pumping-induced drawdown and stream depletion in a leaky aquifer system. Groundwater 2007; 45: 178-186.

Cai H, Liu S, Shi H, Zhou Z, Jiang S, Babovic V. Toward improved lumped groundwater level predictions at catchment scale: Mutual integration of water balance mechanism and deep learning method. Journal of Hydrology 2022a; 613.

Cai S, Mao Z, Wang Z, Yin M, Karniadakis GE. Physics-informed neural networks (PINNs) for fluid mechanics: a review. Acta Mechanica Sinica 2022b; 37: 1727-1738.

Cai S, Wang Z, Wang S, Perdikaris P, Karniadakis GE. Physics-Informed Neural Networks for Heat Transfer Problems. Journal of Heat Transfer 2021; 143.

Cao H, Xie X, Shi J, Jiang G, Wang Y. Siamese Network-Based Transfer Learning Model to Predict Geogenic Contaminated Groundwaters. Environ Sci Technol 2022; 56: 11071-11079.

Chandel VS, Ghosh S. Components of Himalayan river flows in a changing climate. Water Resources Research 2021; 57: e2020WR027589.

Chang C-M, Yeh H-D. Investigation of flow and solute transport at the field scale through heterogeneous deformable porous media. Journal of Hydrology 2016; 540: 142-147.

Chang CM, Yeh HD. Stochastic analysis of stream-groundwater interaction subject to temporally correlated recharge. Journal of Hydrology 2013; 476: 490-495.

Chang Y-C, Yeh H-D, Huang Y-C. Determination of the parameter pattern and values for a one-dimensional multi-zone unconfined aquifer. Hydrogeology Journal 2008; 16: 205-214.

Chen BW, Abdullah NNB, Park S, Gu Y. Efficient multiple incremental computation for Kernel Ridge Regression with Bayesian uncertainty modeling. Future Generation Computer Systems-the International Journal of Escience 2018; 82: 679-688.

Chen X-X, Zhang P, Yin Z-Y. Physics-Informed neural network solver for numerical analysis in geoengineering. Georisk: Assessment and Management of Risk for Engineered Systems and Geohazards 2024; 18: 33-51.

Chen X, Chen X. Stream water infiltration, bank storage, and storage zone changes due to stream-stage fluctuations. Journal of Hydrology 2003; 280: 246-264.

Chen X, Huang JX, Han Z, Gao HK, Liu M, Li ZQ, et al. The importance of short lag-time in the runoff forecasting model based on long short-term memory. Journal of Hydrology 2020; 589: 20.

Chen Z, Xu H, Jiang P, Yu S, Lin G, Bychkov I, et al. A transfer Learning-Based LSTM strategy for imputing Large-Scale consecutive missing data and its application in a water quality prediction system. Journal of Hydrology 2021; 602.

Cheng M, Fang F, Kinouchi T, Navon IM, Pain CC. Long lead-time daily and monthly streamflow forecasting using machine learning methods. Journal of Hydrology 2020; 590: 13.

Cho K, Van Merriënboer B, Bahdanau D, Bengio YJapa. On the properties of neural machine translation: Encoder-decoder approaches. 2014.

Chuang M-H, Huang C-S, Li G-H, Yeh H-D. Groundwater fluctuations in heterogeneous coastal leaky aquifer systems. Hydrology and Earth System Sciences 2010; 14: 1819-1826.

Chung J, Gulcehre C, Cho K, Bengio YJapa. Empirical evaluation of gated recurrent neural networks on sequence modeling. 2014.

Costabile P, Costanzo C, Macchione F. Performances and limitations of the diffusive approximation of the 2-d shallow water equations for flood simulation in urban and rural areas. Applied Numerical Mathematics 2017; 116: 141-156.

Crump KS. Numerical inversion of Laplace transforms using a Fourier series approximation. Journal of the ACM (JACM) 1976; 23: 89-96.

Curry RA, Gehrels J, Noakes DL, Swainson R. Effects of river flow fluctuations on groundwater discharge through brook trout, Salvelinus fontinalis, spawning and incubation habitats. Hydrobiologia 1994; 277: 121-134.

Dagan G. Second order linearized theory of free-surface flow in porous media. La Houille Blanche 1964: 901-910.

De Hoog FR, Knight J, Stokes A. An improved method for numerical inversion of Laplace transforms. SIAM Journal on Scientific and Statistical Computing 1982; 3: 357-366.

de la Fuente A, Meruane V, Meruane C. Hydrological Early Warning System Based on a Deep Learning Runoff Model Coupled with a Meteorological Forecast. Water 2019; 11.

de Mello K, Valente RA, Randhir TO, dos Santos ACA, Vettorazzi CA. Effects of land use and land cover on water quality of low-order streams in Southeastern Brazil: Watershed versus riparian zone. Catena 2018; 167: 130-138.

de Oliveira FP, Silva M, Avanzi JC, Curi N, Leite FP. Soil loss assessment on unpaved forest roads at the Rio Doce Valley, Minas Gerais state, Brazil. Scientia Forestalis 2010; 38: 331-339.

Devito KJ, Fitzgerald D, Hill AR, Aravena R. Nitrate dynamics in relation to lithology and hydrologic flow path in a river riparian zone. Wiley Online Library, 2000.

Dewandel B, Lachassagne P, Wyns R, Marechal JC, Krishnamurthy NS. A generalized 3-D geological and hydrogeological conceptual model of granite aquifers controlled by single or multiphase weathering. Journal of Hydrology 2006; 330: 260-284.

Ding X, Jiang T, Li YN, Xue WL, Zhong Y, Ieee. Device-free Location-independent Human Activity Recognition using Transfer Learning based on CNN. IEEE International Conference on

Communications (IEEE ICC) / Workshop on NOMA for 5G and Beyond. Ieee, Electr Network, 2020.

Dubner H, Abate J. Numerical inversion of Laplace transforms by relating them to the finite Fourier cosine transform. Journal of the ACM (JACM) 1968; 15: 115-123.

Earon R, Joakim R, Wu L, Olofsson B. Insight into the influence of local streambed heterogeneity on hyporheic-zone flow characteristics. Hydrogeology Journal 2020; 28: 2697-2712.

El Idrysy EH, De Smedt F. A comparative study of hydraulic conductivity estimations using geostatistics. Hydrogeology Journal 2007; 15: 459-470.

Eltner A, Bressan PO, Akiyama T, Gonçalves WN, Marcato Junior J. Using Deep Learning for Automatic Water Stage Measurements. Water Resources Research 2021; 57.

Fang S, Huang L, Wan Y, Sun W, Xu J. Outlier Detection for Water Supply Data Based on Joint Auto-Encoder. Computers, Materials & Continua 2020; 64.

Fang YR, Xiao F, Sheng BY, Sha LT, Sun LJ. Cross-scene passive human activity recognition using commodity WiFi. Frontiers of Computer Science 2022; 16: 11.

Feng D, Liu J, Lawson K, Shen C. Differentiable, Learnable, Regionalized Process-Based Models With Multiphysical Outputs can Approach State‐Of‐The‐Art Hydrologic Prediction Accuracy. Water Resources Research 2022; 58.

Feng Q, Feng X, Zhan H. Three-dimensional transient flow to a partially penetrated well with variable discharge in a general three-layer aquifer system. Hydrology and Earth System Sciences Discussions 2020: 1-50.

Feng Q, Liu Z, Zhan H. Semi-analytical solutions for transient flow to a partially penetrated well with variable discharge in a general three-layer aquifer system. Journal of Hydrology 2021a; 598: 126329.

Feng Q, Yuan X, Zhan H. Flow to a partially penetrating well with variable discharge in an anisotropic two-layer aquifer system. Journal of Hydrology 2019; 578: 124027.

Feng QG, Liu ZW, Zhan HB. Semi-analytical solutions for transient flow to a partially penetrated well with variable discharge in a general three-layer aquifer system. Journal of Hydrology 2021b; 598.

Ferencz SB, Cardenas MB, Neilson BT. Analysis of the Effects of Dam Release Properties and Ambient Groundwater Flow on Surface Water-Groundwater Exchange Over a 100-km-Long Reach. Water Resources Research 2019; 55: 8526-8546.

Fox A, Laube G, Schmidt C, Fleckenstein J, Arnon S. The effect of losing and gaining flow conditions on hyporheic exchange in heterogeneous streambeds. Water Resources Research 2016; 52: 7460-7477.

Frame JM, Kratzert F, Klotz D, Gauch M, Shalev G, Gilon O, et al. Deep learning rainfall–runoff predictions of extreme events. Hydrol. Earth Syst. Sci. 2022; 26: 3377-3392.

Freeze RA. ROLE OF SUBSURFACE FLOW IN GENERATING SURFACE RUNOFF .1. BASE FLOW CONTRIBUTIONS TO CHANNEL FLOW. Water Resources Research 1972; 8: 609-&.

Freeze RA. A stochastic-conceptual analysis of one-dimensional groundwater flow in nonuniform homogeneous media. Water resources research 1975; 11: 725-741.

Freeze RA, Harlan RL. Blueprint for a physically-based, digitally-simulated hydrologic response model. Journal of Hydrology 1969; 9: 237-258.

Fritz BG, Arntzen EV. Effect of rapidly changing river stage on uranium flux through the hyporheic zone. Ground Water 2007; 45: 753-760.

Fung GPC, Yu JX, Lu HJ, Yu PS. Text classification without negative examples revisit. Ieee Transactions on Knowledge and Data Engineering 2006; 18: 6-20.

Gardner W. Some steady-state solutions of the unsaturated moisture flow equation with application to evaporation from a water table. Soil science 1958; 85: 228-232.

Goderniaux P, Brouyere S, Fowler HJ, Blenkinsop S, Therrien R, Orban P, et al. Large scale surface-subsurface hydrological model to assess climate change impacts on groundwater reserves. Journal of Hydrology 2009; 373: 122-138.

Gómez-Hernández JJ, Gorelick SM. Effective groundwater model parameter values: Influence of spatial variability of hydraulic conductivity, leakance, and recharge. Water Resources Research 1989; 25: 405-419.

Gomez-Velez JD, Krause S, Wilson JL. Effect of low-permeability layers on spatial patterns of hyporheic exchange and groundwater upwelling. Water Resources Research 2014; 50: 5196-5215.

Govindaraju RS, Kavvas ML. DYNAMICS OF MOVING BOUNDARY OVERLAND FLOWS OVER INFILTRATING SURFACES AT HILLSLOPES. Water Resources Research 1991; 27: 1885-1898.

Guevara-Ochoa C, Medina-Sierra A, Vives L. Spatio-temporal effect of climate change on water balance and interactions between groundwater and surface water in plains. Science of the Total Environment 2020; 722: 18.

Gurrieri JT, Furniss G. Estimation of groundwater exchange in alpine lakes using non-steady mass-balance methods. Journal of Hydrology 2004; 297: 187-208.

Han H, Morrison RR. Improved runoff forecasting performance through error predictions using a deep-learning approach. Journal of Hydrology 2022; 608.

Hantush MM. Modeling stream–aquifer interactions with linear response functions. Journal of Hydrology 2005; 311: 59-79.

Hao H, Hao Y, Li Z, Qi C, Wang Q, Zhang M, et al. Insight into glacio-hydrologicalprocesses using explainable machine-learning (XAI) models. Journal of Hydrology 2024; 634: 131047.

Hassan SMT, Lubczynski MW, Niswonger RG, Su ZB. Surface-groundwater interactions in hard rocks in Sardon Catchment of western Spain: An integrated modeling approach. Journal of Hydrology 2014; 517: 390-410.

He K, Zhang X, Ren S, Sun J. Deep Residual Learning for Image Recognition. 2016 IEEE Conference on Computer Vision and Pattern Recognition (CVPR), 2016, pp. 770-778.

He TH, Wang NZ, Zhang DX. Theory-guided full convolutional neural network: An efficient surrogate model for inverse problems in subsurface contaminant transport. Advances in Water Resources 2021; 157.

Hochreiter S, Schmidhuber J. Long short-term memory. Neural Computation 1997; 9: 1735-1780.

Hoerl AE. Optimum solution of many variables equations. Chemical Engineering Progress 1959; 55: 69-78.

Hotelling H. Analysis of a complex of statistical variables into principal components. Journal of Educational Psychology 1933; 24: 498-520.

Hsieh P-F, Yeh H-D. Semi-analytical and approximate solutions for contaminant transport from an injection well in a two-zone confined aquifer system. Journal of Hydrology 2014; 519: 1171-1176.

Hu CH, Wu Q, Li H, Jian SQ, Li N, Lou ZZ. Deep Learning with a Long Short-Term Memory Networks Approach for Rainfall-Runoff Simulation. Water 2018; 10.

Hu H, Tian Z, Sun L, Wen J, Liang Z, Dong G, et al. Synthesized trade-off analysis of flood control solutions under future deep uncertainty: An application to the central business district of Shanghai. Water research 2019; 166: 115067.

Hu S, Gao J, Zhong D, Deng L, Ou C, Xin P. An innovative hourly water demand forecasting preprocessing framework with local outlier correction and adaptive decomposition techniques. Water 2021; 13: 582.

Huang C-S, Lin W-S, Yeh H-D. Stream filtration induced by pumping in a confined, unconfined or leaky aquifer bounded by two parallel streams or by a stream and an impervious stratum. Journal of Hydrology 2014; 513: 28-44.

Huang CS, Yeh HD. An analytical approach for the simulation of flow in a heterogeneous confined aquifer with a parameter zonation structure. Water Resources Research 2016; 52: 9201-9212.

Huang S, Xia J, Wang Y, Wang W, Zeng S, She D, et al. Coupling Machine Learning Into Hydrodynamic Models to Improve River Modeling With Complex Boundary Conditions. Water Resources Research 2022; 58.

Huang Y, Tian Z, Ke Q, Liu J, Irannezhad M, Fan D, et al. Nature-based solutions for urban pluvial flood risk management. Wiley Interdisciplinary Reviews: Water 2020; 7: e1421.

Hyndman RJ, Athanasopoulos G. Forecasting: principles and practice: OTexts, 2018.

Im S, Kim H, Kim C, Jang C. Assessing the impacts of land use changes on watershed hydrology using MIKE SHE. Environmental Geology 2009; 57: 231-239.

Jafari T, Kiem AS, Javadi S, Nakamura T, Nishida K. Fully integrated numerical simulation of surface water-groundwater interactions using SWAT-MODFLOW with an improved calibration tool. Journal of Hydrology: Regional Studies 2021; 35.

Jang Y, Lee H, Hwang SJ, Shin J. Learning what and where to transfer. International conference on machine learning. PMLR, 2019, pp. 3030-3039.

Jaynes DB, Isenhart TM. Reconnecting tile drainage to riparian buffer hydrology for enhanced nitrate removal. Journal of environmental quality 2014; 43: 631-638.

Jeng D, Li L, Barry D. Analytical solution for tidal propagation in a coupled semi-confined/phreatic coastal aquifer. Advances in Water Resources 2002; 25: 577-584.

Jeong J, Park E. Comparative applications of data-driven models representing water table fluctuations. Journal of Hydrology 2019; 572: 261-273.

Jeong J, Park E, Han WS, Kim KY, Jun SC, Choung S, et al. A predictive estimation method for carbon dioxide transport by data-driven modeling with a physically-based data model. Journal of Contaminant Hydrology 2017; 206: 34-42.

Jiang S, Zheng Y, Solomatine D. Improving AI System Awareness of Geoscience Knowledge: Symbiotic Integration of Physical Approaches and Deep Learning. Geophysical Research Letters 2020; 47.

Jiang S, Zheng Y, Wang C, Babovic V. Uncovering Flooding Mechanisms Across the Contiguous United States Through Interpretive Deep Learning on Representative Catchments. Water Resources Research 2022; 58.

Jing H, He X, Tian Y, Lancia M, Cao G, Crivellari A, et al. Comparison and interpretation of data-driven models for simulating site-specific human-impacted groundwater dynamics in the North China Plain. Journal of Hydrology 2023; 616.

Johengen TH, Biddanda BA, Cotner JB. Stimulation of Lake Michigan plankton metabolism by sediment resuspension and river runoff. Journal of Great Lakes Research 2008; 34: 213-227.

Joo J, Tian Y, Zheng C, Zheng Y, Sun Z, Zhang A, et al. An Integrated Modeling Approach to Study the Surface Water-Groundwater Interactions and Influence of Temporal Damping Effects on the Hydrological Cycle in the Miho Catchment in South Korea. Water 2018; 10.

Joseph J, Ghosh S. Representing Indian Agricultural Practices and Paddy Cultivation in the Variable Infiltration Capacity Model. Water Resources Research 2023; 59: 25.

Kaleris VK, Ziogas AI. The effect of cutoff walls on saltwater intrusion and groundwater extraction in coastal aquifers. Journal of Hydrology 2013; 476: 370-383.

Kalkhoff SJ, Detroy M, Cherryholmes K, Kuzniar R. HERBICIDE AND NITRATE VARIATION IN ALLUVIUM UNDERLYING A CORN FIELD AT A SITE IN IOWA COUNTY, IOWA 1. JAWRA Journal of the American Water Resources Association 1992; 28: 1001-1011.

Kao IF, Zhou YL, Chang LC, Chang FJ. Exploring a Long Short-Term Memory based Encoder-Decoder framework for multi-step-ahead flood forecasting. Journal of Hydrology 2020; 583: 12.

Katsanou K, Karapanagioti HK. Surface Water and Groundwater Sources for Drinking Water. In: Gil A, Galeano LA, Vicente MÁ, editors. Applications of Advanced Oxidation Processes (AOPs) in Drinking Water Treatment. Springer International Publishing, Cham, 2019, pp. 1-19.

Kidmose J, Nilsson B, Engesgaard P, Frandsen M, Karan S, Landkildehus F, et al. Focused groundwater discharge of phosphorus to a eutrophic seepage lake (Lake Væng, Denmark): implications for lake ecological state and restoration. Hydrogeology Journal 2013; 21: 1787-1802.

Kim NW, Chung IM, Won YS, Arnold JG. Development and application of the integrated SWAT–MODFLOW model. Journal of hydrology 2008; 356: 1-16.

Kim Y, Jeong J, Park H, Kwon M, Cho C, Jeong J. Development of a data-driven ensemble regressor and its applicability for identifying contextual and collective outliers in groundwater level time-series data. Journal of Hydrology 2022; 612: 15.

Knights D, Parks KC, Sawyer AH, David CH, Browning TN, Danner KM, et al. Direct groundwater discharge and vulnerability to hidden nutrient loads along the Great Lakes coast of the United States. Journal of Hydrology 2017; 554: 331-341.

Kohlbecker MV, Wheatcraft SW, Meerschaert MM. Heavy-tailed log hydraulic conductivity distributions imply heavy-tailed log velocity distributions. Water resources research 2006; 42.

Kollet S, Sulis M, Maxwell RM, Paniconi C, Putti M, Bertoldi G, et al. The integrated hydrologic model intercomparison project, IH-MIP2: A second set of benchmark results to diagnose integrated hydrology and feedbacks. Water Resources Research 2017; 53: 867-890.

Kollet SJ, Maxwell RM. Integrated surface-groundwater flow modeling: A free-surface overland flow boundary condition in a parallel groundwater flow model. Advances in Water Resources 2006; 29: 945-958.

Kollet SJ, Maxwell RM, Woodward CS, Smith S, Vanderborght J, Vereecken H, et al. Proof of concept of regional scale hydrologic simulations at hydrologic resolution utilizing massively parallel computer resources. Water Resources Research 2010; 46: 7.

Kratzert F, Klotz D, Brenner C, Schulz K, Herrnegger M. Rainfall–runoff modelling using long short-term memory (LSTM) networks. Hydrology and Earth System Sciences 2018; 22: 6005-6022.

Kroszynski UI, Dagan G. Well pumping in unconfined aquifers: The influence of the unsaturated zone. Water Resources Research 1975; 11: 479-490.

Krutz L, Senseman S, Zablotowicz R, Matocha M. Reducing herbicide runoff from agricultural fields with vegetative filter strips: a review. Weed Science 2005; 53: 353-367.

Kulanuwat L, Chantrapornchai C, Maleewong M, Wongchaisuwat P, Wimala S, Sarinnapakorn K, et al. Anomaly detection using a sliding window technique and data imputation with machine learning for hydrological time series. Water 2021; 13: 1862.

Le XH, Ho HV, Lee G, Jung S. Application of Long Short-Term Memory (LSTM) Neural Network for Flood Forecasting. Water 2019; 11.

Lemieux JM, Sudicky EA, Peltier WR, Tarasov L. Dynamics of groundwater recharge and seepage over the Canadian landscape during the Wisconsinian glaciation. Journal of Geophysical Research-Earth Surface 2008; 113.

Lewandowski J, Meinikmann K, Nutzmann G, Rosenberry DO. Groundwater - the disregarded component in lake water and nutrient budgets. Part 2: effects of groundwater on nutrients. Hydrological Processes 2015; 29: 2922-2955.

Li D, Marshall L, Liang Z, Sharma A, Zhou Y. Characterizing distributed hydrological model residual errors using a probabilistic long short-term memory network. Journal of Hydrology 2021a; 603.

Li H, Jiao JJ. Analytical studies of groundwater-head fluctuation in a coastal confined aquifer overlain by a semi-permeable layer with storage. Advances in Water Resources 2001; 24: 565-573.

Li H, Wang X. Submarine groundwater discharge: A review. Advances in Earth Science 2015; 30: 636.

Li J, Chen J-J, Zhan H, Li M-G, Xia X-H. Aquifer recharge using a partially penetrating well with clogging-induced permeability reduction. Journal of Hydrology 2020a; 590: 125391.

Li J, Zhan H, Huang G, You K. Tide-induced airflow in a two-layered coastal land with atmospheric pressure fluctuations. Advances in water resources 2011; 34: 649-658.

Li K, Nan T, Zeng X, Yin L, Wu J, Zhang J. Depth-dependent relation between hydraulic conductivity and electrical resistivity in geologic formations. Journal of Hydrology 2019; 578.

Li S, Zheng Y, Han F, Xu P, Chen A. Ecological Flow Management Identified as Leading Driver of Grassland Greening in the Gobi Desert Using Deep Learning. Geophysical Research Letters 2023; 50.

Li X, Wen Z, Zhan H, Wu F, Zhu Q. Laboratory observations for two-dimensional solute transport in an aquifer-aquitard system. Environmental Science and Pollution Research 2021b; 28: 38664-38678.

Li Y, Bao T, Chen H, Zhang K, Shu X, Chen Z, et al. A large-scale sensor missing data imputation framework for dams using deep learning and transfer learning strategy. Measurement 2021c; 178.

Li Y, Zhang Q, Liu X, Yao J. Water balance and flashiness for a large floodplain system: A case study of Poyang Lake, China. Science of The Total Environment 2020b; 710: 135499.

Liang X, Lettenmaier DP, Wood EF, Burges SJ. A simple hydrologically based model of land surface water and energy fluxes for general circulation models. Journal of Geophysical Research: Atmospheres 1994; 99: 14415-14428.

Liang X, Wood EF, Lettenmaier DP. Surface soil moisture parameterization of the VIC-2L model: Evaluation and modification. Global and Planetary Change 1996; 13: 195-206.

Liang X, Wood EF, Lettenmaier DP. Modeling ground heat flux in land surface parameterization schemes. Journal of Geophysical Research: Atmospheres 1999; 104: 9581-9600.

Liang X, Xie ZH, Huang MY. A new parameterization for surface and groundwater interactions and its impact on water budgets with the variable infiltration capacity (VIC) land surface model. Journal of Geophysical Research-Atmospheres 2003; 108: 17.

Liang X, Zhan H, Schilling K. Spatiotemporal responses of groundwater flow and aquifer-river exchanges to flood events. Water Resources Research 2018a; 54: 1513-1532.

Liang X, Zhan H, Zhang Y-K, Liu J. On the coupled unsaturated–saturated flow process induced by vertical, horizontal, and slant wells in unconfined aquifers. Hydrology and Earth System Sciences 2017a; 21: 1251-1262.

Liang X, Zhan H, Zhang Y-K, Schilling K. Base flow recession from unsaturated-saturated porous media considering lateral unsaturated discharge and aquifer compressibility. Water Resources Research 2017b; 53: 7832-7852.

Liang X, Zhan H, Zhang YK, Schilling K. Base flow recession from unsaturated-saturated porous media considering lateral unsaturated discharge and aquifer compressibility. Water Resources Research 2017c; 53: 7832-7852.

Liang X, Zhang Y-K. Analytic solutions to transient groundwater flow under time-dependent sources in a heterogeneous aquifer bounded by fluctuating river stage. Advances in water resources 2013a; 58: 1-9.

Liang X, Zhang YK, Liu J, Ma E, Zheng C. Solute transport with linear reactions in porous media with layered structure: A semianalytical model. Water Resources Research 2019; 55: 5102-5118.

Liang X, Zlotnik VA, Zhang YK, Xin P. Diagnostic analysis of bank storage effects on sloping floodplains. Water Resources Research 2020; 56: e2019WR026385.

Liang XY, Zhan HB, Liu J, Dong GM, Zhang YK. A simple method of transport parameter estimation for slug injecting tracer tests in porous media. Science of the Total Environment 2018b; 644: 1536-1546.

Liang XY, Zhan HB, Zhang YK, Schilling K. Base flow recession from unsaturated-saturated porous media considering lateral unsaturated discharge and aquifer compressibility. Water Resources Research 2017d; 53: 7832-7852.

Liang XY, Zhang YK. A new analytical method for groundwater recharge and discharge estimation. Journal of Hydrology 2012; 450: 17-24.

Liang XY, Zhang YK. Analytic solutions to transient groundwater flow under time-dependent sources in a heterogeneous aquifer bounded by fluctuating river stage. Advances in Water Resources 2013b; 58: 1-9.

Liao F, Wang G, Shi Z, Cheng G, Kong Q, Mu W, et al. Estimation of groundwater discharge and associated chemical fluxes into Poyang Lake, China: approaches using stable isotopes (δD and δ18O) and radon. Hydrogeology Journal 2018; 26: 1625-1638.

Liu D, Jiang Q, Shi W, Chen Q, Lee JY. Hyporheic exchange mechanism driven by flood wave. Hydrological Processes 2020a; 34: 5429-5440.

Liu W, Bailey RT, Andersen HE, Jeppesen E, Park S, Thodsen H, et al. Assessing the impacts of groundwater abstractions on flow regime and stream biota: Combining SWAT-MODFLOW with flow-biota empirical models. Science of the Total Environment 2020b; 706: 11.

Luijendijk E, Gleeson T, Moosdorf N. Fresh groundwater discharge insignificant for the world's oceans but important for coastal ecosystems. Nat Commun 2020; 11: 1260.

Luo X, Kuang XX, Jiao JJ, Liang SH, Mao R, Zhang XL, et al. Evaluation of lacustrine groundwater discharge, hydrologic partitioning, and nutrient budgets in a proglacial lake in the Qinghai-Tibet Plateau: using Rn-222 and stable isotopes. Hydrology and Earth System Sciences 2018; 22: 5579-5598.

Ma Y, Montzka C, Naz BS, Kollet S. Advancing AI-based pan-European groundwater monitoring. Environmental Research Letters 2022; 17.

Malama B, Kuhlman KL, Barrash W, Cardiff M, Thoma M. Modeling slug tests in unconfined aquifers taking into account water table kinematics, wellbore skin and inertial effects. Journal of Hydrology 2011; 408: 113-126.

Mao Z, Jagtap AD, Karniadakis GE. Physics-informed neural networks for high-speed flows. Computer Methods in Applied Mechanics and Engineering 2020; 360.

Maxwell RM, Condon LE. Connections between groundwater flow and transpiration partitioning. Science 2016; 353: 377-380.

Maxwell RM, Condon LE, Melchior P. A Physics-Informed, Machine Learning Emulator of a 2D Surface Water Model: What Temporal Networks and Simulation-Based Inference Can Help Us Learn about Hydrologic Processes. Water 2021; 13.

Maxwell RM, Kollet SJ, Smith SG, Woodward CS, Falgout RD, Ferguson IM, et al. ParFlow user's manual. International Ground Water Modeling Center Report GWMI 2009; 1: 129.

Mayer PM, Reynolds Jr SK, McCutchen MD, Canfield TJ. Meta-analysis of nitrogen removal in riparian buffers. Journal of environmental quality 2007; 36: 1172-1180.

McCallum JL, Shanafield M. Residence times of stream-groundwater exchanges due to transient stream stage fluctuations. Water Resources Research 2016; 52: 2059-2073.

McDermott D. A critique of pure reason 1. Computational intelligence 1987; 3: 151-160.

McKenzie T, Dulai H, Lee J, Dimova NT, Santos IR, Zhang B, et al. Using Deep Learning to Model the Groundwater Tracer Radon in Coastal Waters. Water Resources Research 2023; 59: 14.

Meinikmann K, Hupfer M, Lewandowski J. Phosphorus in groundwater discharge - A potential source for lake eutrophication. Journal of Hydrology 2015; 524: 214-226.

Miche M, Studerus E, Meyer AH, Gloster AT, Beesdo-Baum K, Wittchen HU, et al. Prospective prediction of suicide attempts in community adolescents and young adults, using regression methods and machine learning. Journal of Affective Disorders 2020; 265: 570-578.

Mo S, Zhong Y, Forootan E, Shi X, Feng W, Yin X, et al. Hydrological Droughts of 2017-2018 Explained by the Bayesian Reconstruction of GRACE(-FO) Fields. Water Resources Research 2022; 58.

Monachesi LB, Guarracino L. Exact and approximate analytical solutions of groundwater response to tidal fluctuations in a theoretical inhomogeneous coastal confined aquifer. Hydrogeology Journal 2011; 19.

Muller S, Schuler L, Zech A, Hesse F. GSTools v1.3: a toolbox for geostatistical modelling in Python. Geoscientific Model Development 2022; 15: 3161-3182.

Muller T, Gros J, Leibold P, Al-Balushi H, Petermann E, Schmidt M, et al. Autonomous Large-Scale Radon Mapping and Buoyant Plume Modeling Quantify Deep Submarine Groundwater Discharge: A Novel Approach Based on a Self-Sufficient Open Ocean Vehicle. Environ Sci Technol 2023; 57: 6540-6549.

Naiman RJ, Decamps H. The ecology of interfaces: Riparian zones. Annual Review of Ecology and Systematics 1997; 28: 621-658.

Napolitano G, Serinaldi F, See L. Impact of EMD decomposition and random initialisation of weights in ANN hindcasting of daily stream flow series: An empirical examination. Journal of Hydrology 2011; 406: 199-214.

Narasimhan TN. Hydrological Cycle and Water Budgets. In: Likens GE, editor. Encyclopedia of Inland Waters. Academic Press, Oxford, 2009, pp. 714-720.

Neuman SP. Theory of flow in unconfined aquifers considering delayed response of the water table. Water Resources Research 1972a; 8: 1031-1045.

Neuman SP. THEORY OF FLOW IN UNCONFINED AQUIFERS CONSIDERING DELAYED RESPONSE OF WATER TABLE. Water Resources Research 1972b; 8: 1031-+.

Nilsson C, Berggren K. Alterations of riparian ecosystems caused by river regulation: Dam operations have caused global-scale ecological changes in riparian ecosystems. How to protect river environments and human needs of rivers remains one of the most important questions of our time. BioScience 2000; 50: 783-792.

Nilsson NJ. Artificial intelligence: a new synthesis: Morgan Kaufmann, 1998.

Niu MY, Horesh L, Chuang I. Recurrent neural networks in the eye of differential equations. arXiv preprint arXiv:1904.12933 2019.

Ou Y, Wang X, Wang L, Rousseau AN. Landscape influences on water quality in riparian buffer zone of drinking water source area, Northern China. Environmental Earth Sciences 2016; 75: 1-13.

Özisik MN. Boundary value problems of heat conduction. Scranton,: International Textbook Co., 1968.

Painter SL, Coon ET, Atchley AL, Berndt M, Garimella R, Moulton JD, et al. Integrated surface/subsurface permafrost thermal hydrology: Model formulation and proof-of-concept simulations. Water Resources Research 2016; 52: 6062-6077.

Pan SJ, Yang Q. A Survey on Transfer Learning. IEEE Transactions on Knowledge and Data Engineering 2010; 22: 1345-1359.

Paniconi C, Putti M. A comparison of Picard and Newton iteration in the numerical solution of multidimensional variably saturated flow problems. Water Resources Research 1994; 30: 3357-3374.

Paniconi C, Wood EF. A detailed model for simulation of catchment scale subsurface hydrologic processes. Water Resources Research 1993; 29: 1601-1620.

Partington D, Brunner P, Simmons CT, Werner AD, Therrien R, Maier HR, et al. Evaluation of outputs from automated baseflow separation methods against simulated baseflow from a physically based, surface water-groundwater flow model. Journal of Hydrology 2012; 458: 28-39.

Pearson K. On lines and planes of closest fit to systems of points in space. Philosophical Magazine 1901; 2: 559-572.

Pedretti D, Barahona-Palomo M, Bolster D, Sanchez-Vila X, Fernandez-Garcia D. A quick and inexpensive method to quantify spatially variable infiltration capacity for artificial recharge ponds using photographic images. Journal of Hydrology 2012; 430: 118-126.

Phoon K-K, Zhang W. Future of machine learning in geotechnics. Georisk: Assessment and Management of Risk for Engineered Systems and Geohazards 2023; 17: 7-22.

Pikul MF, Street RL, Remson I. A numerical model based on coupled one-dimensional Richards and Boussinesq equations. Water Resources Research 1974; 10: 295-302.

Poole DL, Mackworth AK. Artificial Intelligence: foundations of computational agents: Cambridge University Press, 2010.

Prantikos K, Chatzidakis S, Tsoukalas LH, Heifetz A. Physics-informed neural network with transfer learning (TL-PINN) based on domain similarity measure for prediction of nuclear reactor transients. Scientific Reports 2023; 13: 16840.

Pryshlak TT, Sawyer AH, Stonedahl SH, Soltanian MR. Multiscale hyporheic exchange through strongly heterogeneous sediments. Water Resources Research 2015; 51: 9127-9140.

Qin C, Zhao W, Zhong K, Chen W. Prediction of longwall mining-induced stress in roof rock using LSTM neural network and transfer learning method. Energy Science & Engineering 2022; 10: 458-471.

Raab C, Schleif FM. Sparse Transfer Classification for Text Documents. 41st German Conference on Artificial Intelligence (AI). 11117. Springer International Publishing Ag, Berlin, GERMANY, 2018, pp. 169-181.

Raghu M, Poole B, Kleinberg J, Ganguli S, Sohl-Dickstein J. On the expressive power of deep neural networks. international conference on machine learning. PMLR, 2017, pp. 2847-2854.

Raissi M, Perdikaris P, Karniadakis GE. Physics-informed neural networks: A deep learning framework for solving forward and inverse problems involving nonlinear partial differential equations. Journal of Computational Physics 2019; 378: 686-707.

Rathore SS, Lu C, Luo J. A semianalytical method to fast delineate seawater-freshwater interface in two-dimensional heterogeneous coastal aquifers. Water Resources Research 2020; 56: e2020WR027197.

Rathore SS, Zhao Y, Lu C, Luo J. Defining the effect of stratification in coastal aquifers using a new parameter. Water Resources Research 2018; 54: 5948-5957.

Ray DK, Duckles JM, Pijanowski BC. The Impact of Future Land Use Scenarios on Runoff Volumes in the Muskegon River Watershed. Environmental Management 2010; 46: 351-366.

Razavi S, Tolson BA, Burn DH. Review of surrogate modeling in water resources. Water Resources Research 2012; 48.

Refsgaard JC, Christensen S, Sonnenborg TO, Seifert D, Højberg AL, Troldborg L. Review of strategies for handling geological uncertainty in groundwater flow and transport modeling. Advances in Water Resources 2012; 36: 36-50.

Reichstein M, Camps-Valls G, Stevens B, Jung M, Denzler J, Carvalhais N, et al. Deep learning and process understanding for data-driven Earth system science. Nature 2019; 566: 195-204.

Robert A. Characteristics of velocity profiles along riffle-pool sequences and estimates of bed shear stress. Geomorphology 1997; 19: 89-98.

Robinson NA, Xi W, Harmon L, Wegmueller S. Dictionary of environmental and climate change law: Edward Elgar Publishing, 2013.

Rosenberry DO, Lewandowski J, Meinikmann K, Nutzmann G. Groundwater - the disregarded component in lake water and nutrient budgets. Part 1: effects of groundwater on hydrology. Hydrological Processes 2015; 29: 2895-2921.

Rozantsev A, Salzmann M, Fua P. Beyond sharing weights for deep domain adaptation. IEEE transactions on pattern analysis and machine intelligence 2018; 41: 801-814.

Rumynin V, Leskova P, Sindalovskiy L, Nikulenkov A. Effect of depth-dependent hydraulic conductivity and anisotropy on transit time distributions. Journal of Hydrology 2019; 579: 124161.

Saffi M. Analytic solution to a one-dimensional, leaky, heterogeneous transient aquifer model. Hydrological Sciences Journal 2014; 59: 138-153.

Samani N, Sedghi MM. Semi-analytical solutions of groundwater flow in multi-zone (patchy) wedge-shaped aquifers. Advances in Water Resources 2015; 77: 1-16.

Samuel A. Some studies in machine learning using the game of checkers. Reprinted in EA Feigenbaum & J. Feldman (Eds.)(1963). Computers and thought. McGraw-Hill, 1959.

Sandu MA, Virsta A. Applicability of MIKE SHE to Simulate Hydrology in Argesel River Catchment. 4th International Conference on Agriculture for Life, Life for Agriculture. 6. Elsevier Science Bv, Bucharest, ROMANIA, 2015, pp. 517-524.

Sarinnapakorn K, Kubat M. Combining subclassifiers in text categorization: A DST-based solution and a case study. Ieee Transactions on Knowledge and Data Engineering 2007; 19: 1638-1651.

Sawyer A, Kaplan L, Lazareva O, Michael H. Hydrologic dynamics and geochemical responses within a floodplain aquifer and hyporheic zone during Hurricane Sandy. Water Resources Research 2014; 50: 4877-4892.

Sawyer AH, Cardenas MB. Hyporheic flow and residence time distributions in heterogeneous cross-bedded sediment. Water Resources Research 2009; 45.

Schilling K, Zhang Y, Drobney P. Water table fluctuations near an incised stream, Walnut Creek, Iowa. Journal of Hydrology 2004; 286: 236-248.

Sedghi MM, Zhan H. Groundwater flow to a general well configuration in an unconfined aquifer overlying a fractured bedrock. Journal of Hydrology 2019; 575: 569-586.

Sedghi MM, Zhan H. Groundwater flow to a well in a strip-shaped unconfined-fractured aquifer system with a transition zone. Journal of Hydrology 2021; 596: 126087.

Shen C. A Transdisciplinary Review of Deep Learning Research and Its Relevance for Water Resources Scientists. Water Resources Research 2018.

Singh SK. Aquifer response to sinusoidal or arbitrary stage of semipervious stream. Journal of Hydraulic Engineering 2004; 130: 1108-1118.

Smith RE, Woolhise.Da. OVERLAND FLOW ON AN INFILTRATING SURFACE. Transactions-American Geophysical Union 1970; 51: 755-&.

Solomatine DP, Ostfeld A. Data-driven modelling: some past experiences and new approaches. Journal of hydroinformatics 2008; 10: 3-22.

Solomatine DP, Shrestha DL. A novel method to estimate model uncertainty using machine learning techniques. Water Resources Research 2009; 45.

Srisutthiyakorn N. Deep-learning methods for predicting permeability from 2D/3D binary-segmented images. SEG technical program expanded abstracts 2016. Society of Exploration Geophysicists, 2016, pp. 3042-3046.

Srivastava N, Hinton G, Krizhevsky A, Sutskever I, Salakhutdinov R. Dropout: A Simple Way to Prevent Neural Networks from Overfitting. Journal of Machine Learning Research 2014; 15: 1929-1958.

Stehfest H. Algorithm 368: Numerical inversion of Laplace transforms [D5]. Communications of the ACM 1970; 13: 47-49.

Stets EG, Winter TC, Rosenberry DO, Striegl RG. Quantification of surface water and groundwater flows to open- and closed-basin lakes in a headwaters watershed using a descriptive oxygen stable isotope model. Water Resources Research 2010; 46.

Su X, Yeh T-CJ, Shu L, Li K, Brusseau ML, Wang W, et al. Scale issues and the effects of heterogeneity on the dune-induced hyporheic mixing. Journal of Hydrology 2020; 590: 125429.

Sudicky EA, Jones JP, Park YJ, Brookfield AE, Colautti D. Simulating complex flow and transport dynamics in an integrated surface-subsurface modeling framework. Geosciences Journal 2008; 12: 107-122.

Sun AY, Scanlon BR, Zhang Z, Walling D, Bhanja SN, Mukherjee A, et al. Combining Physically Based Modeling and Deep Learning for Fusing GRACE Satellite Data: Can We Learn From Mismatch? Water Resources Research 2019; 55: 1179-1195.

Sun D, Zhan H. Pumping induced depletion from two streams. Advances in Water Resources 2007; 30: 1016-1026.

Sun X, Du Y, Deng Y, Fan H, Tao Y, Ma T. Contribution of groundwater discharge and associated contaminants input to Dongting Lake, Central China, using multiple tracers (222Rn, 18O, Cl−). Environmental Geochemistry and Health 2021; 43: 1239-1255.

Talbot A. The accurate numerical inversion of Laplace transforms. IMA Journal of Applied Mathematics 1979; 23: 97-120.

Tartakovsky AM, Marrero CO, Perdikaris P, Tartakovsky GD, Barajas-Solano D. Physics-Informed Deep Neural Networks for Learning Parameters and Constitutive Relationships in Subsurface Flow Problems. Water Resources Research 2020; 56.

Taylor KL, Grace JB. THE EFFECTS OF VERTEBRATE HERBIVORY ON PLANT COMMUNITY STRUCTURE IN THE COASTAL MARSHES OF THE PEARL RIVER, LOUISIANA, USA. Wetlands 1995; 15: 68-73.

Therrien R, McLaren R, Sudicky E, Panday S. HydroGeoSphere: A three-dimensional numerical model describing fully-integrated subsurface and surface flow and solute transport. Groundwater Simulations Group, University of Waterloo, Waterloo, ON 2010; 830.

Thomas H. Improved methods for national water assessment, water resource contract WR15249270, USGS unnumbered series, final report, Harvard Water Resour. Group, 1981.

Thorne CR, Tovey NK. Stability of composite river banks. Earth Surface Processes and Landforms 1981; 6: 469-484.

Tran H, Leonarduzzi E, De la Fuente L, Hull RB, Bansal V, Chennault C, et al. Development of a Deep Learning Emulator for a Distributed Groundwater–Surface Water Model: ParFlow-ML. Water 2021; 13.

Vandaele R, Dance SL, Ojha V. Deep learning for automated river-level monitoring through river-camera images: an approach based on water segmentation and transfer learning. Hydrology and Earth System Sciences 2021; 25: 4435-4453.

Walton WC. Progress in analytical groundwater modeling. Journal of Hydrology 1979; 43: 149-159.

Wang N, Chang H, Zhang D. Surrogate and inverse modeling for two-phase flow in porous media via theory-guided convolutional neural network. Journal of Computational Physics 2022; 466.

Wang N, Zhang D, Chang H, Li H. Deep learning of subsurface flow via theory-guided neural network. Journal of Hydrology 2020a; 584.

Wang NZ, Chang HB, Zhang DX. Deep-Learning-Based Inverse Modeling Approaches: A Subsurface Flow Example. Journal of Geophysical Research-Solid Earth 2021a; 126.

Wang NZ, Chang HB, Zhang DX. Efficient Uncertainty Quantification and Data Assimilation via Theory-Guided Convolutional Neural Network. Spe Journal 2021b; 26: 4128-4156.

Wang Q, Zhan H, Tang Z. Two-dimensional flow response to tidal fluctuation in a heterogeneous aquifer-aquitard system. Hydrological Processes 2015; 29: 927-935.

Wang QR, Huang J, Liu RM, Men C, Guo LJ, Miao YX, et al. Sequence-based statistical downscaling and its application to hydrologic simulations based on machine learning and big data. Journal of Hydrology 2020b; 586: 15.

Wang W, Squillace P. Herbicide interchange between a stream and the adjacent alluvial aquifer. Environmental science & technology 1994; 28: 2336-2344.

Wang WC, Chau KW, Cheng CT, Qiu L. A comparison of performance of several artificial intelligence methods for forecasting monthly discharge time series. Journal of Hydrology 2009; 374: 294-306.

Wang Z, Lu W, Chang Z, Luo J. A combined search method based on a deep learning combined surrogate model for groundwater DNAPL contamination source identification. Journal of Hydrology 2023; 616.

Ward AS, Gooseff MN, Johnson PA. How can subsurface modifications to hydraulic conductivity be designed as stream restoration structures? Analysis of Vaux's conceptual models to enhance hyporheic exchange. Water Resources Research 2011; 47.

Webster J, Moran ST, Davey R. Growth and sporulation of Tricladium chaetocladium and Lunulospora curvula in relation to temperature. Transactions of the British Mycological Society 1976; 67: 491-495.

Wen Z, Liu K, Chen XL. Approximate analytical solution for non-Darcian flow toward a partially penetrating well in a confined aquifer. Journal of Hydrology 2013; 498: 124-131.

Willard JD, Read JS, Appling AP, Oliver SK, Jia X, Kumar V. Predicting Water Temperature Dynamics of Unmonitored Lakes With Meta-Transfer Learning. Water Resources Research 2021; 57.

Willcox KE, Ghattas O, Heimbach P. The imperative of physics-based modeling and inverse theory in computational science. Nature Computational Science 2021; 1: 166-168.

Wilson AM. Fresh and saline groundwater discharge to the ocean: A regional perspective. Water Resources Research 2005; 41.

Winter TC. Relation of streams, lakes, and wetlands to groundwater flow systems. Hydrogeology Journal 1999; 7: 28-45.

Winter TC, Harvey JW, Franke OL, Alley WM. Ground water and surface water: a single resource. Vol 1139: DIANE Publishing Inc., 1998.

Woolhiser DA, Smith RE, Giraldez JV. Effects of spatial variability of saturated hydraulic conductivity on Hortonian overland flow. Water Resources Research 1996; 32: 671-678.

Wu J, Yin X, Xiao H. Seeing permeability from images: fast prediction with convolutional neural networks. Sci Bull (Beijing) 2018; 63: 1215-1222.

Wunsch A, Liesch T, Broda S. Deep learning shows declining groundwater levels in Germany until 2100 due to climate change. Nature Communications 2022; 13: 1221.

Xiang Z, Yan J, Demir I. A rainfall-runoff model with LSTM-based sequence-to-sequence learning. Water resources research 2020; 56: e2019WR025326.

Xiong R, Zheng Y, Chen N, Tian Q, Liu W, Han F, et al. Predicting Dynamic Riverine Nitrogen Export in Unmonitored Watersheds: Leveraging Insights of AI from Data-Rich Regions. Environ Sci Technol 2022; 56: 10530-10542.

Xu H, Tian Z, Sun L, Ye Q, Ragno E, Bricker J, et al. Compound flood impact of water level and rainfall during tropical cyclone periods in a coastal city: the case of Shanghai. Natural Hazards and Earth System Sciences 2022a; 22: 2347-2358.

Xu T, Liang F. Machine learning for hydrologic sciences: An introductory overview. WIREs Water 2021; 8.

Xu W, Chen J, Zhang XJ. Scale Effects of the Monthly Streamflow Prediction Using a State-of-the-art Deep Learning Model. Water Resources Management 2022b; 36: 3609-3625.

Xu W, Meng FL, Guo WS, Li X, Fu GT. Deep Reinforcement Learning for Optimal Hydropower Reservoir Operation. Journal of Water Resources Planning and Management 2021; 147: 15.

Yang C-H, Wu C-H, Hsieh C-M, Wang Y-C, Tsen I-F, Tseng S-H. Deep learning for imputation and forecasting tidal level. IEEE Journal of Oceanic Engineering 2021; 46: 1261-1271.

Yeh H-D, Kuo C-C. An analytical solution for heterogeneous and anisotropic anticline reservoirs under well injection. Advances in water resources 2010; 33: 419-429.

Yeh TCJ, Liu S. Hydraulic tomography: Development of a new aquifer test method. Water Resources Research 2000; 36: 2095-2105.

Yoon H, Jun SC, Hyun Y, Bae GO, Lee KK. A comparative study of artificial neural networks and support vector machines for predicting groundwater levels in a coastal aquifer. Journal of Hydrology 2011; 396: 128-138.

Yosinski J, Clune J, Bengio Y, Lipson H. How transferable are features in deep neural networks? Advances in neural information processing systems 2014; 27.

Yuan X, Chen C, Lei X, Yuan Y, Muhammad Adnan R. Monthly runoff forecasting based on LSTM–ALO model. Stochastic Environmental Research and Risk Assessment 2018; 32: 2199-2212.

Zakian V. Numerical inversion of Laplace transform. Electronics Letters 1969; 5: 120-121.

Zhai H, Benson CH. The log-normal distribution for hydraulic conductivity of compacted clays: Two or three parameters? Geotechnical & Geological Engineering 2006; 24: 1149-1162.

Zhan H, Zlotnik VA. Groundwater flow to a horizontal or slanted well in an unconfined aquifer. Water Resources Research 2002a; 38: 13-1-13-11.

Zhan HB, Zlotnik VA. Groundwater flow to a horizontal or slanted well in an unconfined aquifer. Water Resources Research 2002b; 38: 11.

Zhang E, Dao M, Karniadakis GE, Suresh S. Analyses of internal structures and defects in materials using physics-informed neural networks. Sci Adv 2022a; 8: eabk0644.

Zhang J, Liang X, Zhang Y-K, Chen X, Ma E, Schilling K. Groundwater responses to recharge and flood in riparian zones of layered aquifers: An analytical model. Journal of Hydrology 2022b; 614.

Zhang S, Ding L, Xie M, He X, Yang R, Tong C. Reliability analysis of slope stability by neural network (NN), principal component analysis (PCA), and transfer learning (TL) techniques. Journal of Rock Mechanics and Geotechnical Engineering 2023.

Zhang X, Zhu Y, Wang J, Ju L, Qian Y, Ye M, et al. GW-PINN: A deep learning algorithm for solving groundwater flow equations. Advances in Water Resources 2022c; 165.

Zhao G, Pang B, Xu Z, Cui L, Wang J, Zuo D, et al. Improving urban flood susceptibility mapping using transfer learning. Journal of Hydrology 2021; 602.

Zhou X, Shi P, Sheil B, Suryasentana S. Knowledge-based U-Net and transfer learning for automatic boundary segmentation. Advanced Engineering Informatics 2024; 59: 102243.

Zhou Y. Real-time probabilistic forecasting of river water quality under data missing situation: Deep learning plus post-processing techniques. Journal of Hydrology 2020; 589.

Zhu S, Zhou JZ, Ye L, Meng CQ. Streamflow estimation by support vector machine coupled with different methods of time series decomposition in the upper reaches of Yangtze River, China. Environmental Earth Sciences 2016; 75.

Zhu Y, Shi LS, Lin L, Yang JZ, Ye M. A fully coupled numerical modeling for regional unsaturated-saturated water flow. Journal of Hydrology 2012; 475: 188-203.

Zlotnik VA, Huang H. Effect of shallow penetration and streambed sediments on aquifer response to stream stage fluctuations (analytical model). Ground Water 1999; 37: 599-599.